U.PORTO

FEUP FACULDADE DE ENGENHARIA
UNIVERSIDADE DO PORTO

The Numerical Analysis of Airplane Windshields due to Bird Strike: A Static Study

João Pedro Monteiro Cabral de Noronha

Thesis submitted to Faculdade de Engenharia da Universidade do Porto as a requirement to obtain the MSc Degree in Mechanical Engineering

Under the supervision of:

Professor Jorge Américo Oliveira Pinto Belinha

Professor Lúcia Maria de Jesus Simas Dinis

Professor Renato Manuel Natal Jorge

February, 2016

“*Sugar is sweet, and so is honey. Macho Madness is on a roll, and it can't be stopped, no***”**

“Macho Man” Randy Savage

Acknowledgements/Agradecimentos

Ao Professor Jorge Belinha, pelo apoio incansável durante este último semestre. Não só por todas as dúvidas (mesmo aquelas que já não faziam sentido eu ainda ter) que esclareceu em relação à tese, mas principalmente por ficar tão entusiasmado quanto eu sempre que os resultados batiam certo. O meu muito obrigado.

Ao Marco Marques, por toda a ajuda prestada ao longo da tese, e pelas inúmeras pausas para café para espairecer, muito obrigado.

Aos meus amigos, Diogo, Eduardo, Jesus, João, Mário, Ripas, Salvador, Touço e às meninas Carolina, Inês, Sofia e Susana que me acompanharam durante estes 7 anos. Não teria sido a mesma coisa sem vocês. Levo histórias para a vida. Se me senti em casa desde o início devo-o a vocês. Sem esquecer também a Roxanne, não só por me ter dado teto nos últimos 2 anos, mas também pelas ótimas sugestões que deu para este trabalho. Obrigado a todos.

Aos meus amigos, Alexandre, Caldeira, Diogo e Tonhadas por todo o apoio, mesmo que muitas vezes online devido à distância. Fazem com que voltar a casa seja sempre um prazer. Muito obrigado.

Ao meu irmão Ricardo, por ser provavelmente a pessoa mais interessante que conheço e por me fazer querer sempre viver a vida ao máximo. A Nova Zelândia está à nossa espera para apanhar amoras. Obrigado.

À Cristina, por me fazer acordar todos os dias com um sorriso. Obrigado por seres a minha motivação para querer dar sempre um pouco mais e por me obrigares a sair da cama todas as manhãs.

Aos meus pais, sem os quais nada disto seria possível. À minha Mãe, por ter tomado conta de mim desde o dia em que eu nasci e ao meu Pai por ser o meu exemplo. Obrigado por tudo.

Por fim, à minha avó Filomena, que sempre cuidou tão bem de mim e é a melhor cozinheira do mundo. Obrigado!

Funding

The author truly acknowledges the work conditions provided by the Applied Mechanics Division (SMAp) of the department of mechanical engineering (DEMec) of FEUP and the computational means provided by the inter-institutional project: “Advanced materials for noise reduction: modeling, optimization and experimental validation” funded by the “Laboratório Associado de Energia Transportes e Aeronáutica”.

Contents

List of Figures

List of Tables

Abstract

Bird strike is a hazard to aviation as old as modern aviation itself, representing a risk to human safety. Because of this, windshields must be designed to resist a bird impact during flight. Experimental testing is usually conducted using a compressed air cannon that uses dead, standard-sized birds as ammunition in order to simulate a high speed bird impact. Although accurate, experimental testing is expensive and time consuming, therefore the use of numerical methods can be a powerful tool to assist in the design/ certification process.

Generally, the impact analysis is performed using the finite element method (FEM). This work proposes to use an alternative approximation methodology – meshless methods. These advanced discretization techniques permit to discretize the problem domain using only an unstructured nodal cloud. In this work, the considered meshless methods use the radial point interpolators to construct the shape functions, leading to interpolation functions possessing a virtual infinite continuity. The literature shows that, when compared with the FEM, meshless methods are capable of producing much more accurate and smoother variable fields.

Here, the bird strike impact is simulated by an instantaneous force applied in nine distinct locations of the windshield, respecting the direction and magnitude suggested in the literature. The numerical 3D model of the windshield was obtained reproducing commercial windshields, considering the multi-layer construction composing this aeronautic part. The 3D model was analysed considering an elasto-static approach assuming the classical 3D deformation theory. The results show that meshless methods are capable to produce more accurate and smooth displacement and stress fields when compared to low order finite element meshes.

Resumo

O impacto com aves durante o voo é um perigo para a aviação tão antigo como a própria aviação, representado um risco para a segurança humana. Devido a isto, os pára-brisas dos aviões têm que ser desenvolvidos de forma a resistir a estes impactos. Os testes experimentais são frequentemente feitos usando um canhão de ar comprimido, que usa aves mortas como munição de forma a simular um impacto com uma ave a alta velocidade. Embora sejam precisos, estes testes experimentais são caros e morosos e portanto, o uso de métodos numéricos funciona como uma poderosa ferramenta no auxílio ao projecto e ao processo de certificação destes componentes aeronáuticos.

Geralmente, esta análise de impacto é feita usando o método dos elementos finitos (MEF). Este trabalho propõe o uso de uma metodologia de aproximação alternativa – os métodos sem malha. Estas técnicas de discretização avançadas permitem discretizar o domínio do problema usando apenas uma nuvem nodal não estruturada. Neste trabalho, consideraram-se métodos sem malha que utilizam os interpoladores de pontos radiais para construir as funções de forma, dando origem a funções interpoladoras possuindo uma continuidade virtual infinita. A literatura mostra que, quando comparado com o MEF, os métodos sem malha são capazes de produzir campos de variáveis muito mais suaves e precisos.

Neste trabalho, o impacto da ave é simulado através de uma força instantânea aplicada em nove localizações distintas do pára-brisas, respeitando a direcção e a magnitude sugeridas na literatura. O modelo 3D do pára-brisas foi reproduzido a partir de pára-brisas de aviões comerciais, considerando a construção laminada destas estruturas aeronáuticas. O modelo 3D foi analisado considerando uma abordagem elasto-estática e assumindo a teoria clássica da deformação 3D. Os resultados mostram que os métodos sem malha são capazes de produzir campos de deslocamento e tensão mais precisos e suaves quando comparados com malhas de elementos finitos de baixa ordem.

Chapter 1

Introduction

Bird strike is a hazard to aviation as old as modern aviation itself. In fact, the first recorded bird strike took place in 1905 [1], a mere 2 years after the Wright brothers catapulted mankind into the modern age by taking off on a 12 second long propeller driven flight for the first time.

Although a lesser hazard to aviation when compared to loss of control in flight, runaway excursion or controlled flight into terrain, bird strike still poses a risk to human safety and therefore must be addressed [2].

Before an airplane is certified to fly, it must go through a whole host of tests in order to prove it meets the certification requirements [3]. This testing is usually done using a compressed air cannon that uses dead, standard-sized birds as ammunition in order to simulate a high speed bird impact [4]. Although accurate, experimental testing is costly and time consuming, so the use of numerical methods serves as a powerful tool to assist in the certification process.

1.1 Meshless Methods

The first seeds of the Finite Element Method (FEM) were planted in 1941 when the concept of elements was born [5], but it wasn't until 1956 that a group of engineers, all them connected to the aeronautical engineering, first solved a plane stress problem using triangular elements [6]. Their studies, along with the dawn of the digital age helped pave the way for the solution of complex structural analysis problems.

The FEM simplifies a complex problem, by dividing the problem's domain into smaller parts, called elements. The collection of elements forms a mesh, which contains, not only the elements but also the connectivity relations between each one [7]. However, due to being mesh-reliant, the FEM has some limitations. When analysing problems where large deformations occur, the mesh connectivity is hard to maintain, without highly distorting the mesh, which leads to inaccurate results. A solution to this would be

re-meshing but this is not only time consuming, but also represents high computational costs and often induces errors [8, 9].

Meshless methods were created with the intention of being an alternative to the FEM by eliminating the issues stated above. Furthermore, when analysing structural problems, stress and displacement fields produced with meshless methods are often much more uniform and close to the analytical solution than those created by low order (three and four nodes) element meshes. Unlike the FEM, which uses the element mesh in order to obtain the approximation, meshless methods build the approximation based on nothing but an arbitrary nodal set, without any prior knowledge of the relation between the nodes [9].

Meshless methods first appeared in 1977, with the introduction of the Smooth Particle Hydrodynamics Method (SPH) [10]. This is one of the oldest meshless methods in existence and was originally developed due to the desire to simulate the formation of binary star systems. In 1990 this method was extended to solid mechanics [11]. However, the SPH was based on a strong form. It wasn't until 1994 that a global weak form based meshless method was introduced with the appearance of the Element Free Galerkin Method (EFGM) [12], which remains one of the most popular meshless methods to this day. The EFGM was developed using the Diffuse Element Method (DEM) [13] as base, which by its turn was the first meshless method using the Moving Least Square (MLS) [14] approximants in the construction of the shape functions. Other important methods that appeared in the same period were the Reproducing Kernel Particle Method (RKPM) [15], which was based on the SPH, and the Meshless Local Petrov-Galerkin (MLPG) [16].

However, all of the previously mentioned methods use approximation shape functions, which means they lack the Kronecker delta function property, making the imposition of essential and natural boundary conditions difficult.

This was solved with the recent development of several interpolation meshless methods. In 2001, the Point Interpolation Method (PIM) [17, 18] was created. A year later, in order to simplify the computation of the shape functions, and to eliminate some singularities that occurred in the PIM, the Radial Point Interpolation Method (RPIM) [19, 20] was developed. The RPIM uses radial basis functions (RBF) combined with polynomial basis functions to construct the shape functions used in the integration of the partial differential equations. More recently, using the RPIM and the natural neighbours geometric concept as a starting point, the Natural Neighbour Radial Point Interpolation Method (NNRPIM) was developed [21].

1.1.1 Radial Point Interpolation Method

Since both the EFGM and the MLPG use the MLS approximation for the construction of shape functions, issues related to the imposition of essential and natural boundary conditions occur. With the intent of tackling the issues caused by these methods, the PIM was proposed and its advantages were clear [17, 18]. The PIM uses the influence-domain concept to establish the nodal connectivity, instead of the global domain of the problem, which improves nodal connectivity. Additionally, its shape functions possess the Kronecker delta property, which means that they pass through every single node, making them interpolation shape functions, which fixes the issue of the essential and natural boundary imposition. Another advantage is that its shape functions are much simpler, when compared to the MLS and much easier to obtain, which leads to higher computer efficiency. However, the PIM only employed polynomials as its basis functions and because of this some singularities could occur, as for example, the perfect alignment of the nodes would produce singular solutions in the shape function construction process [19, 20].

Because of this, this method evolved, and in 2002, the RPIM was proposed [19, 20]. This method combined a RBF with a polynomial basis function. The addition of radial basis functions removed the issue of possible singularities associated with meshless methods based on polynomial basis functions alone. Because of this, and together with having a high convergence rate, this method is still used to this day.

1.1.2 Natural Neighbour Radial Point Interpolation Method

The NNRPIM is the one of the most recent developments in Radial Point Interpolators (RPI). This method combines the RPI with the natural neighbours geometric concept.

The biggest difference between the NNRPIM and the RPIM is how the nodal connectivity is enforced. The concept of influence-domain, used in the RPIM, is substituted by an influence-cell. In order to obtain these influence cells, the NNRPIM uses mathematical concepts such as Voronoï Diagrams and the Delaunay tessellation. The NNRPIM shape functions, used in the Galerkin weak form, are then constructed following the RPIM procedure and thus, possess the Kronecker delta property. Because

of the way the nodal connectivity is enforced, both the displacement and the stress fields obtained are generally smoother and more accurate when compared to the results obtained with other methods. Additionally, this method can be defined as being a 'truly' meshless method, since it only requires the spatial location of the nodes to fully discretize problem domain, not needing any other information. Despite being a recent method, it has already been used in many different applications, such as the static analysis of 3D problems [22], the static analysis of isotropic and orthotropic plates [23], the functionally graded material plate analysis [24], the 3D shell-like approach for laminated plates and shells [25, 26], the dynamic analysis of several solid-mechanics problems [27-30], applications with material nonlinearity [31], thick plate analysis [32], analysis of laminated beams [33], large deformation analysis [34], bone tissue remodelling applications [35-43], axisymmetric analysis of circular plates [44], crack opening path prediction [45].

1.2 Objectives

- Perform an elasto-static analysis of airplane windshields against bird-strike events, using two of the most recent meshless methods in existence, the RPIM and the NNRPIM.

- Test and improve the meshless computational framework, developed at FEUP, which can perform both FEM and meshless methods analysis.

- Extend the use of meshless methods to airplane windshields for the first time.

- Draw further comparisons between the FEM and meshless methods.

1.3 Document structure

This thesis is composed of six major chapters: Introduction, Meshless Methods, Solid Mechanics Fundamentals, Benchmark Examples, Numerical Examples Conclusions and Future Works:

In the first chapter, **Introduction**, a brief state-of-the-art regarding meshless methods is given, with incidence on the RPIM and NNRPIM. The objectives of this work are defined.

In Chapter 2, **Meshless Methods**, the two meshless methods used in this work are thoroughly presented and their formulation is described.

In Chapter 3, **Solid Mechanics Fundamentals**, the basic notions of solid mechanics are presented and explained.

In Chapter 4, **Benchmark examples**, the software used on this thesis is presented and explained. Following this, several solid mechanics benchmark examples are studied, using the FEM, the RPIM and the NNRPIM and then compared against the analytical solution.

In Chapter 5, **Numerical Examples**, using the software described in the previous chapter, several windshield models are analysed, in a bird-strike event. This chapter contains all the results and discussion following this analysis.

In Chapter 6, **Conclusions and Future Works**, the main conclusions of this work are drawn and some recommendations for future works are given in the meshless methods field.

Chapter 2

Meshless Methods

This work was developed using two of the most recently developed meshless methods: The RPIM and the NNRPIM. In this chapter, after a brief description of the general meshless method procedure, both methods are presented and thoroughly explained. The chapter ends with the presentation of the RPI shape functions, which construction procedure is used by both methods.

2.1 General meshless method procedure

The large majority of meshless methods follow the same procedure. After the outline of the solid problem has been defined it is possible to identify both the essential and natural boundaries applied, as seen in Figure 2.1a. Next, it is possible to discretize the domain problem using a nodal set.

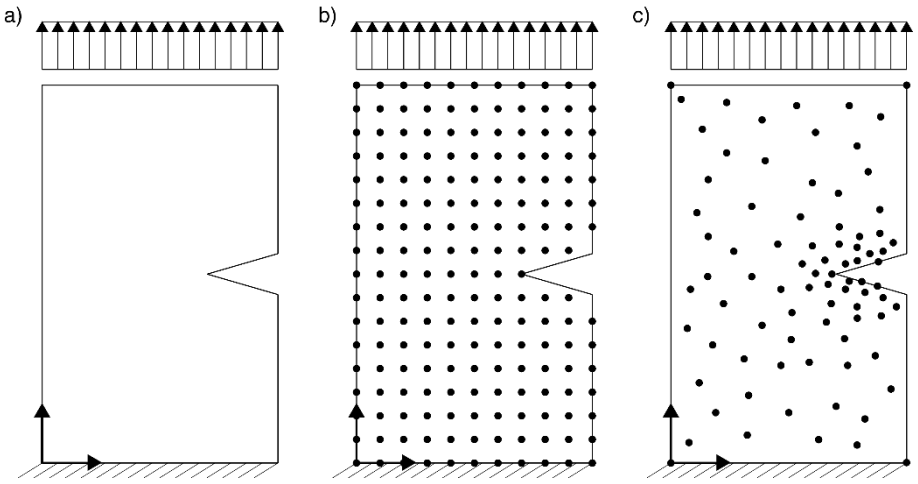

Figure 2.1 - a. Problem domain with the essential and natural boundaries applied. **b.** Regular nodal discretization. **c.** Irregular nodal discretization.

As shown in Figure 2.1b and 2.1c this nodal discretization can either be regular or irregular, which has a direct effect on the numerical analysis outcome, with the irregular discretization often presenting a lower accuracy. However, locations with predictable

stress concentrations, for example, the crack shown in Figure 2.1c, should have a higher nodal density. A way to tackle both the need for a regular mesh and the need for a higher nodal density is to add extra nodes, only on the locations with predictable stress concentrations while maintaining a regular mesh on the rest of the problem domain, therefore not increasing the computational cost significantly.

Following the problem domain discretization, it is possible to obtain the nodal connectivity. While in the FEM this is done using the predefined finite element mesh, in which the nodes belonging to the same element interact directly between themselves and the boundary nodes interact with boundary nodes of nearby elements, in meshless methods such connectivity is ensured by the overlapping of influence-domains, when it comes to RPIM and influence-cells, when it comes to NNRPIM.

The numerical integration takes place after this. A background integration mesh is constructed, which can be nodal dependent or independent, the later having a higher accuracy. On nodal dependent meshes, it is necessary to implement a stabilization method in order to achieve accurate results although this increases the computational cost [46-48]. On the other hand, this means the only information required by methods that use this integration scheme is the spatial location of the nodes, which makes these methods, truly meshless methods. After this has taken place, it is possible to obtain the field variables under study by using either approximation or interpolation shape functions. Both the RPIM and the NNRPIM use interpolation shape functions, based on the combination of radial basis functions (RBF) with polynomial basis functions.

2.2 RPIM Formulation

2.2.1 Influence-domains and nodal connectivity

After an initial nodal discretization of the problem domain, it is necessary to ensure the nodal connectivity between each and every node.

In order to do this it is first necessary to define areas, if the problem in study is two-dimensional (2D) or volumes, if the problem in study is three-dimensional (3D), that contain a certain number of nodes. This is shown for a 2D problem in Figure 2.2.

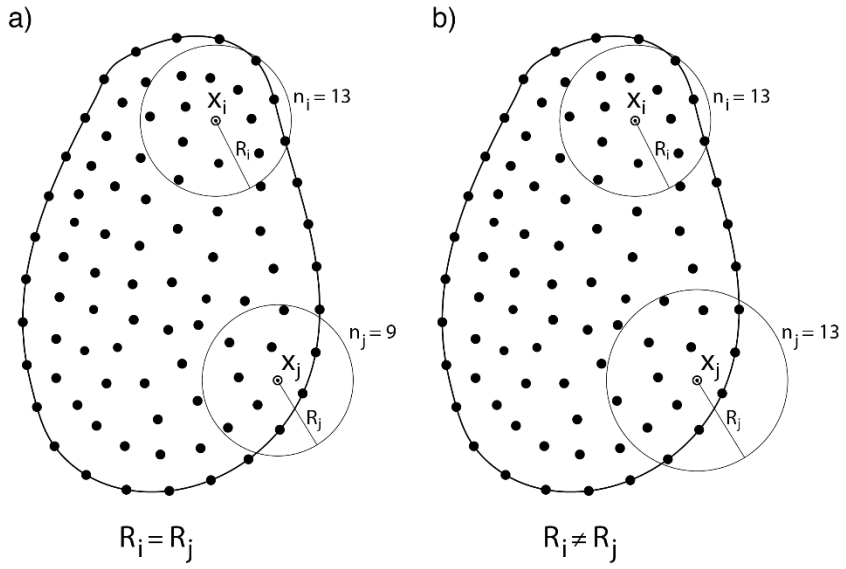

Figure 2.2 - a. Fixed size circular influence-domain. **b.** Variable size circular influence-domain.

Influence-domains can have a fixed or variable size, but the latter is advised since, fixed sized influence-domains often lead to an uneven number of nodes inside the influence-domain of different nodes, as seen in Figure 2.2a, which greatly reduces the numerical analysis accuracy. By using variable sized influence-domains, as seen in Figure 2.2b, it is possible to assure that every node's influence-domain contains the same number of nodes. This allows the construction of shape functions with the same degree of complexity. The literature recommends using between n=[9, 16] nodes inside the influence-domain for two-dimensional (2D) problems and n=[27, 70] nodes for 3D problems [12, 16, 17, 19]. The number of nodes inside the influence-domain does not depend on the density of the nodal discretizations and once selected, the value is valid for all domain discretizations within the same analysis.

2.2.2 Numerical integration

In the RPIM the differential equations are integrated using the Gauss-Legendre integration scheme. In order to do this, first a background mesh must be created. This background mesh can be composed of the cells created by connecting the nodes discretizing the problem domain (leading to either triangular or quadrilateral cells) as seen in Figure 2.3a and 2.3b, or a mesh larger than the problem domain, shown in

Figure 2.3c. In the case presented in Figure 2.3c, the integration points outside the problem domain have to be eliminated from the computation.

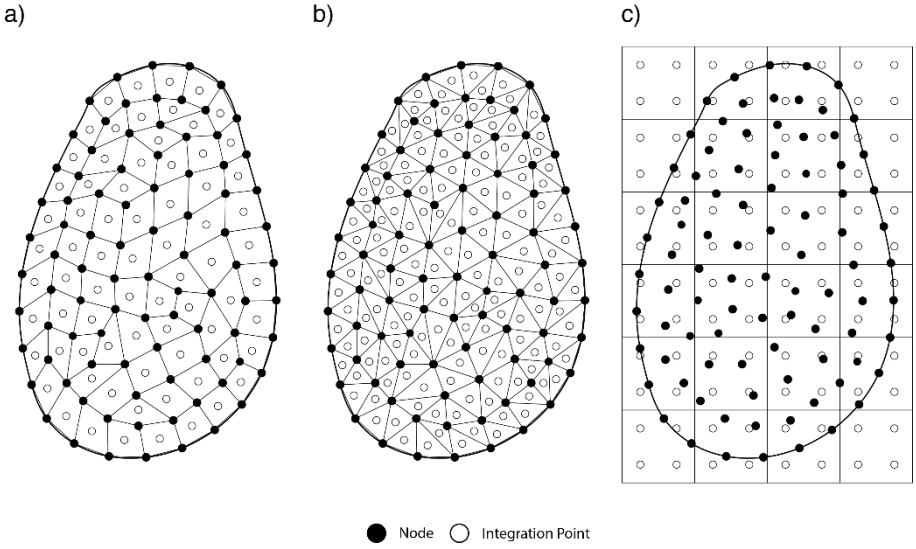

Figure 2.3 - a. Quadrilateral 'cell' background mesh with 1 integration point. **b.** Triangular 'cell' background mesh with 1 integration point. **c.** Quadrilateral grid background mesh with 4 integration points.

The cells of the background mesh can be triangular, (Fig 2.3b) or quadrilateral, (Fig 2.3a and Figure 2.3c). Inside of each one, it is possible to distribute integration points as Figure 2.4a and 2.4b show.

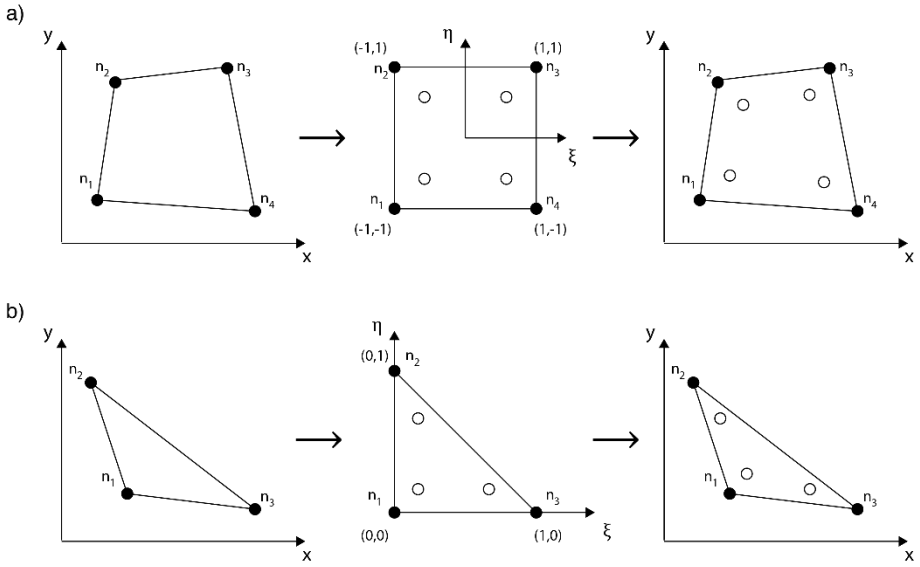

Figure 2.4 - a. Transformation of the initial quadrilateral cell into an isoparametric square shape and application of the 2x2 quadrature point rule followed by the return to the initial quadrilateral shape. **b.** Transformation of the initial triangle cell into an isoparametric triangle shape and application of the 3-point quadrature point rule followed by the return to the initial triangle shape

The following tables display the location and weights of the isoparametric integration points for quadrilateral and triangular 'element' background meshes respectively.

Table 2. 1 - Integration points coordinates and weights for quadrilateral 'cells' [49]

Points	ξ	η	Weight	Representation
a	0	0	4	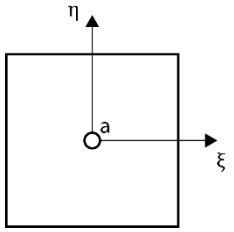
a	$-\frac{1}{\sqrt{3}}$	$-\frac{1}{\sqrt{3}}$	1	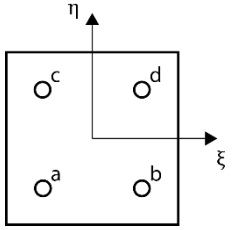
b	$+\frac{1}{\sqrt{3}}$	$-\frac{1}{\sqrt{3}}$	1	
c	$-\frac{1}{\sqrt{3}}$	$+\frac{1}{\sqrt{3}}$	1	
d	$+\frac{1}{\sqrt{3}}$	$+\frac{1}{\sqrt{3}}$	1	
a	$-\sqrt{3/5}$	$-\sqrt{3/5}$	$\frac{25}{81}$	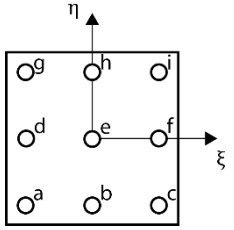
b	0	$-\sqrt{3/5}$	$\frac{40}{81}$	
c	$+\sqrt{3/5}$	$-\sqrt{3/5}$	$\frac{25}{81}$	
d	$-\sqrt{3/5}$	0	$\frac{40}{81}$	
e	0	0	$\frac{64}{81}$	
f	$+\sqrt{3/5}$	0	$\frac{40}{81}$	
g	$-\sqrt{3/5}$	$+\sqrt{3/5}$	$\frac{25}{81}$	
h	0	$+\sqrt{3/5}$	$\frac{40}{81}$	
i	$+\sqrt{3/5}$	$+\sqrt{3/5}$	$\frac{25}{81}$	

Table 2. 2 - Integration points coordinates and weights for triangular 'cells' [49]

Points	ξ	η	Weight	Representation
a	$\frac{1}{3}$	$\frac{1}{3}$	$\frac{1}{2}$	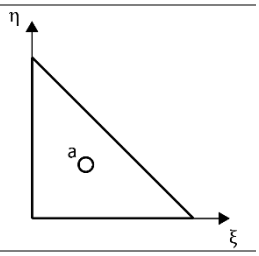
a	$\frac{1}{6}$	$\frac{1}{6}$	$\frac{1}{6}$	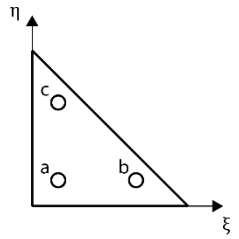
b	$\frac{2}{3}$	$\frac{1}{6}$	$\frac{1}{6}$	
c	$\frac{1}{6}$	$\frac{2}{3}$	$\frac{1}{6}$	
a	$\frac{1}{3}$	$\frac{1}{3}$	$-\frac{27}{96}$	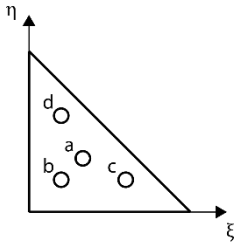
b	$\frac{1}{5}$	$\frac{1}{5}$	$\frac{25}{96}$	
c	$\frac{3}{5}$	$\frac{1}{5}$	$\frac{25}{96}$	
d	$\frac{1}{5}$	$\frac{3}{5}$	$\frac{25}{96}$	

After the distribution of the integration points in the isoparametric shape, the Cartesian coordinates of the integration points are obtained using known isoparametric interpolation functions.

$$x = \sum_{i=1}^{m} N_i(\xi, \eta) \cdot x_i$$
$$y = \sum_{i=1}^{m} N_i(\xi, \eta) \cdot y_i \qquad (2.1)$$

in which, m is the number of nodes defining the element and x_i and y_i are the Cartesian coordinates of the cells nodes.

For quadrilaterals,

$$\begin{aligned} N_1(\xi,\eta) &= \tfrac{1}{4}(1-\xi)(1-\eta) \\ N_2(\xi,\eta) &= \tfrac{1}{4}(1-\xi)(1+\eta) \\ N_3(\xi,\eta) &= \tfrac{1}{4}(1+\xi)(1+\eta) \\ N_4(\xi,\eta) &= \tfrac{1}{4}(1+\xi)(1-\eta) \end{aligned} \tag{2.2}$$

For triangles,

$$\begin{aligned} N_1(\xi,\eta) &= 1-\xi-\eta \\ N_2(\xi,\eta) &= \eta \\ N_3(\xi,\eta) &= \xi \end{aligned} \tag{2.3}$$

The integration weight of the integration point is obtained by multiplying the isoparametric weight, of the integration point with the inverse of the Jacobian matrix determinant of the respective cell.

$$[J] = \begin{pmatrix} \frac{\partial x}{\partial \xi} & \frac{\partial x}{\partial \eta} \\ \frac{\partial y}{\partial \xi} & \frac{\partial y}{\partial \eta} \end{pmatrix} \tag{2.4}$$

The differential equation integration is then performed using,

$$\int_{-1}^{1}\int_{-1}^{1} f(\boldsymbol{x})dx\,dy = \sum_{i=1}^{m}\sum_{j=1}^{n} \omega_i\,\omega_j\,f(\boldsymbol{x}) \tag{2.5}$$

in which ω_i is the weight of the integration point $\boldsymbol{x}$.

This integration can also be 3 dimensional, in which case, tetrahedral solids are used.

2.3 NNRPIM Formulation

2.3.1 Natural neighbours

Unlike the RPIM, which relies on the use of influence-domains, to determine the nodal connectivity, the NNRPIM uses the natural neighbour concept, first introduced in 1980 [50], as a way to obtain influence-cells, which work as the essential structure of nodal connectivity in this method. The influence-cells are determined based on the geometric and spatial relations between the Voronoï cells, obtained from the Voronoï diagram of the nodal distribution, hence being called influence-cells and not influence-domains.

The Voronoï diagram concept can be applicable to any D-dimensional space, but, in order to simplify the concept presentation, only the two dimensional procedure is presented.

Considering a set of N distinct nodes, discretizing a certain space domain $\Omega \in \mathbb{R}^2$,

$$N = \{n_0, n_1, \dots, n_N\} \in \mathbb{R}^2 \tag{2.6}$$

as shown in Figure 2.5a.

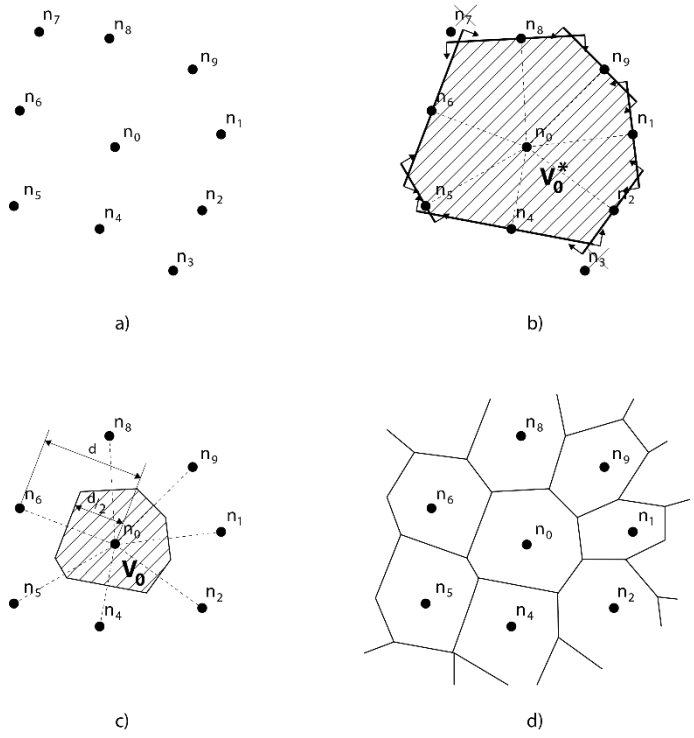

Figure 2.5 - a. Neighbour nodes of node n_0. **b.** Provisional Voronoï cell, V_0^*. **c.** Voronoï cell, V_0. **d.** Voronoï diagram

The Voronoï diagram of N is the collection of i sub-regions V_i, closed and convex, in which, each sub-region is associated with the node i in a way that any point in the interior of V_i is closer to n_i than to any node n_j,

$$V_I = \{x \in \mathbb{R}^2 : E_n(x, x_i) < E_n(x, x_j), \forall\, j \neq i\} \tag{2.7}$$

being $E_n(x_i, x_j)$ the distance between nodes with coordinates defined by x_i and x_j.

The Voronoï diagram is thus defined by,

$$V = \{V_0, V_1, \dots, V_N\} \tag{2.8}$$

Taking the node n_0 as an example, it is possible to obtain a provisional Voronoï cell, V_0^* which contains all the neighbour nodes of n_0 as seen in Figure 2.5b. Nodes located outside the ones contained in the provisional Voronoï cell are discarded. This is done by choosing a potential neighbour, for example node n_5 and determining the normal vector $\boldsymbol{u}_{50}$,

$$\boldsymbol{u}_{50} = \frac{(\boldsymbol{x}_0 - \boldsymbol{x}_5)}{\|\boldsymbol{x}_0 - \boldsymbol{x}_5\|} \tag{2.9}$$

being $\boldsymbol{u}_{50} = \{u_{50}, v_{50}, w_{50}\}$. All nodes that do not respect,

$$u_{50}x + v_{50}y + w_{50}z \;\geq\; (u_{50}x_5 + v_{50}y_5 + w_{50}z_5) \tag{2.10}$$

are discarded.

Having obtained the provisional Voronoï cell for node n_0, it is possible to obtain the Voronoï cell, V_0. As shown in Figure 2.5c the distance between node n_0 and the boundary of Voronoï cell, V_0 is half of node's n_0 and the neighbour node in question Euclidian norm. Using, once again, node n_5 as an example, the distance between n_0 and the boundary referring to node n_5 is given by,

$$d_{n_0,n_5} = \frac{E(x_o, x_5)}{2} \tag{2.11}$$

Following the same procedure for each node discretizing the problem domain, it is possible to obtain the Voronoï diagram as seen in Figure 2.5d.

2.3.2 Influence cells and nodal connectivity

The nodal connectivity of the NNRPIM method is, just like in the RPIM, obtained by the overlapping of the influence-cells.

Influence-cells can be divided in two categories, accordingly to their level of nodal connectivity:

- **First degree influence-cells:** contain the first degree natural neighbours of a certain interest point.
- **Second degree influence-cells:** contain, not only the first degree natural neighbour of a certain interest point but also, the natural neighbours of all the nodes belonging to the first degree influence cells.

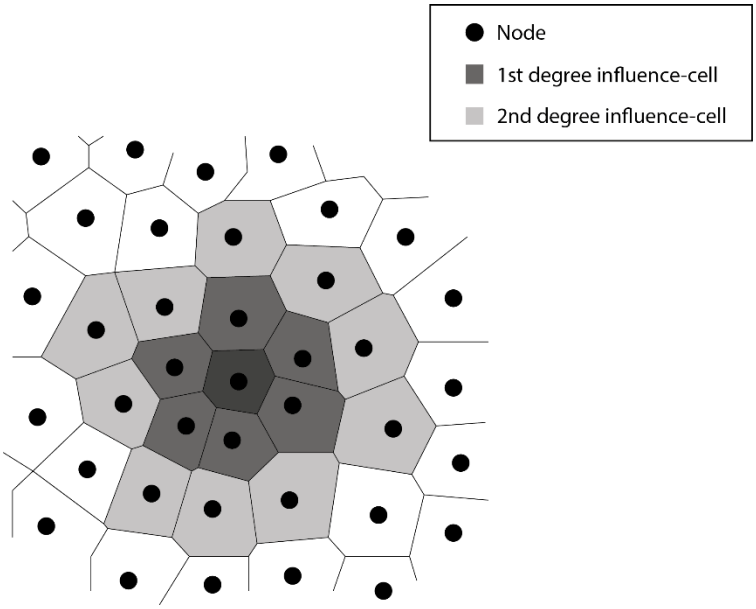

Figure 2.6 - Voronoï Diagram

Figure 2.6 shows a Voronoï diagram, containing both first and second degree influence-cells. From the picture alone, it is possible to observe that second degree influence-cells have a higher nodal connectivity, which is confirmed by the literature [35, 51].

2.3.3 Numerical integration

The way the differential equations that rule the physical problem are integrated is one of the biggest advantages of the NNRPIM. Following the construction of the Voronoï diagram, it is possible to obtain a nodal dependent integration mesh based purely on the nodal distribution spatial information.

This is done by taking the previously obtained Voronoï diagram and dividing each of its Voronoï cells into smaller sub-areas.

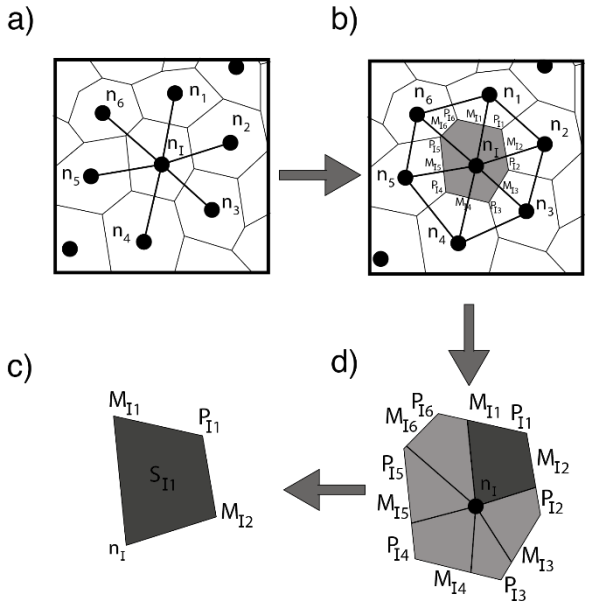

Figure 2.7 - a. Delaunay Tessellation. **b.** Delaunay Tessellation with P_{Ii} intersection points and M_{Ii} middle points**. c.** Generated quadrilaterals. **d.** Sub-cell.

Using the Delaunay tessellation, shown in Figure 2.7b, the nodes of Voronoï cells sharing common boundaries are connected, and the overlap of both the Delaunay tessellation and the influence-cell boundaries leads to a smaller sub-cell.

Therefore it is possible to divide each Voronoï cell, V_I into n sub-cells S_{Ii} in which n is the total number of natural neighbors of a certain Voronoï cell, V_I. The area of the Voronoï cell, V_I is given by the sum of all sub-cell areas,

$$A_{V_I} = \sum_{i=1}^{n} A_{S_{Ii}} \, , \; \forall \, A_{S_{Ii}} \geq 0 \qquad (2.12)$$

Based on the Gauss-Legendre numerical integration, integration points are inserted in the barycenter of each sub-cell as shown in Figure 2.8a and 2.8b.

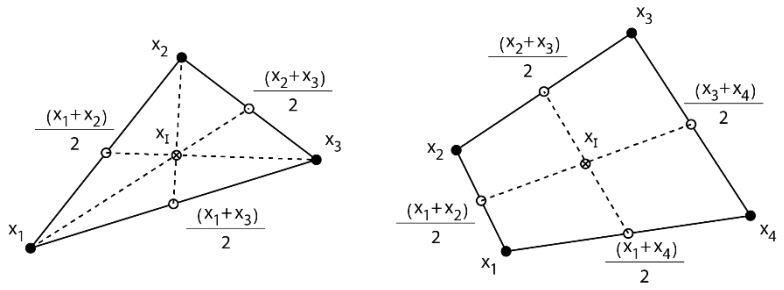

Figure 2.8 - Integration point inserted on a triangular and quadrilateral sub-cell respectively.

The example pictured above only uses 1 integration point in each sub-cell. In order to add more integration points, first the sub-cell is divided again into smaller quadrilateral sub-cells as seen in Figure 2.9 and then process follows what was described for the RPIM using quadrilateral integration cells.

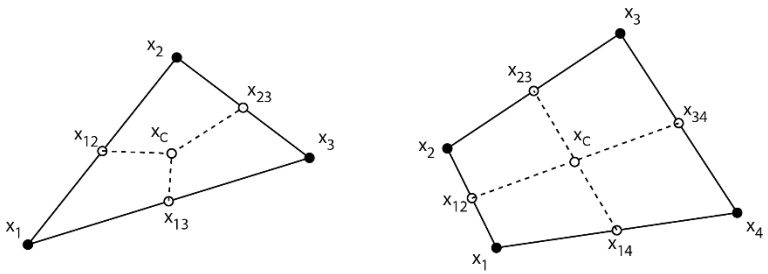

Figure 2.9 - Quadrilateral and Triangular sub-cells with multiple integration points.

However, adding more integration points doesn't increase significantly the solution accuracy and in addition greatly increases the computational cost [35]. Thus, this work follows the literature suggestion [35] and uses only 1 integration point per sub-cell.

By repeating this process for the remaining Voronoï cells, the domain integration mesh is obtained.

2.4 Shape functions

Both the RPIM and the NNRPIM use the same shape functions, based on a combination of radial basis functions with polynomial functions. Methods using only polynomial functions possessed possible singularities [19, 20] and the combination of these functions eliminates this issue. One of the biggest advantages of both these

method's shape functions is that they possess the Kronecker delta property, meaning that they are interpolating shape functions.

Considering a shape function $u(\boldsymbol{x})$, defined in a certain influence-domain, discretized by a set of N distinct nodes. The shape function, $u(\boldsymbol{x})$ is assumed to pass through all the interest points belonging to the influence-domain. The shape function value for a certain interest point $\boldsymbol{x}_I$ comes,

$$u(\boldsymbol{x}_I) = \sum_{i=1}^{n} R_i(\boldsymbol{x}_I)\, a_i(\boldsymbol{x}_I) + \sum_{j=1}^{m} p_j(\boldsymbol{x}_I)\, b_j(\boldsymbol{x}_I) = \boldsymbol{R}^T(\boldsymbol{x}_I)\, \boldsymbol{a} + \boldsymbol{p}^T(\boldsymbol{x}_I)\, \boldsymbol{b} \quad (2.13)$$

which can be rewritten as,

$$u(\boldsymbol{x}_I) = \sum_{i=1}^{n} R_i(\boldsymbol{x}_I)\, a_i(\boldsymbol{x}_I) + \sum_{j=1}^{m} p_j(\boldsymbol{x}_I)\, b_j(\boldsymbol{x}_I) = \{\boldsymbol{R}^T(x_I),\ \boldsymbol{p}^T(x_I)\} \begin{Bmatrix} \boldsymbol{a} \\ \boldsymbol{b} \end{Bmatrix} \quad (2.14)$$

where $R_i(\boldsymbol{x}_I)$ is the radial basis function (RBF), $p_j(\boldsymbol{x}_I)$ is the polynomial basis function, n is the number of nodes inside the influence-domain of the interest point $\boldsymbol{x}_I$ and $a_i\ (\boldsymbol{x}_I)$ and $b_j\ (\boldsymbol{x}_I)$ are non constant coefficients of $R_i(\boldsymbol{x}_I)$ and $p_j(\boldsymbol{x}_I)$ respectively.

The vectors of equation 2.14 are as follow,

$$\begin{aligned} \boldsymbol{a}^T(\boldsymbol{x}_I) &= [a_1(\boldsymbol{x}_I), a_2(\boldsymbol{x}_I), \dots, a_n(\boldsymbol{x}_I)] \\ \boldsymbol{b}^T(\boldsymbol{x}_I) &= [b_1(\boldsymbol{x}_I), b_2(\boldsymbol{x}_I), \dots, b_m(\boldsymbol{x}_I)] \\ \boldsymbol{R}^T(\boldsymbol{x}_I) &= [R_1(\boldsymbol{x}_I), R_2(\boldsymbol{x}_I), \dots, R_n(\boldsymbol{x}_I)] \\ \boldsymbol{p}^T(\boldsymbol{x}_I) &= [p_1(\boldsymbol{x}_I), p_2(\boldsymbol{x}_I), \dots, p_m(\boldsymbol{x}_I)] \end{aligned} \quad (2.15)$$

The RBF used, for a general 2D problem has the following general form,

$$R_{ij} = \left(r_{ij}^2 + c^2\right)^p \quad (2.16)$$

where c and p are shape parameters which, accordingly to the literature, should be considered as $c = 0.0001$ and $p = 0.9999$ in order to maximize the method's

performance [35, 51] and r_{ij} is the Euclidian norm between the integration point x_I and a certain node x_i,

$$r_{ij} = \sqrt{(x_I - x_i)^2} \tag{2.17}$$

The polynomial basis functions used have the following monomial terms as,

$$\boldsymbol{p}^T(\boldsymbol{x}_I) = [1, x, y, x^2, xy, y^2, \dots] \tag{2.18}$$

This leads to the following polynomial basis, for the 1D problem,

$$Null\ basis - \ \boldsymbol{x}^T = \{x\};\ \ \boldsymbol{p}^T(\boldsymbol{x}) = \{0\};\ \ m = 0 \tag{2.19}$$

$$Constant\ basis - \ \boldsymbol{x}^T = \{x\};\ \ \boldsymbol{p}^T(\boldsymbol{x}) = \{1\};\ \ m = 1 \tag{2.20}$$

$$Linear\ basis - \ \boldsymbol{x}^T = \{x\};\ \ \boldsymbol{p}^T(\boldsymbol{x}) = \{1, x\};\ \ m = 2 \tag{2.21}$$

$$Quadratic\ basis - \ \boldsymbol{x}^T = \{x\};\ \ \boldsymbol{p}^T(\boldsymbol{x}) = \{1, x, x^2\};\ \ m = 3 \tag{2.22}$$

and for the 2D problem,

$$Null\ basis - \ \boldsymbol{x}^T = \{x, y\};\ \ \boldsymbol{p}^T(\boldsymbol{x}) = \{0\};\ \ m = 0 \tag{2.23}$$

$$Constant\ basis - \ \boldsymbol{x}^T = \{x, y\};\ \ \boldsymbol{p}^T(\boldsymbol{x}) = \{1\};\ \ m = 1 \tag{2.24}$$

$$Linear\ basis - \ \boldsymbol{x}^T = \{x, y\};\ \ \boldsymbol{p}^T(\boldsymbol{x}) = \{1, x, y\};\ \ m = 3 \tag{2.25}$$

$$Quadratic\ basis - \ \boldsymbol{x}^T = \{x, y\};\ \ \boldsymbol{p}^T(\boldsymbol{x}) = \{1, x, y, x^2, xy, y^2\};\ \ m = 6 \tag{2.26}$$

The same procedure can be applied to a 3D problem.

The polynomial term must however satisfy the following requirement, in order to guarantee a unique approximation,

$$\sum_{i=1}^{n} p_j(\boldsymbol{x}_i)\, a_i = 0, \quad j = 1,2,\dots,m \tag{2.27}$$

The function can be written in matrix form,

$$\begin{bmatrix} \boldsymbol{R} & \boldsymbol{p} \\ \boldsymbol{p}^T & \boldsymbol{0} \end{bmatrix} \begin{Bmatrix} \boldsymbol{a} \\ \boldsymbol{b} \end{Bmatrix} = \begin{Bmatrix} \boldsymbol{u_s} \\ \boldsymbol{0} \end{Bmatrix} = \boldsymbol{G} \begin{Bmatrix} \boldsymbol{a} \\ \boldsymbol{b} \end{Bmatrix} \tag{2.28}$$

Solving equation 2.28,

$$\begin{Bmatrix} \boldsymbol{a} \\ \boldsymbol{b} \end{Bmatrix} = \boldsymbol{G}^{-1} \begin{Bmatrix} \boldsymbol{u_s} \\ \boldsymbol{0} \end{Bmatrix} \tag{2.29}$$

Finally, by substituting equation 2.29 in equation 2.13 the shape function is finally expressed as

$$u(\boldsymbol{x}_I) = \{\boldsymbol{R}^T(\boldsymbol{x}_I),\ \boldsymbol{p}^T(\boldsymbol{x}_I)\}\, \boldsymbol{G}^{-1} \begin{Bmatrix} \boldsymbol{u_s} \\ \boldsymbol{0} \end{Bmatrix} = \varphi(\boldsymbol{x}_I)\, \boldsymbol{u}_s \tag{2.30}$$

in which $\varphi(\boldsymbol{x}_I)$ is the shape function defined by

$$\varphi(\boldsymbol{x}_I) = \{\boldsymbol{R}^T(\boldsymbol{x}_I),\ \boldsymbol{p}^T(\boldsymbol{x}_I)\}\, \boldsymbol{G}^{-1} = [\varphi_1(\boldsymbol{x}_I), \varphi_2(\boldsymbol{x}_I), \dots, \varphi_n(\boldsymbol{x}_I)] \tag{2.31}$$

As stated earlier in the chapter, the RPIM and NNRPIM shape functions are interpolating, since they respect the Kronecker delta property,

$$\varphi_i(\boldsymbol{x}_j) = \begin{cases} 1, & i = j, \quad j = 1,2,\dots,n \\ 0, & i \neq j, \quad j = 1,2,\dots,n \end{cases} \tag{2.32}$$

which means they pass through every single node within the influence-domain (or influence-cell), in opposition to approximation shape functions which do not. Interpolation shape functions permit to easily impose the essential and natural boundary conditions, using direct imposition methods, reducing the computational cost associated to this task when compared with approximation shape functions.

Chapter 3

Solid Mechanics Fundamentals

Solid mechanics' main goal is to understand the response of a structure that is subjected to external stimuli (applied forces, induced stresses, temperature, etc.). This response comes in the form of stresses, strains and displacements. By knowing the configuration of the structure, its material characteristics as well as the applied loads, it is possible to estimate the strain/stress fields of the structure using known relations [52].

In this work, all solids were considered as being linear-elastic, i.e., a linear relationship between stress and strain is assumed and after the removal of the applied loads, the solid returns to its undeformed shape. Moreover, since this is a static study, only static loads were considered, meaning that stresses, strains and displacements are not considered as a function of time.

The present chapter addresses the fundamentals of solid mechanics in order to fully understand the subsequent chapters.

3.1 Components of stress

Under the action of external loads, internal forces are produced. These internal forces are defined by the amount of force per unit area, entitled stress. The stress a body is under, on a certain point, is given by the stress tensor

$$\mathfrak{S} = \begin{bmatrix} \sigma_{xx} & \tau_{xy} & \tau_{xz} \\ \tau_{yx} & \sigma_{yy} & \tau_{yz} \\ \tau_{zx} & \tau_{zy} & \sigma_{zz} \end{bmatrix} \tag{3.1}$$

which can be written in vector form as,

$$\boldsymbol{\sigma} = \{\sigma_{xx} \quad \sigma_{yy} \quad \sigma_{zz} \quad \tau_{xy} \quad \tau_{yz} \quad \tau_{zx}\}^T \tag{3.2}$$

Stress can be divided into two categories, normal stress, which is perpendicular to the plane in which it acts, denoted by the letter σ and shear tress, which is tangential to the acting plane, denoted by the letter τ.

3.2 Equilibrium equations

Even though stresses vary over the volume of a body, these cannot vary arbitrarily between two given points. The three dimensional equilibrium equations of an infinitesimal element are given by,

$$\begin{aligned} \frac{\partial_{\sigma_{xx}}}{\partial_x} + \frac{\partial_{\tau_{yx}}}{\partial_y} + \frac{\partial_{\tau_{zx}}}{\partial_z} + F_x = 0 \\ \frac{\partial_{\tau_{xy}}}{\partial_x} + \frac{\partial_{\sigma_{yy}}}{\partial_y} + \frac{\partial_{\tau_{zy}}}{\partial_z} + F_y = 0 \\ \frac{\partial_{\tau_{xz}}}{\partial_x} + \frac{\partial_{\tau_{yz}}}{\partial_y} + \frac{\partial_{\sigma_{zz}}}{\partial_z} + F_y = 0 \end{aligned} \tag{3.3}$$

and must be verified for every point throughout the volume of the body. These equations can be simplified resulting in,

$$\nabla \mathfrak{S} + \boldsymbol{F} = \mathbf{0} \tag{3.4}$$

where $\nabla = \{\partial/\partial x, \partial/\partial y, \partial/\partial z\}$ is the gradient, $\mathfrak{S}$ is the stress tensor and $\boldsymbol{F}$ is the body force vector.

3.3 Components of strain

Since no material is perfectly rigid, when subject to external loads, a body will become deformed. Considering the solid shown in Figure 3.1,

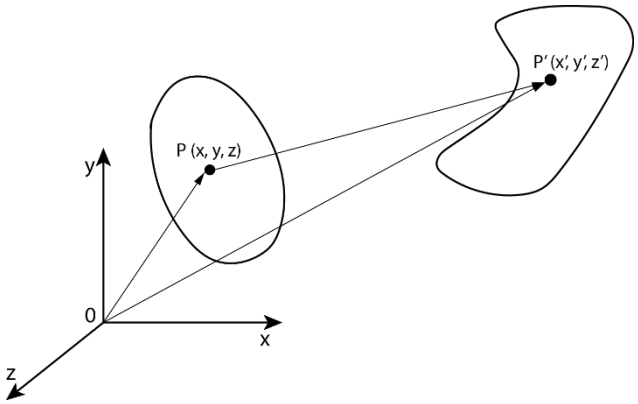

Figure 3.1 - Linear deformation of a virtual body.

Prior to applying any external loads, point P occupies a certain location in space. This position changes as soon external loads are applied, and this leads point P to occupy the position P'. For any given point of the solid, the equation that defines the displacement field comes,

$$\boldsymbol{u}(u,v,w) = \begin{Bmatrix} u(x,y,z) \\ v(x,y,z) \\ w(x,y,z) \end{Bmatrix} \tag{3.5}$$

Strain and displacements are be related by,

$$\varepsilon_{xx} = \frac{\partial u}{\partial x} \qquad \gamma_{xy} = \frac{\partial v}{\partial x} + \frac{\partial u}{\partial y}$$

$$\varepsilon_{yy} = \frac{\partial v}{\partial y} \qquad \gamma_{yz} = \frac{\partial w}{\partial y} + \frac{\partial v}{\partial z} \tag{3.6}$$

$$\varepsilon_{zz} = \frac{\partial w}{\partial z} \qquad \gamma_{zx} = \frac{\partial u}{\partial z} + \frac{\partial w}{\partial x}$$

Similarly to what happens in stresses, strain can also be divided in two categories, normal strain, represented by the letter ε, and shear strain, represented by the letter γ. While the first refers to the relative change of length of a certain line segment, the later refers to the change in angle of two previously perpendicular lines segments.

The strain tensor comes,

$$\mathfrak{E} = \begin{bmatrix} \varepsilon_{xx} & \gamma_{xy} & \gamma_{xz} \\ \gamma_{yx} & \gamma_{yy} & \gamma_{yz} \\ \gamma_{zx} & \gamma_{zy} & \varepsilon_{zz} \end{bmatrix} \tag{3.7}$$

which can be written in vector form as,

$$\boldsymbol{\varepsilon} = \{\varepsilon_{xx} \quad \varepsilon_{yy} \quad \varepsilon_{zz} \quad \gamma_{xy} \quad \gamma_{yz} \quad \gamma_{zx}\}^T \tag{3.8}$$

The equations shown in (3.6) can be represented in matrix form as the product of the partial differential equation operator matrix $\boldsymbol{L}$ and the displacement field $\boldsymbol{u}$.

$$\boldsymbol{\varepsilon} = \boldsymbol{L}\,\boldsymbol{u} \tag{3.9}$$

Where $\boldsymbol{L}$ is given by,

$$\boldsymbol{L} = \begin{bmatrix} \frac{\partial}{\partial x} & 0 & 0 & \frac{\partial}{\partial y} & 0 & \frac{\partial}{\partial z} \\ 0 & \frac{\partial}{\partial y} & 0 & \frac{\partial}{\partial x} & \frac{\partial}{\partial z} & 0 \\ 0 & 0 & \frac{\partial}{\partial z} & 0 & \frac{\partial}{\partial y} & \frac{\partial}{\partial x} \end{bmatrix}^T \tag{3.10}$$

3.4 Constitutive relations

As already mentioned in this chapter, all solids used in this work were considered as being isotropic and linear-elastic. Due to this, not only is the material fully defined by just its Elastic Modulus, E and by its Poisson's Ratio υ but the components of stress and strain relation is given by the generalized Hooke's law,

$$\boldsymbol{\sigma} = \boldsymbol{c}\,\boldsymbol{\varepsilon} \tag{3.11}$$

where $\boldsymbol{c}$ is the material constitutive matrix defined by,

$$\boldsymbol{c} = \frac{E}{(1+\upsilon)(1-2\upsilon)}\begin{bmatrix} 1-\upsilon & \upsilon & \upsilon & 0 & 0 & 0 \\ \upsilon & 1-\upsilon & \upsilon & 0 & 0 & 0 \\ \upsilon & \upsilon & 1-\upsilon & 0 & 0 & 0 \\ 0 & 0 & 0 & (1-2\upsilon) & 0 & 0 \\ 0 & 0 & 0 & 0 & (1-2\upsilon) & 0 \\ 0 & 0 & 0 & 0 & 0 & (1-2\upsilon) \end{bmatrix} \quad (3.12)$$

3.5 Plane stress and plain strain

Three-dimensional (3D) problems that meet certain criteria can be simplified as two-dimensional problems. This simplifies the analysis and does not affect significantly the solution accuracy.

3.5.1 Plane stress

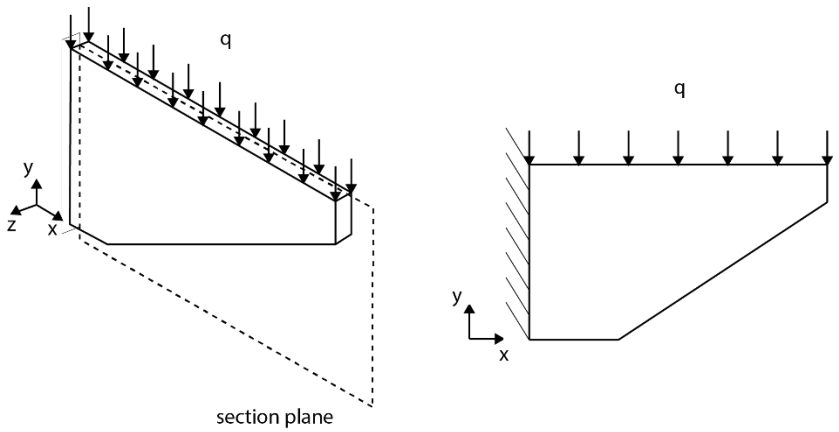

Figure 3.2 - Plane stress problem

In thin walled bodies, like the thin plate shown in Figure 3.2, where the x and y dimensions are much larger than the thickness z, loaded with forces parallel to the plane of the plate along its thickness, the normal stress σ_z and the shear stresses τ_{xz} and τ_{yz} can be considered as zero. The stress and strain tensor can thus be represented in vector form by respectively,

$$\boldsymbol{\sigma} = \{\sigma_{xx} \quad \sigma_{yy} \quad \tau_{xy}\}^T \quad (3.13)$$

$$\boldsymbol{\varepsilon} = \{\varepsilon_{xx} \quad \varepsilon_{yy} \quad \gamma_{xy}\}^T \tag{3.14}$$

The material matrix takes the following form,

$$\boldsymbol{c} = \frac{E}{(1-\upsilon^2)}\begin{bmatrix} 1 & \upsilon & 0 \\ \upsilon & 1 & 0 \\ 0 & 0 & \dfrac{(1-\upsilon)}{2} \end{bmatrix} \tag{3.15}$$

3.5.1 Plane strain

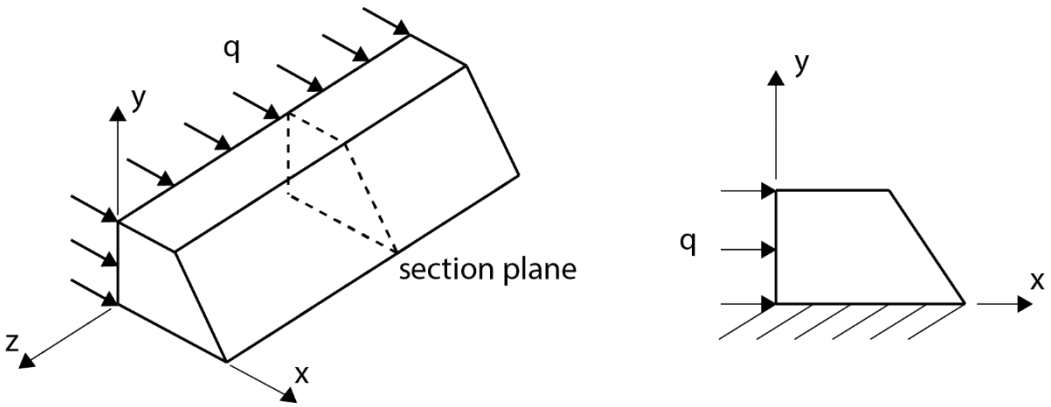

Figure 3.3 – Plane strain problem

An analogous simplification can be made for solids in which the thickness z is much larger than the other dimensions, loaded with forces perpendicular to its thickness, while maintaining the same cross-section as shown in Figure 3.3.

Both the normal stress σ_z and the shear stresses τ_{xz} and τ_{yz} can once again be considered as zero. The stress and strain vectors take the same form as equations (3.13) and (3.14).

The material matrix takes the form,

$$\boldsymbol{c} = \frac{E}{(1-2\nu)(1+\nu)}\begin{bmatrix} 1-\nu & \upsilon & 0 \\ \upsilon & 1-\nu & 0 \\ 0 & 0 & \dfrac{(1-2\upsilon)}{2} \end{bmatrix} \tag{3.16}$$

3.6 Strong form and weak form formulation

The set of differential equations governing the structural behaviour of an arbitrary solid must respect the equilibrium equations presented in equation (3.3). Solving these equations is not always efficient, especially in problems with intricate domains, several material interfaces and complex boundary conditions. That is why the weak formulation is often used. Instead of solving the differential equations, which may not always have a straightforward solution, the weak form produces a set of discretized system equations in an integral form. The weak form is established for each integration point. This means that accuracy of the solution is dependent on the density of the mesh discretizing the problem domain, with a finer mesh yielding better results. Furthermore, it also makes the implementation of boundary conditions easier, as they can be applied locally to any arbitrary node.

3.6.1 Galerkin weak form

Both the RPIM and NNRPIM formulation used in this work use the Galerkin weak formulation to obtain approximate solutions to the strong form, which is based on an energy principle.

Hamilton's principle, one of the most used energy principles, allows for the derivation of the partial differential equations of the problem and states *"Of all the admissible time histories of displacement the most accurate solution makes the Lagrangian functional a minimum."* [53]

The Lagrangian function contains all the physical information regarding the problem, as well the forces acting on it, and can be represented as,

$$L = T - U + W_f \tag{3.17}$$

in which T is the kinetic energy, U is the strain energy and W_f is the work produced by external forces.

Combining equation (3.17) with Hamilton's principle,

$$\int_{t1}^{t2} \left[\delta T - \delta U + \delta W_f\right] dt = 0 \tag{3.18}$$

which can be rewritten as,

$$\delta \int_{t1}^{t2} L\, dt = 0 \tag{3.19}$$

Considering a solid, in which Ω denotes a domain of $\mathbb{R}^3$, Γ the exterior boundary, Γ_t the natural boundary in which an external force $\boldsymbol{f}$ is applied, Γ_u the essential boundary where displacements are constrained and $\boldsymbol{b}$ a body force applied on the solid, as shown in Figure 3.4.

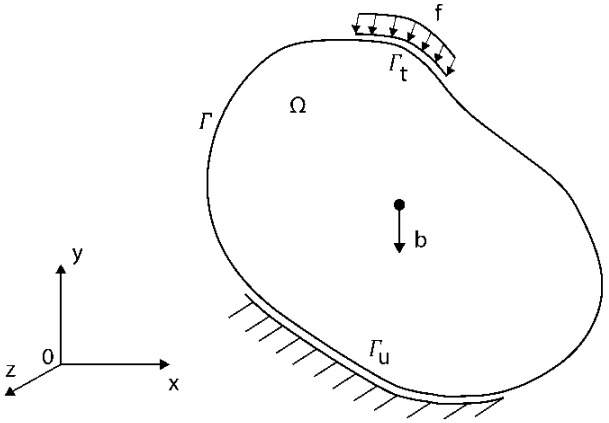

Figure 3.4 – 3D Solid mechanics problem

The kinetic energy is defined,

$$T = \frac{1}{2} \int_{\Omega} \rho\, \dot{\boldsymbol{u}}^T \dot{\boldsymbol{u}}\, d\Omega \tag{3.20}$$

where $\dot{\boldsymbol{u}}$ is the velocity, displacement's first derivative, and ρ is the density of the material point. The strain energy, for a linear-elastic material can be expressed as,

$$U = \frac{1}{2} \int_{\Omega} \boldsymbol{\varepsilon}^T \boldsymbol{\sigma}\, d\Omega \tag{3.21}$$

The work produced by external forces comes,

$$W_f = \int_{\Omega} \boldsymbol{u}^T \boldsymbol{b}\, d\Omega + \int_{\Gamma_t} \boldsymbol{u}^T \boldsymbol{f}\, d\Gamma \tag{3.22}$$

By substituting equations (3.20), (3.21) and (3.22) in equation (3.18) the following is obtained,

$$\int_{t1}^{t2} \left[\frac{1}{2} \int_{\Omega} \delta(\rho\, \dot{\boldsymbol{u}}^T \dot{\boldsymbol{u}})\, d\Omega - \frac{1}{2} \int_{\Omega} \delta(\boldsymbol{\varepsilon}^T \boldsymbol{\sigma})\, d\Omega + \int_{\Omega} \delta \boldsymbol{u}^T \boldsymbol{b}\, d\Omega + \int_{\Gamma_t} \delta \boldsymbol{u}^T \boldsymbol{f}\, d\Gamma \right] dt = 0 \tag{3.23}$$

Since only static problems were considered in this work, the first term of equation (3.23) can be discarded, which leads to,

$$\int_{t1}^{t2} \left[-\frac{1}{2} \int_{\Omega} \delta(\boldsymbol{\varepsilon}^T \boldsymbol{\sigma})\, d\Omega + \int_{\Omega} \delta \boldsymbol{u}^T \boldsymbol{b}\, d\Omega + \int_{\Gamma_t} \delta \boldsymbol{u}^T \boldsymbol{f}\, d\Gamma \right] dt = 0 \tag{3.24}$$

Several simplifications can be made to the first term of the integral (3.24). The integrand function can be written as,

$$\delta(\boldsymbol{\varepsilon}^T \boldsymbol{\sigma}) = \delta \boldsymbol{\varepsilon}^T \boldsymbol{\sigma} + \boldsymbol{\varepsilon}^T \delta \boldsymbol{\sigma} \tag{3.25}$$

Given that both terms in (3.25) are scalars,

$$\boldsymbol{\varepsilon}^T \delta \boldsymbol{\sigma} = (\boldsymbol{\varepsilon}^T \delta \boldsymbol{\sigma})^T = \delta \boldsymbol{\sigma}^T \boldsymbol{\varepsilon} \tag{3.26}$$

Attending to the generalized Hooke's law shown in (3.11), and the symmetric property of material matrix shown in (3.12), $\boldsymbol{c}^T = \boldsymbol{c}$, it is possible to write (3.26) as,

$$\delta \boldsymbol{\sigma}^T \boldsymbol{\varepsilon} = \delta \boldsymbol{\varepsilon}^T \boldsymbol{\sigma} \tag{3.27}$$

Substituting (3.27) in (3.25),

$$\delta(\boldsymbol{\varepsilon}^T \boldsymbol{\sigma}) = 2\, (\delta \boldsymbol{\varepsilon}^T \boldsymbol{\sigma}) \tag{3.28}$$

By replacing (3.28) in (3.24),

$$\int_{t1}^{t2}\left[-\int_{\Omega}\delta\boldsymbol{\varepsilon}^{T}\boldsymbol{\sigma}d\Omega+\int_{\Omega}\delta\boldsymbol{u}^{T}\boldsymbol{b}\,d\Omega+\int_{\Gamma_t}\delta\boldsymbol{u}^{T}\boldsymbol{f}\,d\Gamma\right]dt=0 \qquad (3.29)$$

In order for the time integration to be valid for any pair of initial and final time, t_1 and t_2 respectively, the integrand of (3.29) must be null. This leads to the "Galerkin weak form" equation,

$$-\int_{\Omega}\delta\boldsymbol{\varepsilon}^{T}\boldsymbol{\sigma}d\Omega+\int_{\Omega}\delta\boldsymbol{u}^{T}\boldsymbol{b}\,d\Omega+\int_{\Gamma_t}\delta\boldsymbol{u}^{T}\boldsymbol{f}\,d\Gamma=0 \qquad (3.30)$$

Substituting equations (3.9) and (3.11) in (3.30) the generic Galerkin weak form written in terms of displacement is obtained,

$$\int_{\Omega}\delta(\boldsymbol{L}\,\boldsymbol{u})^{T}\boldsymbol{c}\,(\boldsymbol{L}\,\boldsymbol{u})\,d\Omega-\int_{\Omega}\delta\boldsymbol{u}^{T}\boldsymbol{b}\,d\Omega-\int_{\Gamma_t}\delta\boldsymbol{u}^{T}\boldsymbol{f}\,d\Gamma=0 \qquad (3.31)$$

3.7 Discrete System Equations

The discrete system of equations for meshless methods, are obtained based on the principle of virtual work, with the shape functions presented in chapter 2 being used as trial functions.

The approximation of the variable field in an integration point $\boldsymbol{x}_I$ comes,

$$\boldsymbol{u}(\boldsymbol{x}_I)=\sum_{i=1}^{n}\varphi_i\,(\boldsymbol{x}_I)\,\boldsymbol{u}_i \qquad (3.32)$$

in which $\varphi_i(\boldsymbol{x}_I)$ is the shape function and $\boldsymbol{u}_i$ is the nodal displacement, of the n nodes belonging to the influence domain of integration point $\boldsymbol{x}_I$.

By the principle of virtual work, the trial function or virtual displacement is defined as,

$$\delta \boldsymbol{u}(\boldsymbol{x}_I) = \sum_{i=1}^{n} \varphi_i\,(\boldsymbol{x}_I)\;\delta \boldsymbol{u}_i \tag{3.33}$$

which can be substituted in equation (3.31) so that the following is obtained,

$$\int_{\Omega} \left(\sum_{i=1}^{n} \varphi_i\,(\boldsymbol{x}_I)\;\delta \boldsymbol{u}_i \right)^T \boldsymbol{L}^T \boldsymbol{c}\, \boldsymbol{L} \left(\sum_{j=1}^{n} \varphi_j\,(\boldsymbol{x}_I)\;\boldsymbol{u}_j \right) d\Omega - \int_{\Omega} \left(\sum_{i=1}^{n} \varphi_i\,(\boldsymbol{x}_I)\;\delta \boldsymbol{u}_i \right)^T \boldsymbol{b} - \int_{\Gamma_t} \left(\sum_{i=1}^{n} \varphi_i\,(\boldsymbol{x}_I)\;\delta \boldsymbol{u}_i \right)^T \boldsymbol{f}\, d\Gamma = 0 \tag{3.34}$$

Equation (3.34) can be rewritten as,

$$\sum_{i=1}^{n}\sum_{j=1}^{n} \delta \boldsymbol{u}_i{}^T \int_{\Omega} \boldsymbol{B}^T \boldsymbol{c}\, \boldsymbol{B}\; d\Omega\; \boldsymbol{u} - \sum_{i=1}^{n} \delta \boldsymbol{u}_i{}^T \int_{\Omega} \varphi_i{}^T(\boldsymbol{x}_I)\; \boldsymbol{b}\; d\Omega - \sum_{i=1}^{n} \delta \boldsymbol{u}_i{}^T \int_{\Omega} \varphi_i{}^T(\boldsymbol{x}_I)\; \boldsymbol{f}\; d\Gamma = 0 \tag{3.34}$$

where the deformability matrix $\boldsymbol{B}$ is given by,

$$\boldsymbol{B} = \begin{bmatrix} \dfrac{\partial \varphi_i}{\partial x} & 0 & 0 & \dfrac{\partial \varphi_i}{\partial y} & 0 & \dfrac{\partial \varphi_i}{\partial z} \\ 0 & \dfrac{\partial \varphi_i}{\partial y} & 0 & \dfrac{\partial \varphi_i}{\partial x} & \dfrac{\partial \varphi_i}{\partial z} & 0 \\ 0 & 0 & \dfrac{\partial \varphi_i}{\partial z} & 0 & \dfrac{\partial \varphi_i}{\partial y} & \dfrac{\partial \varphi_i}{\partial x} \end{bmatrix}^T \tag{3.35}$$

Equation (3.34) can be represented as,

$$\delta \boldsymbol{U}^T\,(\boldsymbol{K}\boldsymbol{U} - \boldsymbol{F}) = 0 \tag{3.36}$$

Where $\boldsymbol{U} = \boldsymbol{u}$ and $\boldsymbol{F}$ is the sum of the second and third term of equation (3.34). Thus, equation (3.35) can be finally translated in the following linear equation,

$$(\boldsymbol{K}\boldsymbol{U} - \boldsymbol{F}) = \boldsymbol{0} \tag{3.37}$$

As explained in the previous chapter, because of possessing the Kronecker delta property, essential boundaries can be directly applied in the stiffness, $\boldsymbol{K}$, matrix.

Chapter 4

Benchmark Examples

In order to validate the formulation presented in the previous chapters, several benchmark examples from Solid Mechanics were studied. The objective was to study the convergence and accuracy of the RPIM and NNRPIM and to compare the computational cost of both meshless methods with other numerical methods. This chapter contains a brief introduction to the software used throughout this work and the convergence study that validates it.

4.1 FEMAS

FEMAS is a meshless computational framework, developed at FEUP, implemented in the commercial software Matlab using the formulation presented in Chapter 2. FEMAS possesses a graphical user interface (GUI), permitting to build the numerical model and analyse it using several numerical discretization techniques.

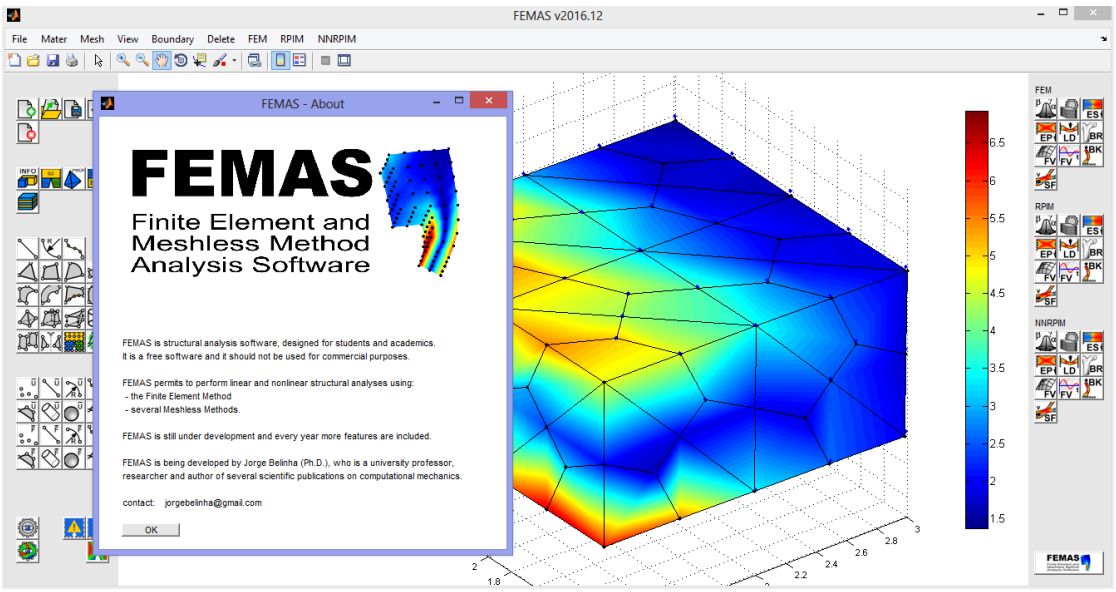

Figure 4.1 – FEMAS graphical user interface.

FEMAS supports numerical analysis using the RPIM, the NNRPIM and the FEM (for comparison purposes) and can currently perform the following analyses:

- Static linear-elastic
- Elasto-plastic
- Crack opening path
- Bone tissue remodelling
- Free vibration
- Buckling
- Fluid flow (low velocities)

The computational framework uses the classical three-dimensional deformation theory (for 3D problems) and the plane stress and plane strain two-dimensional deformation theory (for 2D problems) and allows the use of both isotropic and anisotropic materials. The software permits to build autonomously the 2D or 3D numerical model. The user controls the nodal discretization, the material disposition and the location of the essential and natural boundary conditions. All these tasks are performed without the use of any external CAD software. Nevertheless, meshes generated in other CAD software can also be imported and read using FEMAS.

The workflow of the elastic static analysis performed by FEMAS can be divided in three phases, pre-process, process and post-process,

Table 4. 1 – Phases description

	#	Phase	Phase description
Pre-process	1.	Pre-process	Nodal discretization is determined. Influence-domains are found (meshless methods); elements are created (FEM). Integration mesh is determined.
Process	2.	Shape function	Shape functions are determined for all integration points
	3.	Stiffness matrix	Local stiffness matrix is determined and the global stiffness matrix is assembled
	4.	Natural boundary	Natural boundary is determined, and external forces are applied
	5.	Essential boundary	Essential boundary is determined and constrained displacements are imposed
	6.	Displacement field	Displacement field vector is determined
	7.	Strain/ stress field	Strain and stress fields are determined
Post-process	8.	Field images	The variable fields are presented in the FEMAS GUI.

Furthermore, FEMAS allows to present the displacement, stress and strain fields along the solid domain using both figures and arrays, which permits further data analyses.

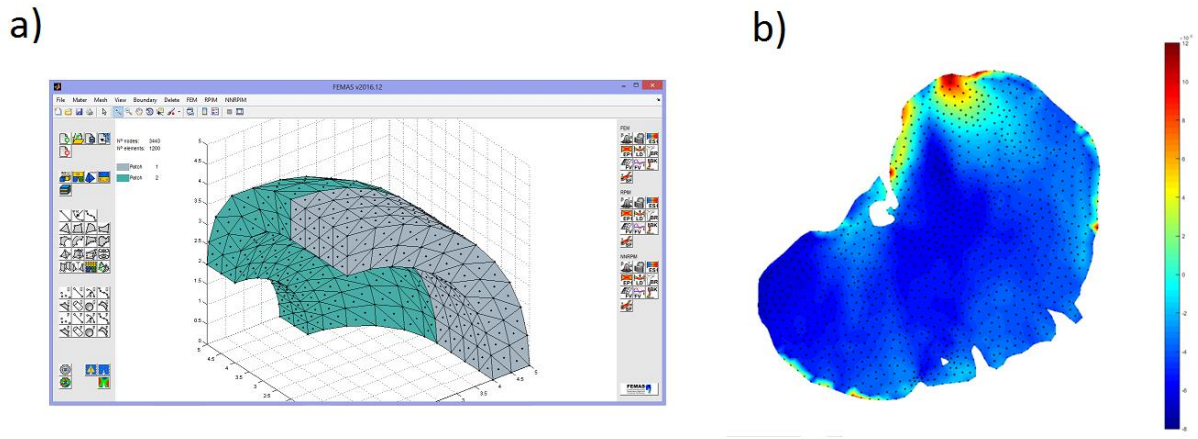

Figure 4.2 – a. 3D model of a spherical shell built in FEMAS. **b.** Stress field of a human brain during impact, obtained with FEMAS

4.2 Benchmark examples

The examples shown below were studied with the aforementioned software. These examples, two 2D problems and two 3D problems, are solid mechanics problems with known analytical exact solutions. Results obtained with the meshless methods were compared against the analytical exact solution and the solution obtained using the FEM. The FEM analysis was done using triangular elements (for 2D problems) and tetrahedral elements (for 3D problems), with the element nodes being coincident with the meshless discretization.

In order to study the convergence of the methods, four different meshes were used for each example, each one progressively more refined that the other, following a 2^n rule as seen in Figure 4.3. Only regular meshes were used as the effect of irregular meshes has already been studied [35, 51].

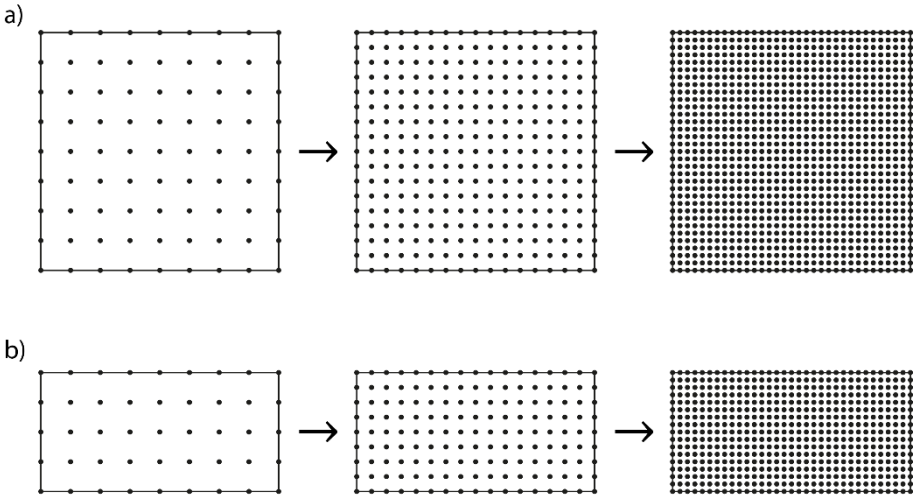

Figure 4.3 - Mesh refining process for the two 2D problems studied

In three-dimensional meshes, 3 nodes are added in depth, being the thickness of the problem dependent on the nodal mesh (in order to maintain a regular mesh).

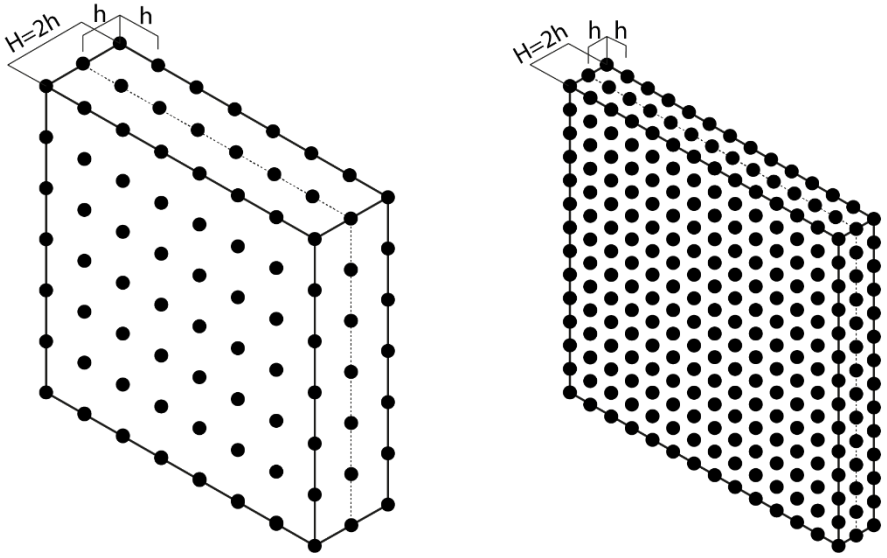

Figure 4.4 - Mesh refining process for the 3D problems studied

All examples were considered as having the following mechanical properties: E= 1000 Pa and ν=0.3.

In order to compare the methods, the total average relative error between the analytical and the experimental solution was calculated using,

$$E_{med} = \frac{1}{N} \cdot \sum_{i=1}^{N} \frac{\sqrt{\left(S_{experimental} - S_{analytical}\right)^2}}{\sqrt{S_{analytical}{}^2}} \qquad (4.1)$$

in which N is the number of nodes discretizing the problem domain and S is the field variable in study.

The following parameters were used in the RPIM and NNRPIM analysis, as recommended by the literature [35]:

Table 4. 2 – RPIM parameters.

RPIM	
2D	**3D**
Nodes in the influence-domain: **16**	Nodes in the influence-domain: **70**
c= **0.0001**	c= **0.0001**
p= **0.9999**	p= **0.9999**
Polynomial Basis: **Constant**	Polynomial Basis: **Constant**
Integration points: **1 per triangle**	Integration points: **1 per tetrahedron**

Table 4. 3 – NNRPIM parameters.

NNRPIM	
2D	**3D**
c= **0.0001**	c= **0.0001**
p= **0.9999**	p= **0.9999**
Influence-cell: **2nd order**	Influence-cell: **2nd order**
Polynomial Basis: **Constant**	Polynomial Basis: **Constant**
Integration points: **1 per sub-cell**	Integration points: **1 per sub-cell**

4.2.1 2D Square Plate

Considering a solid domain $\Omega \in \mathbb{R}^2$, loaded with the following stress field,

$$\sigma_{xx}(x,y) = \sigma_0 \cdot \left(\frac{x^2}{L^2} - \frac{y^2}{D^2}\right)$$

$$\sigma_{yy}(x,y) = \sigma_0 \cdot \left(\frac{(L^2 - 2D^2) \cdot x^2}{L^2 \cdot D^2} + \frac{y^2}{L^2}\right) \tag{4.2}$$

$$\tau_{xx}(x,y) = -\sigma_0 \cdot \left(\frac{2 \cdot x \cdot y}{L^2}\right)$$

with $\sigma_0 = 100\ Pa$, as seen in Figure 4.5.

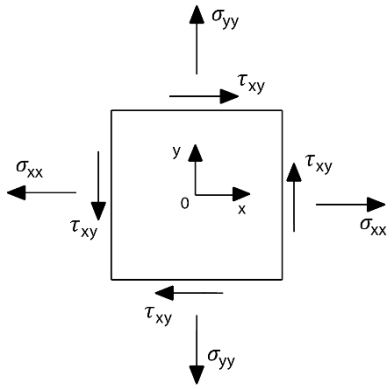

Figure 4.5 - Square plate under parabolic stress.

Due to the problem symmetry, the following simplification can be made,

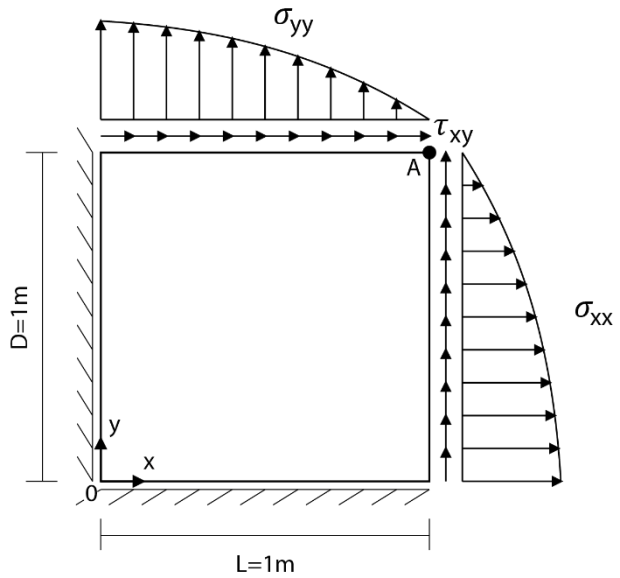

Figure 4.6 - Quarter of square plate under parabolic stress.

Because of this simplification, the following displacements must be constrained: $u = 0: \forall y \in \mathbb{R}^2 \ \wedge x = 0$ and $v = 0: \forall x \in \mathbb{R}^2 \ \wedge y = 0$ with $u = (u, v)$. The analytical displacement field can be obtained from equation (4.2) and it comes,

$$u(x,y) = \frac{\sigma_0}{E} \cdot \left(\frac{x^3}{3L^2} - \frac{x \cdot y^2}{D^2} - \nu \cdot \left(\frac{x^3 \cdot (L^2 - 2D^2)}{3L^2 \cdot D^2} + \frac{x \cdot y^2}{L^2} \right) \right)$$

$$v(x,y) = \frac{\sigma_0}{E} \cdot \left(\frac{x^2 \cdot y \cdot (L^2 - 2D^2)}{L^2 \cdot D^2} - \frac{y^3}{3L^2} - \nu \cdot \left(\frac{x^2 \cdot y}{L^2} - \frac{y^3}{3D^2} \right) \right) \quad (4.3)$$

The following graphs show the total average relative error between the results obtained with FEMAS, using the three different methods, and the analytical solution, calculated using equation (4.1) for four different meshes ($9 \times 9 = 81$ nodes, $17 \times 17 = 289$ nodes, $33 \times 33 = 1089$ nodes and $65 \times 65 = 4225$ nodes).

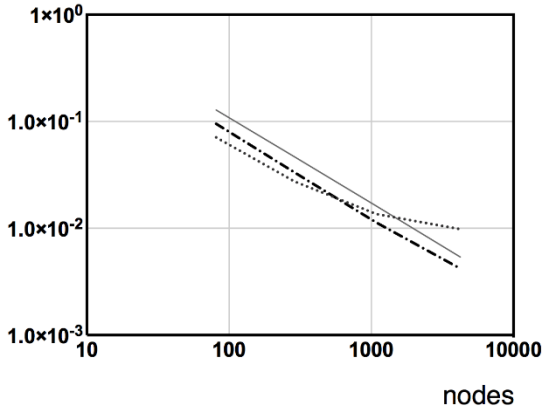

Figure 4.7 - Average relative normal stress error, σ_{xx}

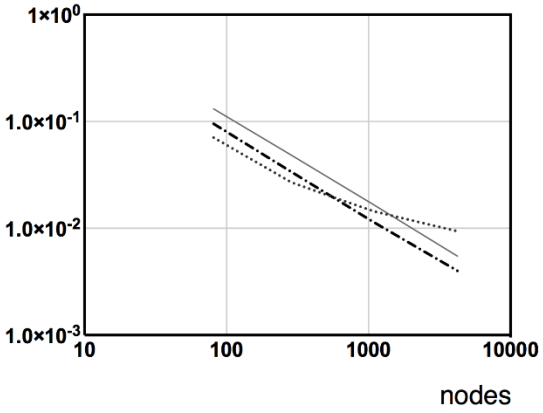

Figure 4.8 - Average relative normal stress error, σ_{yy}

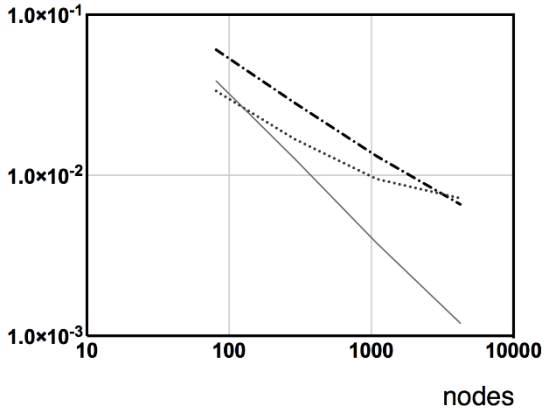

Figure 4.9 - Average relative shear stress error, τ_{xy}

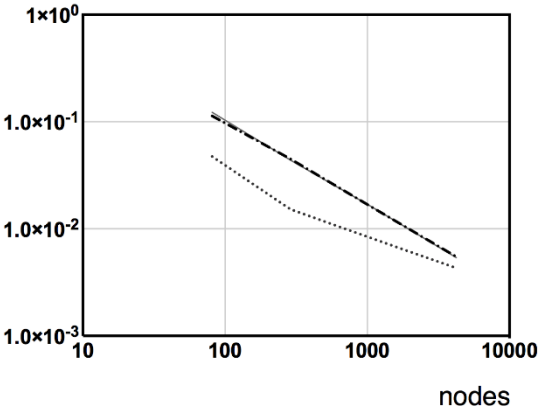

Figure 4.10 - Average relative displacement error, u

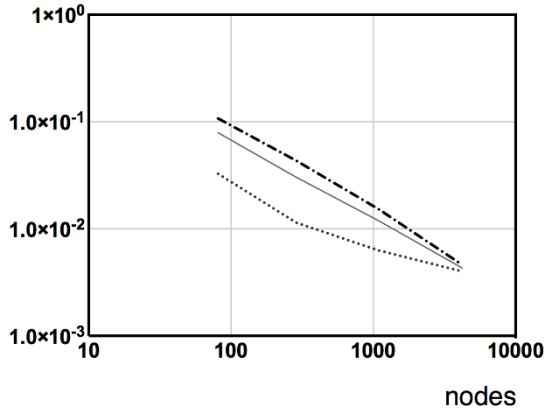

Figure 4.11 - Average relative displacement error, v

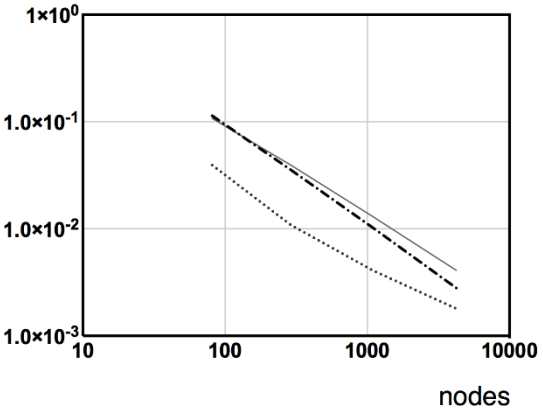

Figure 4.12 - Average relative displacement error, |u|

Looking at the results it is possible to observe that both meshless methods showed very high accuracy, with the total average relative error never being above 1%. It can also be seen that both the RPIM and the NNRPIM provide much more accurate results

than the ones obtained through the FEM (except for the shear stress, in which the FEM provides a slightly better result).

The results also show the high convergence rate of the methods, as seen by the decrease of the average relative error associated with the mesh refinement.

In order to better understand the convergence of the methods, the total displacement of a single node, represented by A in Figure 4.6 was studied.

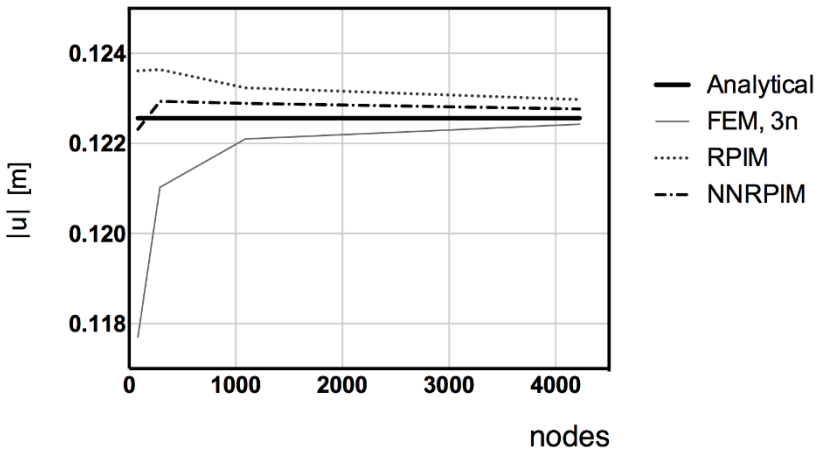

Figure 4.13 - Point A displacement.

From the observation of figure 4.13, it can be drawn that both the RPIM and the NNRPIM require less nodes discretizing the problem domain than the FEM to achieve an accurate solution, and that they both converge faster.

In figures 4.14 and 4.15 the normal and shear stresses obtained are shown along interest line $x = 0$ and $y = [0, D]$.

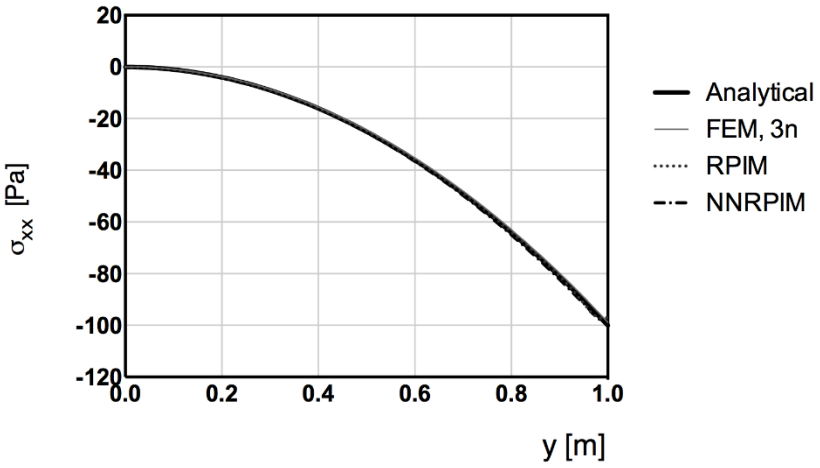

Figure 4. 14 - Normal stress $\boldsymbol{\sigma_{xx}}$ obtained along $\boldsymbol{x = 0}$ and $\boldsymbol{y = [0, D]}$.

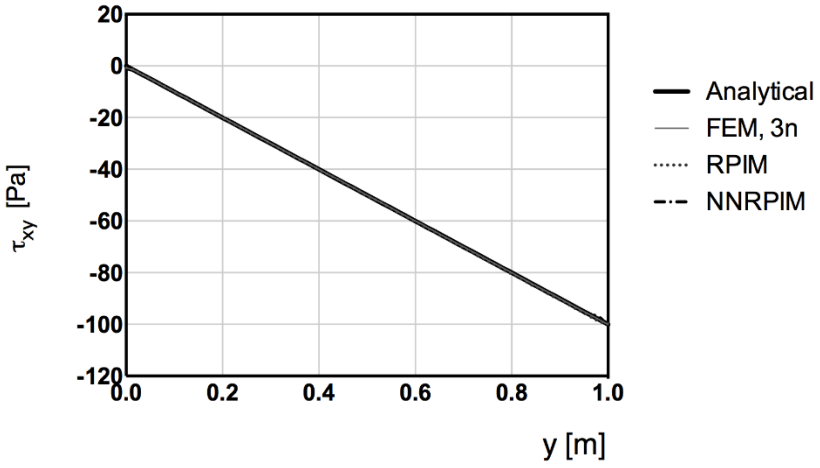

Figure 4.15 - Shear stress $\boldsymbol{\tau_{xy}}$ obtained along $\boldsymbol{x} = \frac{L}{2}$ and $\boldsymbol{y} = [\mathbf{0}, \boldsymbol{D}]$.

The normal and shear stress values, obtained with both the RPIM and the NNRPIM are extremely close to the analytical solution.

The computational time for each analysis, using a $65 \times 65 = 4225$ nodes mesh is shown below.

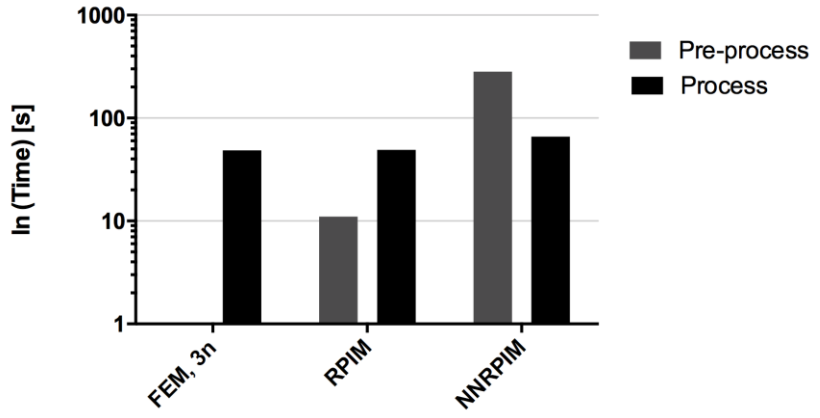

Figure 4.16 - Computation time for both phases of each analysis for 65x65=4225 nodes.

Although the Process phase of all the three methods takes approximately the same time, as seen in figure 4.16, there are several discrepancies regarding the pre-process phase. While in the FEM the pre-process is very fast, the RPIM and NNRPIM require more time to finish this phase. This happens because of the way nodal connectivity is enforced, as seen in Chapter 2, with influence-domains having to be constructed for every node discretizing the problem domain. The NNRPIM has a higher computational cost than the RPIM since in order to obtain the influence-domains, first, each node's Voronoï cell must be constructed and assembled in the Voronoï diagram. Throughout this work, second-degree influence-cells were used in the NNRPIM analysis, which also

leads to an even higher computation time. However, this provides higher nodal connectivity and subsequently, higher accuracy in the results. In addition to all this, meshless methods use more nodes to construct shape functions than the FEM therefore the construction of the meshless shape functions takes more time than the equivalent. process of the FEM.

On the other hand, by looking at Figure 4.13, it is clear that a coarser mesh could also be used and still achieve accurate results, which would significantly reduce the analysis time.

4.2.2 3D Square Plate

A solid domain $\Omega \in \mathbb{R}^3$, similar to the previous example, is taken under consideration as seen in Figure 4.17.

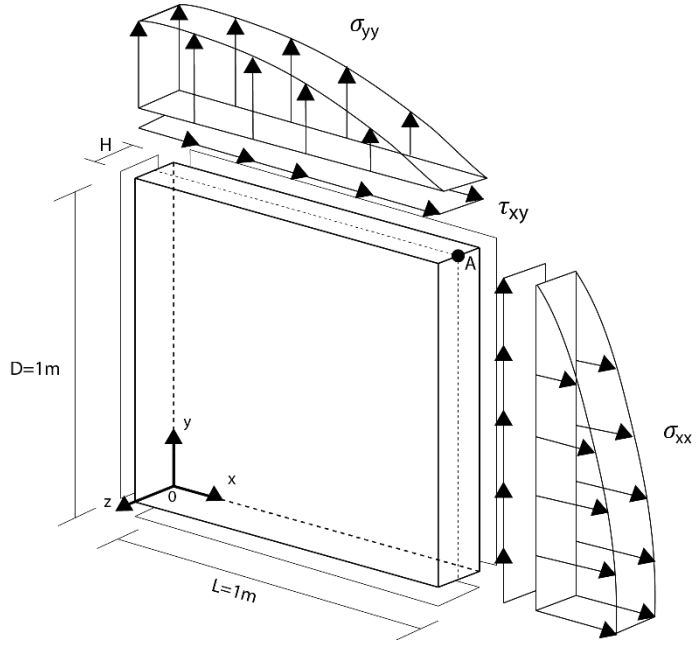

Figure 4.17 - Quarter of 3D square plate under parabolic stress.

This domain is subject to the same stress field as presented in equation (4.2) and the same displacement constraints $u = 0: \forall_{y,z} \in \mathbb{R}^3 \wedge x = 0$ and $v = 0: \forall_{x,z} \in \mathbb{R}^3 \wedge y = 0$ as well as an added displacement constraint $w = 0: \forall_{x,y} \in \mathbb{R}^3 \wedge z = 0$ with $u = (u, v, w)$.

The analytical displacement field is the same as equation (4.3), once again obtained from equation (4.2), neglecting the displacement in the Oz direction.

As stated earlier in the chapter, thickness H is dependent on the nodal discretization. Denser nodal meshes are studied with a smaller thickness, H, in order to maintain a regular mesh. In this work, all three-dimensional examples were discretized with 3 nodes in the thickness, so the relation comes,

$$H = 2 \times h \tag{4.4}$$

in which H represents the solid thickness and h is the nodal spacing.

Since we are neglecting stresses and displacements in the oz direction, this change of thickness does not affect the solution.

All the results were obtained along the centre line of the solid, $z = H/2$.

The following graphs show the medium error between the results obtained with FEMAS, using the three different methods, and the analytical solution, calculated using equation (4.1) for four different meshes ($9 \times 9 \times 3 = 243$ nodes, $17 \times 17 \times 3 = 867$ nodes, $33 \times 33 \times 3 = 3267$ nodes and $65 \times 65 \times 3 = 12675$ nodes).

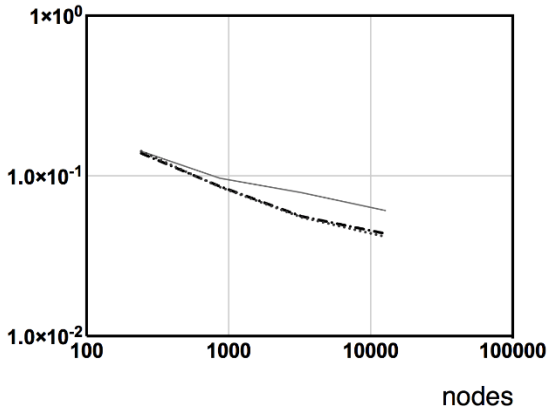

Figure 4.18 – Average relative normal stress error, σ_{xx}

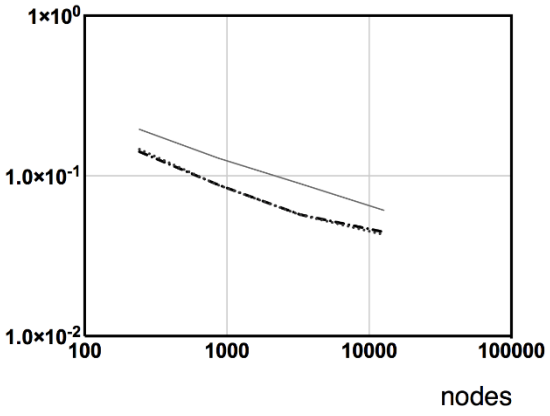

Figure 4.19 - Average relative normal stress error, σ_{yy}

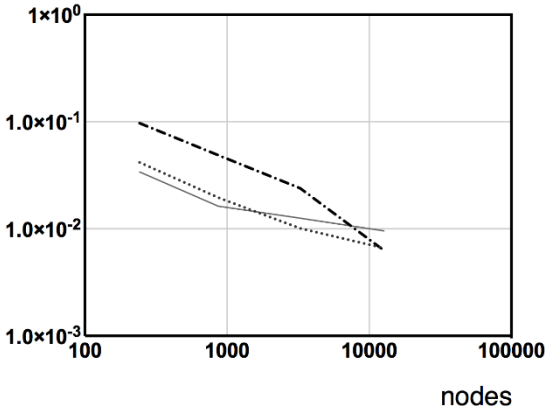

Figure 4.20 - Average relative shear stress error, τ_{xy}

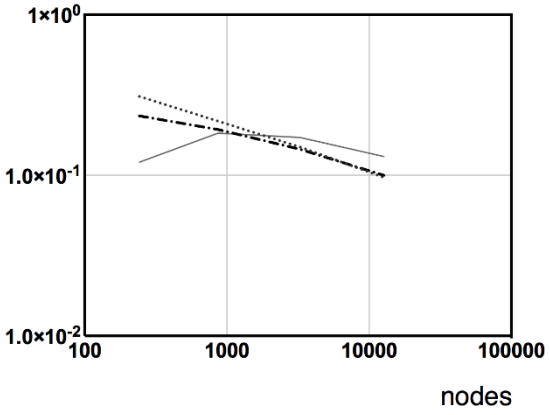

Figure 4.21 - Average relative displacement error, u

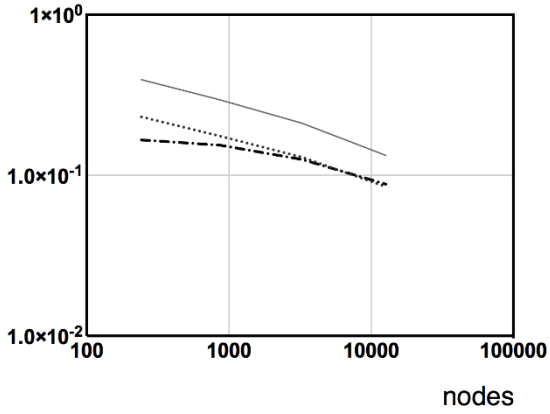

Figure 4.22 - Average relative displacement error, v

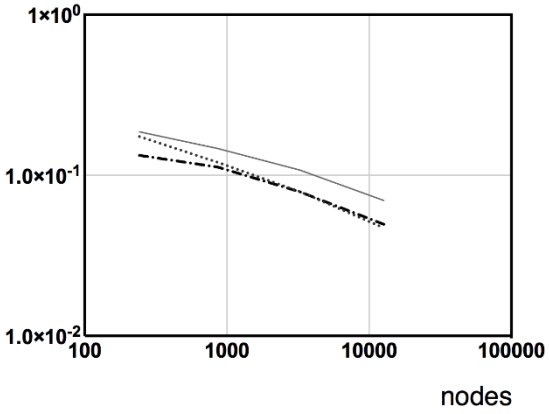

Figure 4.23 - Average relative displacement error, |u|

The results obtained with the RPIM and NNRPIM show a reduced error when compared to the ones obtained through the FEM for every analysis. It is also possible to observe that both meshless methods converge with increasingly denser meshes (notice that the medium error drops).

By only taking into consideration node A, as seen in Figure 4.17, the following results were obtained for the total displacement.

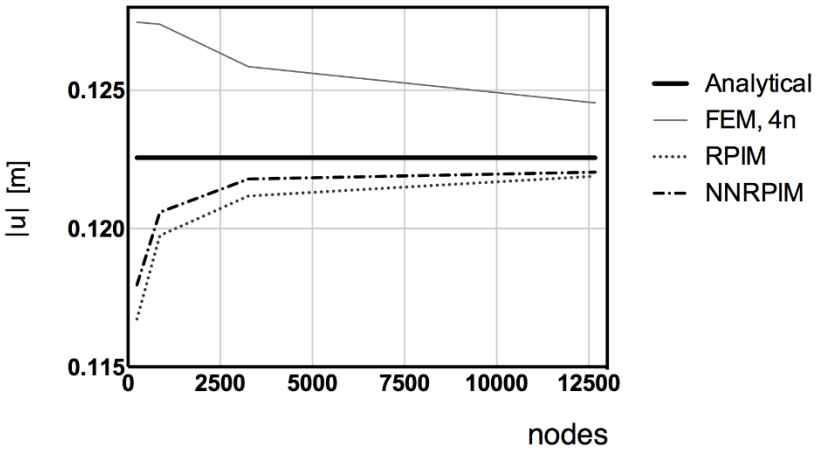

Figure 4.24 - Point A displacement.

It is possible to see that both meshless methods converge much faster and need fewer nodes to obtain an accurate solution.

In figures 4.25 and 4.26 the normal and shear stresses obtained are shown along interest line $x = 0$ and $y = [0, D]$.

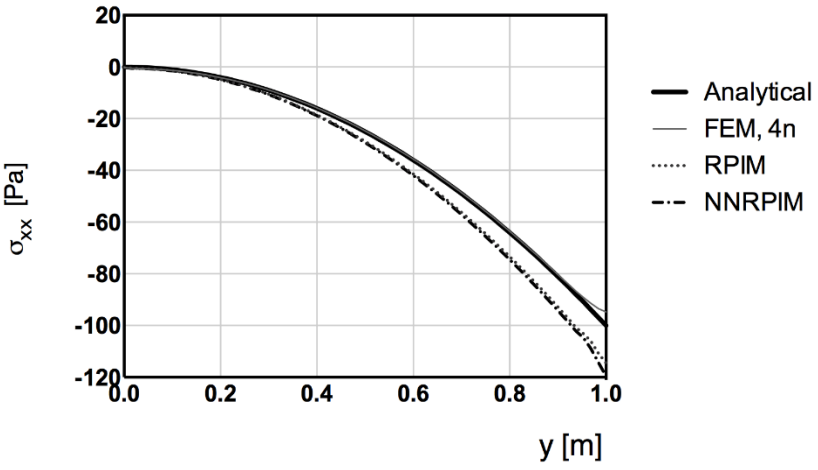

Figure 4.25 - Normal stress $\boldsymbol{\sigma_{xx}}$ obtained along $\boldsymbol{x = 0}$ and $\boldsymbol{y = [0, D]}$.

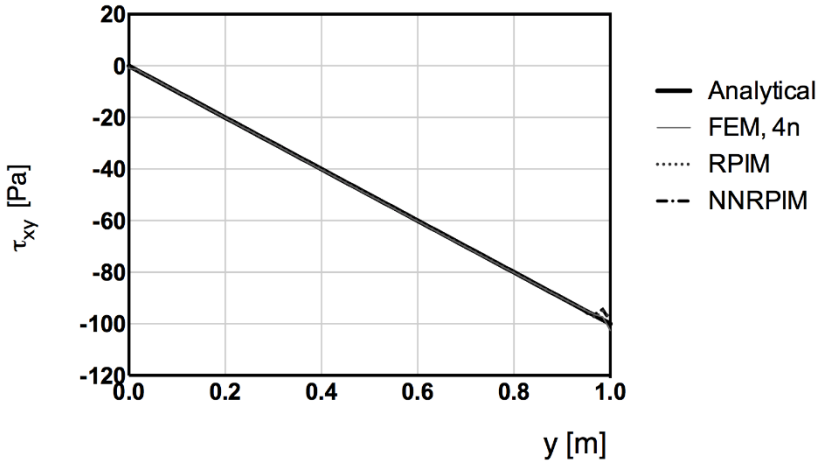

Figure 4.26 - Shear stress $\boldsymbol{\tau_{xy}}$ obtained along $\boldsymbol{x} = \frac{\boldsymbol{L}}{\boldsymbol{2}}$ and $\boldsymbol{y} = [\boldsymbol{0}, \boldsymbol{D}]$.

The discrepancy seen in Figure 4.25 happens because of the way the stresses are obtained on the nodes. Initially the stresses are obtained for the integration points, and then an average is calculated, between all the surrounding integration points. Nodes closer to the walls have a higher probability of presenting lower stresses because of this.

The computational time for each analysis, using a $65 \times 65 \times 3 = 12675$ nodes mesh is shown below.

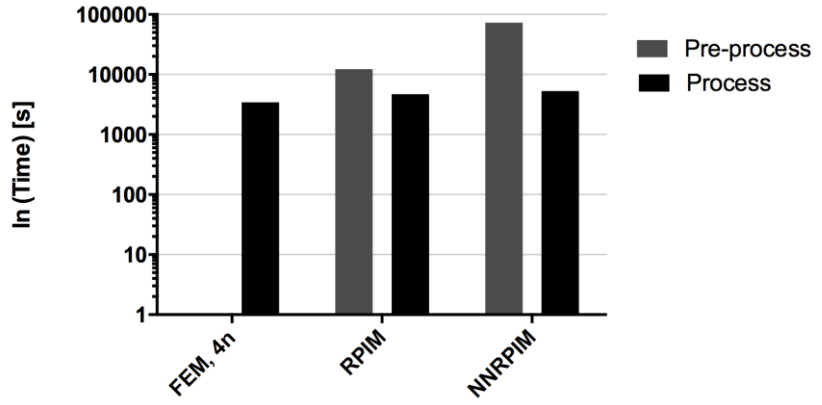

Figure 4.27 - Computation time for both phases of each analysis for 65x65x3=12675 nodes.

Once again, the computation time for the pre-process of both the RPIM and the NNRPIM is much larger than the needed for the FEM. However, if a coarser mesh had been used, this time would drop significantly and still yield accurate results, as seen in Figure 4.24.

4.2.3 2D Cantilever Beam

Considering a cantilever beam defined by a solid domain $\Omega \in \mathbb{R}^2$, loaded with the following stress field,

$$\sigma_{xx}(x,y) = -\frac{P \cdot (L-x)}{I} \cdot y$$

$$\sigma_{yy}(x,y) = 0 \tag{4.5}$$

$$\tau_{xx}(x,y) = -\frac{P \cdot D^2}{8\,I} \cdot \left(1 - \frac{4\,y^2}{D^2}\right)$$

with $P = 10\ N$ and $I = \frac{D^3}{12}$, as seen in Figure 4.26.

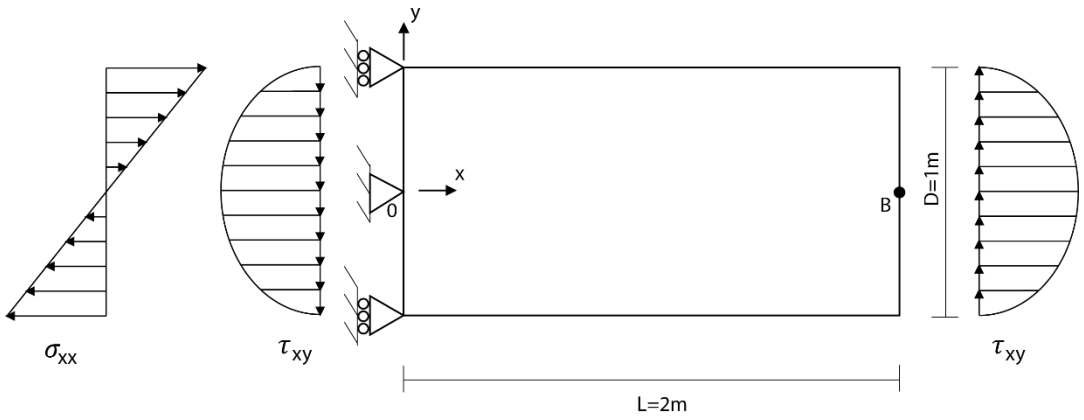

Figure 4.28 - 2D Cantilever Beam.

The following displacements are constrained: $u = 0 : x = 0 \wedge \left\{y = -\frac{D}{2} \vee y = \frac{D}{2}\right\}$ and $\{u, v\} = 0 : \{x, y\} = \{0,0\}$ with $u = (u, v)$. The analytical displacement field is obtained through the stress field shown in equation (4.5) and comes,

$$u(x,y) = -\frac{2\,P}{E \cdot D^3} \cdot \left[3x \cdot (2L - x) \cdot y + (2 + \nu) \cdot \left(y^2 - \frac{D^2}{4}\right) \cdot y\right]$$

$$v(x,y) = \frac{2\,P}{E \cdot D^3} \cdot \left[x^2 \cdot (3L - x) + 3\nu \cdot (L - x) \cdot y^2 + x \cdot (4 + 5\nu) \cdot \frac{D^2}{4}\right] \tag{4.6}$$

The medium error between the results obtained with FEMAS, using the three different methods, and the analytical solution are calculated using equation (4.1), using increasingly denser meshes ($5 \times 9 = 45$ nodes, $9 \times 17 = 153$ nodes, $17 \times 33 = 561$ nodes and $33 \times 65 = 2145$ nodes) is shown in the following graphs,

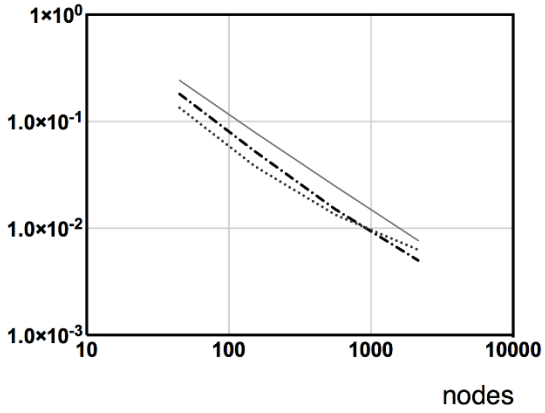

Figure 4.29 - Average relative normal stress error, σ_{xx}

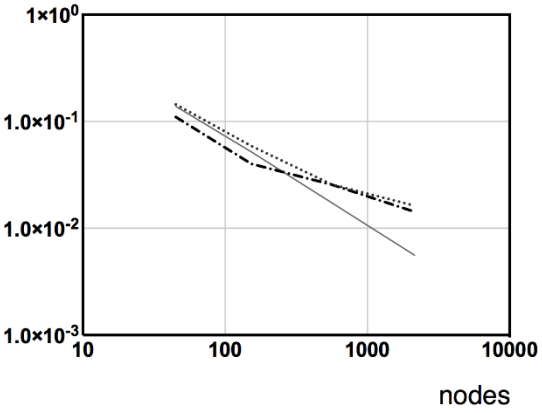

Figure 4.30 - Average relative shear stress error, τ_{xy}

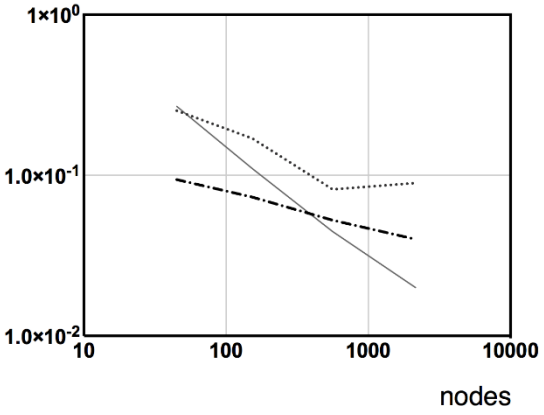

Figure 4.31 - Average relative displacement error, u

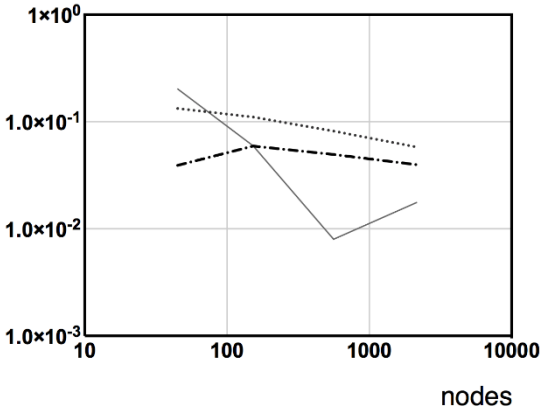

Figure 4.32 - Average relative displacement error, v

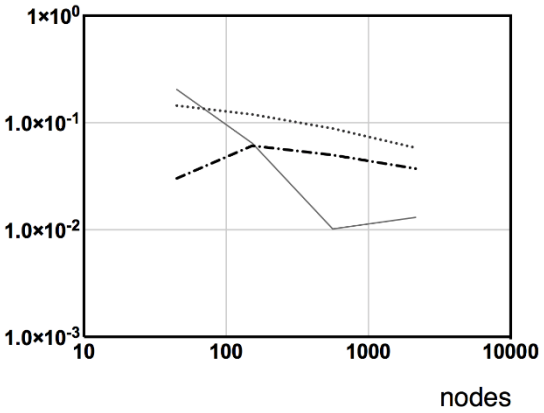

Figure 4.33 - Average relative displacement error, |u|

The results obtained show the high accuracy of the RPIM and NNRPIM, with the medium error obtained for the normal stress staying below 1%, and for the shear stress staying below 1%. Displacements in the NNRPIM are always below 4% medium error, and in the RPIM they are below 9%.

Taking node B, as seen in Figure 4.28, into consideration the following displacements are obtained by increasing the nodal mesh discretization.

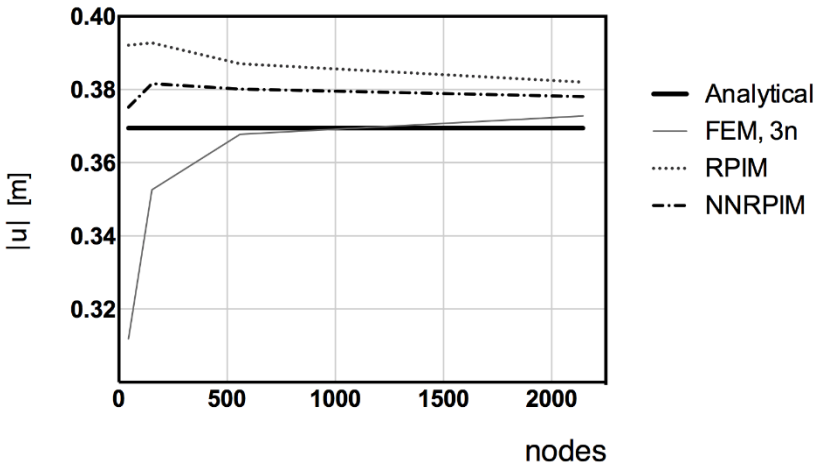

Figure 4.34 - Point B displacement.

It is possible to see that the RPIM and NNRPIM converged much faster than the FEM. While the later has intersected the analytical answer, by looking at the method's slope on figure 4.34 it is possible to see it still hasn't converged, and if we continued increasing the nodal mesh discretization, the results would be further away from the analytical solution. This is also observed by looking at figures 4.32 and 4.33, in which the medium error goes down and then up.

In figures 4.35 and 4.36 the normal and shear stresses obtained are shown along interest line $x = 0$ and $y = \left[-\frac{D}{2}, -\frac{D}{2}\right]$.

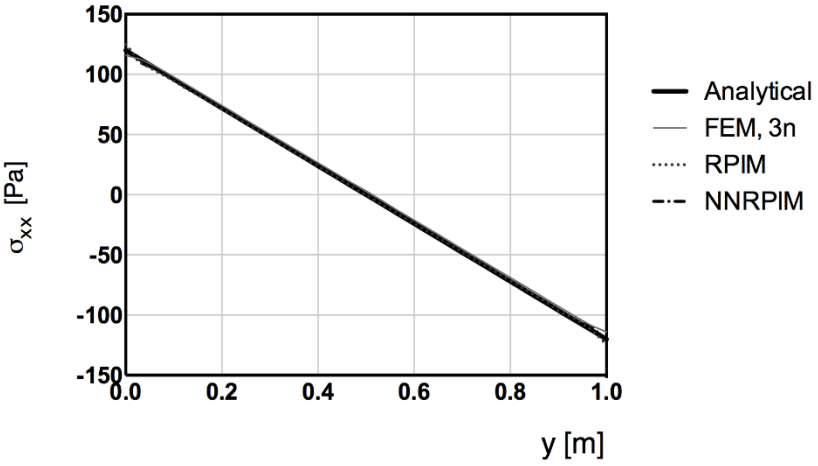

Figure 4.35 - Normal stress $\boldsymbol{\sigma_{xx}}$ obtained along $\boldsymbol{x = 0}$ and $\boldsymbol{y} = [-\frac{\boldsymbol{D}}{\boldsymbol{2}}, \frac{\boldsymbol{D}}{\boldsymbol{2}}]$.

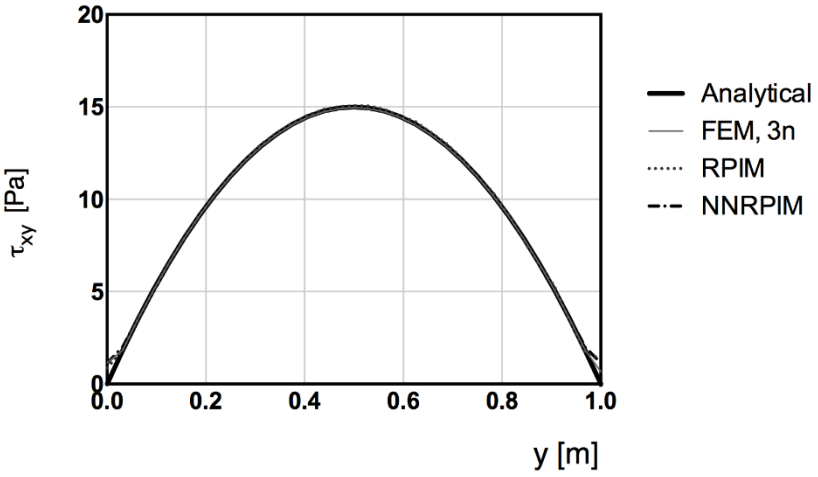

Figure 4.36 - Shear stress $\boldsymbol{\tau_{xy}}$ obtained along $\boldsymbol{x} = \frac{\boldsymbol{L}}{\boldsymbol{2}}$ and $\boldsymbol{y} = [-\frac{\boldsymbol{D}}{\boldsymbol{2}}, \frac{\boldsymbol{D}}{\boldsymbol{2}}]$.

The normal and shear stress values, obtained with both the RPIM and the NNRPIM are extremely close to the analytical solution.

The computational time for each analysis, using a $33 \times 65 = 2145$ nodes mesh is shown below.

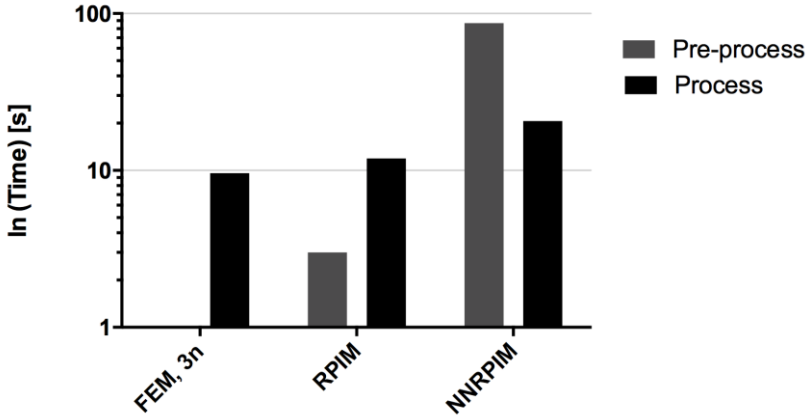

Figure 4.37 - Computation time for both phases of each analysis for 33x65=2145 nodes.

Once again, although the Process phase of all the three methods takes approximately the same time, as seen in figure 4.37, there are several discrepancies regarding the pre-process phase. This was already explained above. On the other hand, a coarser mesh could be used, which can be confirmed by Figure 4.32.

4.2.4 3D Cantilever Beam

Similarly to what was done in the 3D Square plate example, the domain is now considered as $\Omega \in \mathbb{R}^3$, as seen in figure 4.38.

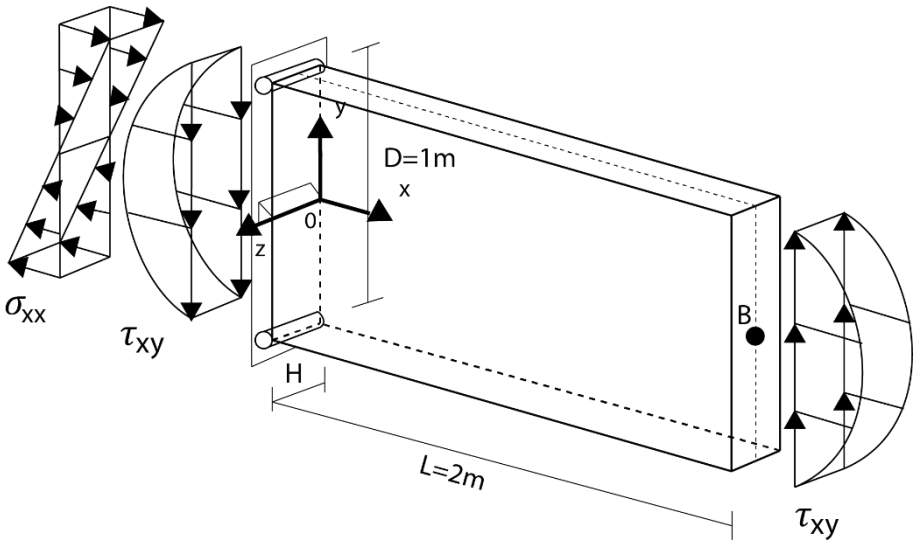

Figure 4.38 - 3D Cantilever beam.

This domain is subject to the same stress field as presented in equation (4.5) and the similar displacement constraints , which now become $u = 0 : \forall_z \in \mathbb{R}^3 \ \wedge x = 0 \wedge \left\{ y = -\frac{D}{2} \vee y = \frac{D}{2} \right\}$ and $\{u, v\} = 0 : \forall_{x,z} \in \mathbb{R}^2 \ \wedge \{x, y\} = \{0,0\}$ with $u = (u, v, w)$.

The analytical displacement field is the same as equation (4.5), once again obtained from equation (4.5), neglecting the displacement in the Oz direction. Along thickness 3 elements were considered and all the results were obtained along the centre line of the solid, $z = H/2$.

The following graphs show the average relative error between the results obtained with FEMAS, using the three different methods, and the analytical solution, calculated using equation (4.1) for four different meshes ($5 \times 9 \times 3 = 135$ nodes, $9 \times 17 \times 3 = 459$ nodes, $17 \times 33 \times 3 = 1683$ nodes and $33 \times 65 \times 3 = 6435$ nodes).

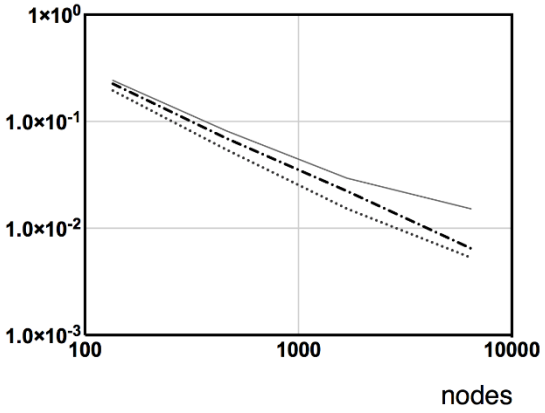

Figure 4.39 - Average relative normal stress error, σ_{xx}

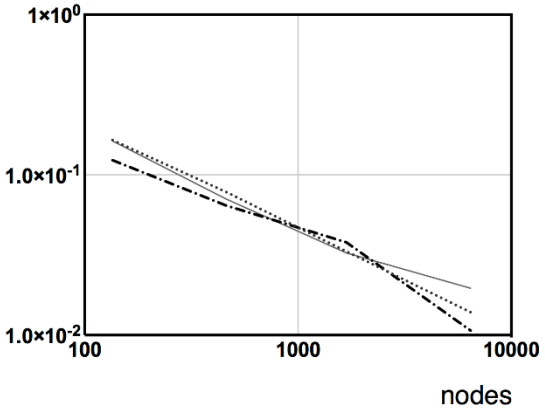

Figure 4.40 - Average relative shear stress error, τ_{xy}

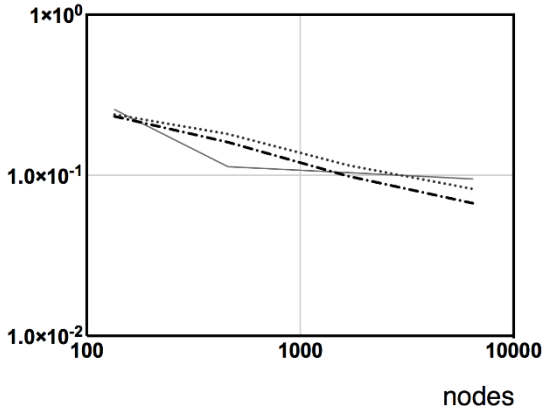

Figure 4.41 - Average relative displacement error, u

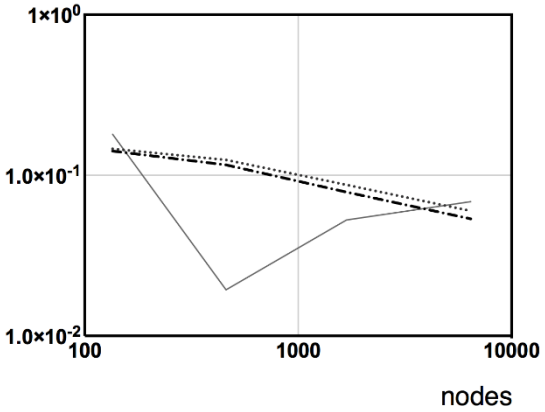

Figure 4.42 - Average relative displacement error, v

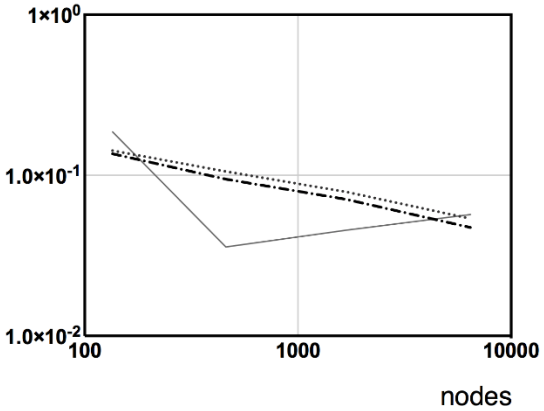

Figure 4.43 - Average relative displacement error, |u|

The meshless methods provide a much more accurate solution, with medium errors for the normal and shear stress staying at below 1% and 2% respectively. The displacement error is below 9% in the RPIM and below 7% in the NNRPIM.

Taking node B, as seen in Figure 4.38, into consideration the following displacements are obtained by increasing the nodal mesh discretization.

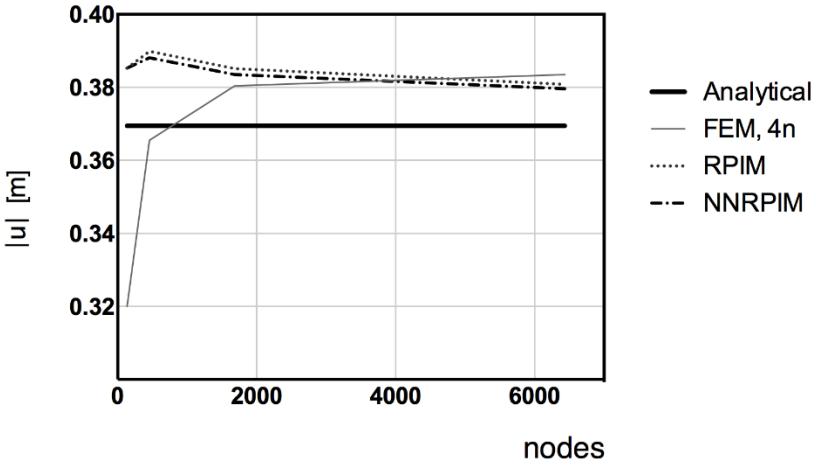

Figure 4.44 - Point B displacement.

As seen in the previous example, the FEM hasn't converged yet, and if the nodal mesh was increased the final result would be worse than the meshless methods.

In Figures 4.45 and 4.46 the normal and shear stresses obtained are shown along interest line $x = 0$ and $y = \left[-\frac{D}{2}, \frac{D}{2}\right]$.

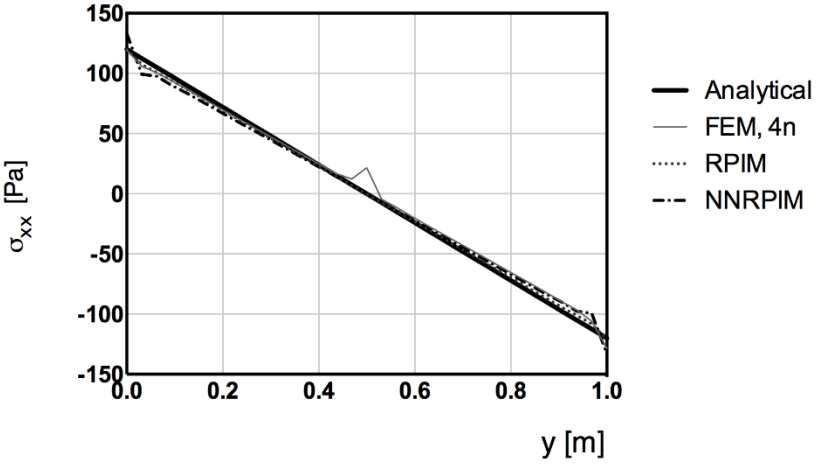

Figure 4.45 - Normal stress $\boldsymbol{\sigma_{xx}}$ obtained along $\boldsymbol{x = 0}$ and $\boldsymbol{y = [-\frac{D}{2}, \frac{D}{2}]}$.

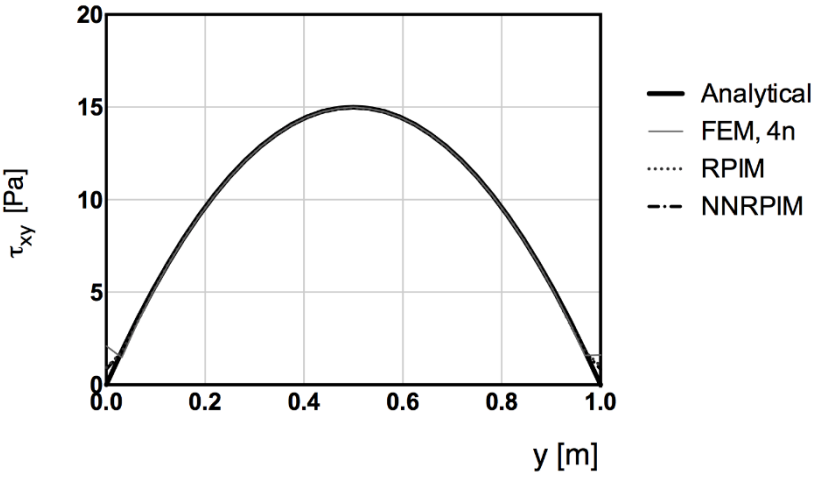

Figure 4.46 - Shear stress $\boldsymbol{\tau_{xy}}$ obtained along $\boldsymbol{x} = \frac{L}{2}$ and $\boldsymbol{y} = [-\frac{D}{2}, \frac{D}{2}]$.

The normal and shear stress values, obtained with both the RPIM and the NNRPIM are extremely close to the analytical solution.

The computational time for each analysis, using a $33 \times 65 \times 3 = 6435$ nodes mesh is shown below.

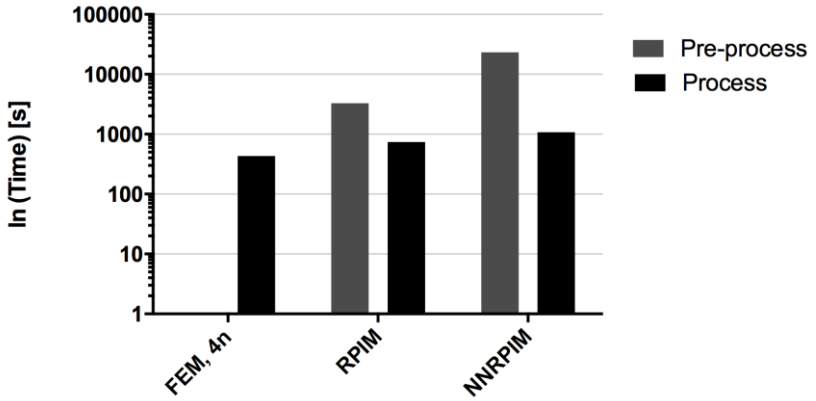

Figure 4.47 - Computation time for both phases of each analysis for 33x65x3=6435 nodes.

Once again, it can be seen that the RPIM and NNRPIM pre-processing take much longer, but the use of a coarser mesh would reduce this time and still provide accurate results.

Chapter 5

Numerical Examples

Commercial airplane cabin windows serve three main functions: provide a view outside, allow natural light inside the cabin and resist the pressure differential. Besides fulfilling these functions, and since they are located in a prominent section of the airplane, flight deck windshields have to also be resistant against a bird strike event.

The present chapter starts with a description of the windshield in study, addressing its geometry, materials and the forces acting on it. Next a brief convergence study is presented, focusing only the proposed geometry. The chapter ends with the analysis of several 3D windshield configurations and a 2D analysis of the frame that surrounds the windshield, against a bird strike event.

5.1 Problem description

Due to its location (the front of the airplane), the main windshields, shown in Figure 5.1, are often struck by birds when at low heights, usually during take-off or landing.

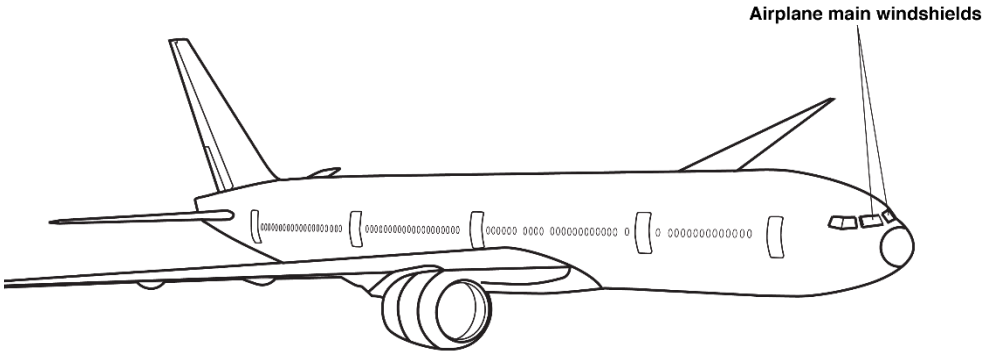

Figure 5.1 - Commercial airplane model.

In order for an airplane to be certified to fly, one of the requirements issued by the European Aviation Safety Agency (EASA) states that the aeroplane windshield must be designed to withstand an impact with a 1.8kg bird when the relative velocity between the airplane and the bird is equal to the airplane cruise velocity, V_c, at sea level, or 0.85

V_c at 2400m, whichever is the more critical, and assure a continued safe flight and landing, with no penetration of the airplane main windshields [54].

Due to the need of being both impact resistant and shatter proof, commercial airplane's flight deck windshields are frequently multi-layer constructions, consisting of at least two layers of glass, bound together with a vinyl interlayer.

Glass is a very appealing material in aeronautics, not only because of its outstanding strength and durability, which can be further strengthened by thermally tempering, but also because of the superior optical quality it offers. The PVB interlayer has great optical properties as well as excellent tear and tensile strength and prevents the windshield from shattering if any of the glass panes break.

5.1.1 Windshield

The windshield used in this work was based on the main windshields found on the Boeing 737-700, which are built from two layers of thermally tempered glass bound together with a Plasticized Polyvinyl Butyral (PVB) interlayer, as seen in Figure 5.2 [55].

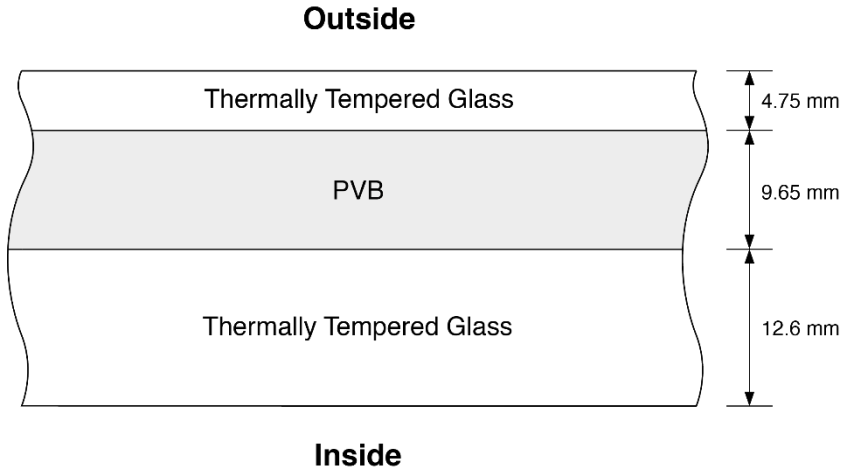

Figure 5.2 - Construction of the airplane flight deck main windshield.

Whereas glass behaves like a linear elastic material under increasing loads [56], PVB exhibits viscoelastic behaviour [57]. However, since the duration of bird impact loading is in the range of milliseconds, this material can be considered as being linear elastic [58]. Since bird strikes usually happen at low heights, the mechanical properties of both materials were considered at room temperature and are shown in the table below,

Table 5. 1 - Windshield materials mechanical properties.

Material	Thermally Tempered Glass [56]	PVB [58]	
Young's Modulus, E	70	0.985	[GPa]
Poisson's ratio, ν	0.22	0.45	-

The general main windshield dimensions and position in the cockpit are shown in Figures 5.3 and 5.4.

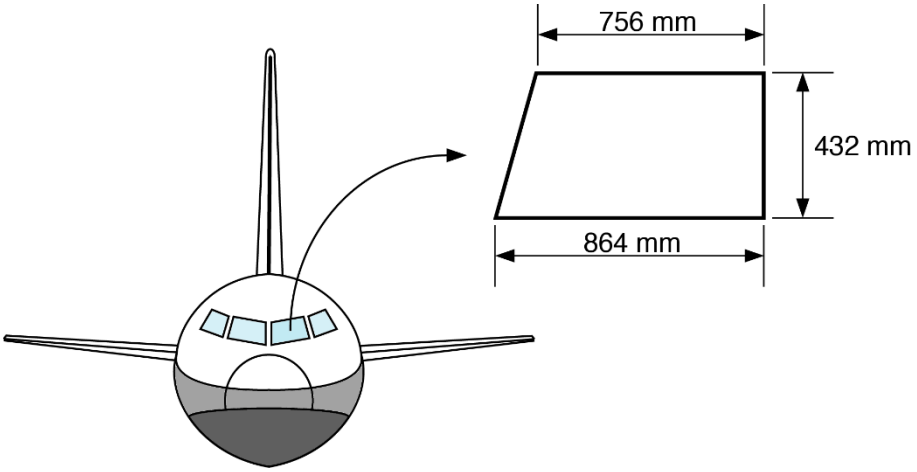

Figure 5.3 - General main windshield dimensions.

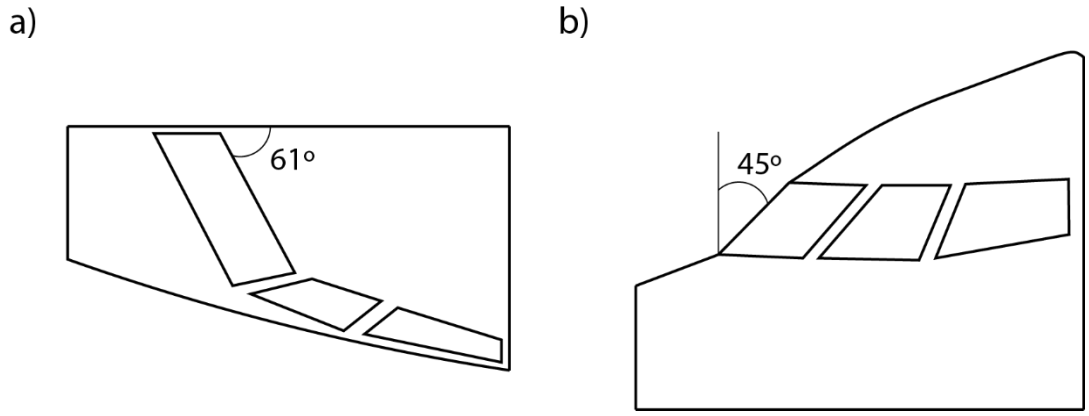

Figure 5.4 - a. General main windshield position – Top view. **b.** General main windshield position – Side view.

5.1.2 Windshield edge attachment

Another important aspect to the construction of the windshield is how it is attached to the airplane frame. Earlier approaches to this problem used countersunk

head screws drilled directly into the windshield, but this proved to be problematic since it often induced unwanted stress concentrations.

Currently, this is done with the use of a clamped attachment. First, a monoblock dry seal, such as silicone, surrounds the windshield peripheral edges providing both air and leak tightness between the inside and the outside of the airplane. Following this, a monoblock flange, with a shape similar to the shape of both the windshield edges and the airplane structure is used to clamp both the windshield/ silicone assembly together with the airplane frame through the use of countersunk head screws, drilled onto both the flange and the frame [59]. An example of this attachment is shown in figure 5.5.

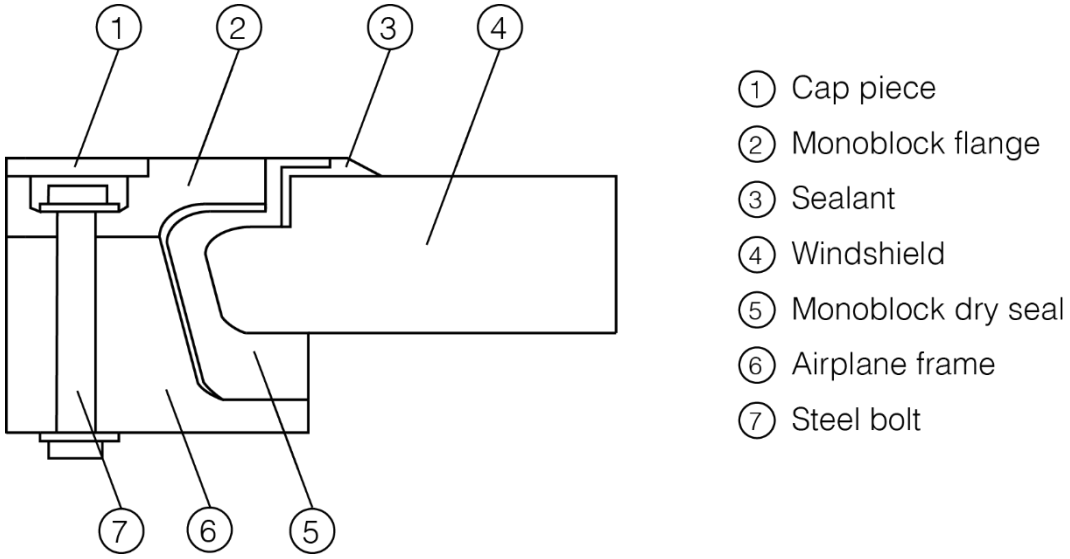

Figure 5.5 - Windshield surrounding structure example.

This was later adapted to allow for a 2D study of the windshield structure, using the computational framework presented in Chapter 4. This adaptation was done in order to make nodes of different parts of the structure coincident and is shown in Figure 5.6.

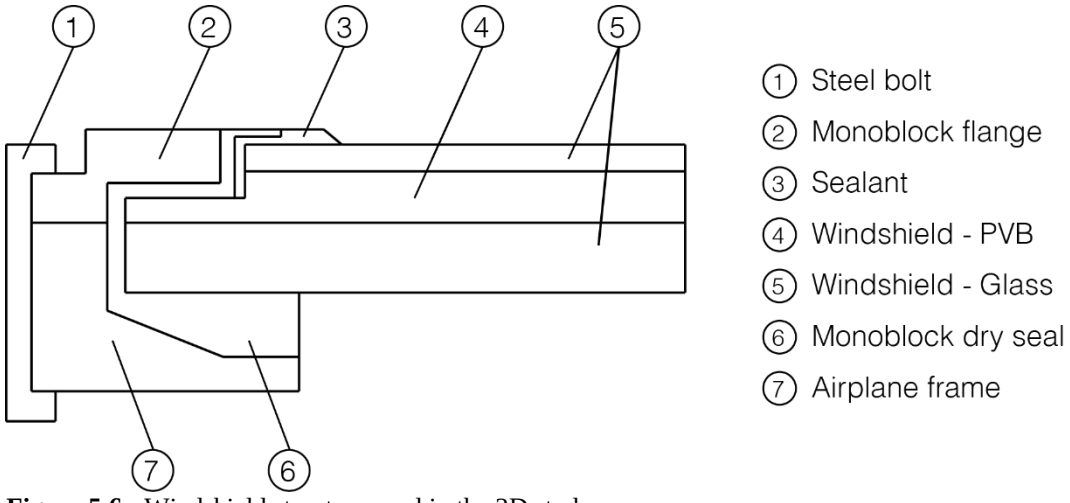

Figure 5.6 - Windshield structure used in the 2D study.

Once again, the materials used were considered as linear-elastic and their mechanical properties are shown in the table below.

Table 5. 2 - Windshield surrounding structure materials mechanical properties.

Component	**1 – Steel Bolt**	**2 – Monoblock Flange**	**3 - Sealant**	**6 – Monoblock dry seal**	**7 – Airplane frame**	**Units**
Material	Steel [55, 60]	Aluminium 2024-T351 [55, 61]	Acrylic Latex [55, 62]	Silicone [55, 63]	Aluminium 7075-T351 [55, 64]	-
Young's Modulus, E	207E+9	73.1E+9	1E+6	1E+6	72E+9	[GPa]
Poisson's ratio, v	0.3	0.33	0.45	0.463	0.33	-

5.1.3 Bird impact force

The impact force of the bird was obtained from the literature, since the FEMAS does not encompass a contact-impact coupling algorithm. According to previous works, when the relative velocity between the airplane and a 1.8kg bird is 200 m/s, the peak impact force is approximately 100kN [65].

It should be noted that the referenced work used a different windshield geometry and material, but this way it is assured that the forces used are realistic.

As stated previously, bird strikes usually occur at low heights, mostly during take-off or landing, which leads to the bird impact against the airplane to happen at an angle. However, in order to study the worst case scenario, it was decided that the impact would happen when both the airplane and the bird were flying horizontally relative to the sea level, as depicted in Figure 5.7.

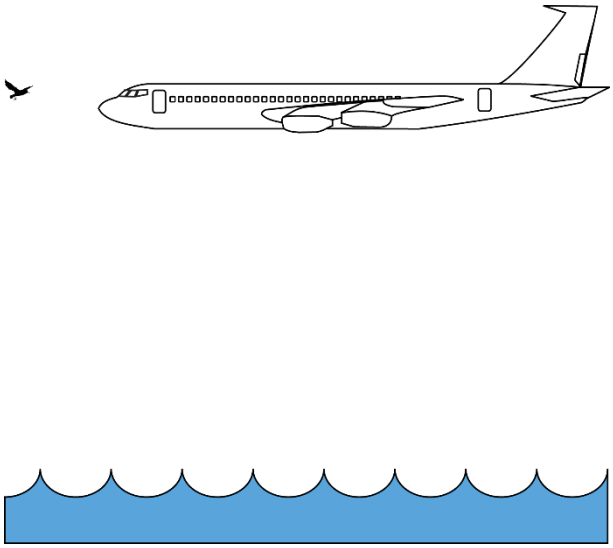

Figure 5.7 - Impact representation.

The impact was then applied in nine different locations of the windshield, as represented in Figure 5.8.

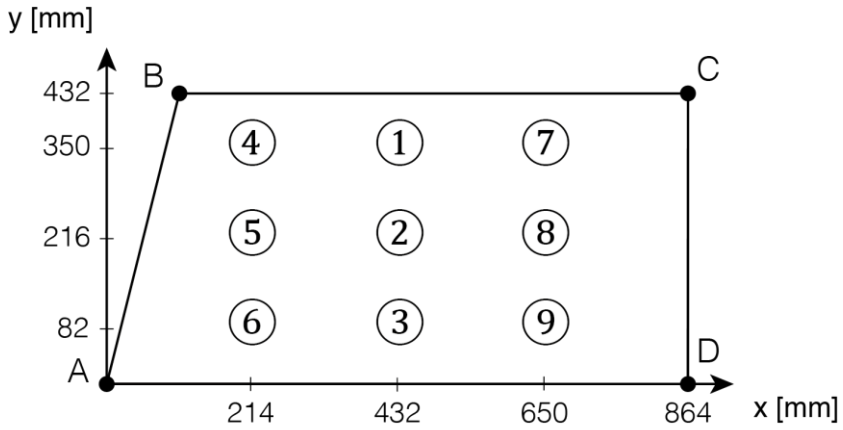

Figure 5.8 - Impact force locations.

Therefore, in this work the bird strike impact is simulated by an instantaneous force, F=100kN, applied in nine distinct locations of the windshield, respecting the windshield geometry, and airplane position relative to the sea level, as seen in Figure 5.9.

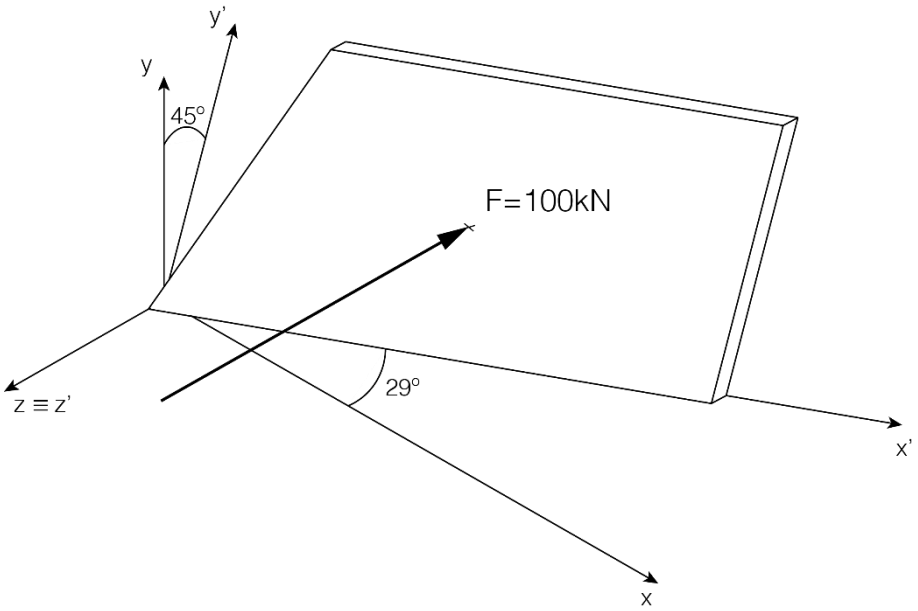

Figure 5.9 - Representation of the impact, using point 2 as a guideline.

The 3D model was analysed considering an elasto-static approach assuming the classical 3D deformation theory. The 2D model was analysed considering the plane-strain deformation theory.

5.2 Windshield geometry convergence study

Prior to studying the bird impacts on the windshield, another convergence study was performed, this time only focusing the proposed windshield geometry. This convergence study aims to establish whether or not the nodal discretization used in the rest of the study was adequate. Once again, four different nodal discretizations were used along the windshield, each one progressively more refined than the other.

- Nodes: 1114
- No. Thickness nodes: 2
- Regular Mesh

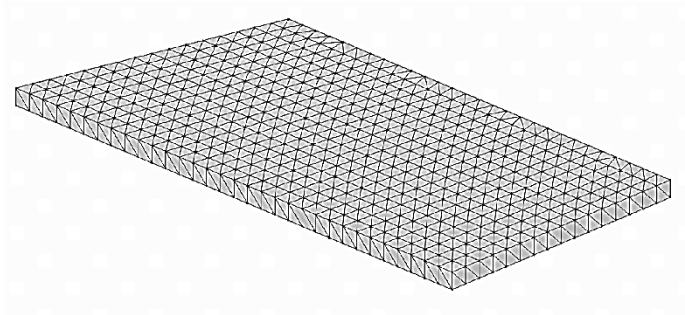

Figure 5.10 – 1114 nodes mesh.

- Nodes: 1671
- No. Thickness nodes: 3
- Irregular Mesh

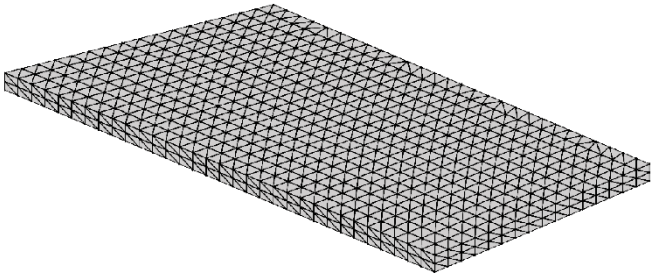

Figure 5.11 - 1671 nodes mesh.

- Nodes: 3657
- No. Thickness nodes: 3
- Irregular Mesh

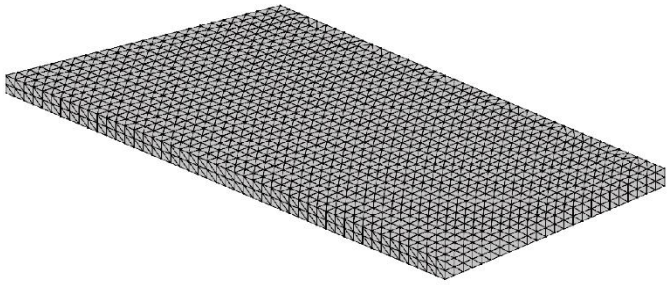

Figure 5.12 – 3657 nodes mesh.

- Nodes: 6411
- No. Thickness nodes: 3
- Regular Mesh

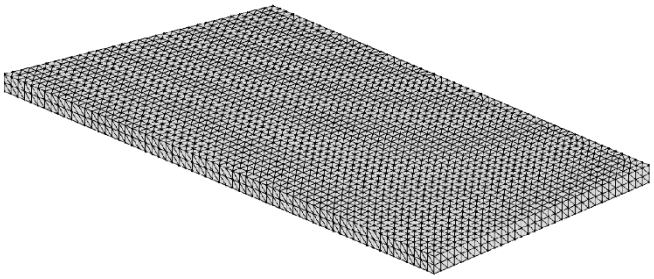

Figure 5.13 – 6411 nodes mesh.

The windshield material properties are: E=1000Pa and ν=0.3. Following this, a 1N force was applied on the upper face of the windshield, clamped along its thickness, distributed along 9 nodes surrounding the main force application point, in each of the different meshes in the location and direction shown in Figure 5.14.

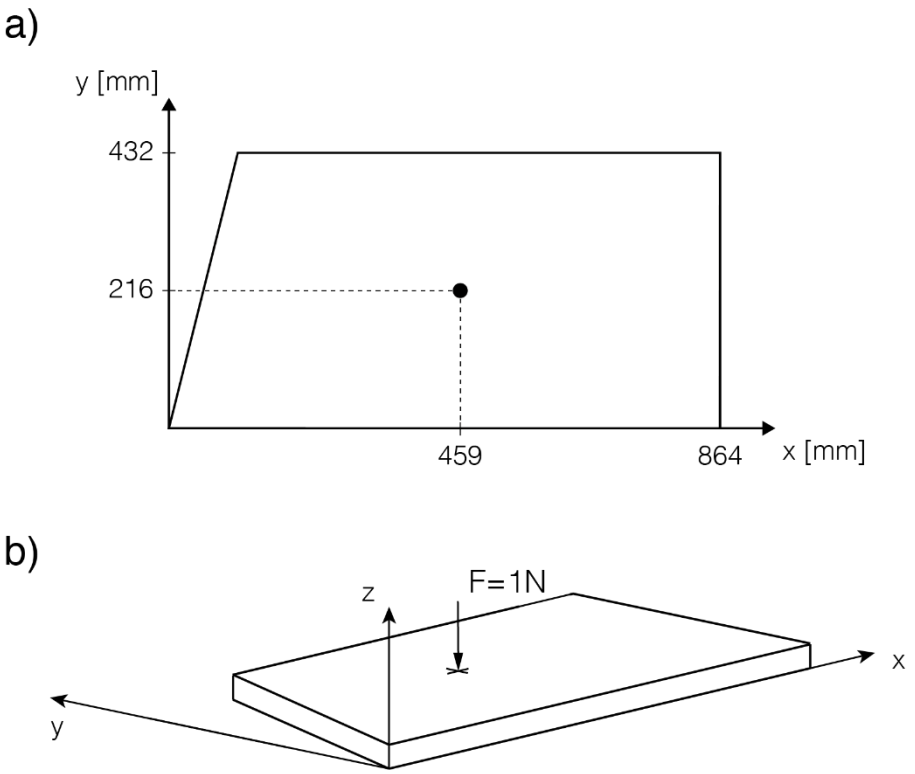

Figure 5.14 - a. Force application location. **b.** Force direction and magnitude.

The tetrahedron elements, used in the classic 3D FEM analysis, are known to be extremely stiff in bending problems [66, 67] and because of this wouldn't be suitable for comparison with the RPIM and NNRPIM. Therefore, another four meshes were created, using hexahedron elements. These new meshes are sensibly similar to the other tetrahedral meshes, only varying in 48 nodes at most from the counterpart. The force was applied in the same location in all analysed 3D models. The results were calculated for the load conditions presented in Figure 5.14.

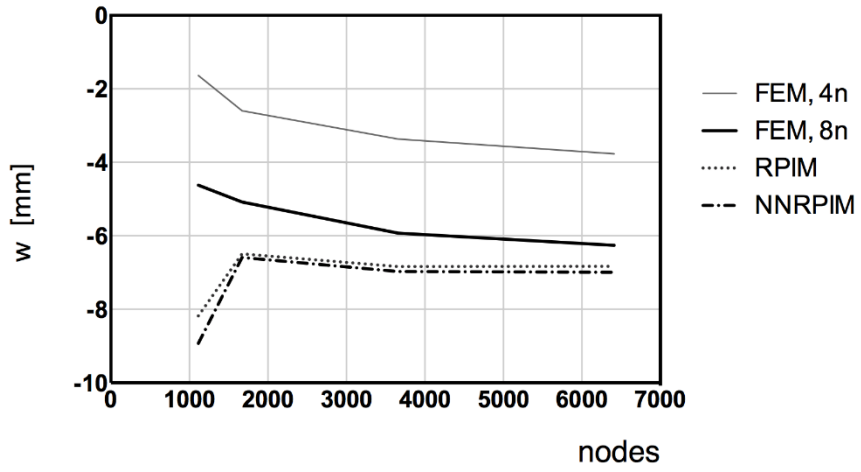

Figure 5.15 - Displacement in the w direction, with the increase of nodal discretization.

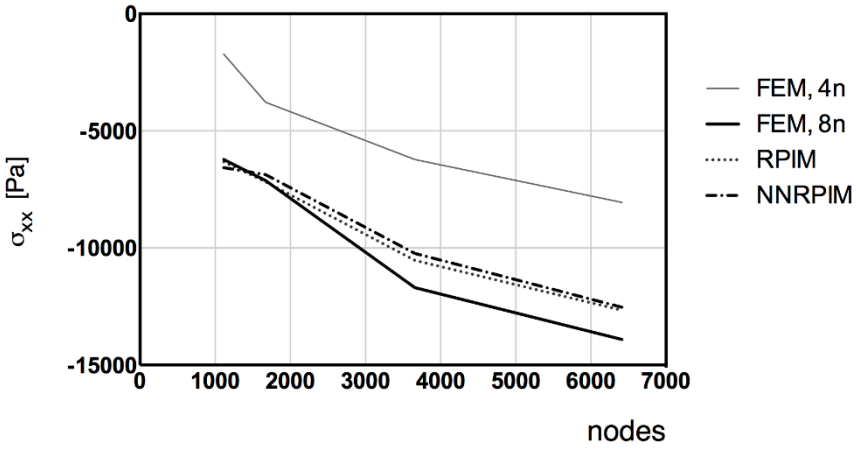

Figure 5.16 - Stress in the x direction, with the increase of nodal discretization.

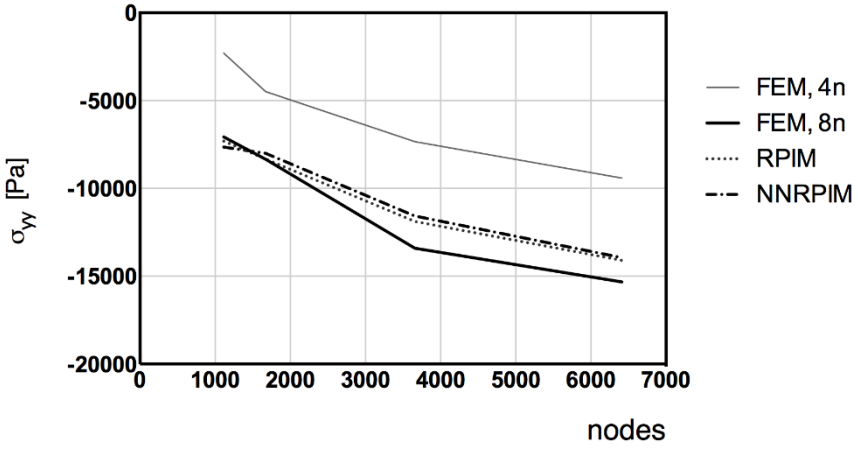

Figure 5.17 - Stress in the y direction, with the increase of nodal discretization.

Looking at Figure 5.15, it is possible to confirm that tetrahedron elements are too stiff when compared to hexahedron elements since the displacement is much lower. All the four meshes are converging, with the RPIM and the NNRPIM having already converged, much faster and with fewer nodes that the other two methods.

Figures 5.16 and 5.17 show that all four methods are extremely close to converging, which can be seen by the curve's slope, which is close to zero.

Even though a more refined mesh would yield slightly more accurate results, if more nodes were added, in order to preserve the regularity of the mesh, the discretization would have 4x more nodes which would make it impossible to analyze using FEMAS, due to computational constraints. Therefore, the 6411 mesh was the one used throughout this work.

5.3 Clamped Windshield

5.3.1 3D Windshield analysis

As a first approach to the problem, the windshield was considered as being clamped, in order to simulate the windshield and corresponding surrounding structure union. Since all the 3D models possess only 3 nodes along the windshield thickness, the 2 layers of glass together with the PVB layer were homogenised as one, leading to a fictitious homogenised windshield material defined by: E=45.3 GPa and ν=0.302.

By applying the previously mentioned bird impact force in the nine impact locations, the following results were obtained, for the von Mises Stress and total displacement, which are calculated by,

$$\sigma_{ef} = \frac{1}{\sqrt{2}}\sqrt{\left(\left(\sigma_{xx} - \sigma_{yy}\right)^2 + \left(\sigma_{yy} - \sigma_{zz}\right)^2 + (\sigma_{zz} - \sigma_{xx})^2 + 6\left(\sigma_{xy}^2 + \sigma_{yz}^2 + \sigma_{zx}^2\right)\right)} \quad (5.1)$$

$$|u| = \sqrt{\left((u_x)^2 + \left(u_y\right)^2 + (u_z)^2\right)} \quad (5.2)$$

Impact location # 1

The displacement for each impact point was calculated across the thickness and following this, the average of the three nodal displacements discretizing the thickness comes,

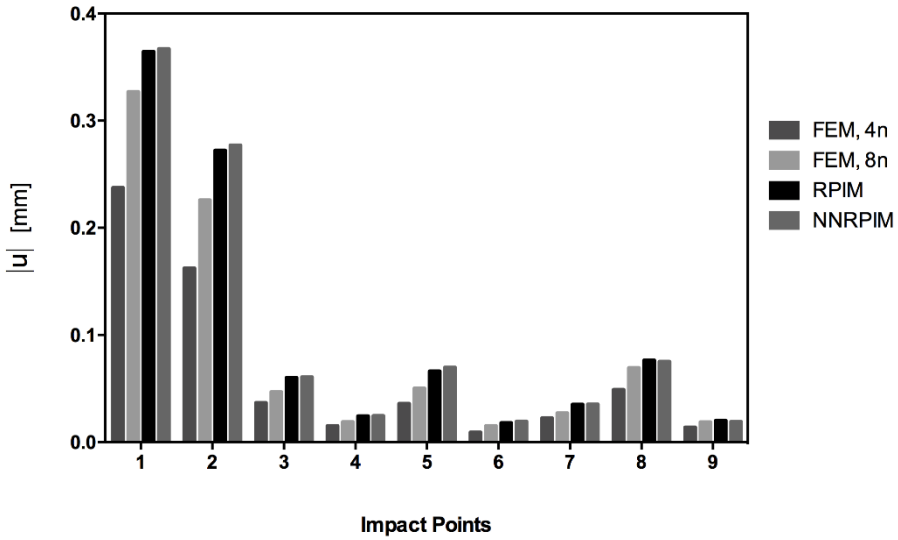

Figure 5.18 – Average nodal displacement along the thickness of each impact location caused by the impact to location 1.

The von Mises stress for each impact point was calculated across the thickness and following this, the average of the three nodal von Mises stresses discretizing the thickness comes,

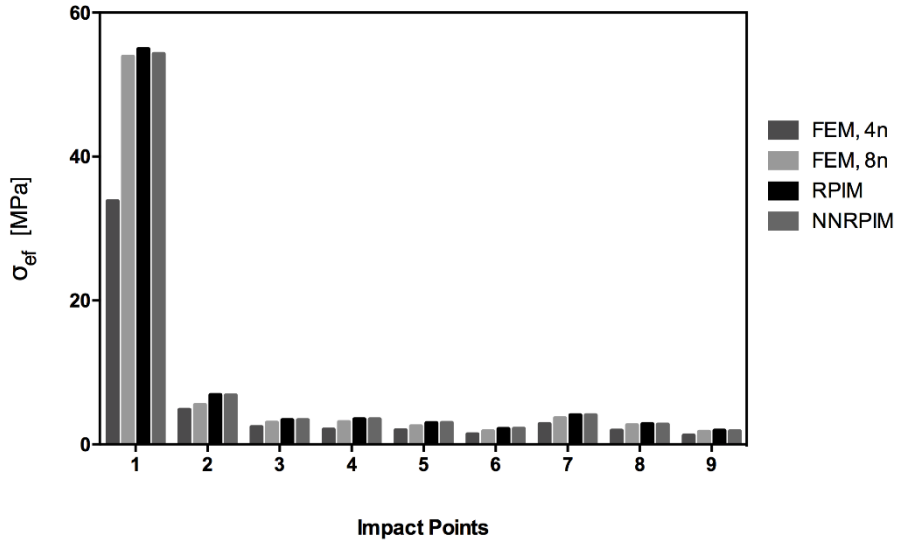

Figure 5.19 - Average nodal stress along the thickness of each impact location caused by the impact to location 1.

The von Mises stress for each node of the ABCD border of the windshield, shown in Figure 5.8, was calculated across the thickness and following this, the average of the three nodal von Mises stresses discretizing the ABCD border thickness comes,

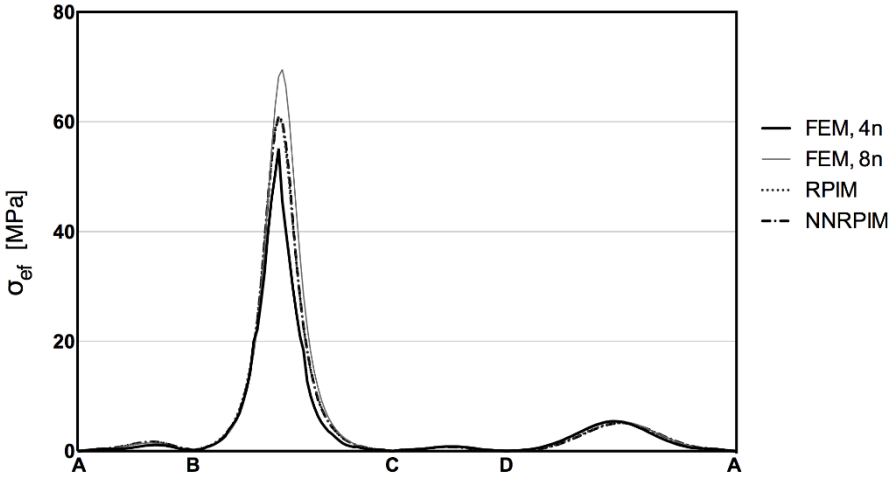

Figure 5.20 - Average nodal stress along the thickness of the clamped section of the windshield caused by the impact to location 1.

The following displacement field is obtained,

FEM, 4n

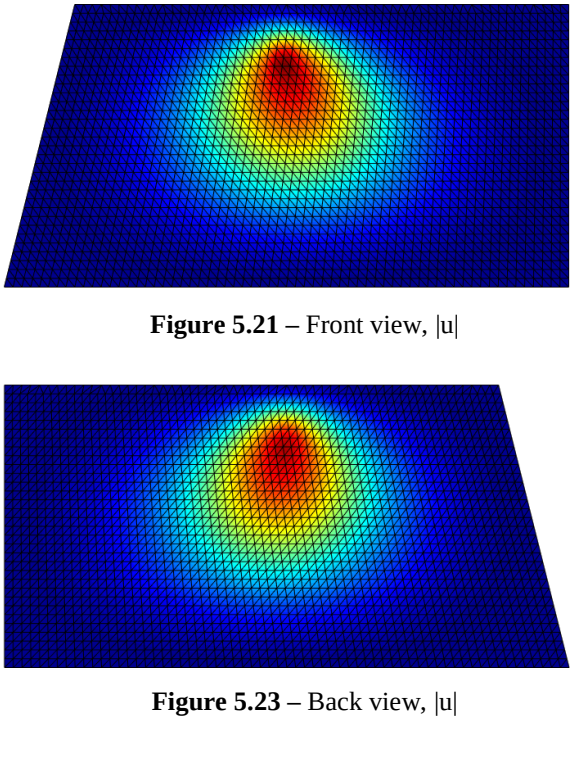

Figure 5.21 – Front view, |u|

Figure 5.23 – Back view, |u|

FEM, 8n

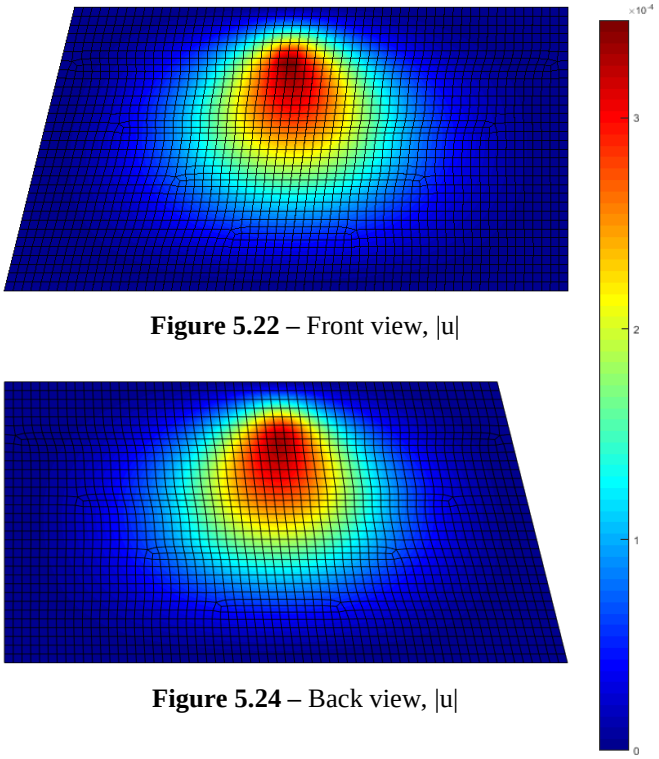

Figure 5.22 – Front view, |u|

Figure 5.24 – Back view, |u|

RPIM

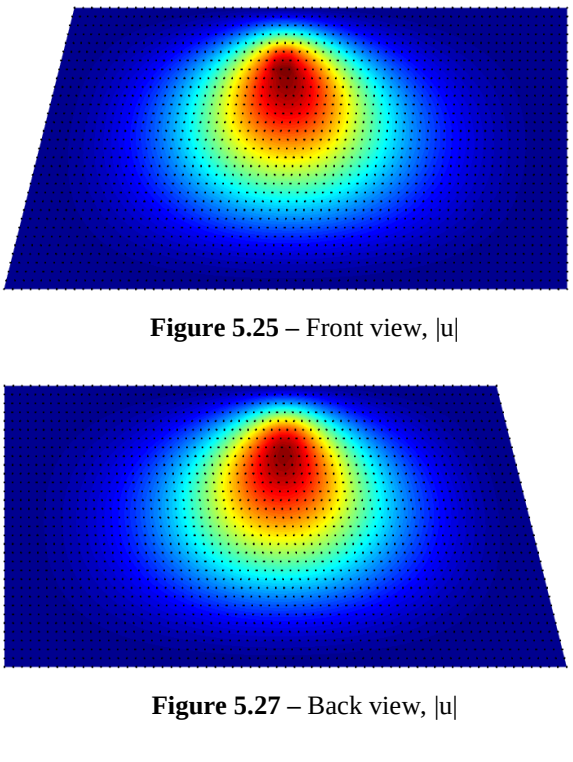

Figure 5.25 – Front view, |u|

Figure 5.27 – Back view, |u|

NNRPIM

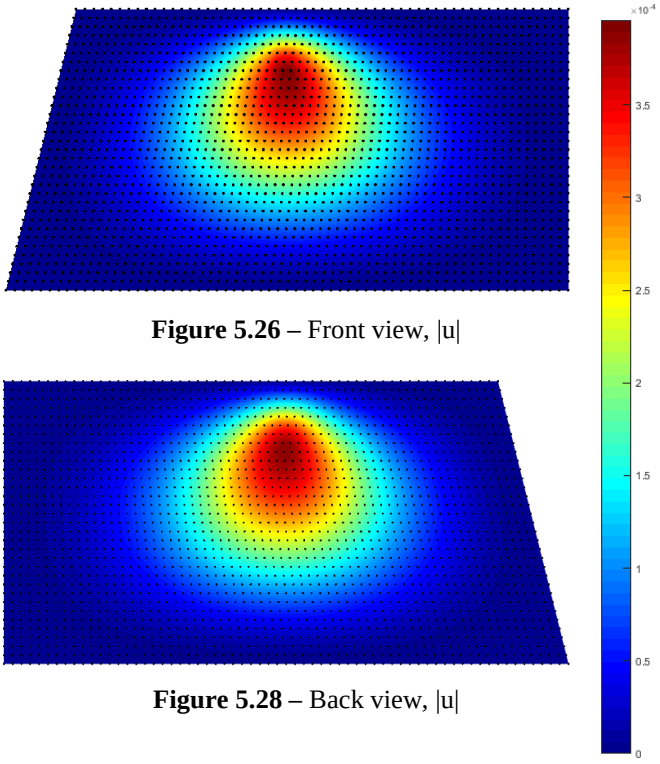

Figure 5.26 – Front view, |u|

Figure 5.28 – Back view, |u|

The following stress field is obtained,

FEM, 4n

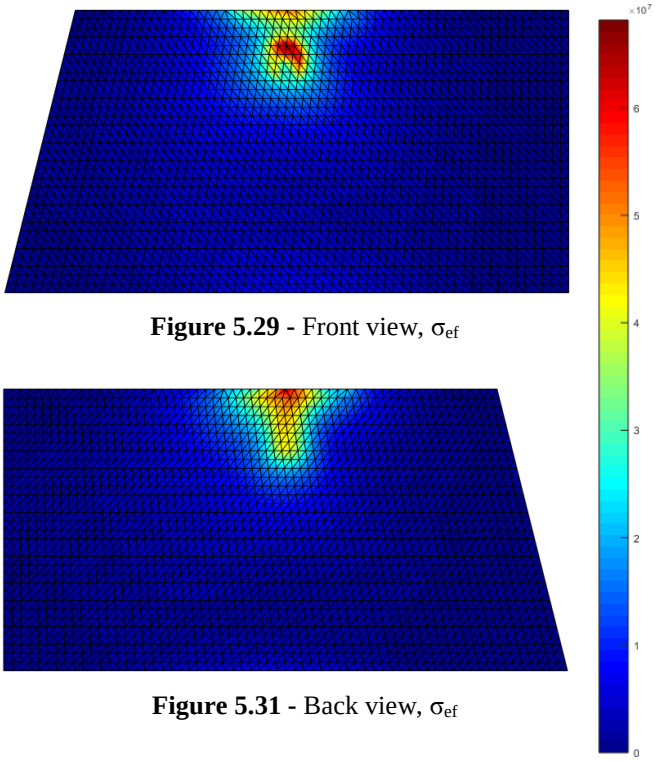

Figure 5.29 - Front view, σ_{ef}

Figure 5.31 - Back view, σ_{ef}

FEM, 8n

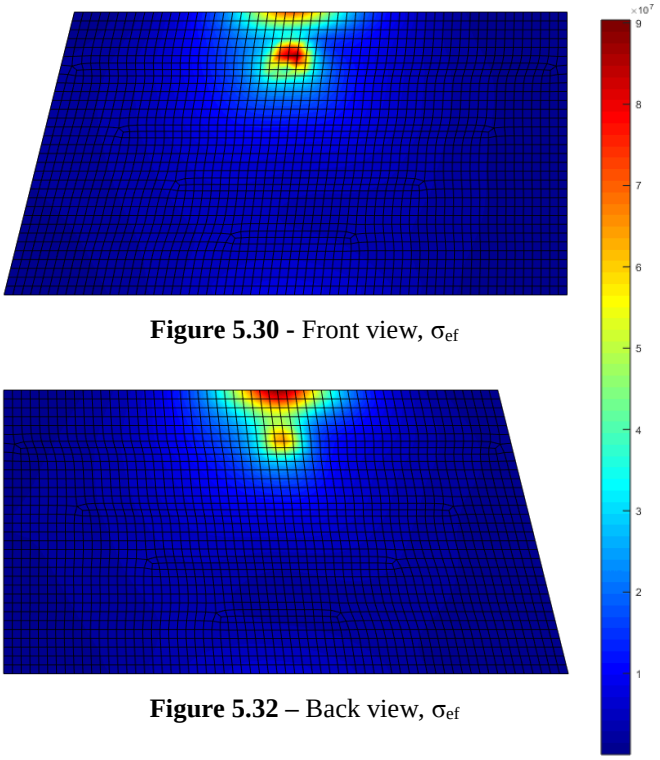

Figure 5.30 - Front view, σ_{ef}

Figure 5.32 – Back view, σ_{ef}

RPIM

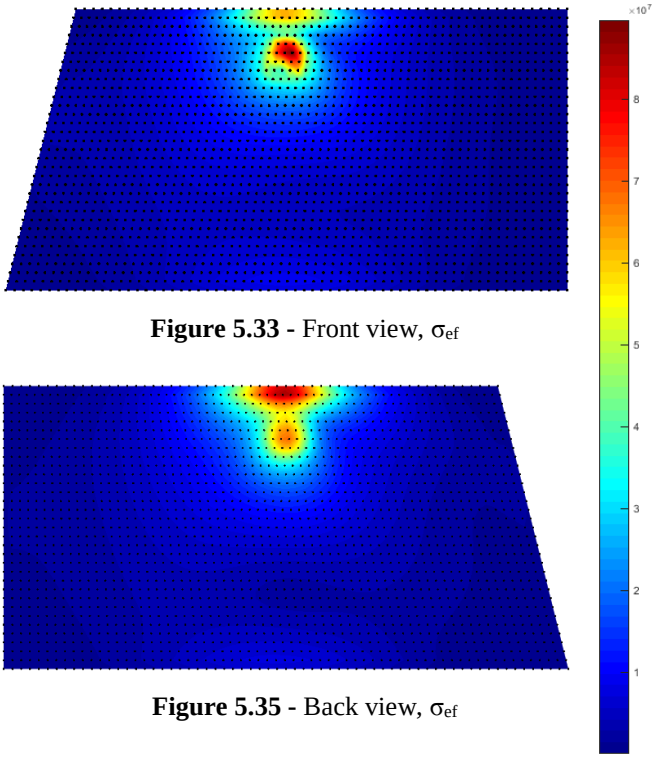

Figure 5.33 - Front view, σ_{ef}

Figure 5.35 - Back view, σ_{ef}

NNRPIM

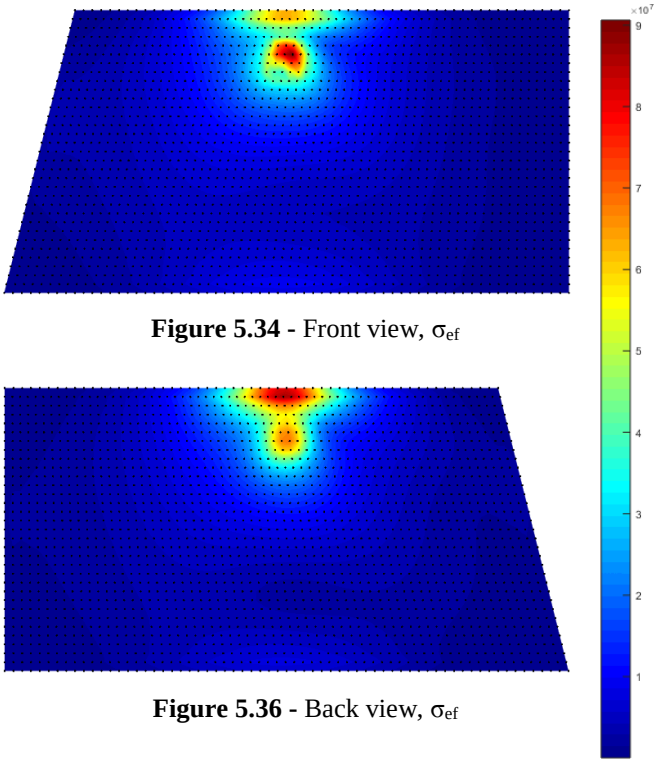

Figure 5.34 - Front view, σ_{ef}

Figure 5.36 - Back view, σ_{ef}

Impact location # 2

The displacement for each impact point was calculated across the thickness and following this, the average of the three nodal displacements discretizing the thickness comes,

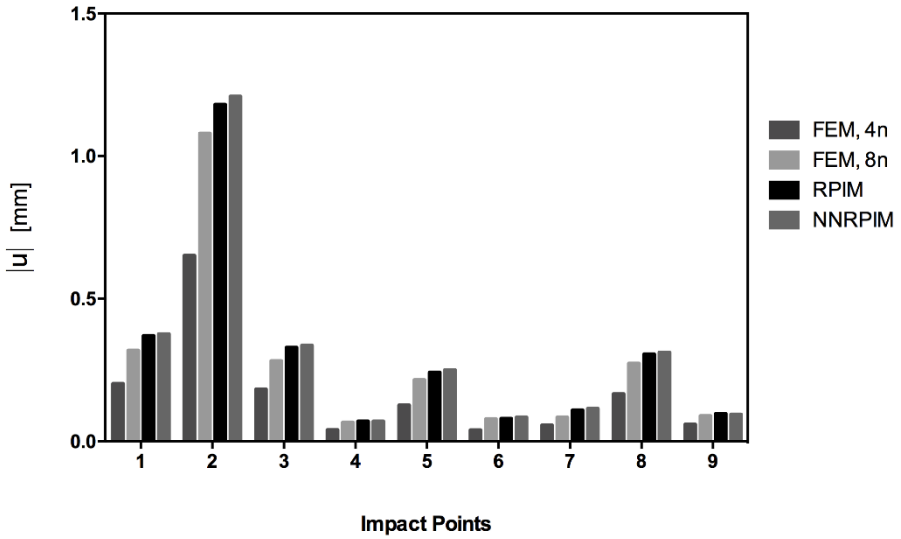

Figure 5.37 - Average nodal displacement along the thickness of each impact location caused by the impact to location 2.

The von Mises stress for each impact point was calculated across the thickness and following this, the average of the three nodal von Mises stresses discretizing the thickness comes,

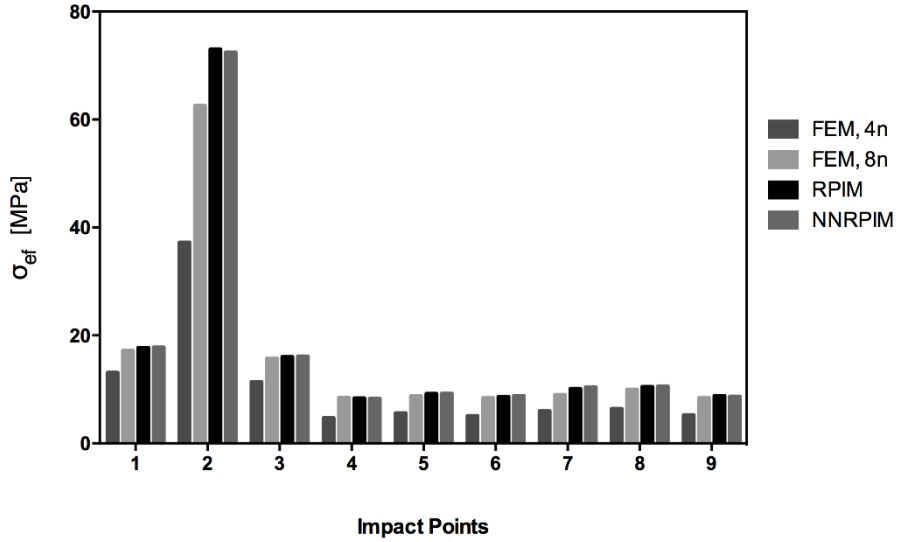

Figure 5.38 - Average nodal stress along the thickness of each impact location caused by the impact to location 2.

The von Mises stress for each node of the ABCD border of the windshield, shown in Figure 5.8, was calculated across the thickness and following this, the average of the three nodal von Mises stresses discretizing the ABCD border thickness comes,

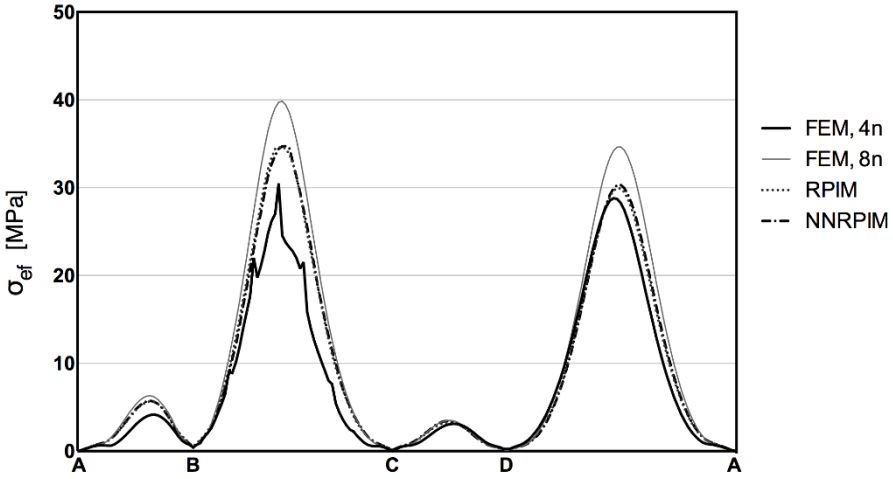

Figure 5.39 - Average nodal stress along the thickness of the clamped section of the windshield caused by the impact to location 2.

The following displacement field is obtained,

FEM, 4n

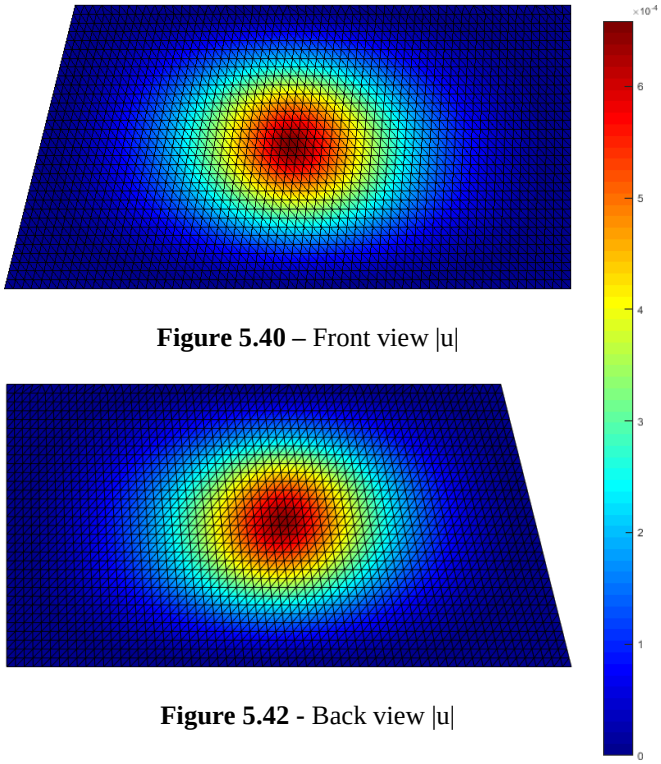

Figure 5.40 – Front view |u|

Figure 5.42 - Back view |u|

FEM, 8n

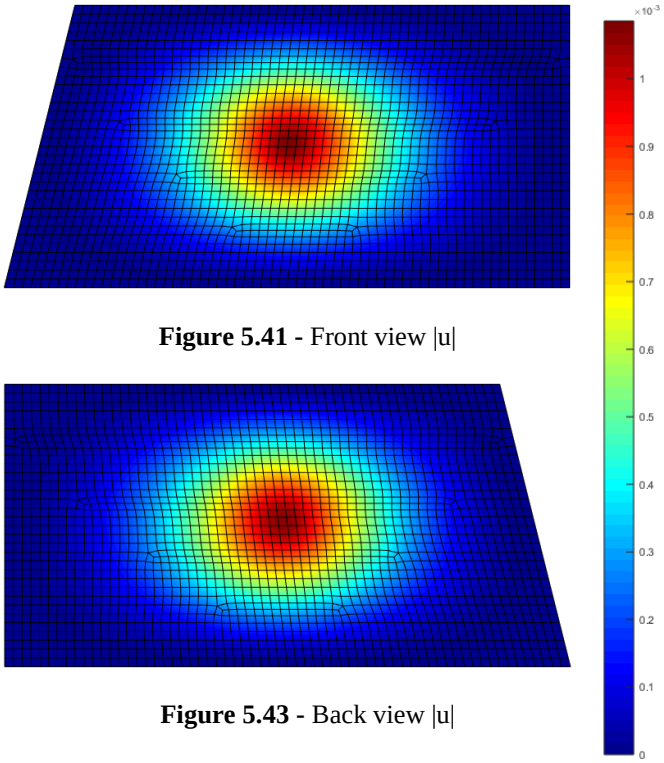

Figure 5.41 - Front view |u|

Figure 5.43 - Back view |u|

RPIM

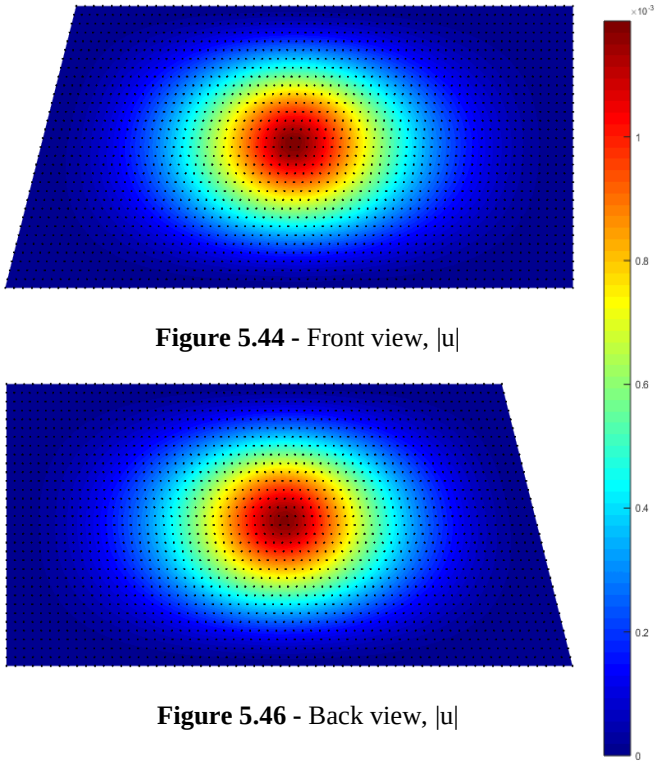

Figure 5.44 - Front view, |u|

Figure 5.46 - Back view, |u|

NNRPIM

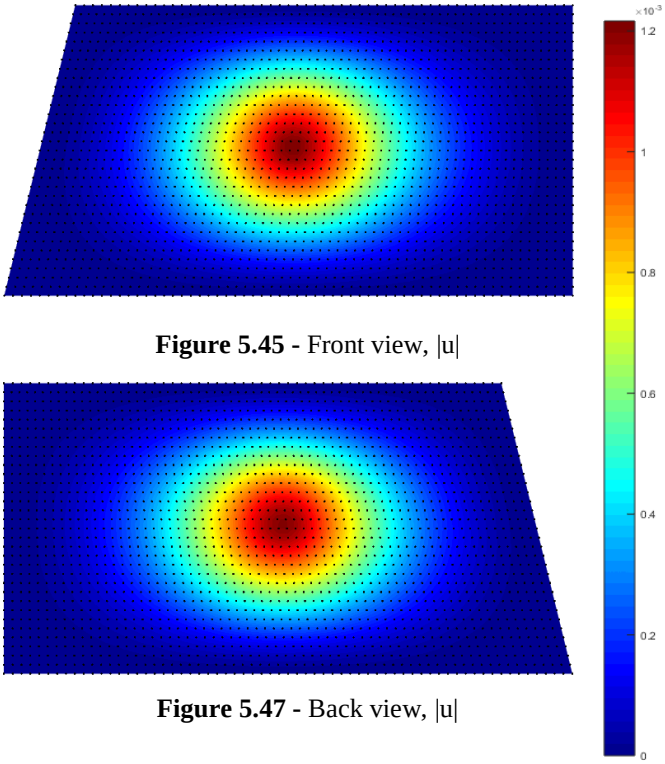

Figure 5.45 - Front view, |u|

Figure 5.47 - Back view, |u|

The following stress field is obtained,

FEM, 4n

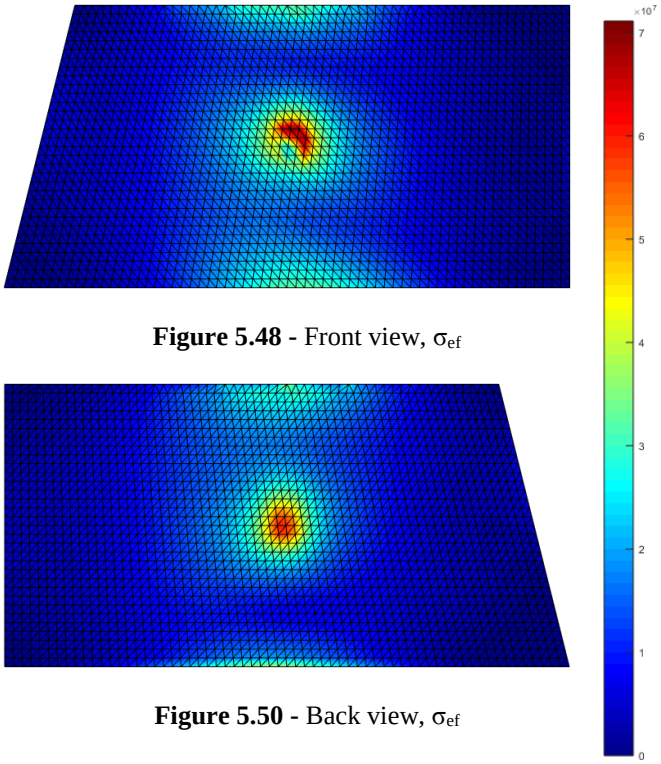

Figure 5.48 - Front view, σ_{ef}

Figure 5.50 - Back view, σ_{ef}

FEM, 8n

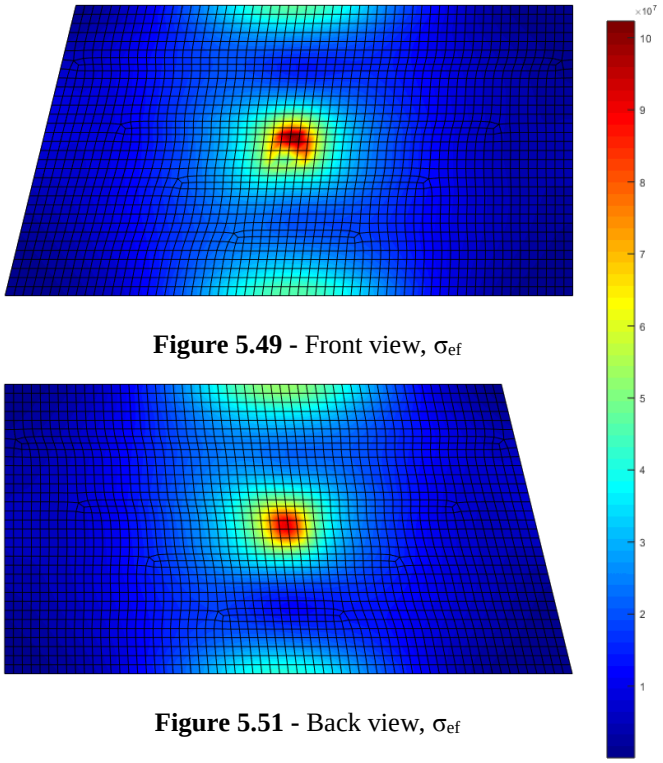

Figure 5.49 - Front view, σ_{ef}

Figure 5.51 - Back view, σ_{ef}

RPIM

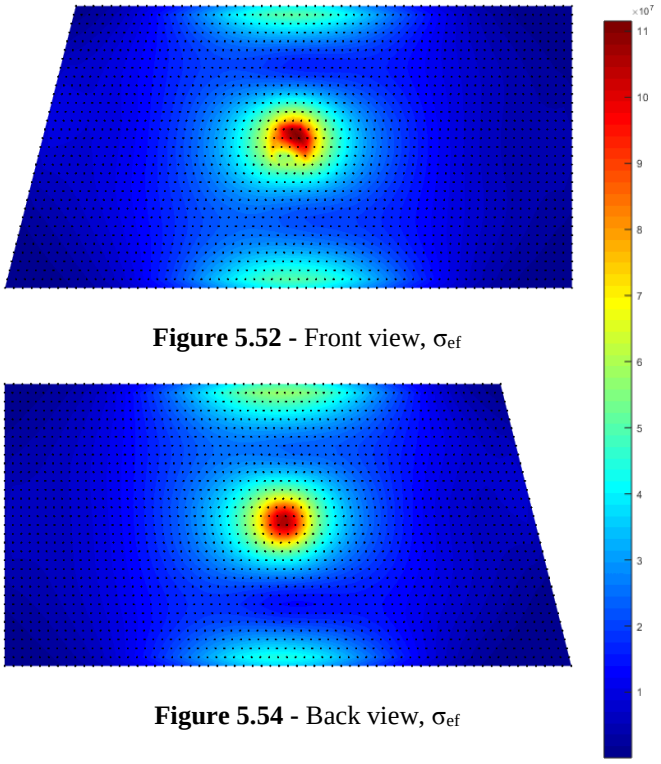

Figure 5.52 - Front view, σ_{ef}

Figure 5.54 - Back view, σ_{ef}

NNRPIM

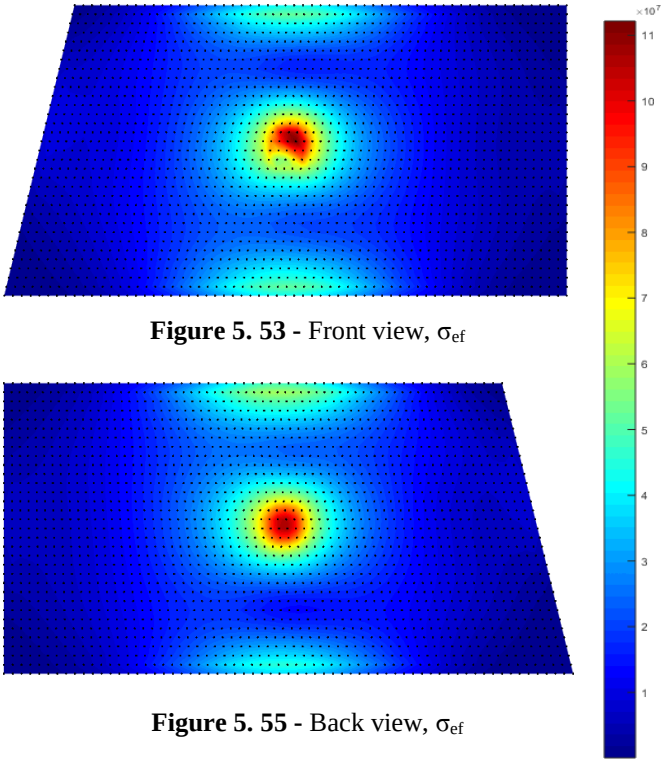

Figure 5. 53 - Front view, σ_{ef}

Figure 5. 55 - Back view, σ_{ef}

Impact location # 3

The displacement for each impact point was calculated across the thickness and following this, the average of the three nodal displacements discretizing the thickness comes,

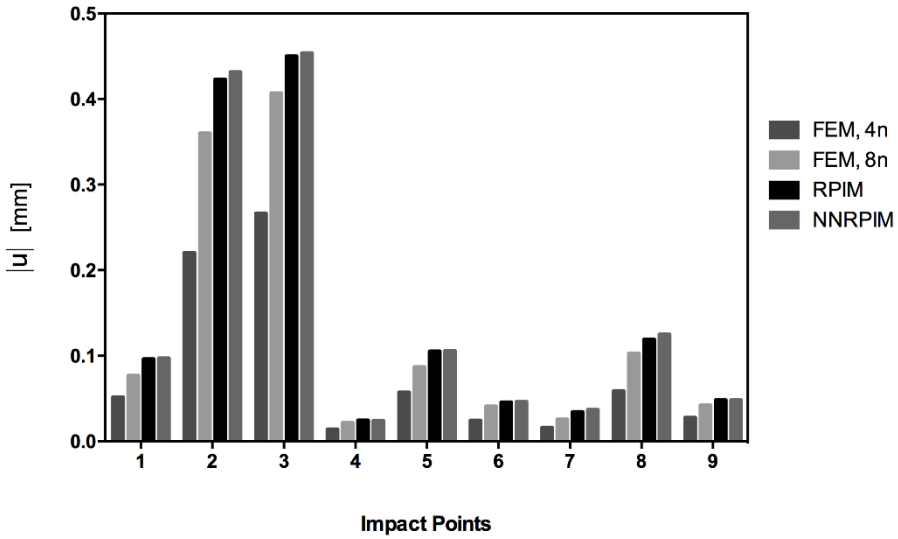

Figure 5.56 - Average nodal displacement along the thickness of each impact location caused by the impact to location 3.

The von Mises stress for each impact point was calculated across the thickness and following this, the average of the three nodal von Mises stresses discretizing the thickness comes,

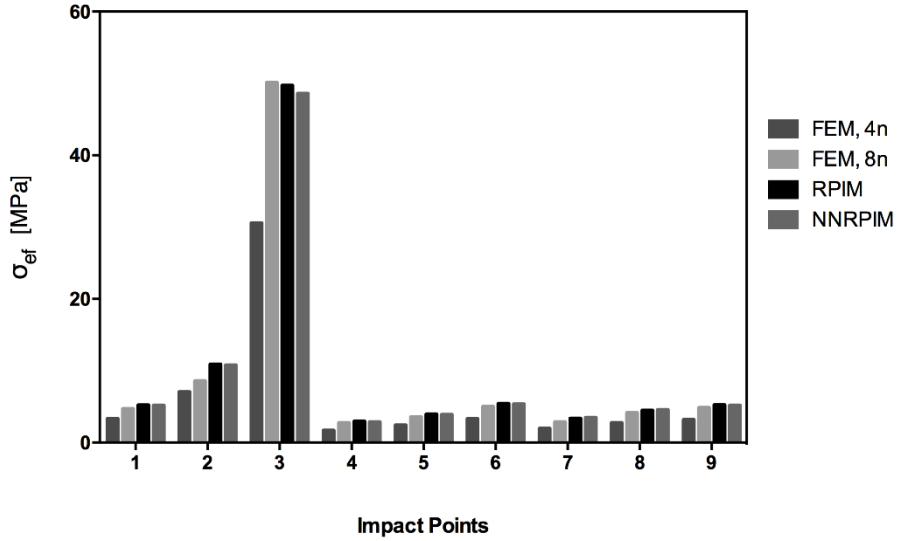

Figure 5.57 - Average nodal stress along the thickness of each impact location caused by the impact to location 3.

The von Mises stress for each node of the ABCD border of the windshield, shown in Figure 5.8, was calculated across the thickness and following this, the average of the three nodal von Mises stresses discretizing the ABCD border thickness comes,

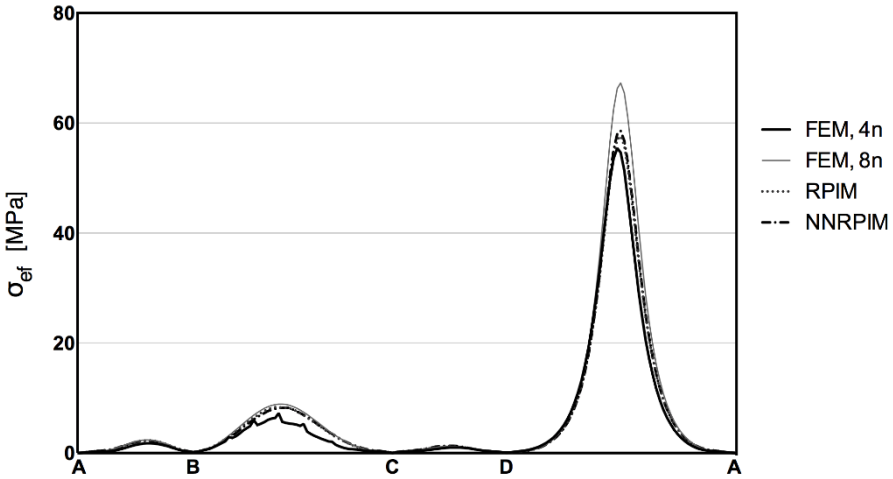

Figure 5.58 - Average nodal stress along the thickness of the clamped section of the windshield caused by the impact to location 3.

The following displacement field is obtained,

FEM, 4n

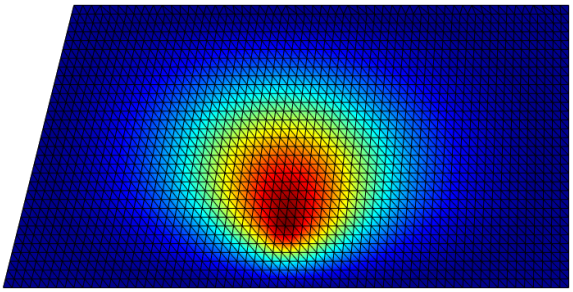

Figure 5.59 - Front view, |u|

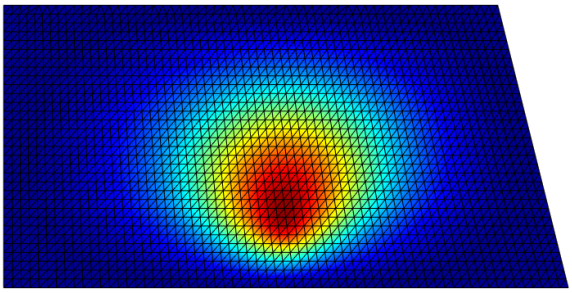

Figure 5.61 - Back view, |u|

FEM, 8n

Figure 5.60 - Front view, |u|

Figure 5.62 - Back view, |u|

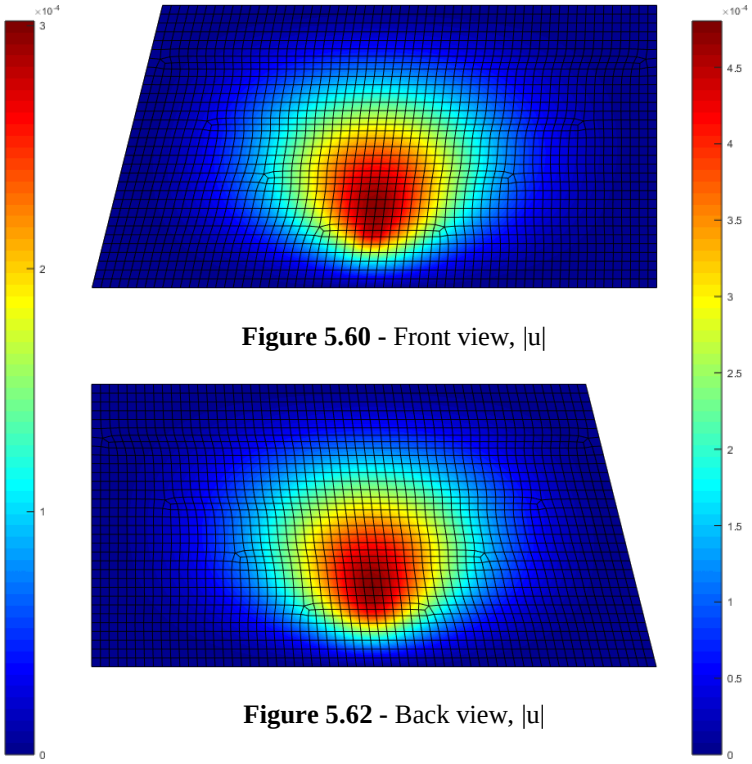

RPIM

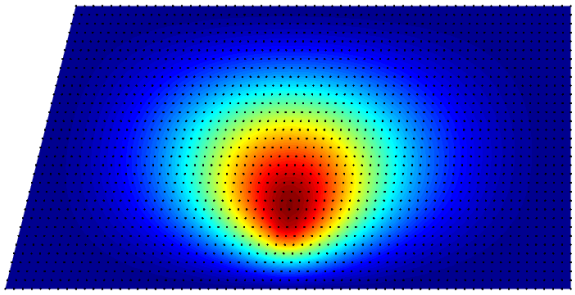

Figure 5.63 - Front view, |u|

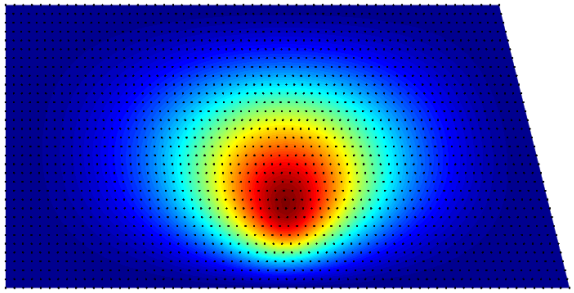

Figure 5.65 - Back view, |u|

NNRPIM

Figure 5. 64 - Front view, |u|

Figure 5.66 - Back view, |u|

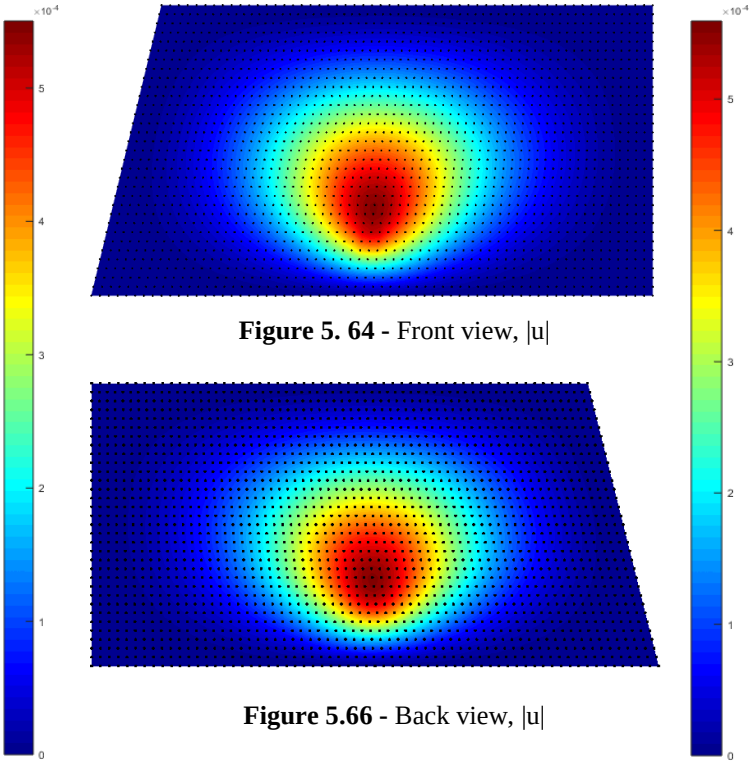

The following stress field is obtained,

FEM, 4n

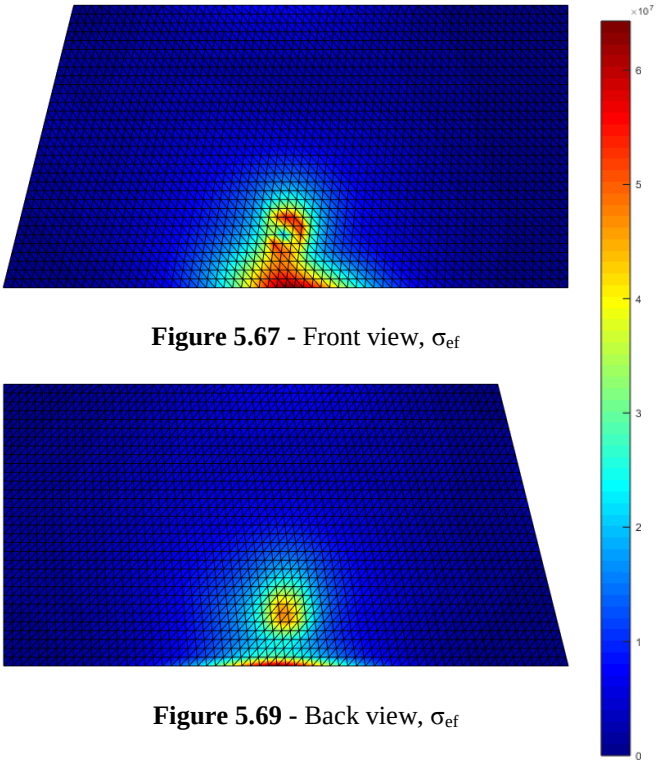

Figure 5.67 - Front view, σ_{ef}

Figure 5.69 - Back view, σ_{ef}

FEM, 8n

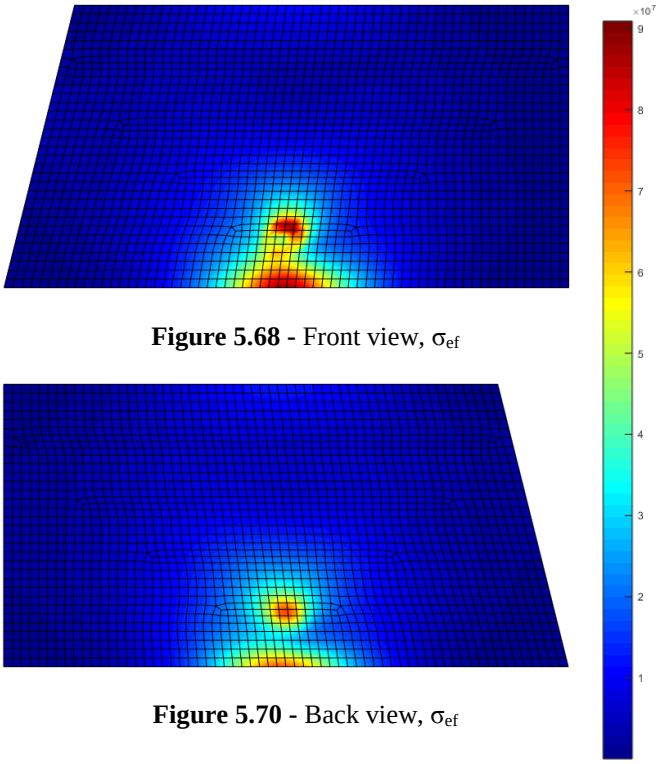

Figure 5.68 - Front view, σ_{ef}

Figure 5.70 - Back view, σ_{ef}

RPIM

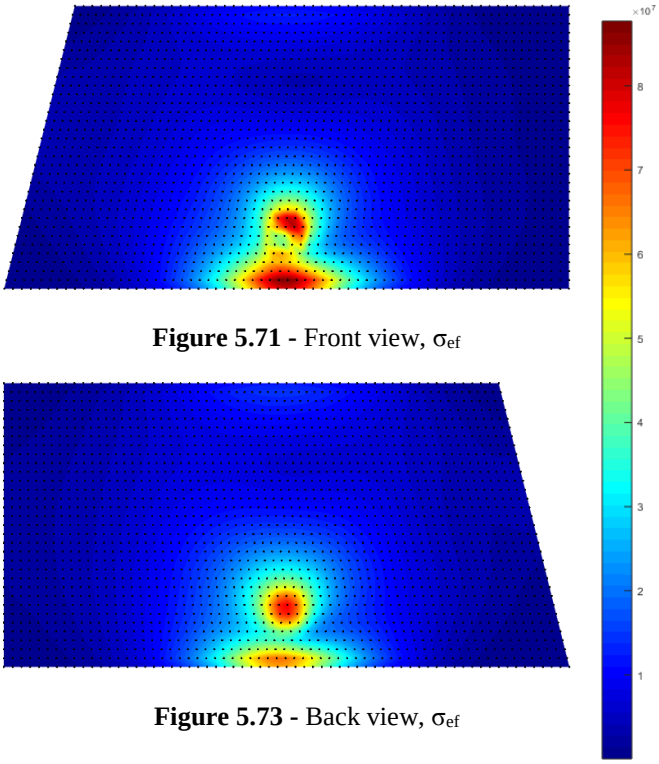

Figure 5.71 - Front view, σ_{ef}

Figure 5.73 - Back view, σ_{ef}

NNRPIM

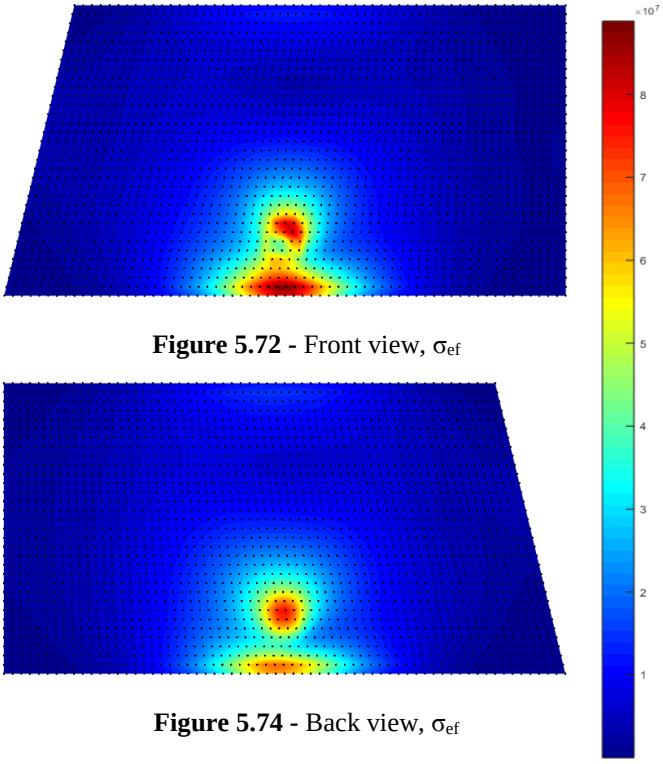

Figure 5.72 - Front view, σ_{ef}

Figure 5.74 - Back view, σ_{ef}

Impact location # 4

The displacement for each impact point was calculated across the thickness and following this, the average of the three nodal displacements discretizing the thickness comes,

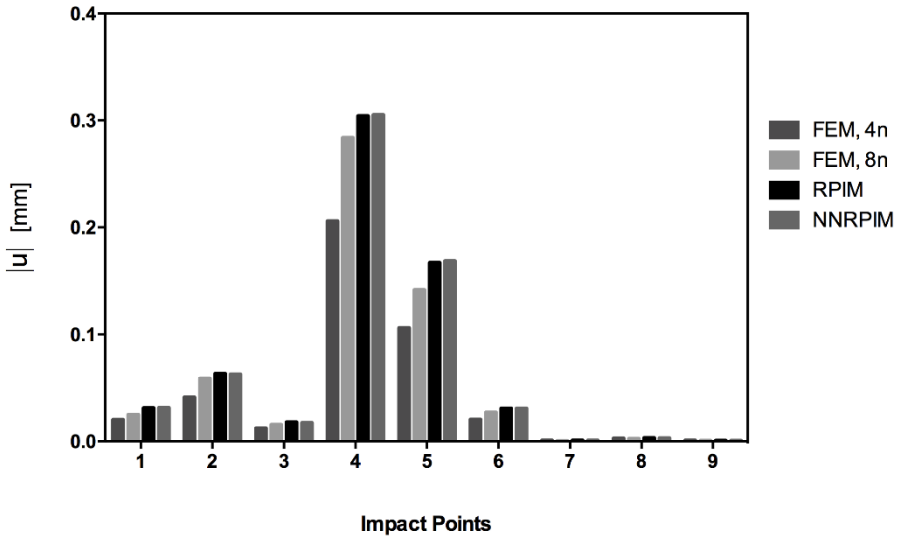

Figure 5.75 - Average nodal displacement along the thickness of each impact location caused by the impact to location 4.

The von Mises stress for each impact point was calculated across the thickness and following this, the average of the three nodal von Mises stresses discretizing the thickness comes,

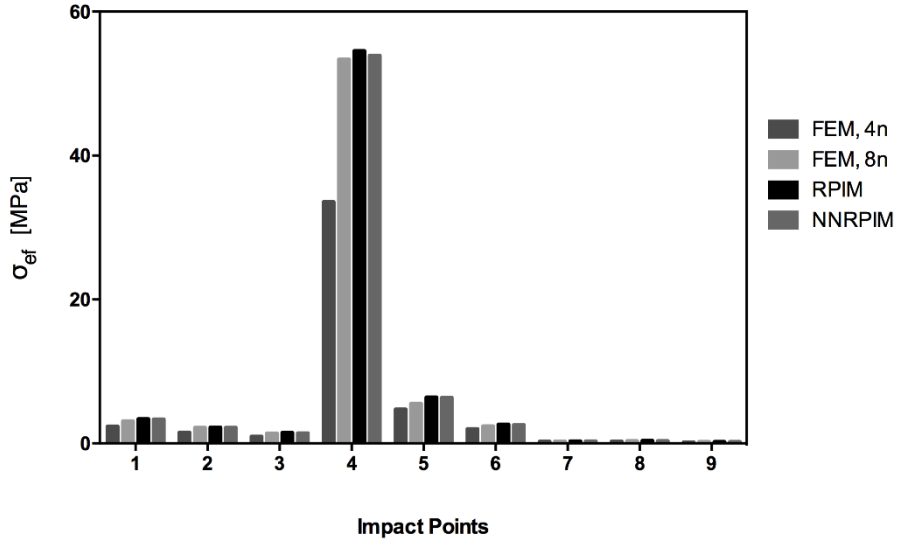

Figure 5.76 - Average nodal stress along the thickness of each impact location caused by the impact to location 4.

The von Mises stress for each node of the ABCD border of the windshield, shown in Figure 5.8, was calculated across the thickness and following this, the average of the three nodal von Mises stresses discretizing the ABCD border thickness comes,

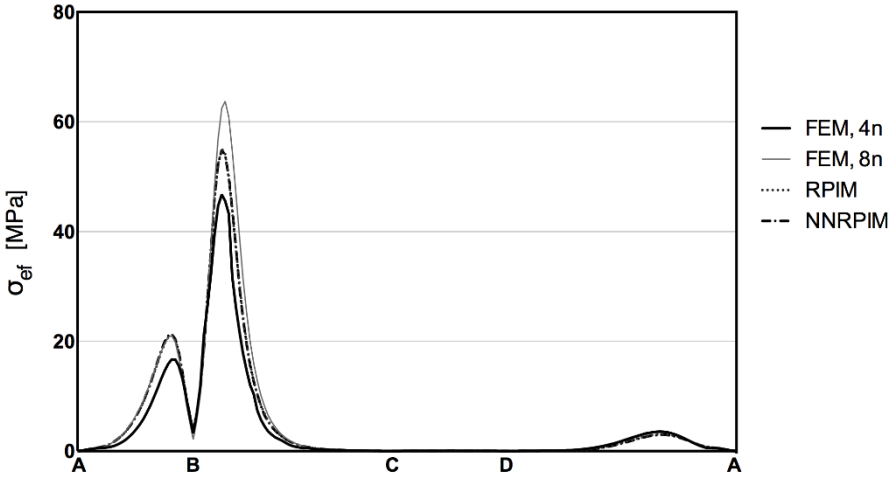

Figure 5.77 - Average nodal stress along the thickness of the clamped section of the windshield caused by the impact to location 4.

The following displacement field is obtained,

FEM, 4n

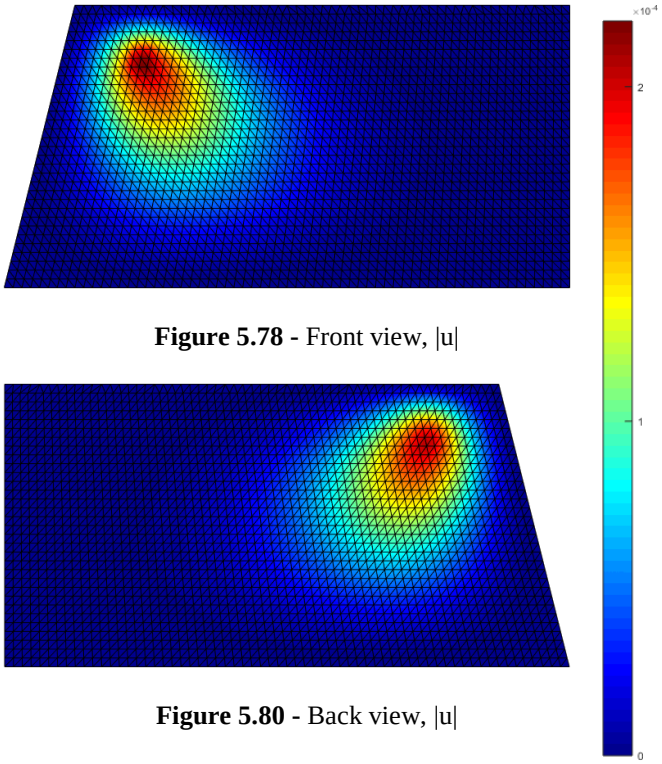

Figure 5.78 - Front view, |u|

Figure 5.80 - Back view, |u|

FEM, 8n

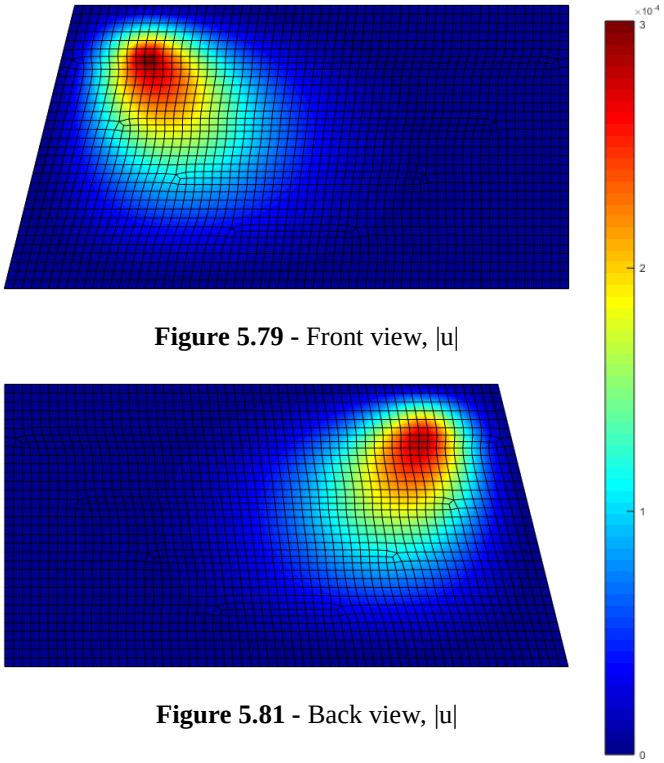

Figure 5.79 - Front view, |u|

Figure 5.81 - Back view, |u|

RPIM

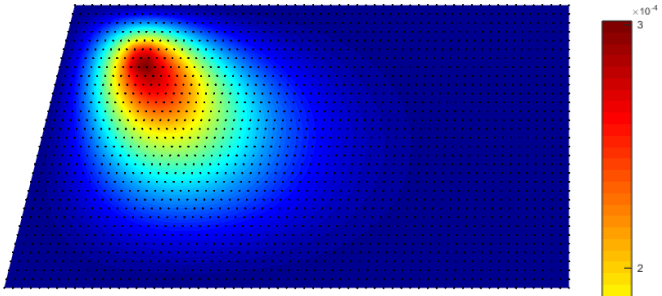

Figure 5.82 - Front view, |u|

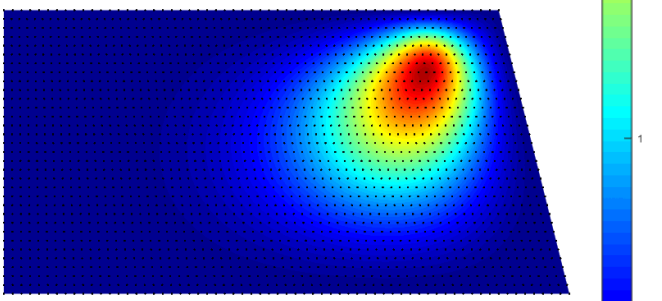

Figure 5.84 - Back view, |u|

NNRPIM

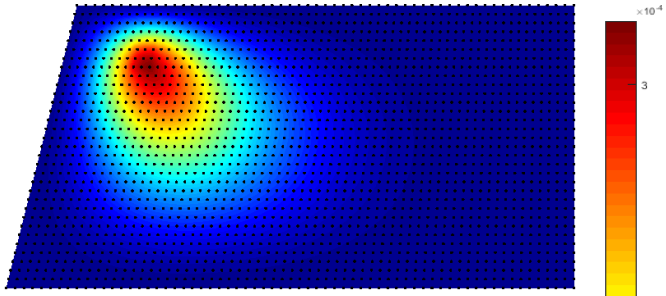

Figure 5.83 - Front view, |u|

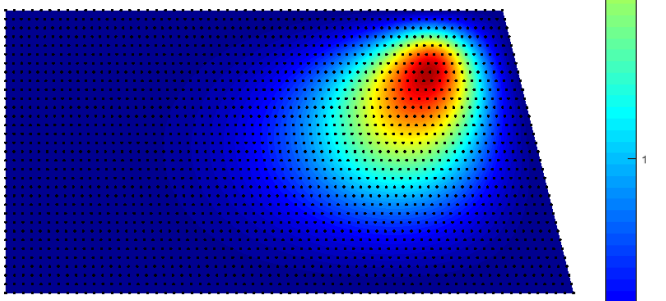

Figure 5.85 - Back view, |u|

The following stress field is obtained,

FEM, 4n

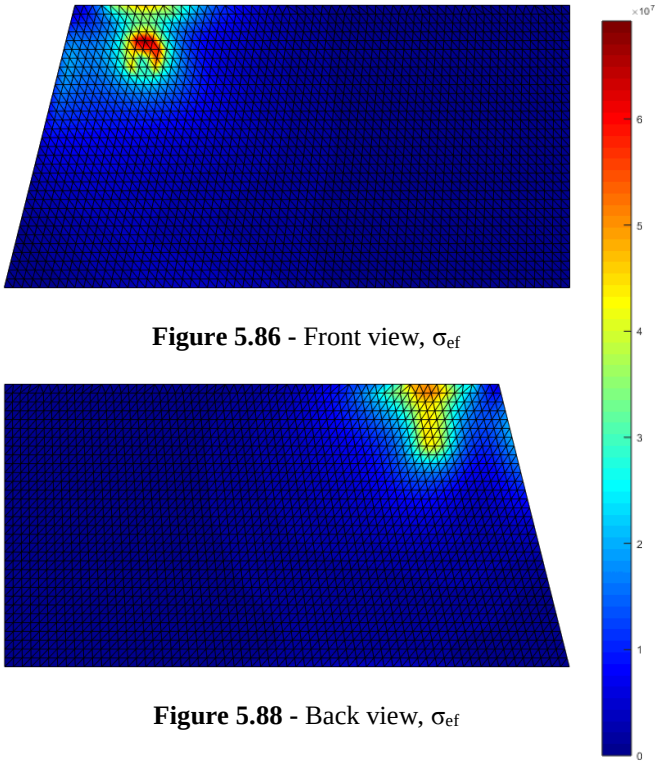

Figure 5.86 - Front view, σ_{ef}

Figure 5.88 - Back view, σ_{ef}

FEM, 8n

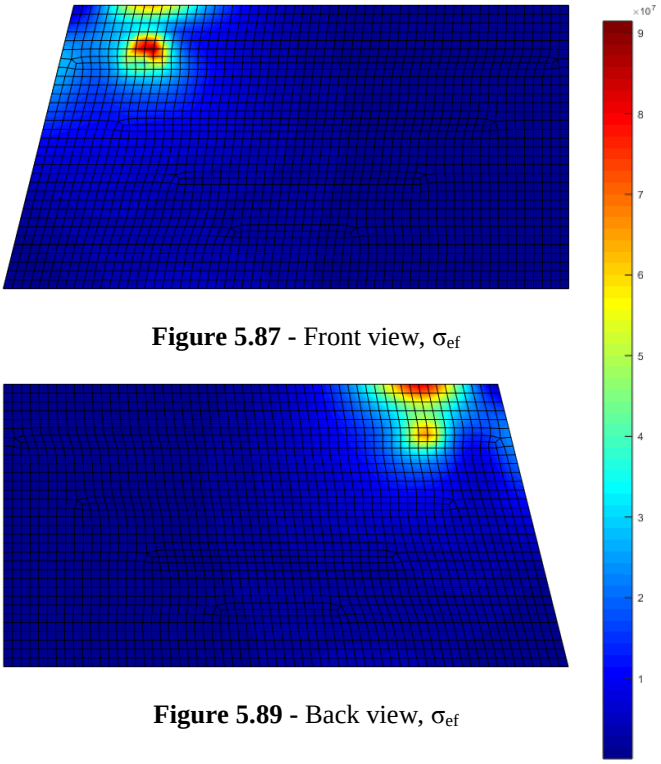

Figure 5.87 - Front view, σ_{ef}

Figure 5.89 - Back view, σ_{ef}

RPIM

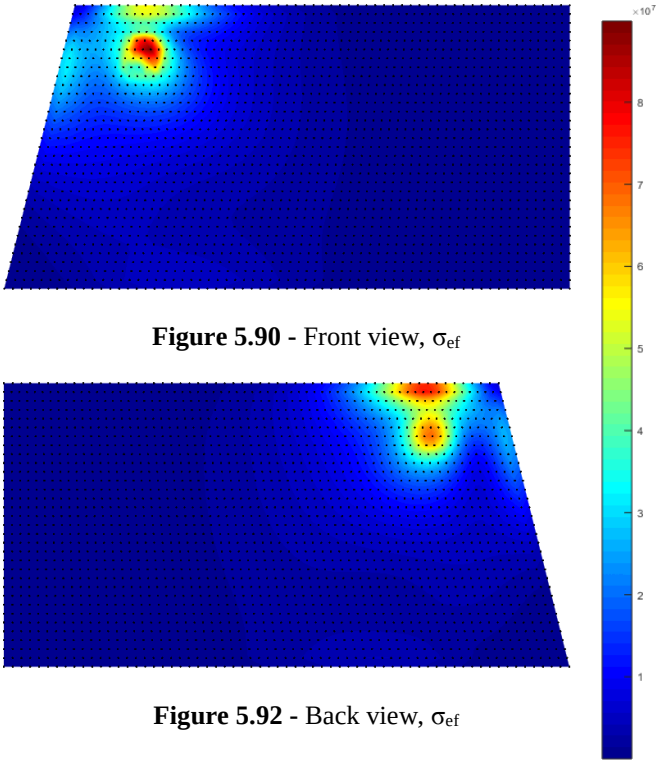

Figure 5.90 - Front view, σ_{ef}

Figure 5.92 - Back view, σ_{ef}

NNRPIM

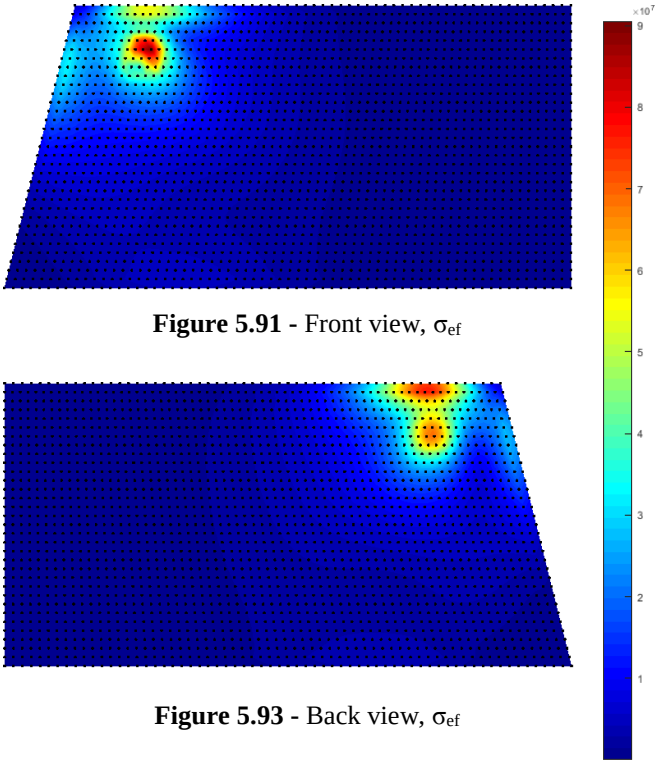

Figure 5.91 - Front view, σ_{ef}

Figure 5.93 - Back view, σ_{ef}

Impact location # 5

The displacement for each impact point was calculated across the thickness and following this, the average of the three nodal displacements discretizing the thickness comes,

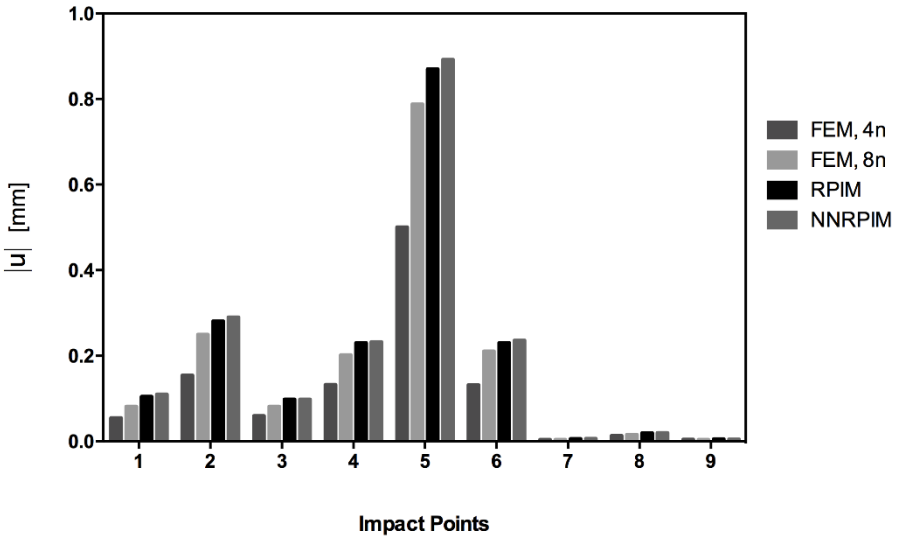

Figure 5.94 - Average nodal displacement along the thickness of each impact location caused by the impact to location 5.

The von Mises stress for each impact point was calculated across the thickness and following this, the average of the three nodal von Mises stresses discretizing the thickness comes,

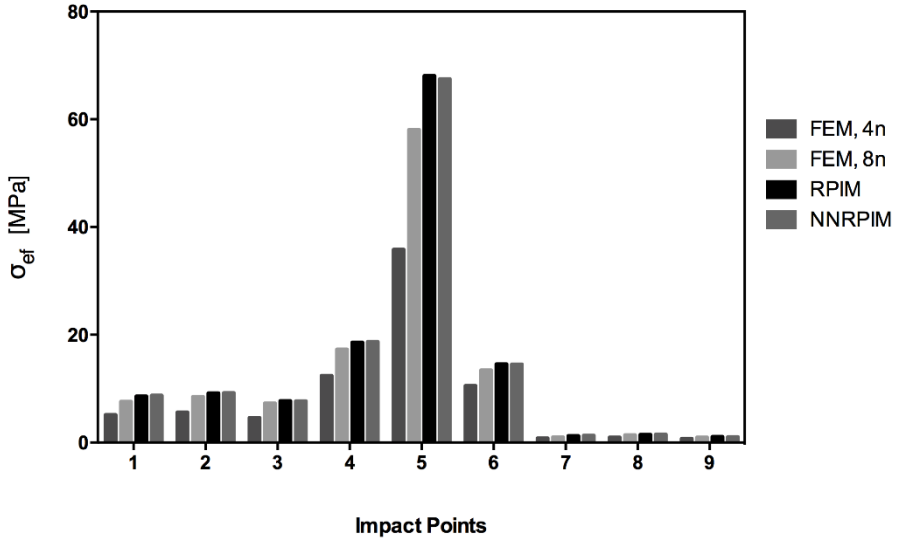

Figure 5.95 - Average nodal stress along the thickness of each impact location caused by the impact to location 5.

The von Mises stress for each node of the ABCD border of the windshield, shown in Figure 5.8, was calculated across the thickness and following this, the average of the three nodal von Mises stresses discretizing the ABCD border thickness comes,

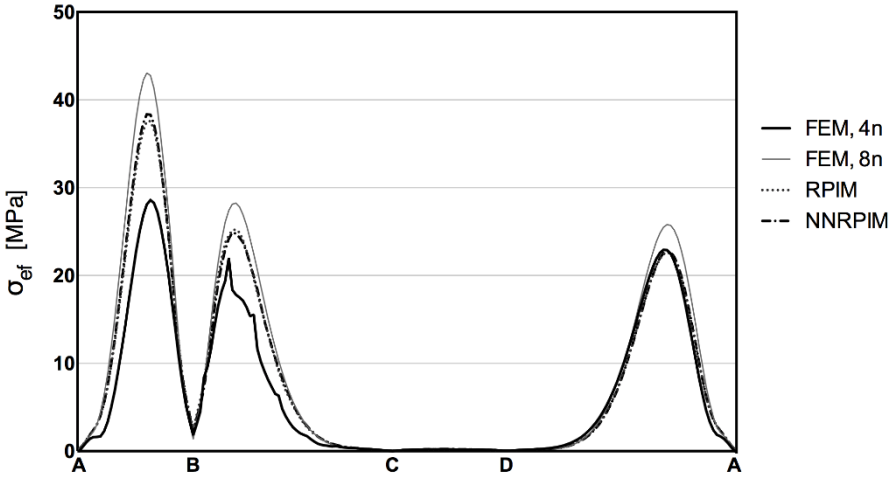

Figure 5.96 - Average nodal stress along the thickness of the clamped section of the windshield caused by the impact to location 5.

The following displacement field is obtained,

FEM, 4n

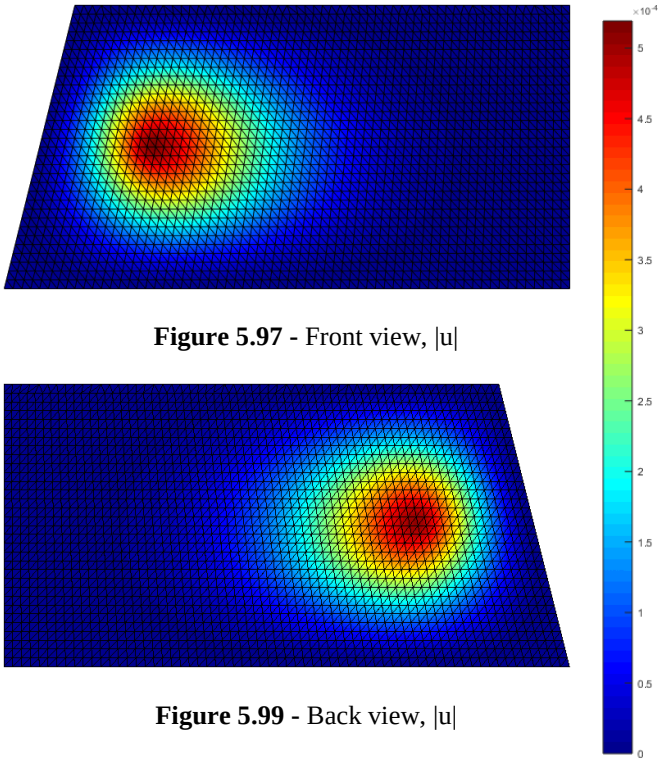

Figure 5.97 - Front view, |u|

Figure 5.99 - Back view, |u|

FEM, 8n

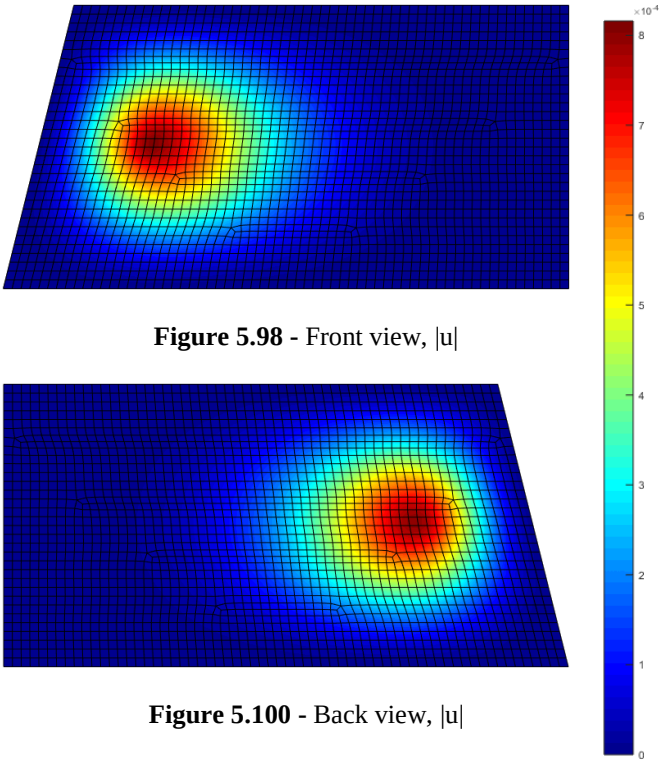

Figure 5.98 - Front view, |u|

Figure 5.100 - Back view, |u|

RPIM

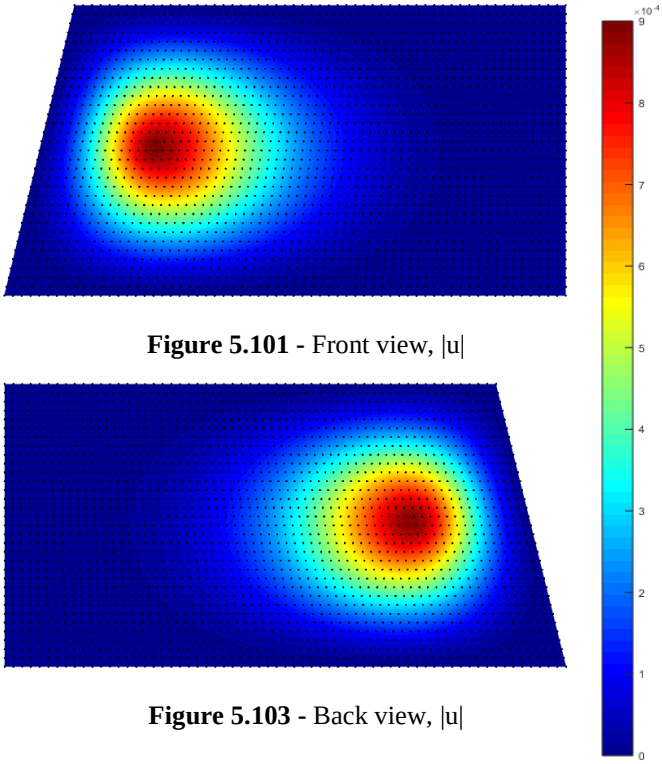

Figure 5.101 - Front view, |u|

Figure 5.103 - Back view, |u|

NNRPIM

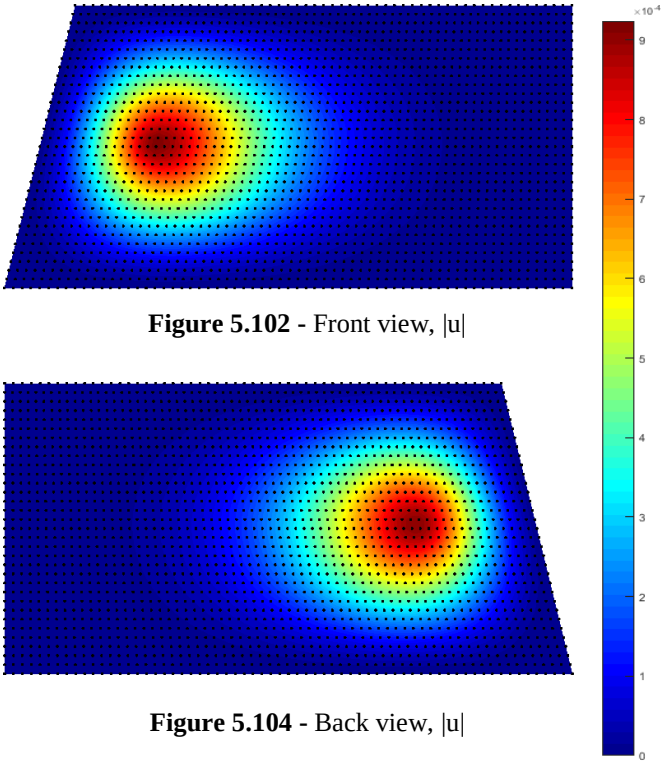

Figure 5.102 - Front view, |u|

Figure 5.104 - Back view, |u|

The following stress field is obtained,

FEM, 4n

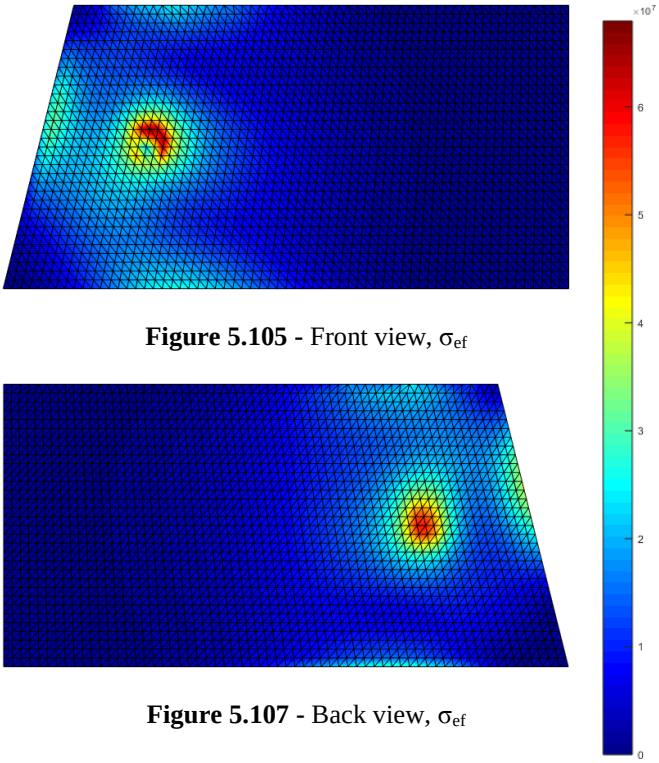

Figure 5.105 - Front view, σ_{ef}

Figure 5.107 - Back view, σ_{ef}

FEM, 8n

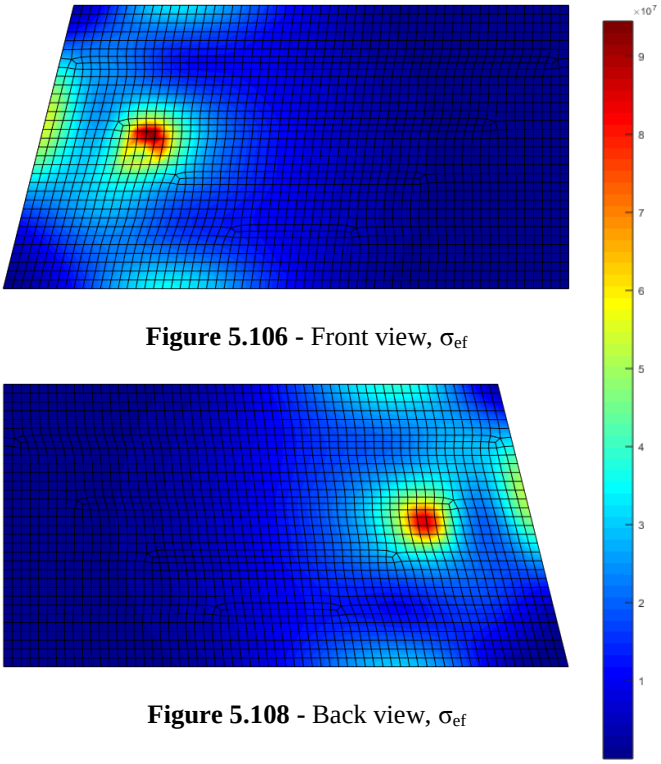

Figure 5.106 - Front view, σ_{ef}

Figure 5.108 - Back view, σ_{ef}

RPIM

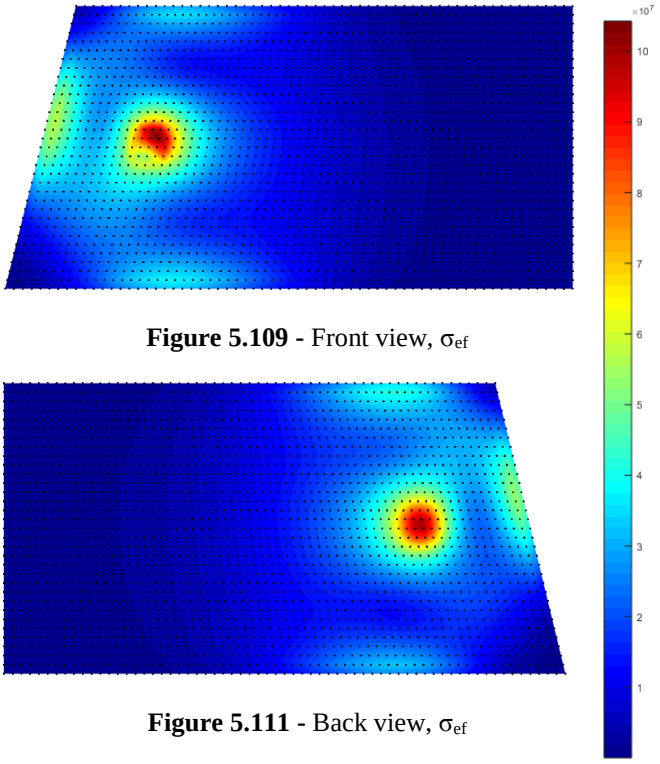

Figure 5.109 - Front view, σ_{ef}

Figure 5.111 - Back view, σ_{ef}

NNRPIM

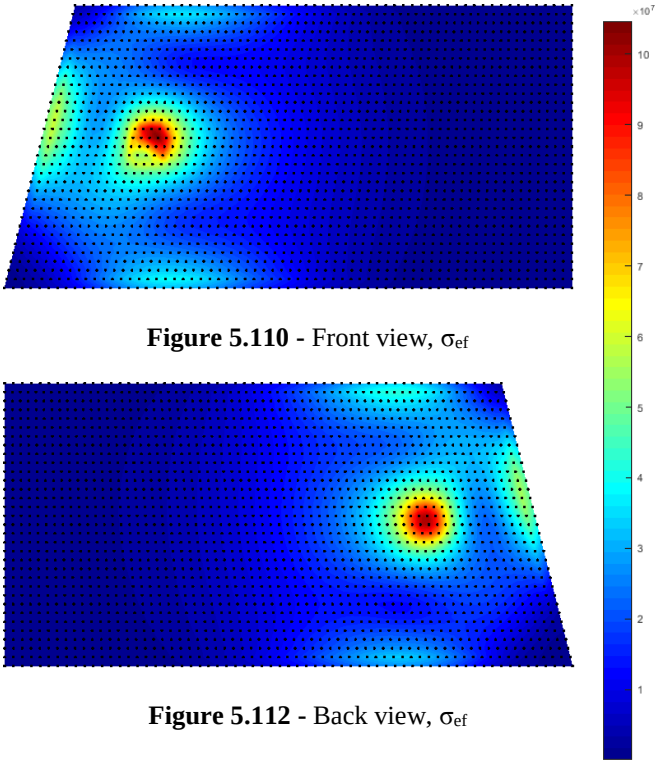

Figure 5.110 - Front view, σ_{ef}

Figure 5.112 - Back view, σ_{ef}

Impact location # 6

The displacement for each impact point was calculated across the thickness and following this, the average of the three nodal displacements discretizing the thickness comes,

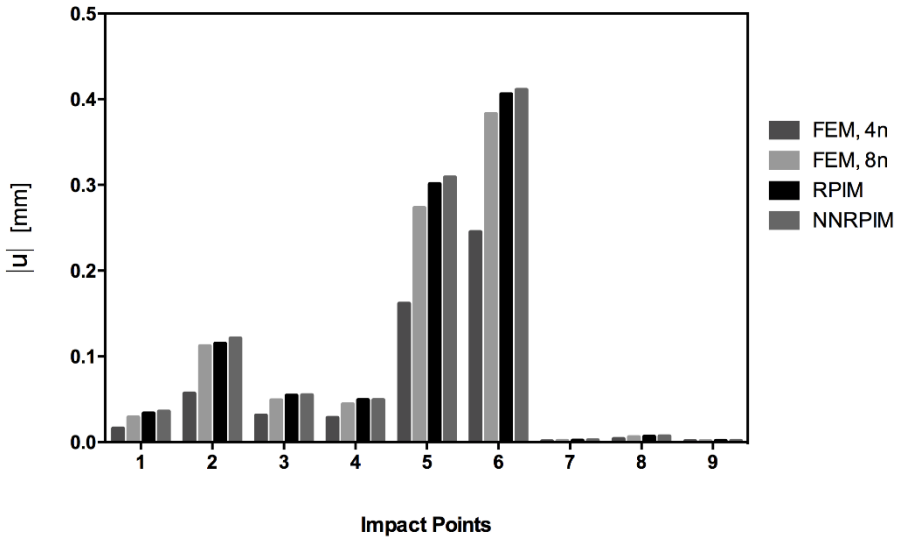

Figure 5.113 - Average nodal displacement along the thickness of each impact location caused by the impact to location 6.

The von Mises stress for each impact point was calculated across the thickness and following this, the average of the three nodal von Mises stresses discretizing the thickness comes,

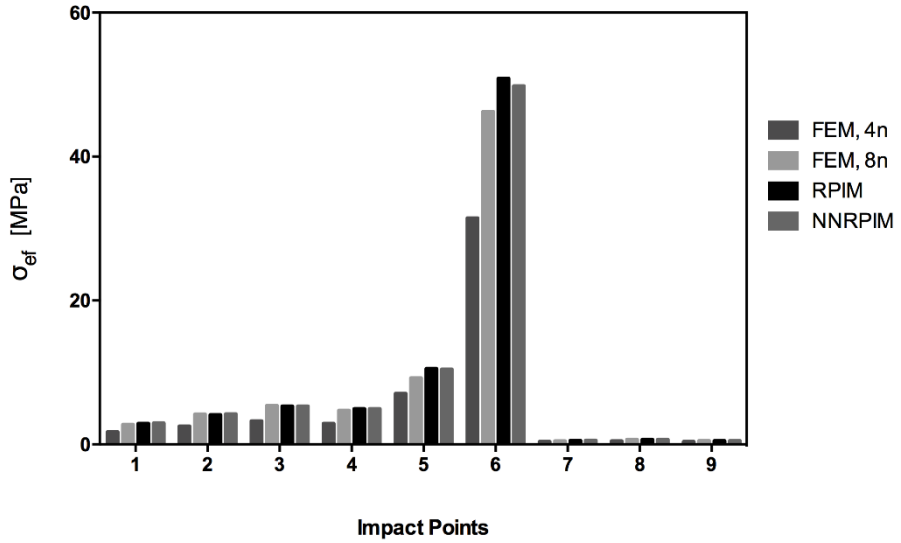

Figure 5.114 - Average nodal stress along the thickness of each impact location caused by the impact to location 6.

The von Mises stress for each node of the ABCD border of the windshield, shown in Figure 5.8, was calculated across the thickness and following this, the average of the three nodal von Mises stresses discretizing the ABCD border thickness comes,

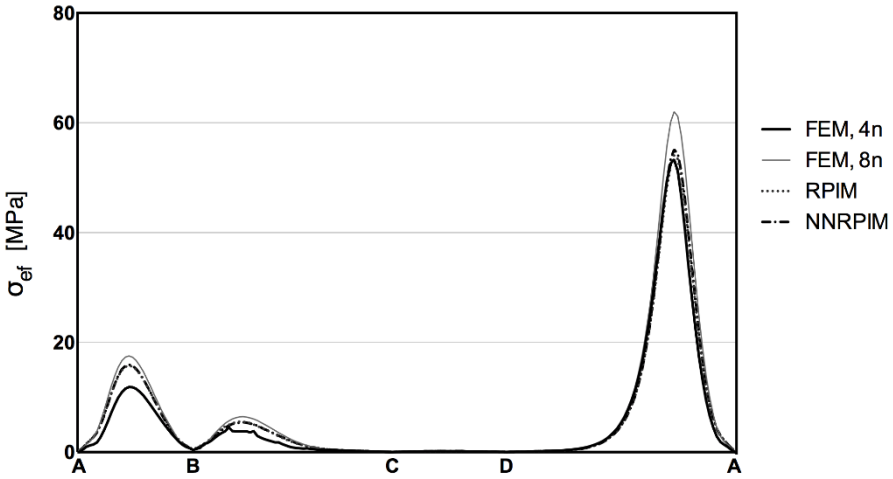

Figure 5.115 - Average nodal stress along the thickness of the clamped section of the windshield caused by the impact to location 6.

The following displacement field is obtained,

FEM, 4n

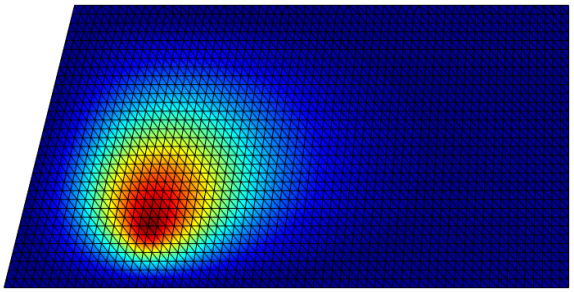

Figure 5.116 - Front view, |u|

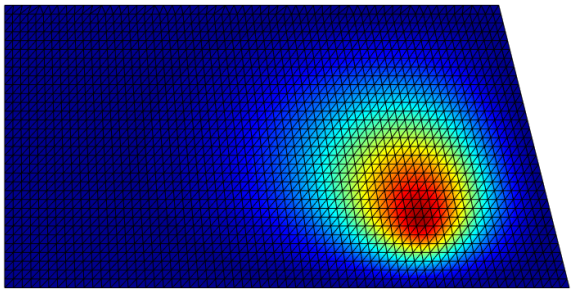

Figure 5.118 - Back view, |u|

FEM, 8n

Figure 5.117 - Front view, |u|

Figure 5.119 - Back view, |u|

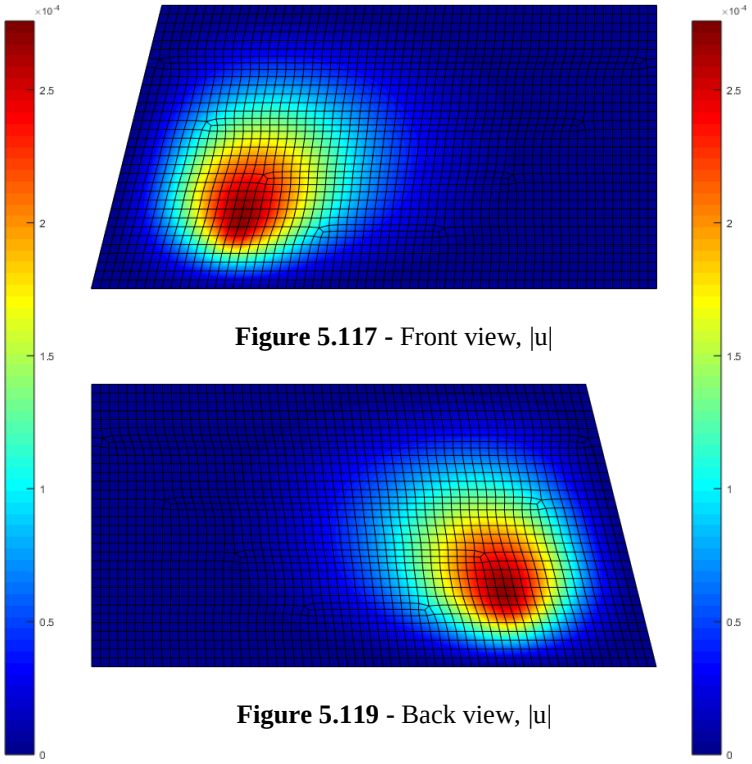

RPIM

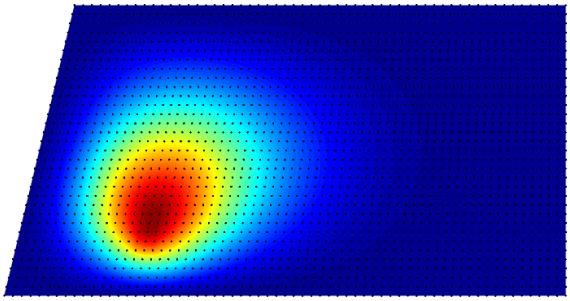

Figure 5.120 - Front view, |u|

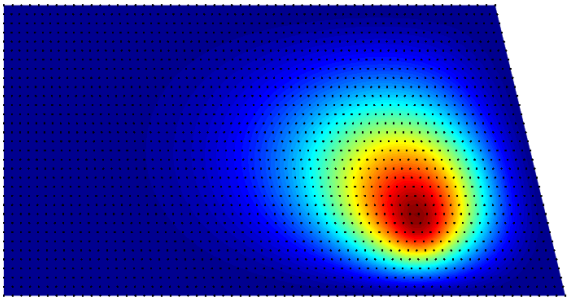

Figure 5.122 - Back view, |u|

NNRPIM

Figure 5.121 - Front view, |u|

Figure 5.123 - Back view, |u|

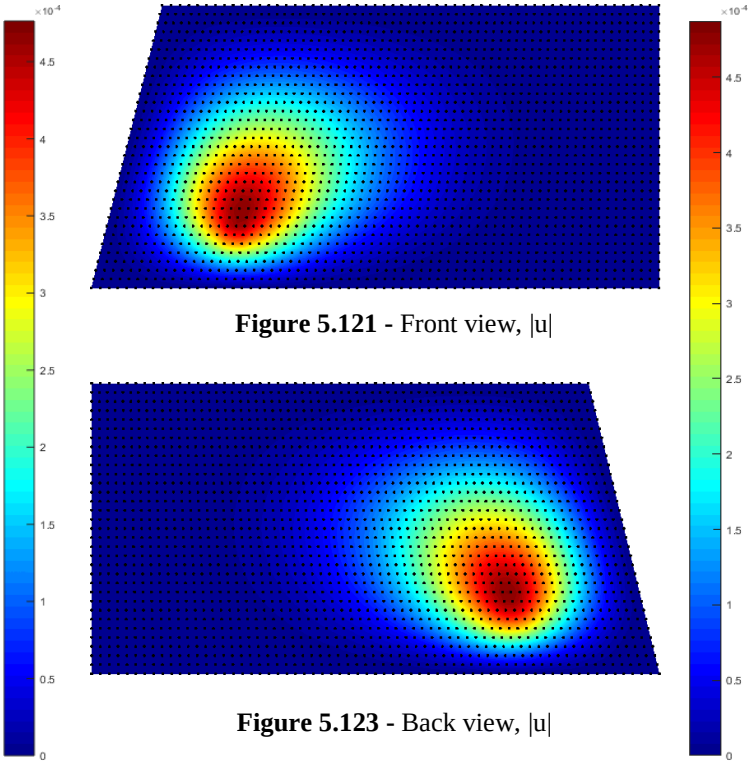

The following stress field is obtained,

FEM, 4n

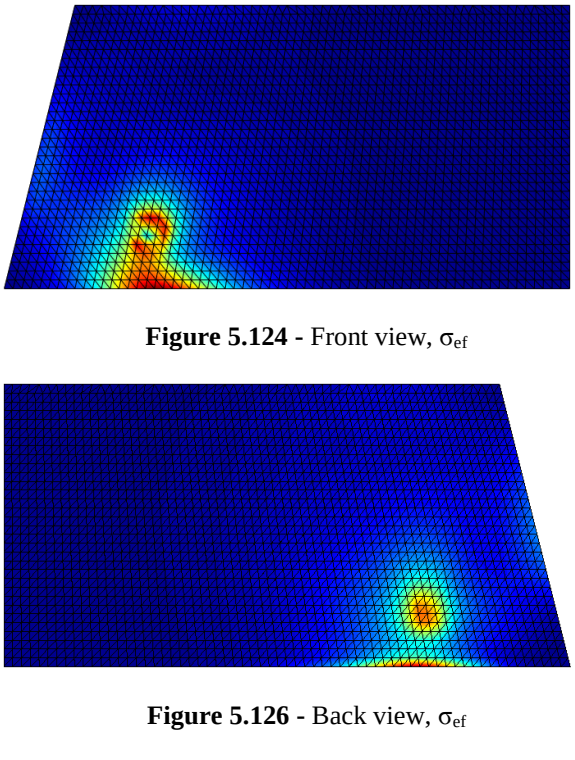

Figure 5.124 - Front view, σ_{ef}

Figure 5.126 - Back view, σ_{ef}

FEM, 8n

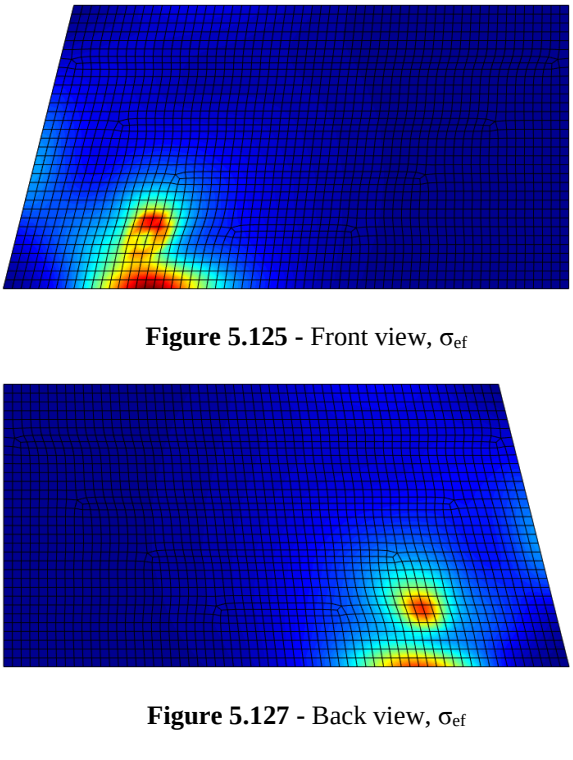

Figure 5.125 - Front view, σ_{ef}

Figure 5.127 - Back view, σ_{ef}

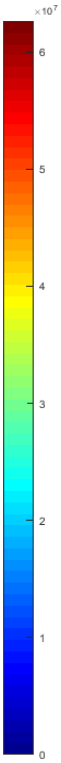

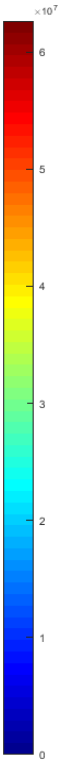

RPIM

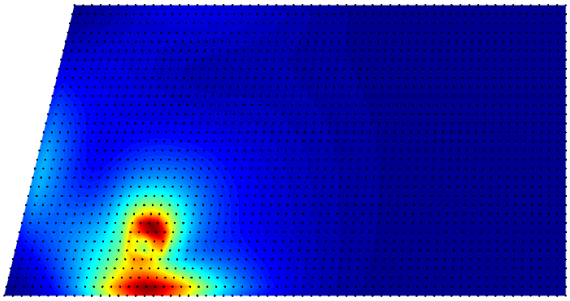

Figure 5.128 - Front view, σ_{ef}

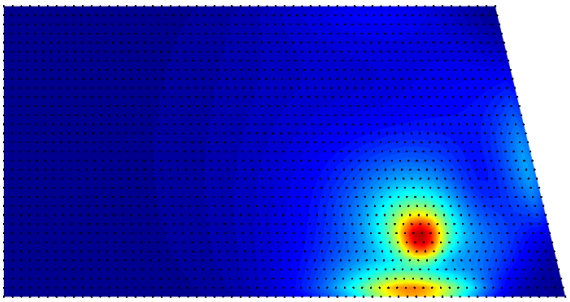

Figure 5.130 - Back view, σ_{ef}

NNRPIM

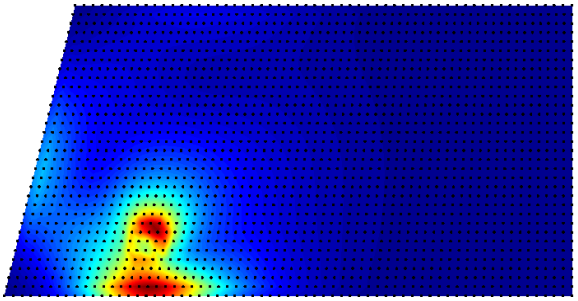

Figure 5.129 - Front view, σ_{ef}

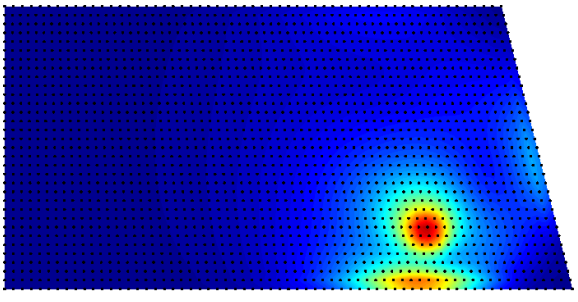

Figure 5.131 - Back view, σ_{ef}

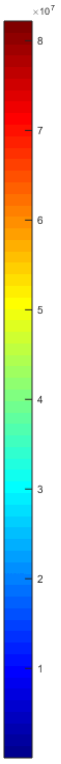

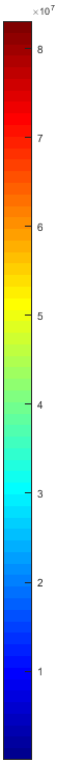

Impact location # 7

The displacement for each impact point was calculated across the thickness and following this, the average of the three nodal displacements discretizing the thickness comes,

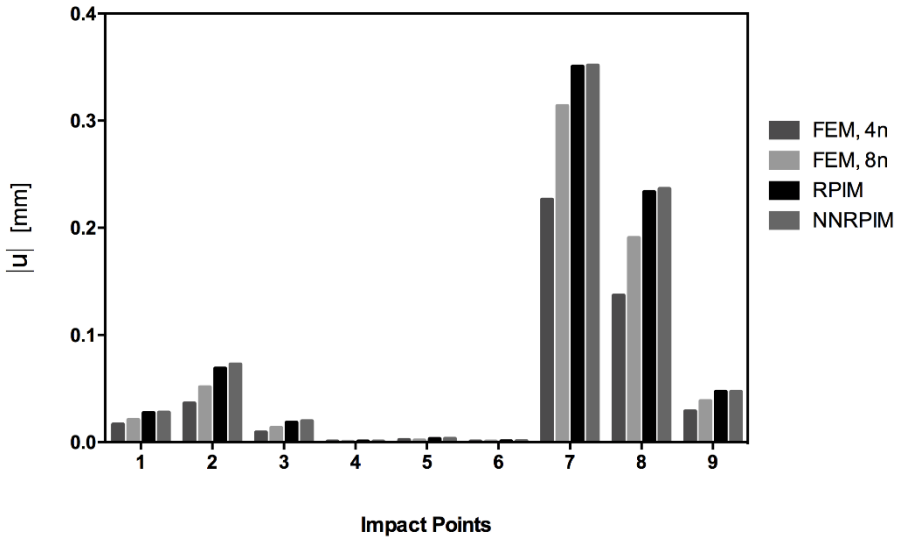

Figure 5.132 - Average nodal displacement along the thickness of each impact location caused by the impact to location 7.

The von Mises stress for each impact point was calculated across the thickness and following this, the average of the three nodal von Mises stresses discretizing the thickness comes,

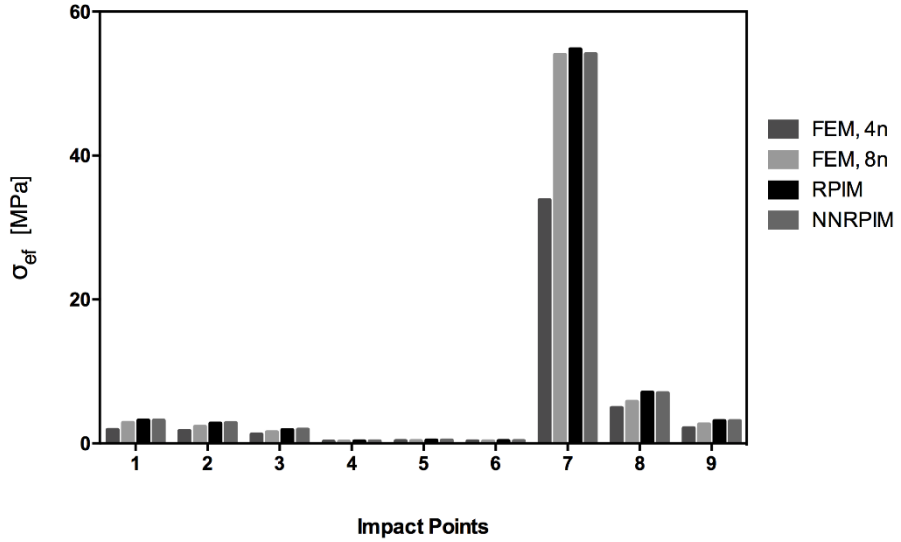

Figure 5.133 - Average nodal stress along the thickness of each impact location caused by the impact to location 7.

The von Mises stress for each node of the ABCD border of the windshield, shown in Figure 5.8, was calculated across the thickness and following this, the average of the three nodal von Mises stresses discretizing the ABCD border thickness comes,

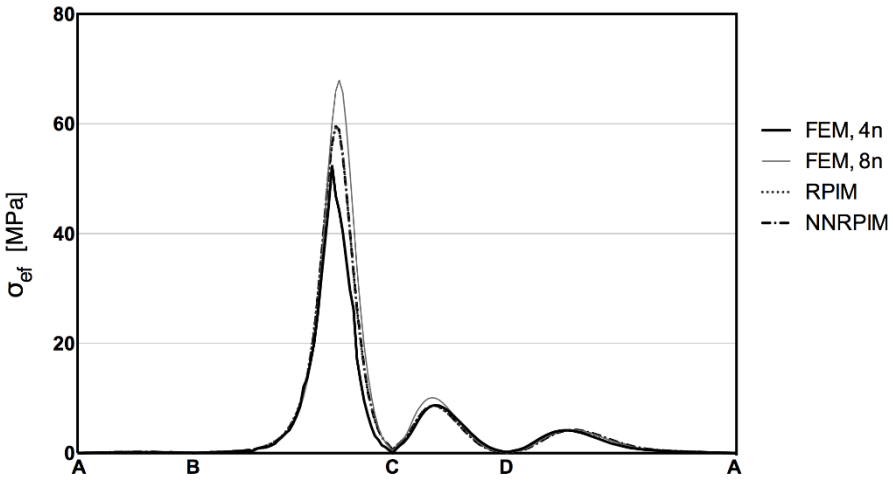

Figure 5.134 - Average nodal stress along the thickness of the clamped section of the windshield caused by the impact to location 7.

The following displacement field is obtained,

FEM, 4n

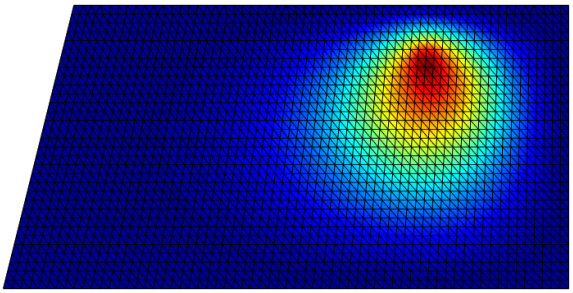

Figure 5.135 - Front view, |u|

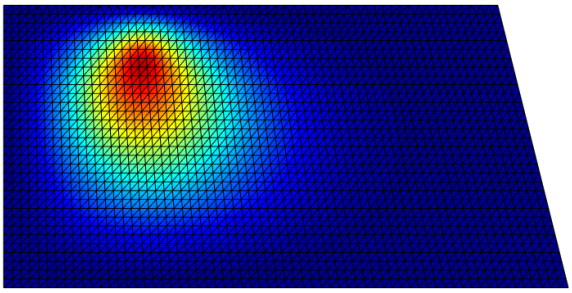

Figure 5.137 - Back view, |u|

FEM, 8n

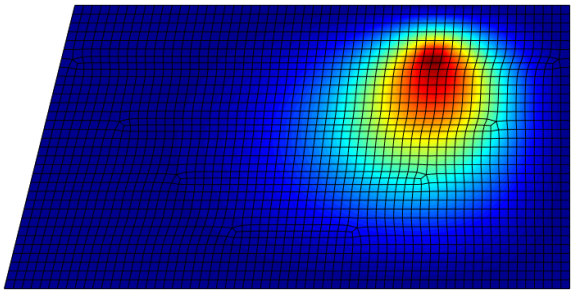

Figure 5.136 - Front view, |u|

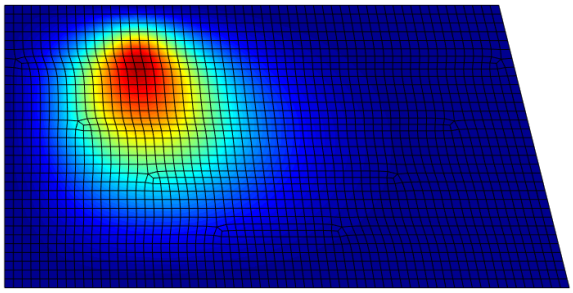

Figure 5.138 - Back view, |u|

RPIM

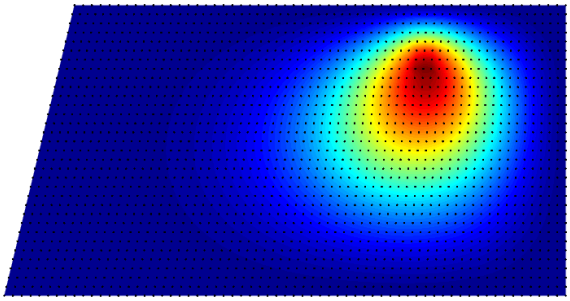

Figure 5.139 - Front view, |u|

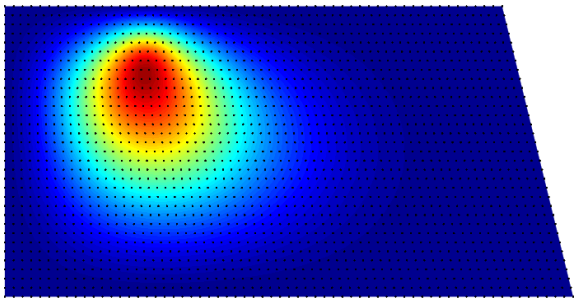

Figure 5.141 - Back view, |u|

NNRPIM

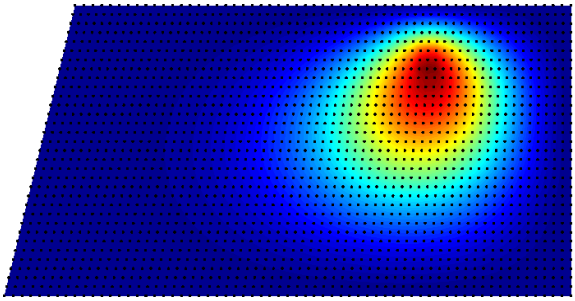

Figure 5.140 - Front view, |u|

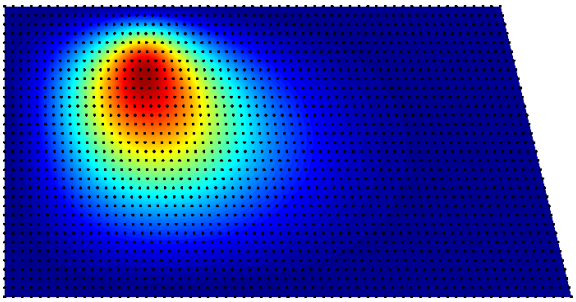

Figure 5.142 - Back view, |u|

The following stress field is obtained,

FEM, 4n

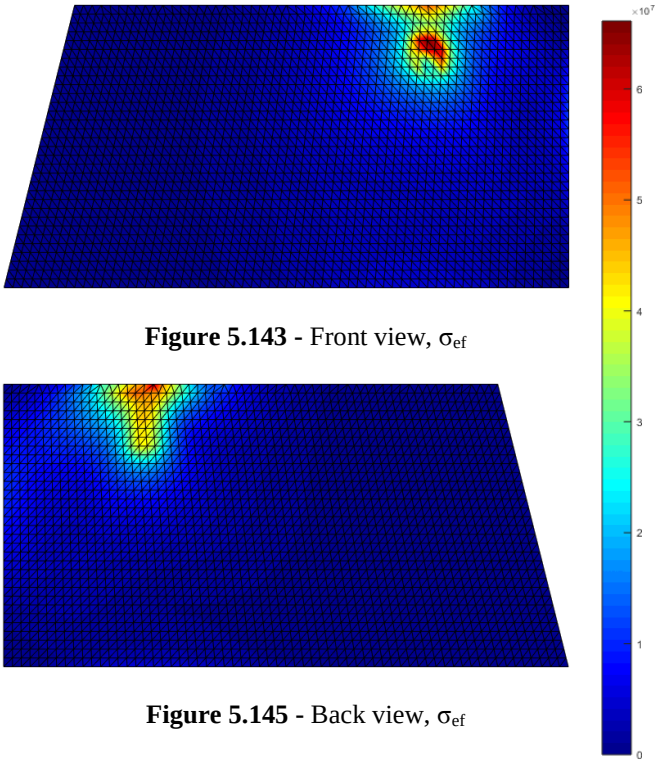

Figure 5.143 - Front view, σ_{ef}

Figure 5.145 - Back view, σ_{ef}

FEM, 8n

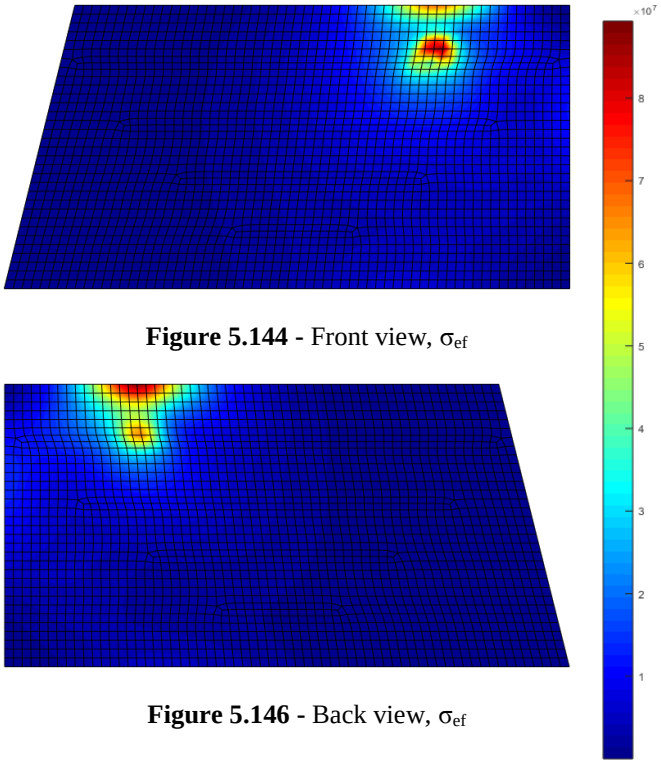

Figure 5.144 - Front view, σ_{ef}

Figure 5.146 - Back view, σ_{ef}

RPIM

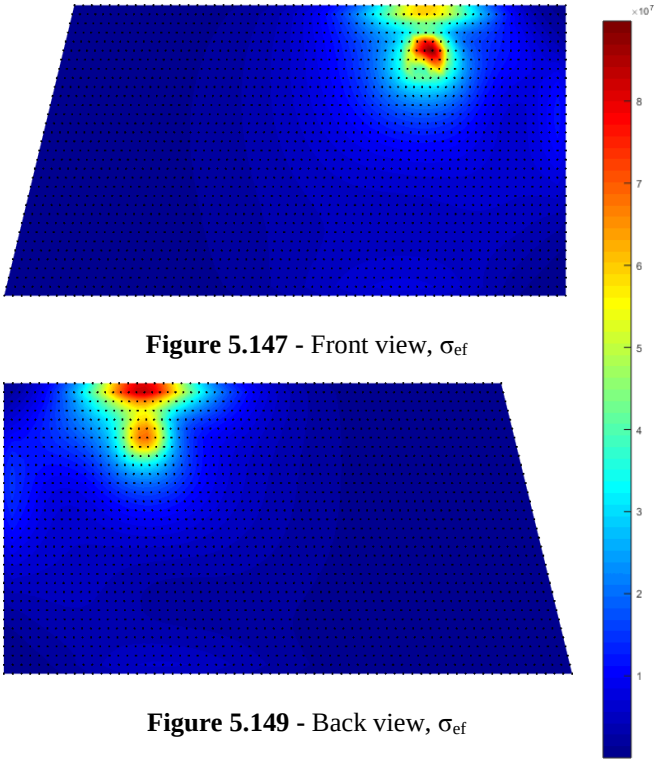

Figure 5.147 - Front view, σ_{ef}

Figure 5.149 - Back view, σ_{ef}

NNRPIM

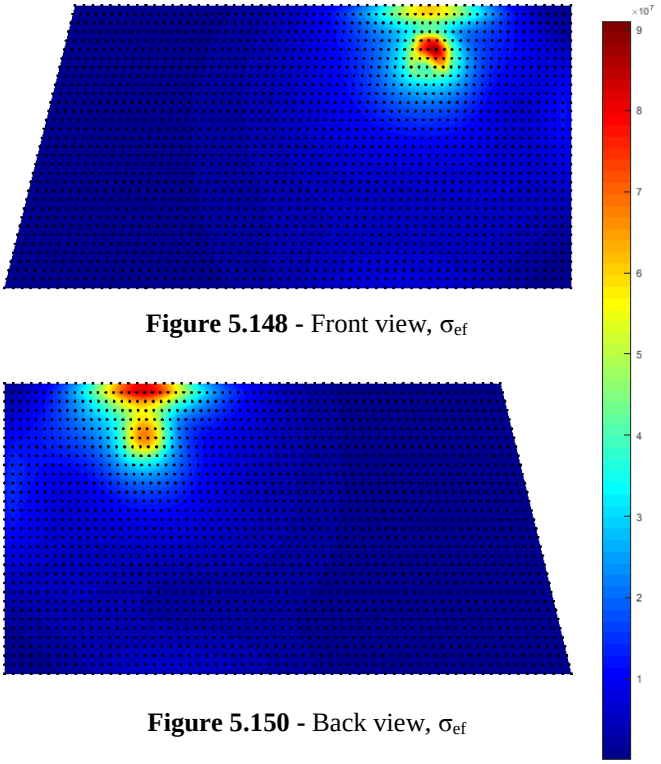

Figure 5.148 - Front view, σ_{ef}

Figure 5.150 - Back view, σ_{ef}

Impact location # 8

The displacement for each impact point was calculated across the thickness and following this, the average of the three nodal displacements discretizing the thickness comes,

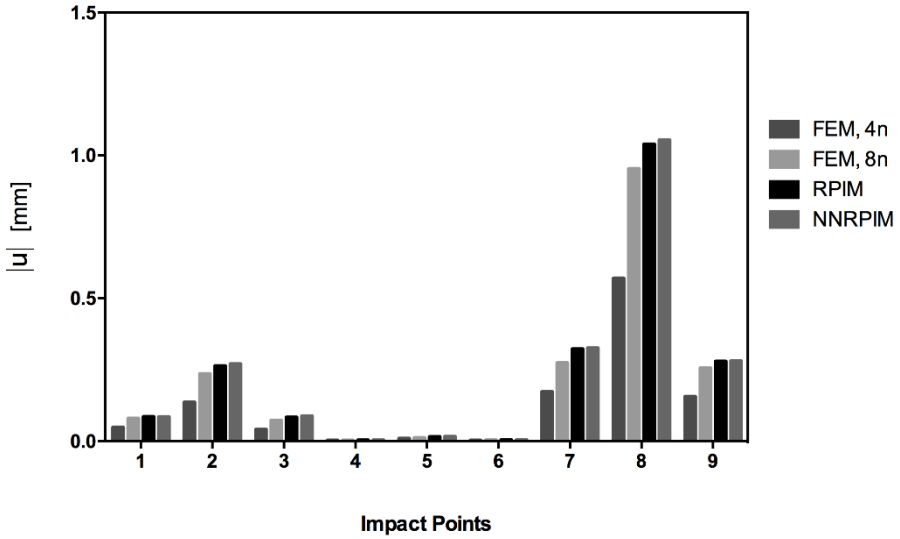

Figure 5.151 - Average nodal displacement along the thickness of each impact location caused by the impact to location 8.

The von Mises stress for each impact point was calculated across the thickness and following this, the average of the three nodal von Mises stresses discretizing the thickness comes,

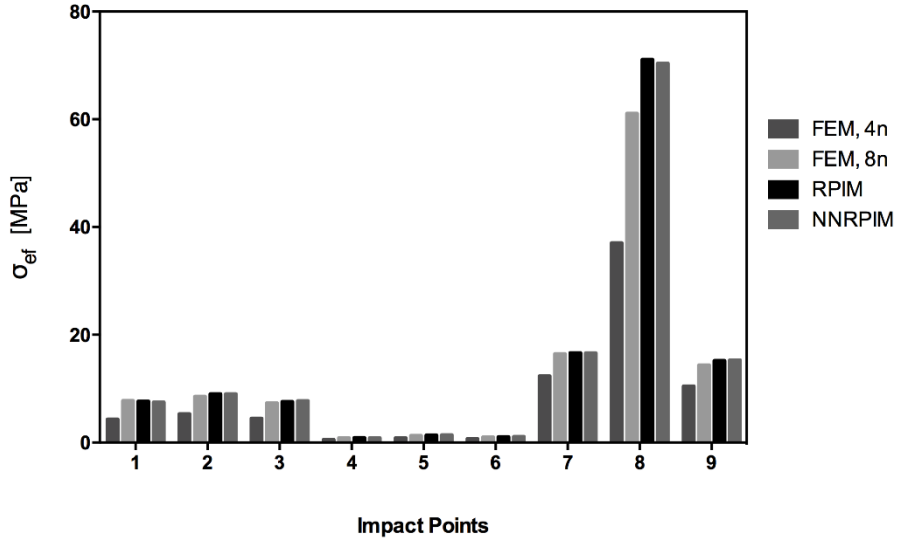

Figure 5.152 - Average nodal stress along the thickness of each impact location caused by the impact to location 8.

The von Mises stress for each node of the ABCD border of the windshield, shown in Figure 5.8, was calculated across the thickness and following this, the average of the three nodal von Mises stresses discretizing the ABCD border thickness comes,

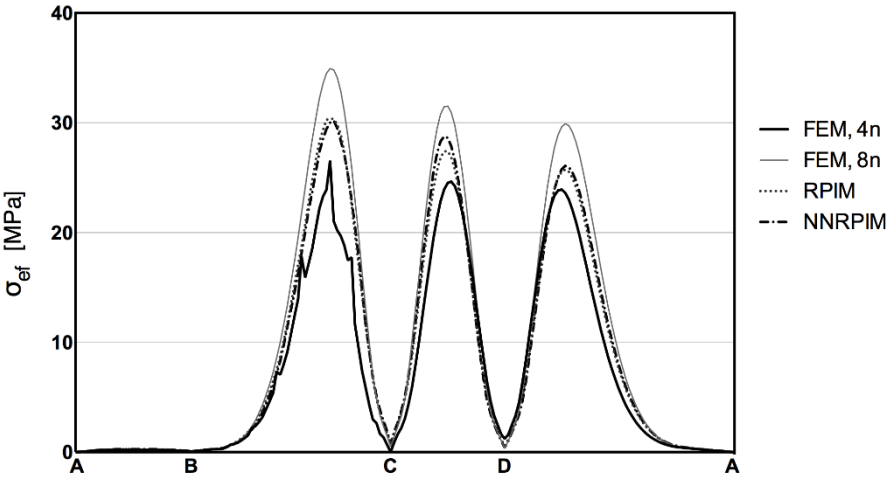

Figure 5.153 - Average nodal stress along the thickness of the clamped section of the windshield caused by the impact to location 8.

The following displacement field is obtained,

FEM, 4n

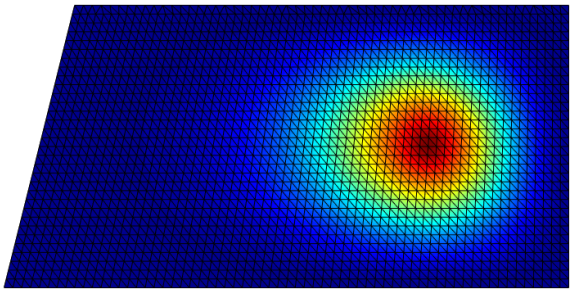

Figure 5.154 - Front view, |u|

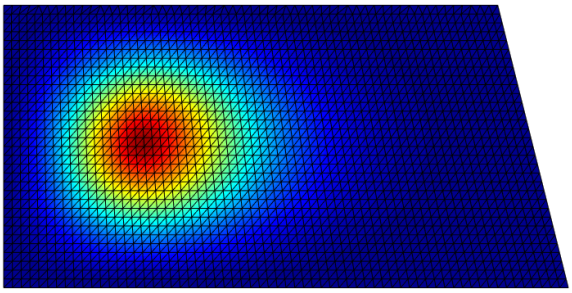

Figure 5.156 - Back view, |u|

FEM, 8n

Figure 5.155 - Front view, |u|

Figure 5.157 - Back view, |u|

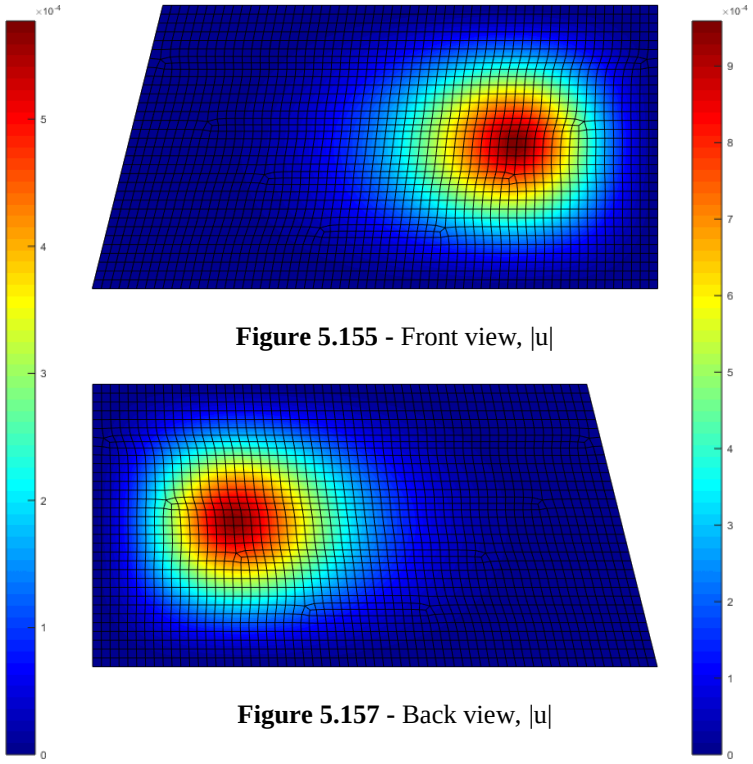

RPIM

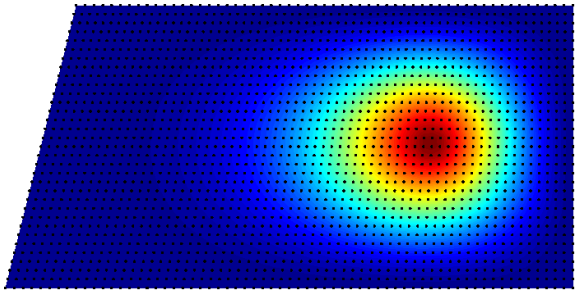

Figure 5.158 - Front view, |u|

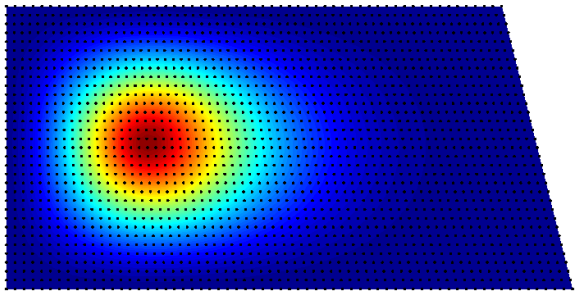

Figure 5.160 - Back view, |u|

NNRPIM

Figure 5.159 - Front view, |u|

Figure 5.161 - Back view, |u|

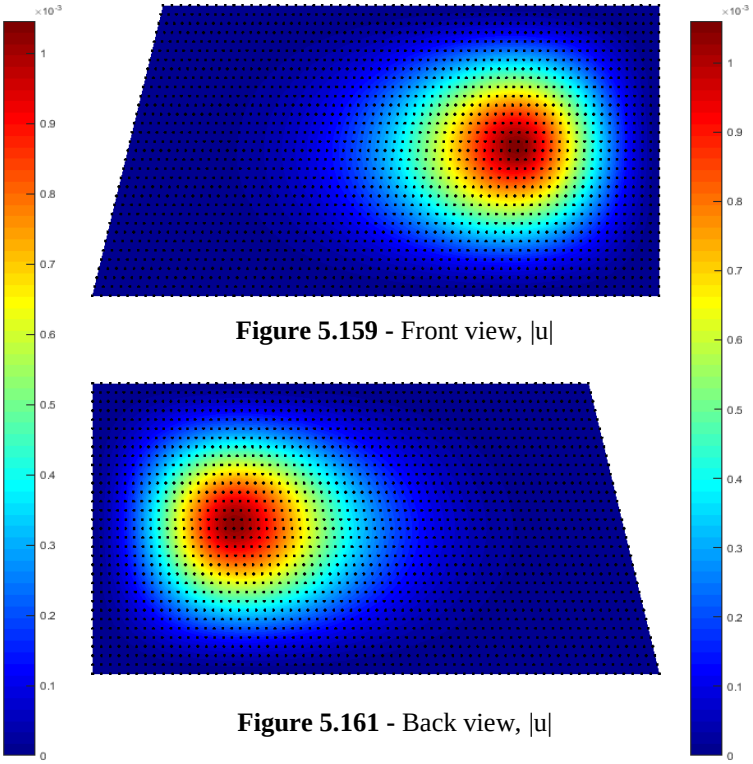

The following stress field is obtained,

FEM, 4n

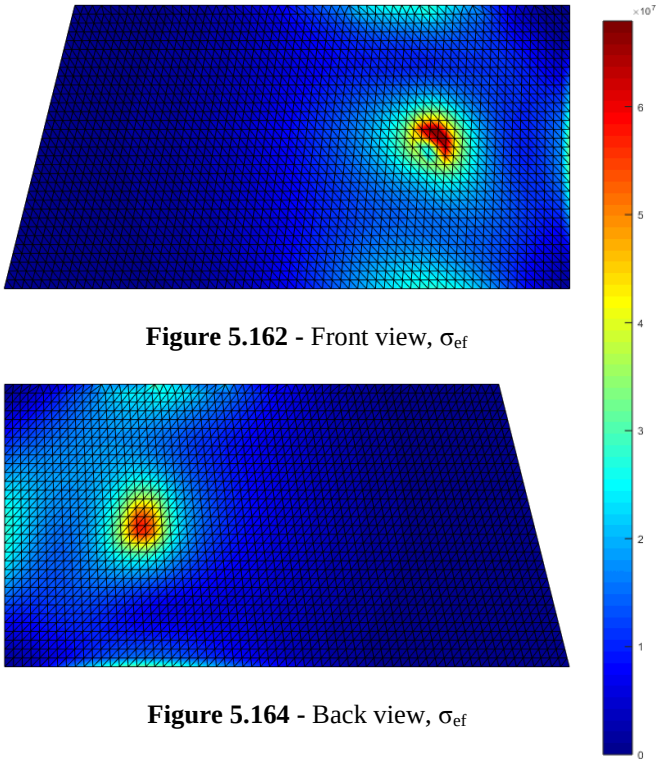

Figure 5.162 - Front view, σ_{ef}

Figure 5.164 - Back view, σ_{ef}

FEM, 8n

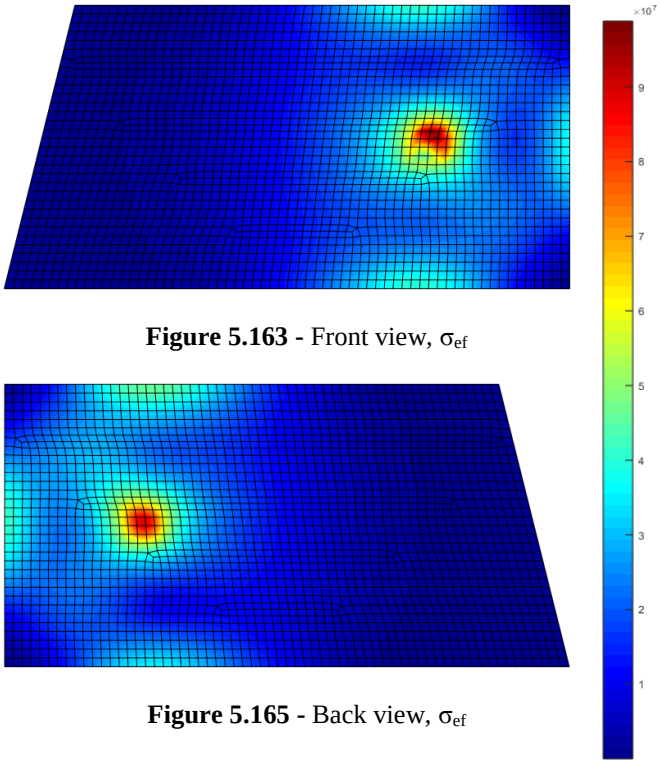

Figure 5.163 - Front view, σ_{ef}

Figure 5.165 - Back view, σ_{ef}

RPIM

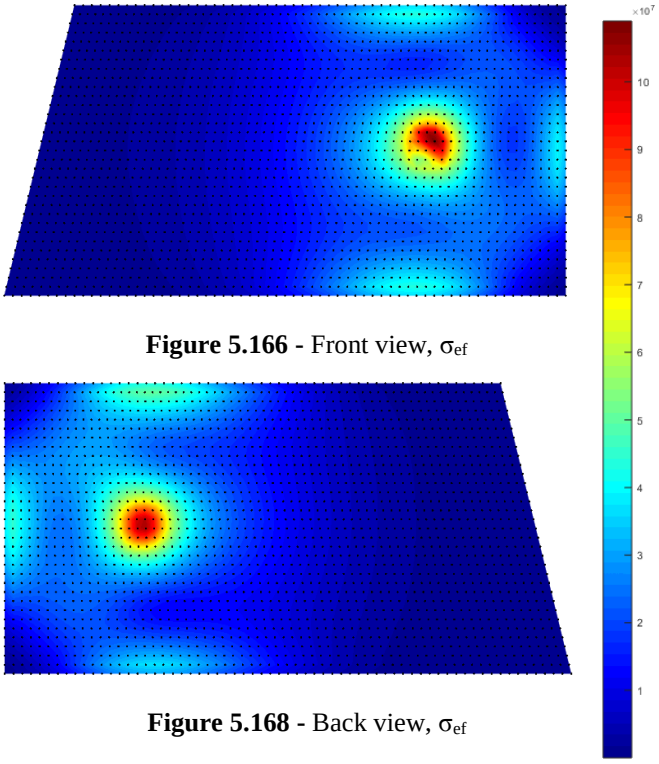

Figure 5.166 - Front view, σ_{ef}

Figure 5.168 - Back view, σ_{ef}

NNRPIM

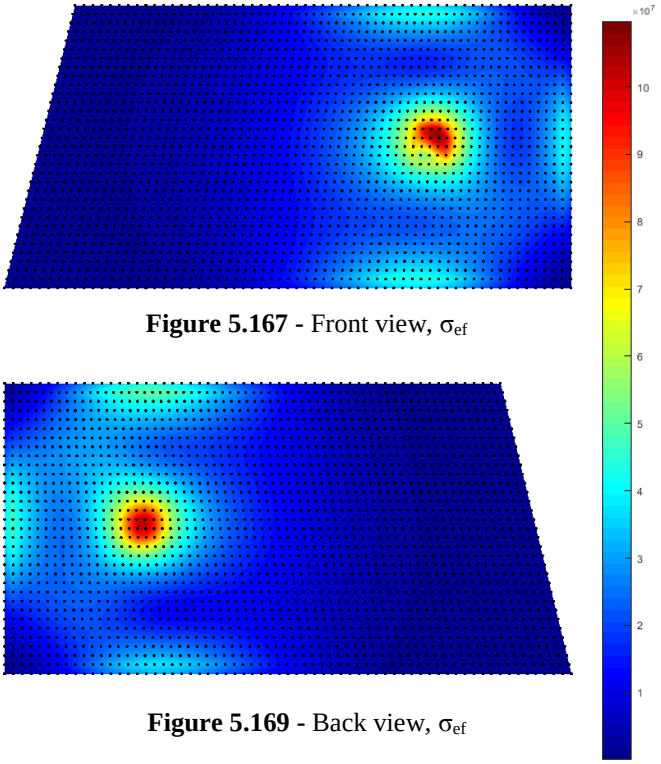

Figure 5.167 - Front view, σ_{ef}

Figure 5.169 - Back view, σ_{ef}

Impact location # 9

The displacement for each impact point was calculated across the thickness and following this, the average of the three nodal displacements discretizing the thickness comes,

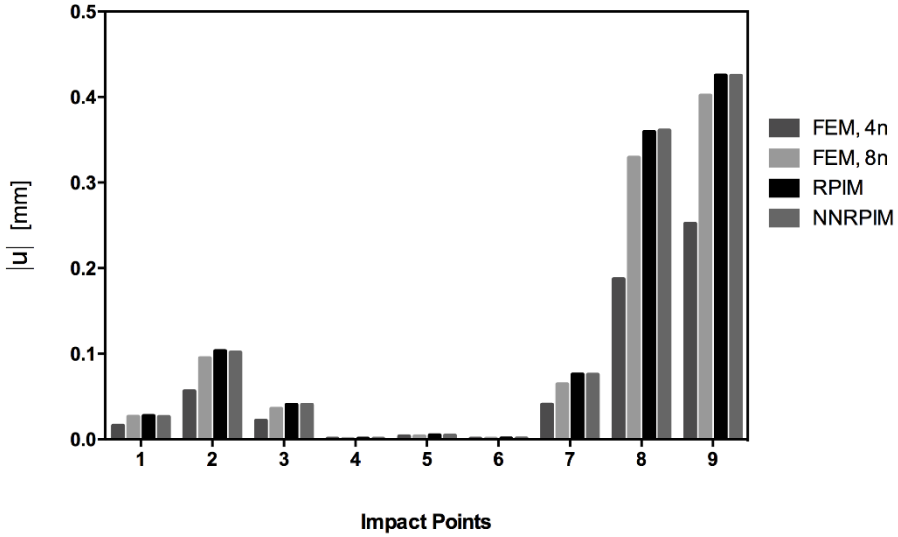

Figure 5.170 - Average nodal displacement along the thickness of each impact location caused by the impact to location 9.

The von Mises stress for each impact point was calculated across the thickness and following this, the average of the three nodal von Mises stresses discretizing the thickness comes,

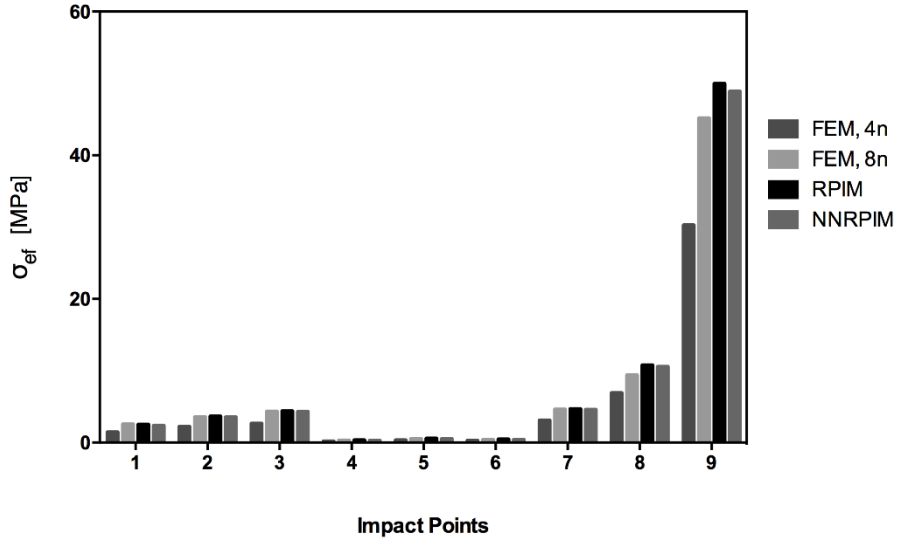

Figure 5.171 - Average nodal stress along the thickness of each impact location caused by the impact to location 9.

The von Mises stress for each node of the ABCD border of the windshield, shown in Figure 5.8, was calculated across the thickness and following this, the average of the three nodal von Mises stresses discretizing the ABCD border thickness comes,

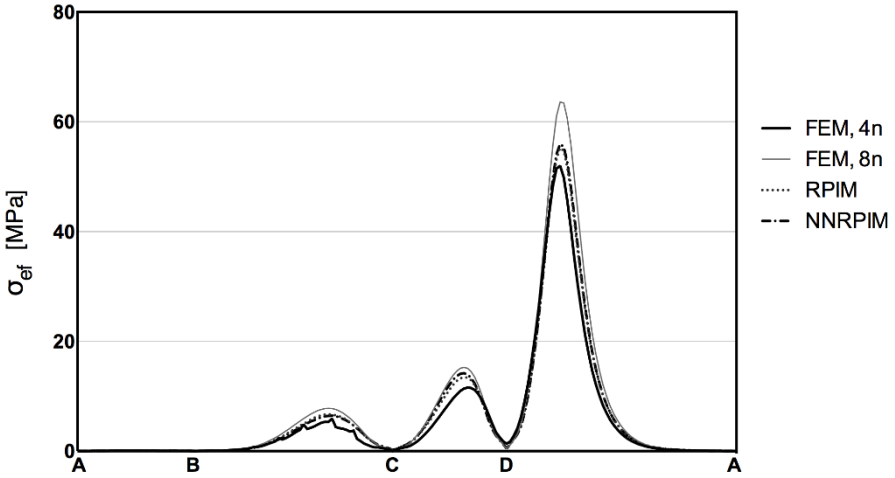

Figure 5.172 - Average nodal stress along the thickness of the clamped section of the windshield caused by the impact to location 9.

The following displacement field is obtained,

FEM, 4n

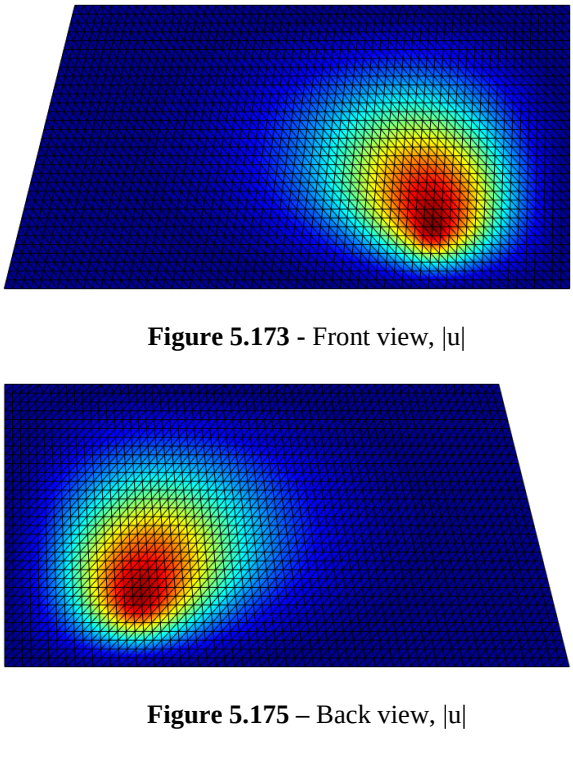

Figure 5.173 - Front view, |u|

Figure 5.175 – Back view, |u|

FEM, 8n

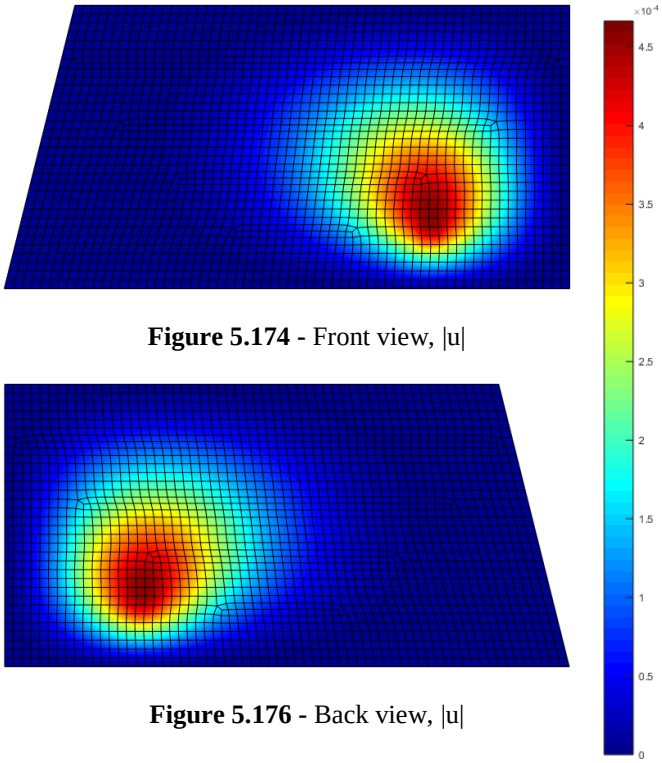

Figure 5.174 - Front view, |u|

Figure 5.176 - Back view, |u|

RPIM

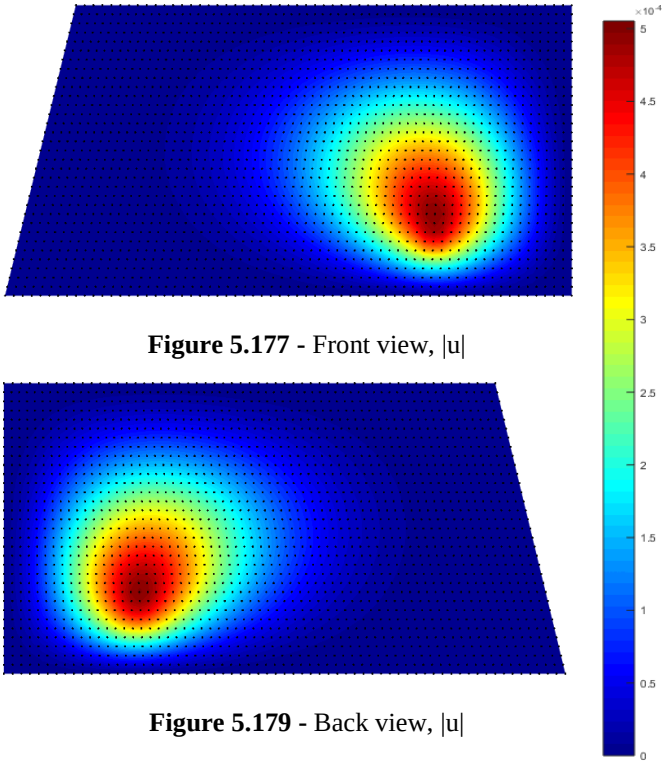

Figure 5.177 - Front view, |u|

Figure 5.179 - Back view, |u|

NNRPIM

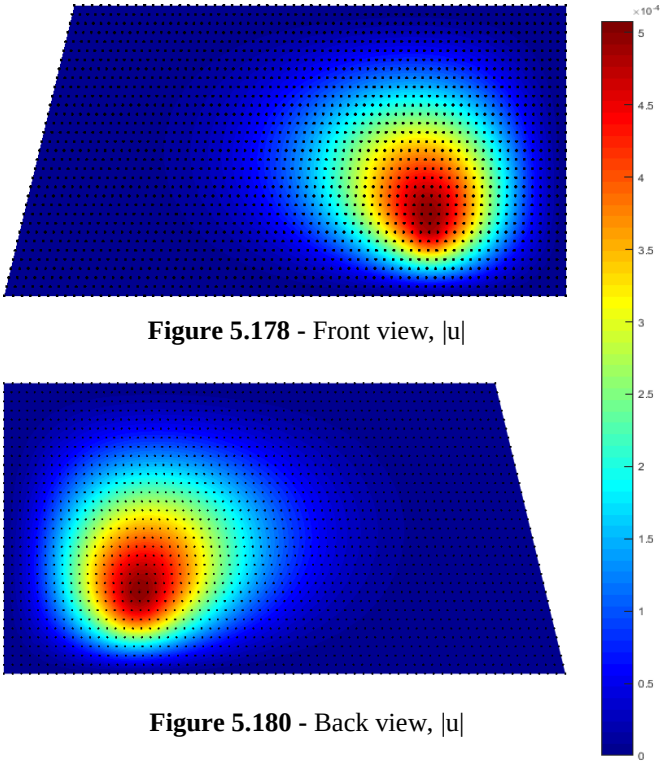

Figure 5.178 - Front view, |u|

Figure 5.180 - Back view, |u|

The following stress field is obtained,

FEM, 4n

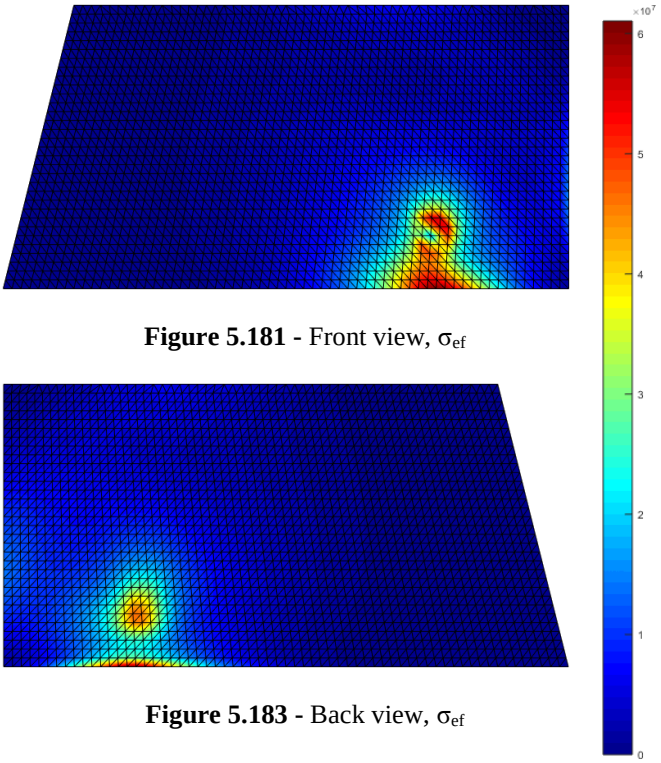

Figure 5.181 - Front view, σ_{ef}

Figure 5.183 - Back view, σ_{ef}

FEM, 8n

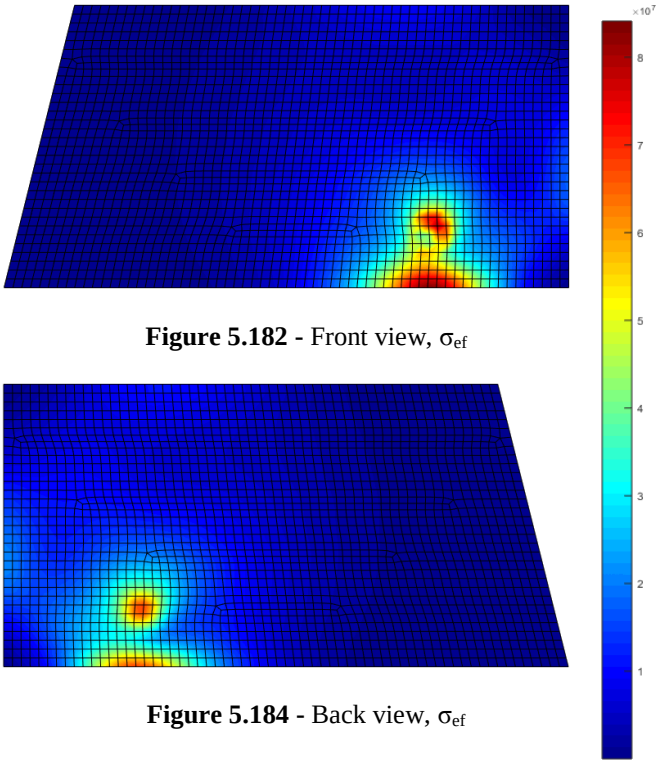

Figure 5.182 - Front view, σ_{ef}

Figure 5.184 - Back view, σ_{ef}

RPIM

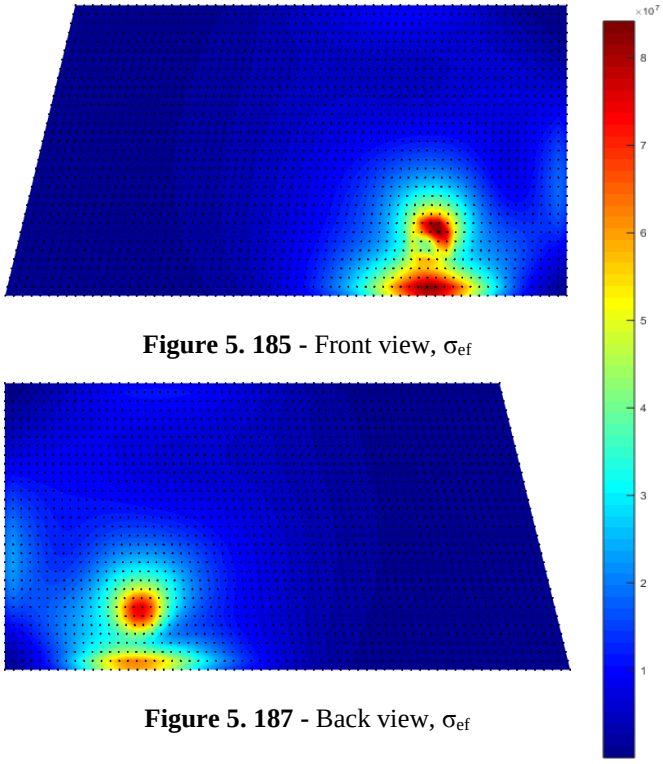

Figure 5. 185 - Front view, σ_{ef}

Figure 5. 187 - Back view, σ_{ef}

NNRPIM

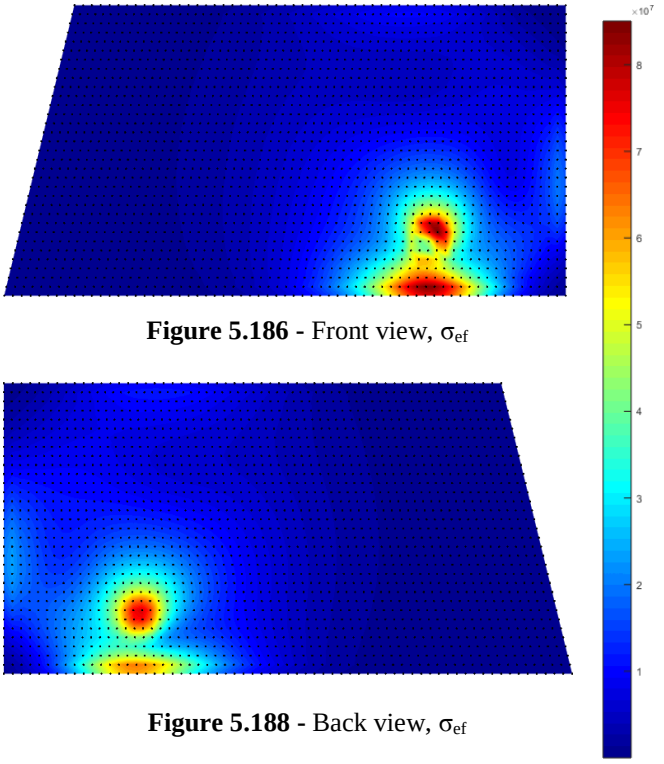

Figure 5.186 - Front view, σ_{ef}

Figure 5.188 - Back view, σ_{ef}

By looking at the results for each impact point through the use of the meshless methods (RPIM and NNRPIM) and the FEM using both a tetrahedral (FEM, 4n) and a hexahedral mesh (FEM, 8n) it is possible to observe that even though the results obtained with all four methods lead to fairly similar displacement and stress distributions, there are small differences intrinsic to each method.

Therefore, the discussion of the previously shown results is better done in two parts. First, by comparing the meshless methods with the FEM using a tetrahedral mesh (FEM, 4n) and then with the FEM using a hexahedral mesh (FEM, 8n).

Even though tetrahedral elements are the most used elements in computational mechanics, as this work shows, they are unreliable for stress and strain analysis. By looking at the average nodal displacement graphs of each impact location it is possible to observe one of the biggest differences between the meshless methods and the FEM, 4n. As stated previously, tetrahedral elements are known to be extremely stiff when it comes to bending problems, which means that, no matter how greatly the discretization is increased, the displacement value obtained with the FEM, 4n will always be inferior to the optimal solution. This was confirmed by both the convergence study done for the windshield geometry (in which the displacement values obtained with the FEM, 4n had already converged, while still being distant from the other method's solutions) and by looking at the aforementioned graphs. Although, it is possible to observe that this happens for every impact location, it is particularly clear in any impact location that takes place close to the centre line of the windshield, namely location #2, #5 and #8, in which there are the biggest discrepancies between the answer of the FEM, 4n and the meshless methods, with the first only reaching slightly over half of the average nodal displacement values of the meshless methods, as shown in Figures 5.37, 5.94 and 5.151. When the impact takes place on these locations, since the bending span is larger, the results show larger differences.

A similar discrepancy happens with the von Mises stresses obtained for each impact location, due to the same reasons.

The graphs showing the average nodal stresses along the ABCD border of the windshield also confirm these results. The obtained von Mises stress using the FEM, 4n is always lower than the obtained with the meshless methods. A prominent fact observed is that the average nodal stress along the thickness of the windshield, is often fairly irregular. This is most striking for impact locations, #2, #5 and #8, namely in Figures 5.39, 5.96 and 5.153. This happens due the way FEMAS interpolates the stress

values from the integration points to the nodes. Nevertheless, the stress magnitude shown is in accordance with the stress magnitude obtained in the integration points.

The other major difference between the FEM, 4n and the meshless methods is in the stress fields obtained. Although the general distribution of the stress fields obtained through different methods are comparable, the values obtained with the FEM, 4n are always lower. But, the biggest difference comes in the form of the smoothness and accuracy of the stress fields. By taking impact #8 as an example, when comparing Figure 5.162 with Figures 5.166 and 5.167 as well as Figure 5.164 with Figures 5.168 and 5.169 it is possible to observe that the obtained stress field using the meshless methods and the FEM, 4n are quite different. While in stress fields obtained with the meshless methods it is possible to observe clear stress concentration zones, and their changes over the windshield geometry, with the FEM, 4n these areas are not clearly defined. Another example where this difference is most striking is for impact location #7, in which the FEM, 4n does not portray the stress concentration zone of the impact point, as seen when comparing Figure 5.145 with Figures 5.149 and 5.150.

There are no major differences when comparing the displacement fields of the FEM, 4n with the meshless methods, because of the way these fields are obtained.

On the other hand, hexahedral element meshes yield much better results than their tetrahedral counterparts. The displacement and stress values obtained are similar to the ones obtained with the meshless methods throughout the windshield geometry, and the displacement and stress fields obtained all show the same distribution as the meshless methods.

5.3.2 2D Surrounding structure analysis

Following the 3D study of the windshield, a 2D analysis of a section of the surrounding structure was performed. By looking at the previous 3D study it was clear that an impact on location #1 lead to the higher von Mises stresses on the clamped section of the windshield. Therefore, a section of the windshield where the maximum von Mises stress occurred was singled out from the problem, as seen in Figure 5.189.

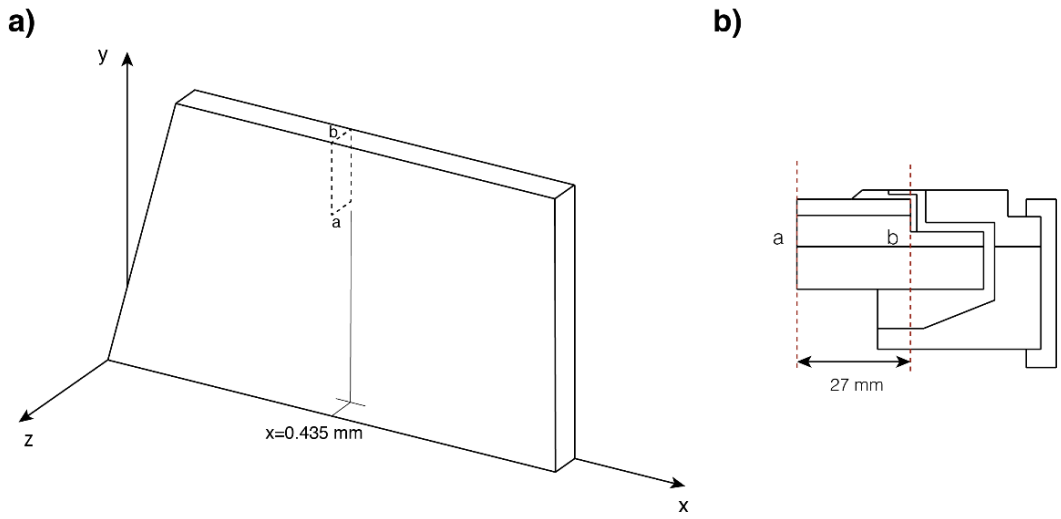

Figure 5.189 – Section of the windshield.

The 2D section of the windshield structure is the one described in Figure 5.6 with the same materials having been considered. The steel bolt is considered as being clamped, while the rest of the structure has no boundary restrictions.

The dimensions of the 2D section of the windshield structure are shown below,

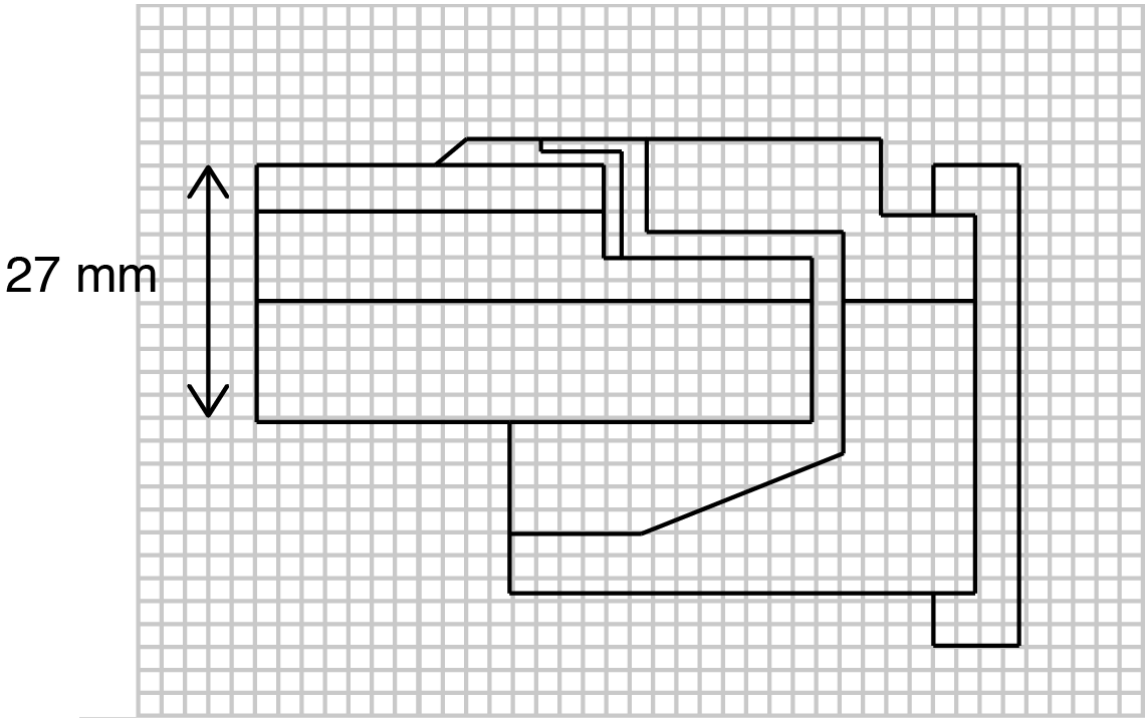

Figure 5.190 – 2D section of the windshield and surrounding structure dimensions.

The section was discretised with 13227 nodes, as seen in Figure 5.191.

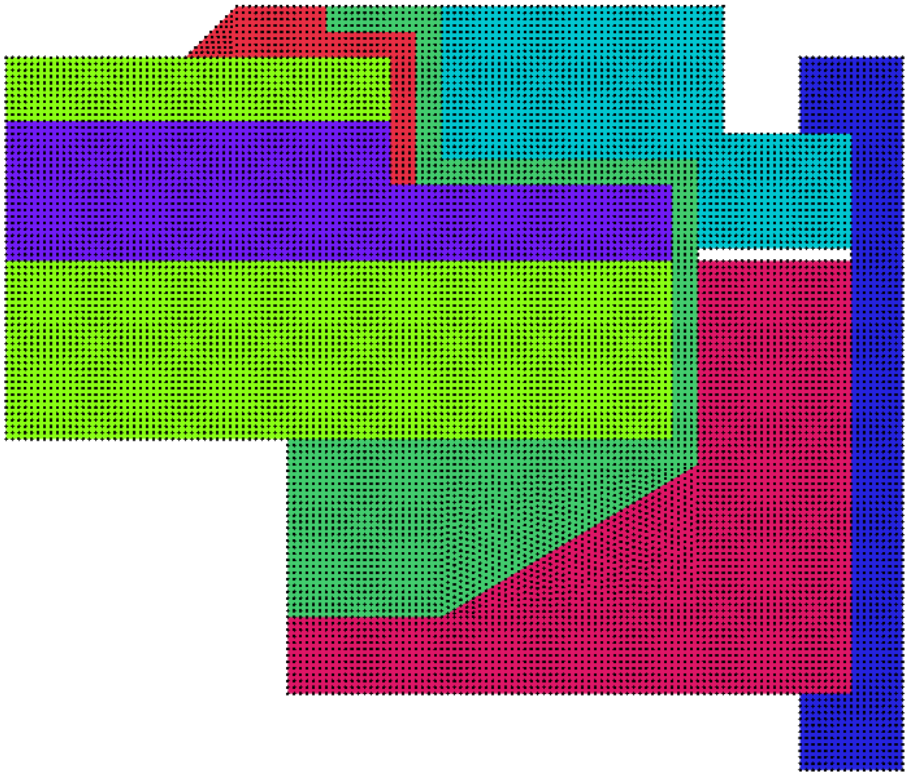

Figure 5. 191 – 13227 nodes discretization of the 2D section.

The rectangular gap seen on the right side is necessary due to the meshless method procedure. If the gap didn't exist there would be no separation of the two different aluminium sections (shown in light blue and red colour), and they would deform as one.

The displacement of the three nodes along the thickness of the 3D model caused by the impact on location # 1 were obtained with FEMAS and a quadratic distribution of the vertical displacement was imposed on the 2D problem along section a, as seen in Figure 5.192.

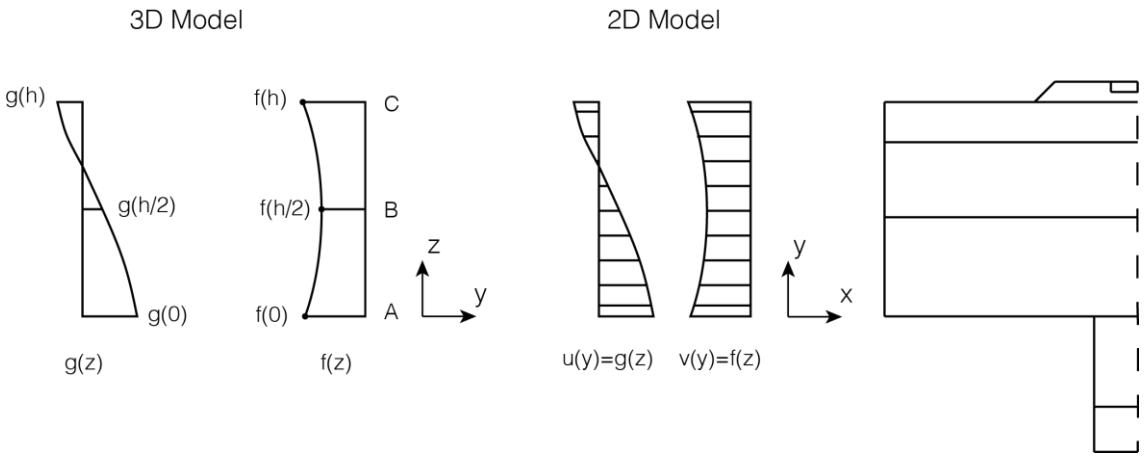

Figure 5.192 – Representation of the imposed displacements.

Since each one of the four methods (FEM 4n, FEM 8n, RPIM and NNRPIM) produced distinct results for the 3D analysis, four distinct displacement functions were obtained and applied to the respective 2D model.

Section b was considered as representing the clamped part of the 3D windshield. The main goals were to study the mechanical behaviour the windshield structure, and obtain similiar von Mises stresses in section b as the ones obtained for the 3D example. The 2D plane strain deformation theory was used.

The following results were obtained, when considering the displacements obtained with the 4 methods.

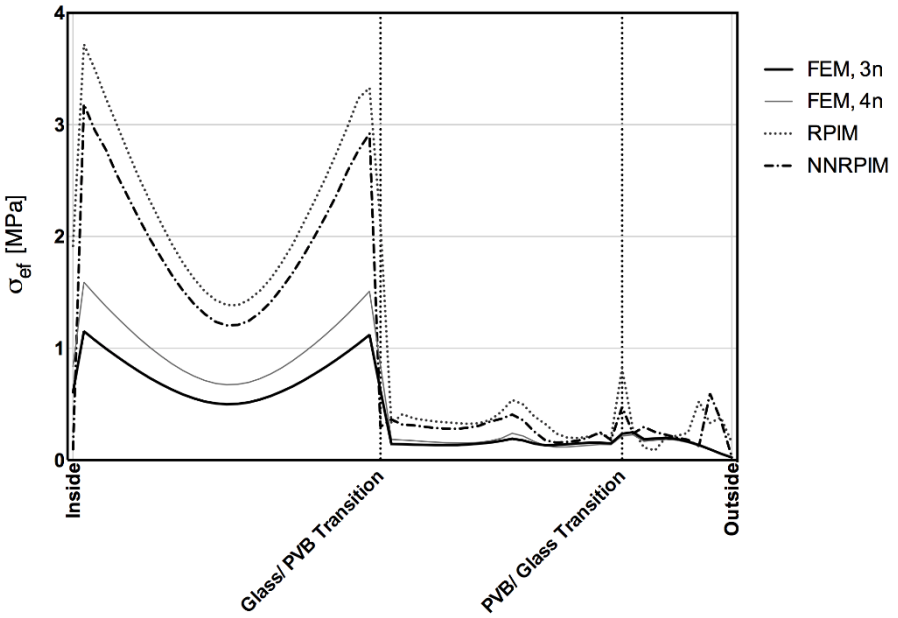

Figure 5.193 – Von Mises stress along the thickness of the clamped section of the windshield.

However, when comparing the results with the ones obtained for the 3 nodes in thickness, the results show a large discrepancy.

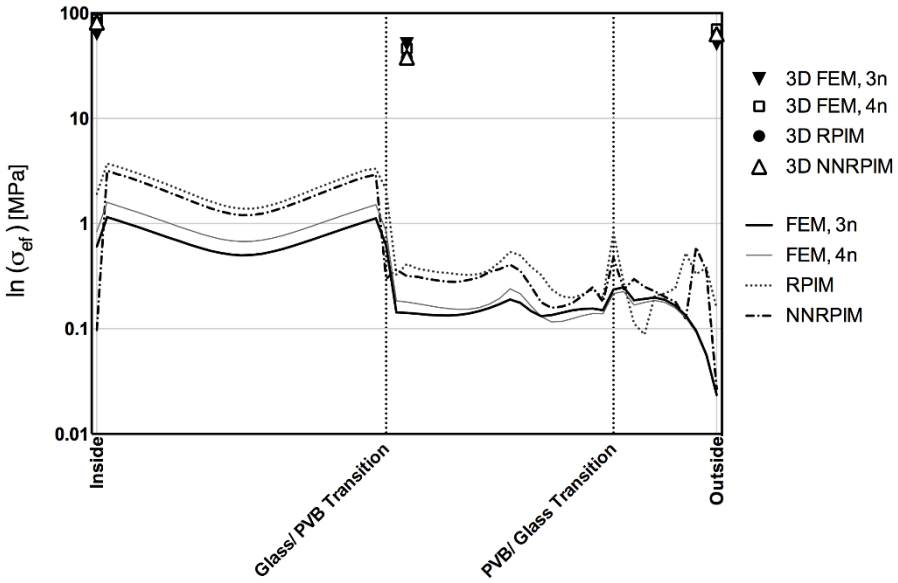

Figure 5.194 - Von Mises stress along stress along the thickness of the clamped section of the windshield with the values obtained in the 3D study for the 3 nodes discretizing the thickness.

When looking at the results of any of the methods used, the reason for this difference was clear.

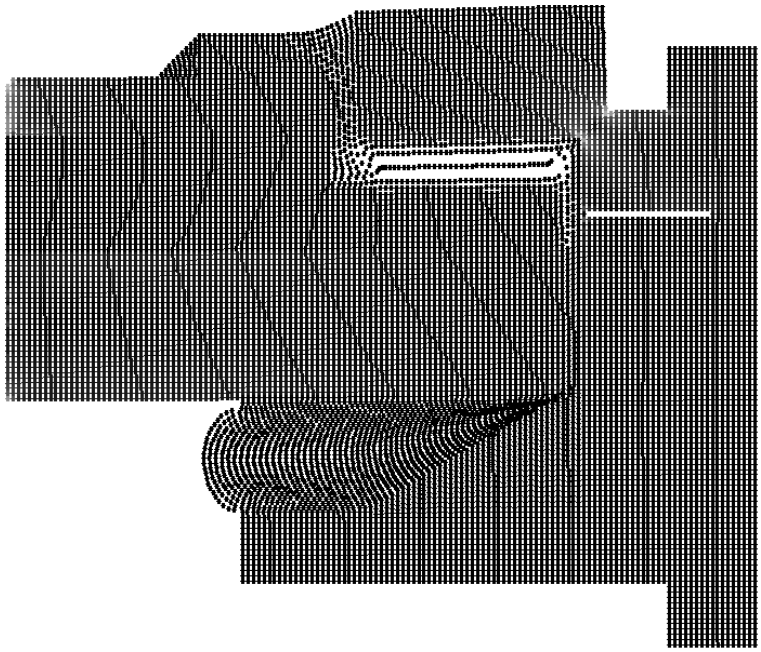

Figure 5.195 – 2D study deformed configuration using a 30x scale.

This disparity in results is due to the fact that the silicone surrounding the windshield, as well as the sealant, is particularly soft which leads to it not absorbing any stresses, causing the 2D section to deform heavily, which by itself lowers the stress values.

Because of this, the actual essential boundary conditions of the problem should be simply supported and not clamped. Before performing another study of the 3D windshield using the new essential boundary conditions, another 2D analysis was performed, this time considering all materials surrounding the windshield as having E=270GPa and ν=0.3 in order to simulate the clamping of the windshield. The following results were then obtained,

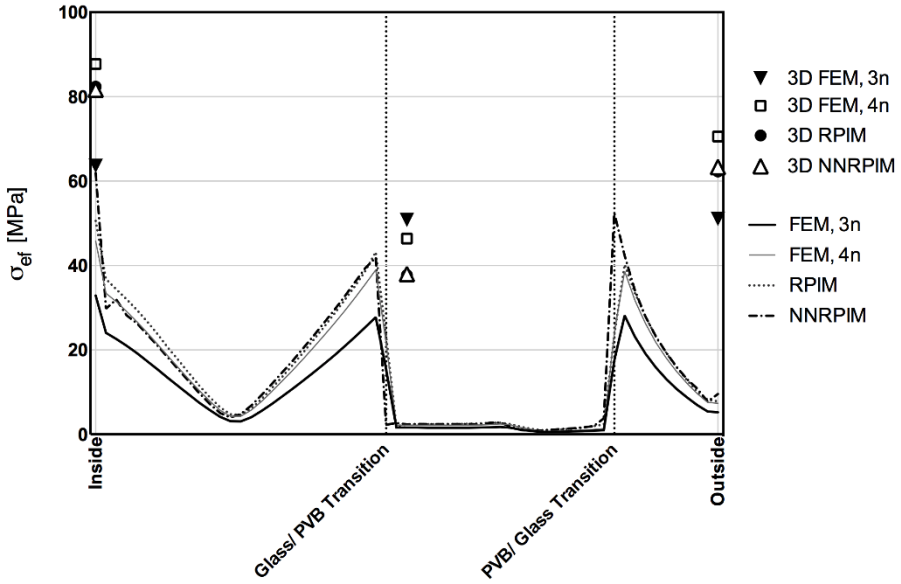

Figure 5.196 - Von Mises stress along stress along the thickness of the clamped section of the windshield with the values obtained in the 3D study for the 3 nodes discretizing the thickness.

By looking at Figure 5.195 it is possible to establish a correlation between the results obtained in the 3D problem and the ones obtained by analysing a 2D section of the windshield and its corresponding surrounding structure.

5.4 Simply supported Windshield

5.4.1 3D Windshield analysis

The 3D analysis was repeated, this time with a simply supported windshield, to accurately represent the windshield interaction with the surrounding structure. Another change made was the homogenisation of the three layers constituting the windshield. This time, the outer glass layer was left untouched and the inner glass and PVB layers were homogenised.

This lead to the first layer being defined as having E= 70GPa and ν=0.22 and the second layer as having E=22.6GPa and ν=0.378. Once again, only 3 nodes were considered in thickness, and the middle line of nodes surrounding the windshield was considered as being fully constrained (as opposed to having all 3 nodes in thickness surrounding the windshield fully constrained) in order to obtain a hinged support.

The following results were then obtained.

Impact location # 1

The displacement for each impact point was calculated across the thickness and following this, the average of the three nodal displacements discretizing the thickness comes,

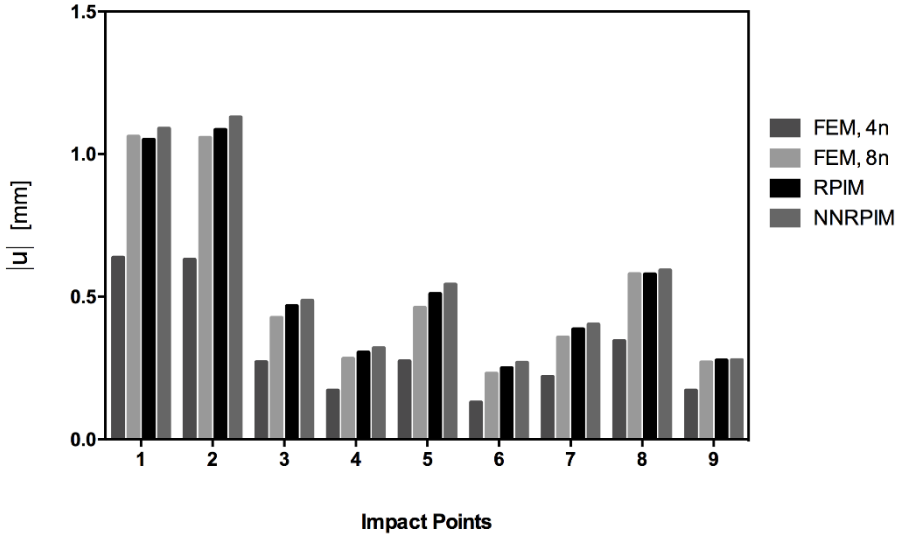

Figure 5.197 - Average nodal displacement along the thickness of each impact location caused by the impact to location 1.

The von Mises stress for each impact point was calculated across the thickness and following this, the average of the three nodal von Mises stresses discretizing the thickness comes,

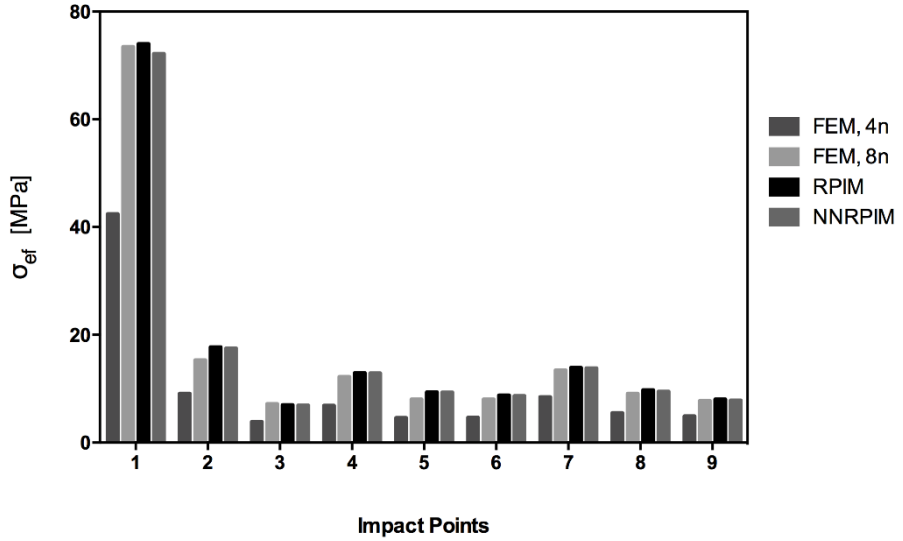

Figure 5.198 - Average nodal stress along the thickness of each impact location caused by the impact to location 1.

The von Mises stress for each node of the ABCD border of the windshield, shown in Figure 5.8, was calculated across the thickness and following this, the average of the three nodal von Mises stresses discretizing the ABCD border thickness comes,

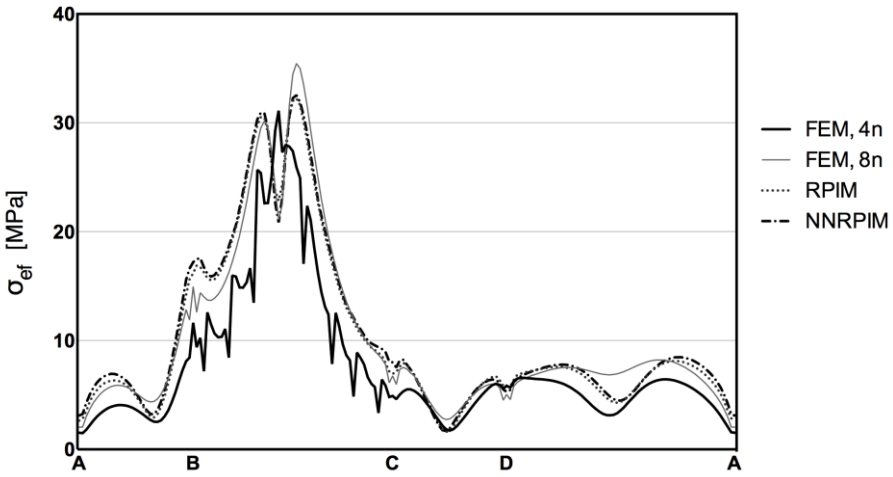

Figure 5.199 - Average nodal stress along the thickness of the clamped section of the windshield caused by the impact to location 1.

The following displacement field was obtained,

FEM, 4n

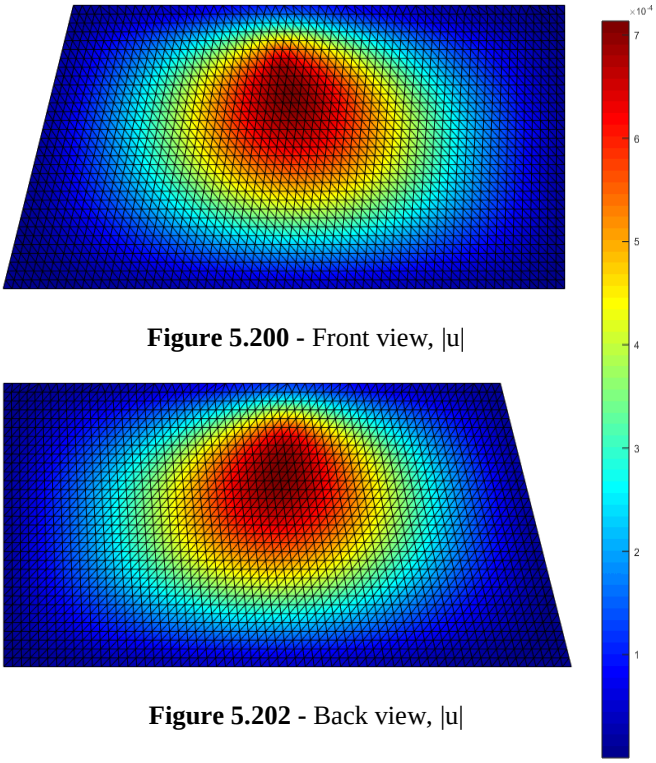

Figure 5.200 - Front view, |u|

Figure 5.202 - Back view, |u|

FEM, 8n

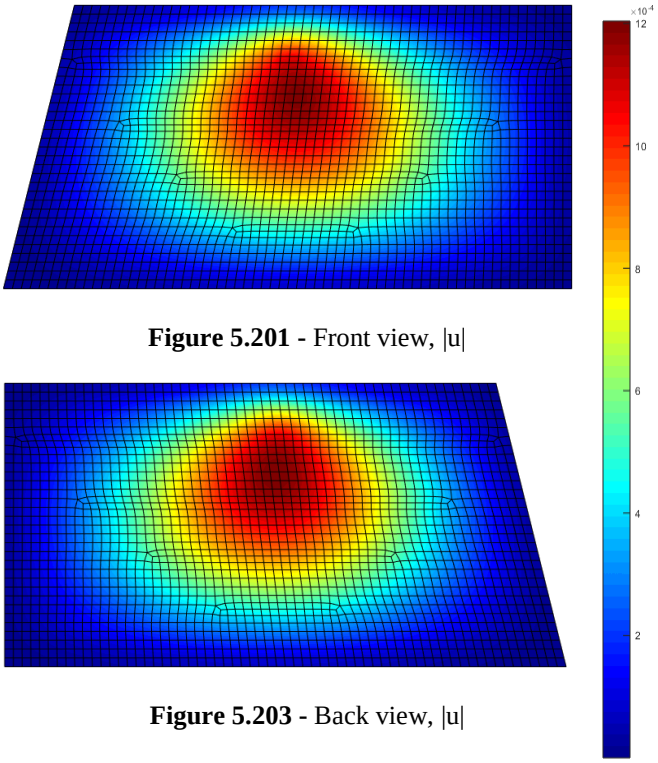

Figure 5.201 - Front view, |u|

Figure 5.203 - Back view, |u|

RPIM

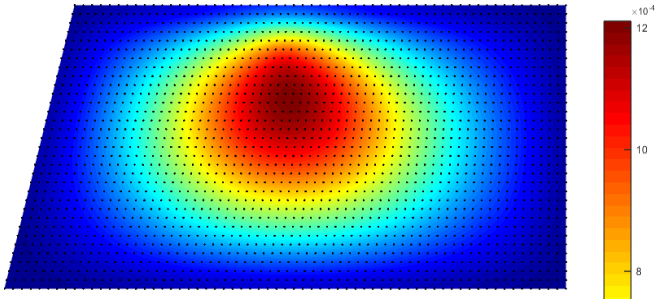

Figure 5.204 - Front view, |u|

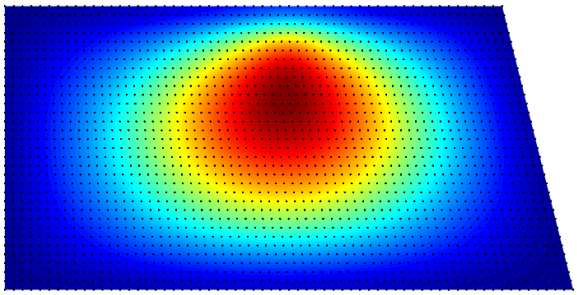

Figure 5.206 - Back view, |u|

NNRPIM

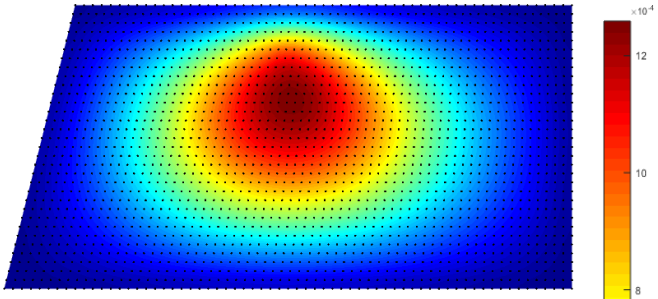

Figure 5.205 - Front view, |u|

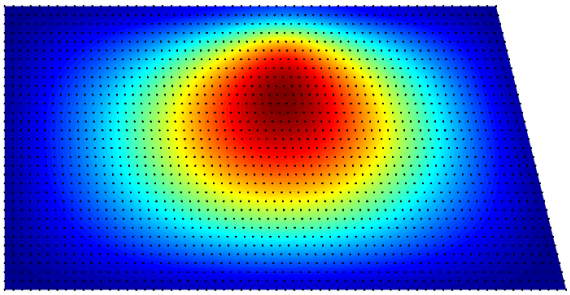

Figure 5.207 - Back view, |u|

The following stress field was obtained,

FEM, 4n

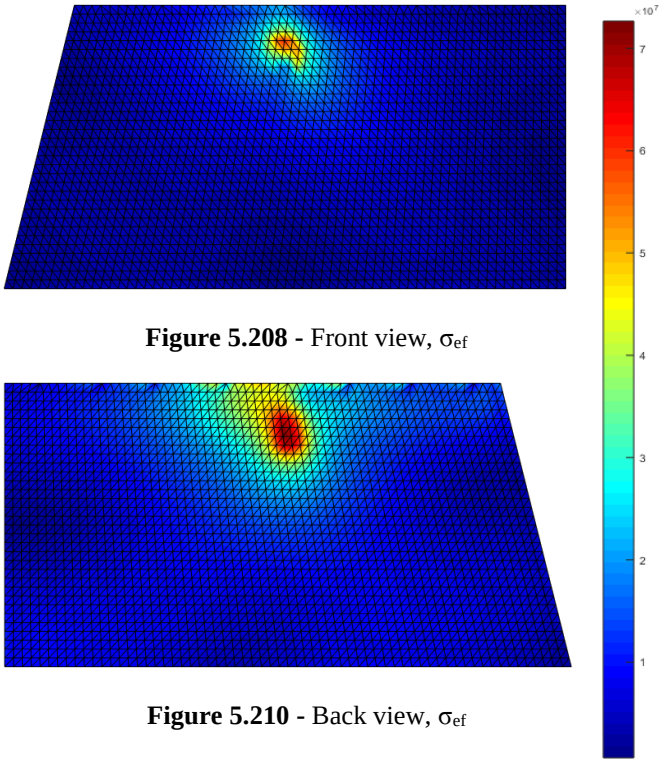

Figure 5.208 - Front view, σ_{ef}

Figure 5.210 - Back view, σ_{ef}

FEM, 8n

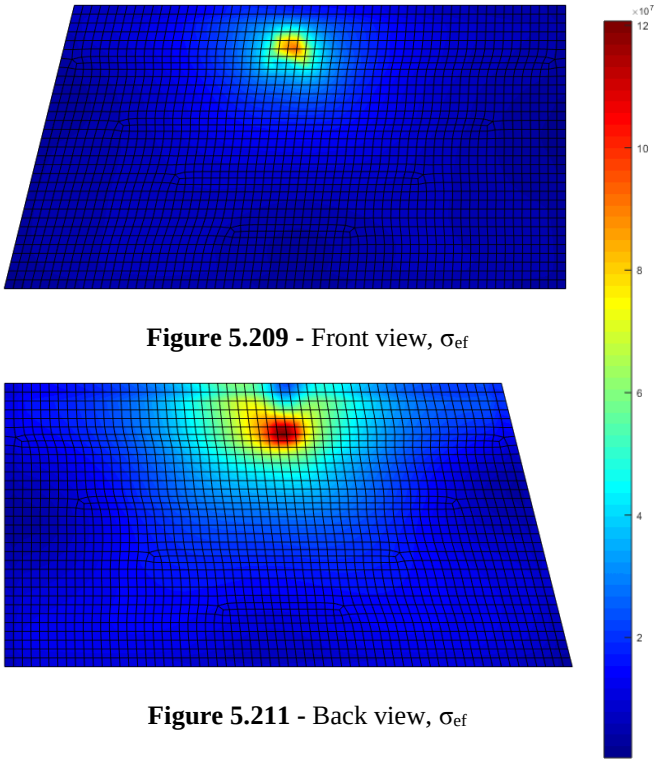

Figure 5.209 - Front view, σ_{ef}

Figure 5.211 - Back view, σ_{ef}

RPIM

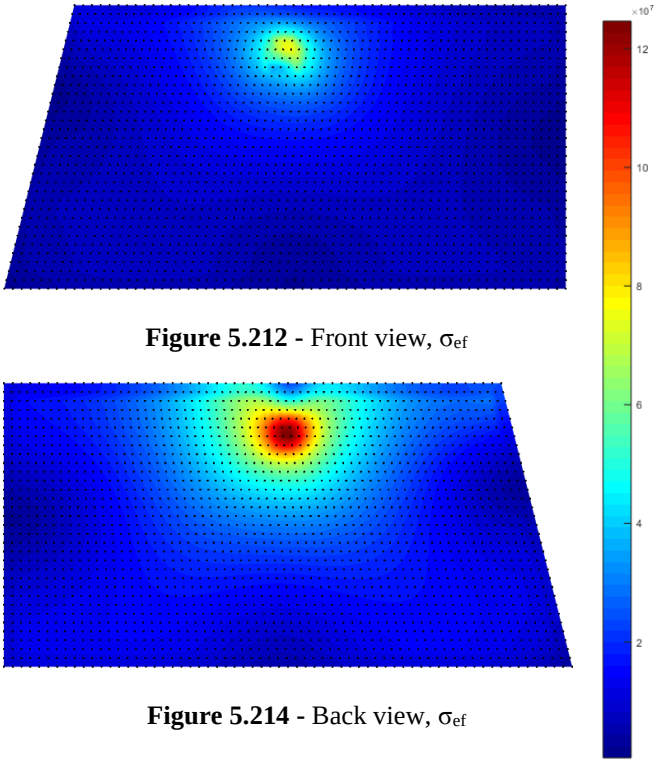

Figure 5.212 - Front view, σ_{ef}

Figure 5.214 - Back view, σ_{ef}

NNRPIM

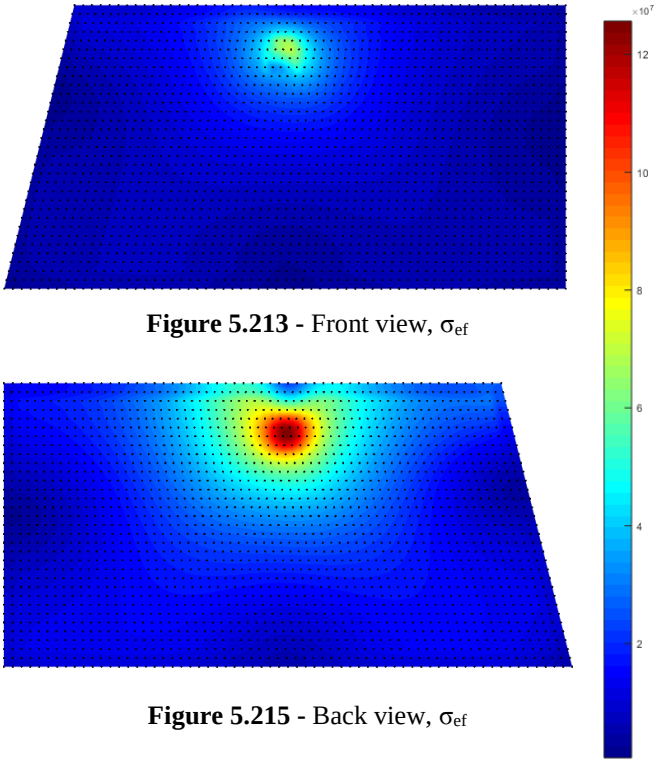

Figure 5.213 - Front view, σ_{ef}

Figure 5.215 - Back view, σ_{ef}

Impact location # 2

The displacement for each impact point was calculated across the thickness and following this, the average of the three nodal displacements discretizing the thickness comes,

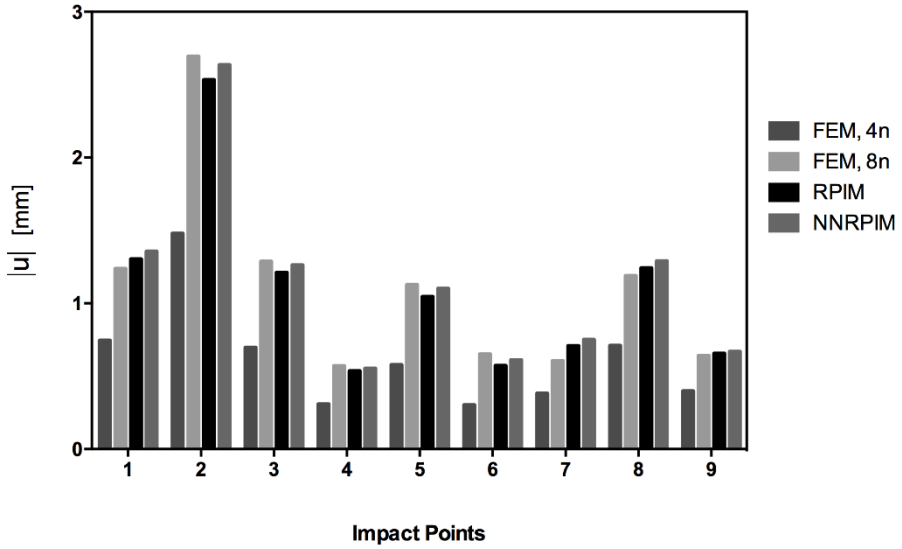

Figure 5.216 - Average nodal displacement along the thickness of each impact location caused by the impact to location 2.

The von Mises stress for each impact point was calculated across the thickness and following this, the average of the three nodal von Mises stresses discretizing the thickness comes,

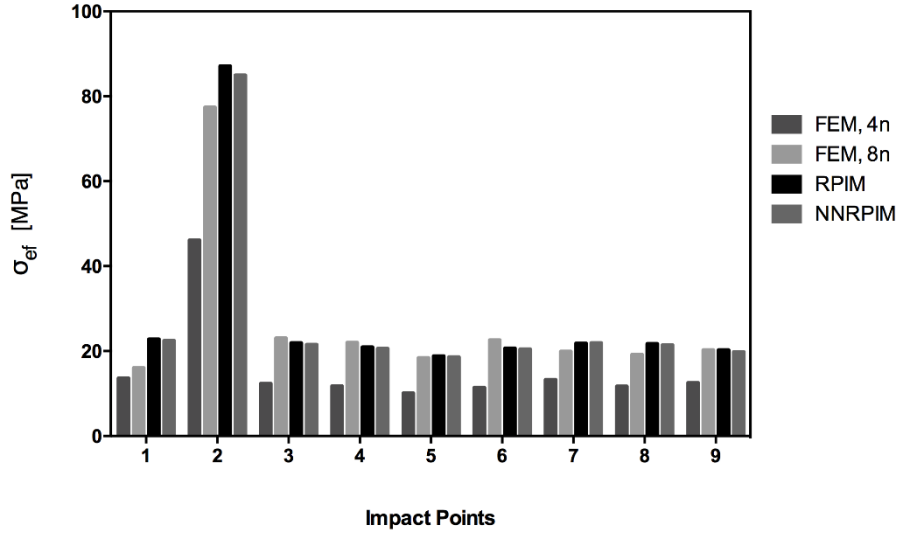

Figure 5.217 - Average nodal stress along the thickness of each impact location caused by the impact to location 2.

The von Mises stress for each node of the ABCD border of the windshield, shown in Figure 5.8, was calculated across the thickness and following this, the average of the three nodal von Mises stresses discretizing the ABCD border thickness comes,

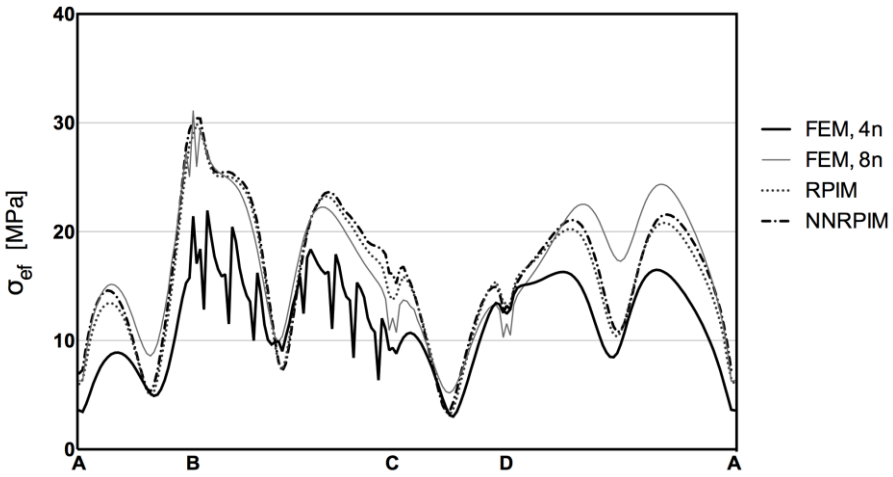

Figure 5.218 - Average nodal stress along the thickness of the clamped section of the windshield caused by the impact to location 2.

The following displacement field was obtained,

FEM, 4n

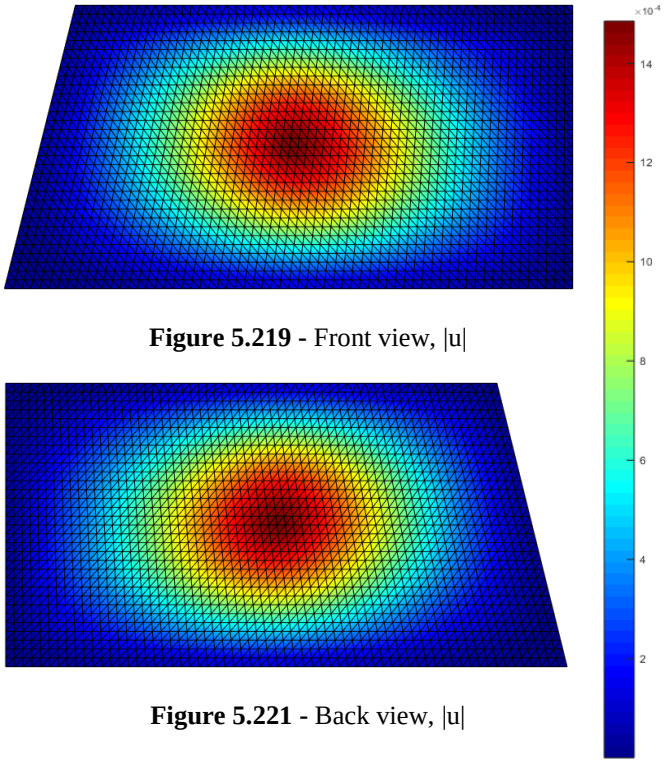

Figure 5.219 - Front view, |u|

Figure 5.221 - Back view, |u|

FEM, 8n

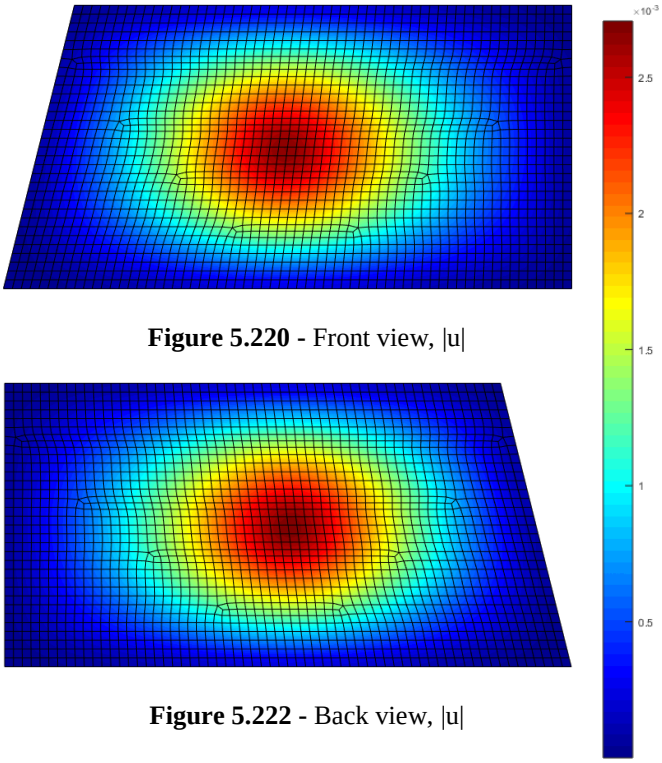

Figure 5.220 - Front view, |u|

Figure 5.222 - Back view, |u|

RPIM

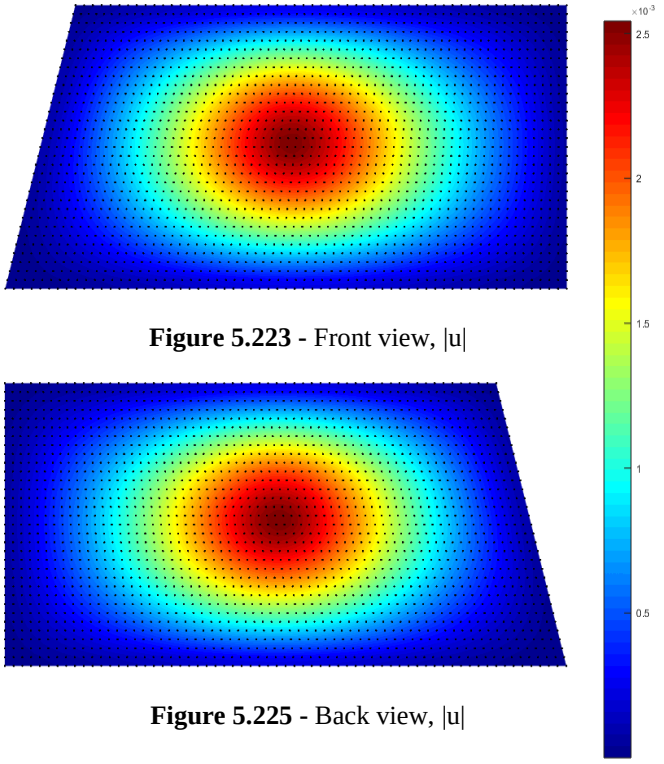

Figure 5.223 - Front view, |u|

Figure 5.225 - Back view, |u|

NNRPIM

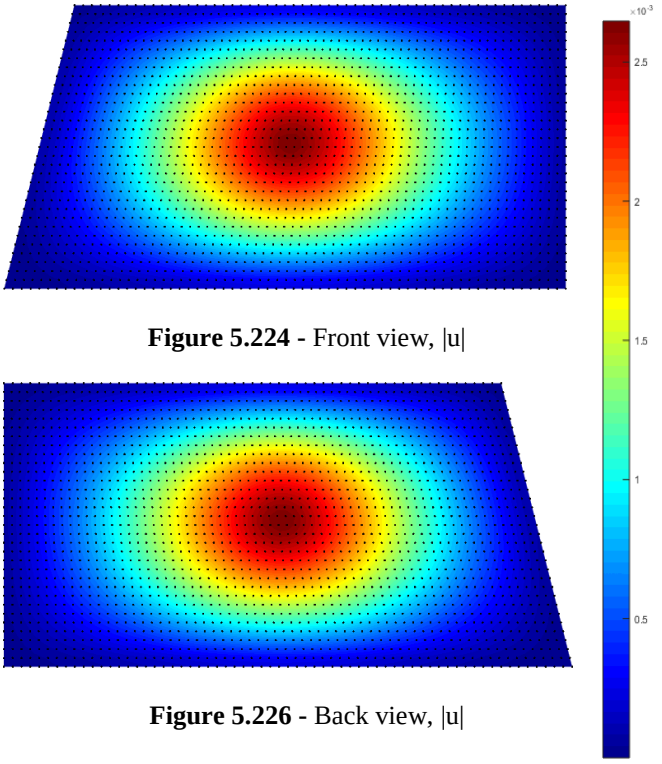

Figure 5.224 - Front view, |u|

Figure 5.226 - Back view, |u|

The following stress field was obtained,

FEM, 4n

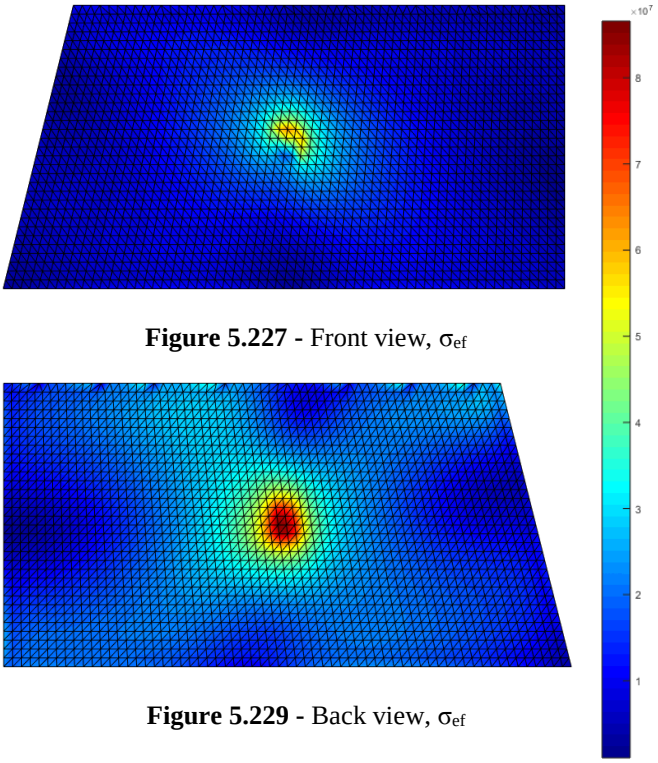

Figure 5.227 - Front view, σ_{ef}

Figure 5.229 - Back view, σ_{ef}

FEM, 8n

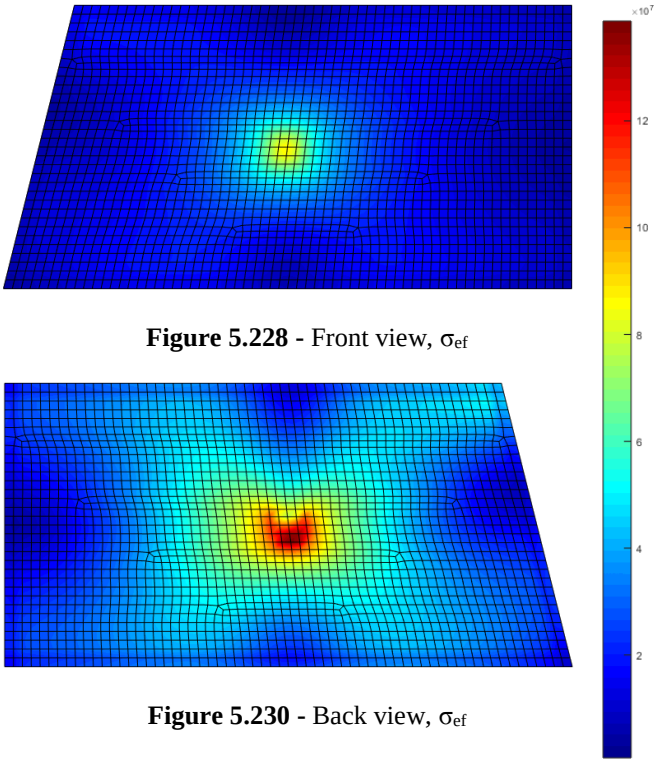

Figure 5.228 - Front view, σ_{ef}

Figure 5.230 - Back view, σ_{ef}

RPIM

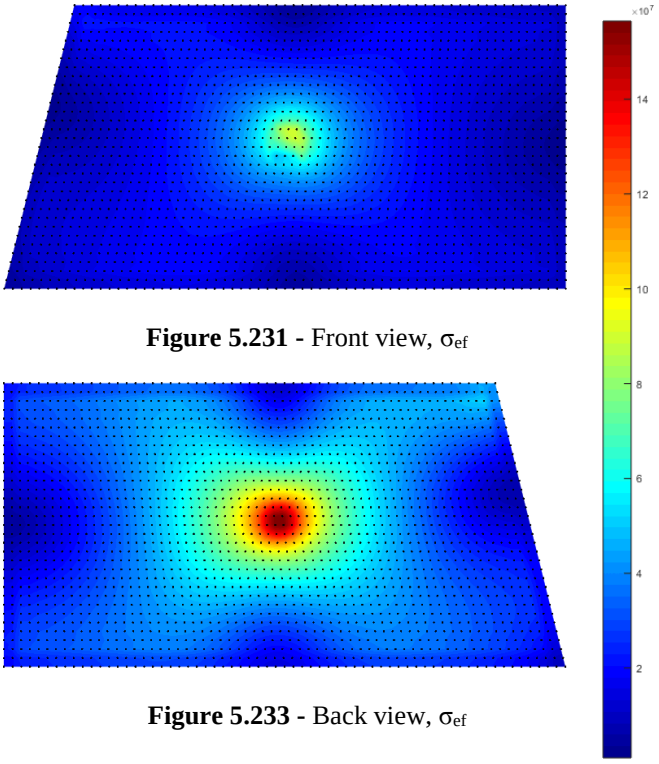

Figure 5.231 - Front view, σ_{ef}

Figure 5.233 - Back view, σ_{ef}

NNRPIM

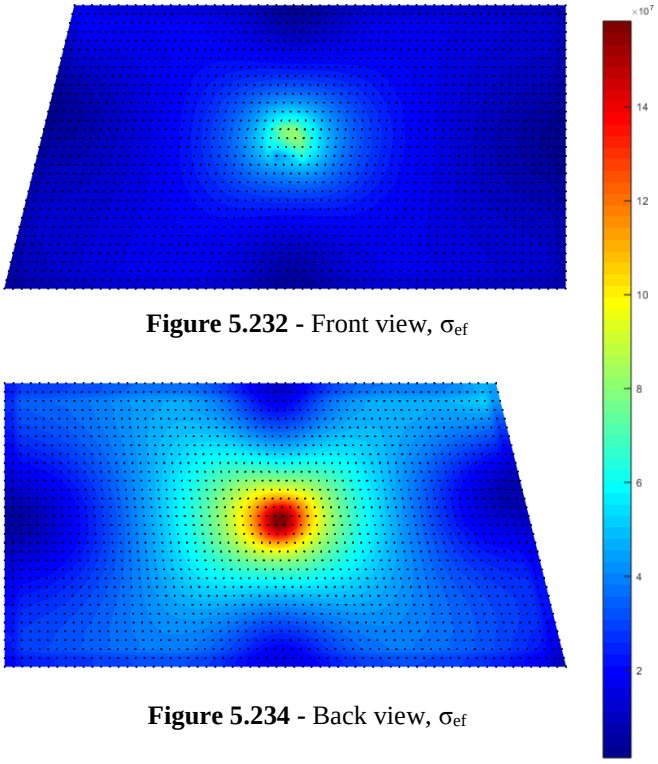

Figure 5.232 - Front view, σ_{ef}

Figure 5.234 - Back view, σ_{ef}

Impact location # 3

The displacement for each impact point was calculated across the thickness and following this, the average of the three nodal displacements discretizing the thickness comes,

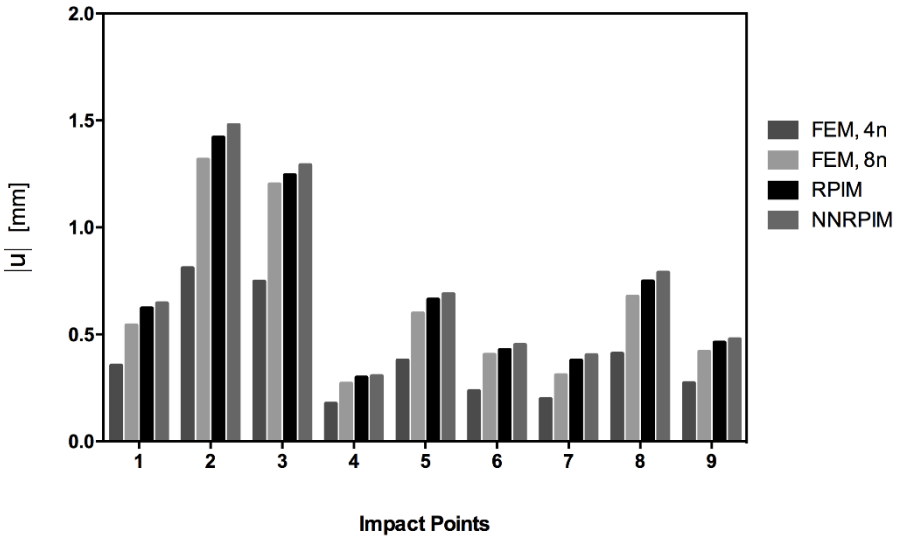

Figure 5.235 - Average nodal displacement along the thickness of each impact location caused by the impact to location 3.

The von Mises stress for each impact point was calculated across the thickness and following this, the average of the three nodal von Mises stresses discretizing the thickness comes,

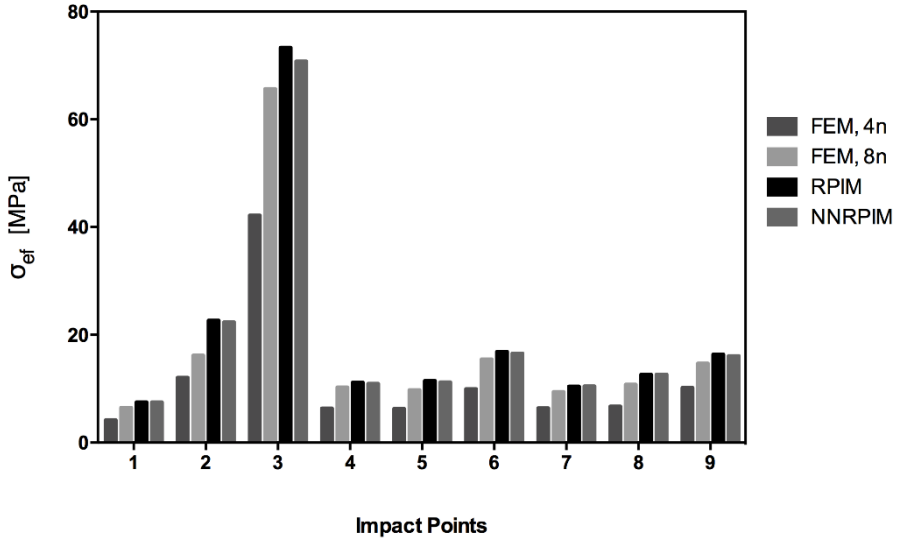

Figure 5.236 - Average nodal stress along the thickness of each impact location caused by the impact to location 3.

The von Mises stress for each node of the ABCD border of the windshield, shown in Figure 5.8, was calculated across the thickness and following this, the average of the three nodal von Mises stresses discretizing the ABCD border thickness comes,

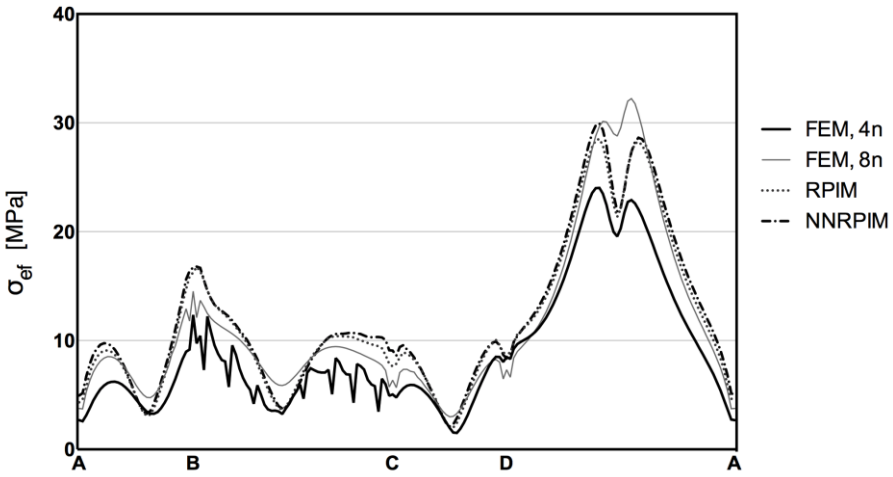

Figure 5.237 - Average nodal stress along the thickness of the clamped section of the windshield caused by the impact to location 3.

The following displacement field was obtained,

FEM, 4n

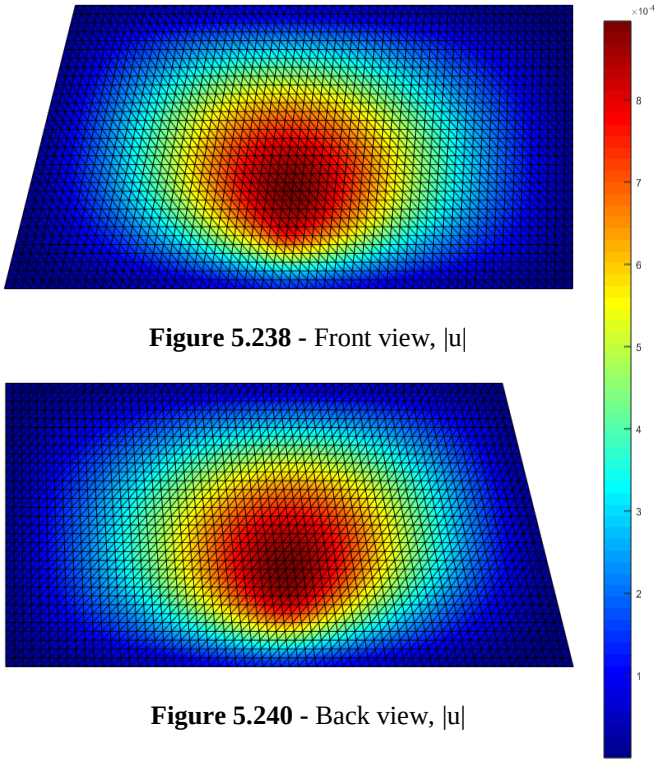

Figure 5.238 - Front view, |u|

Figure 5.240 - Back view, |u|

FEM, 8n

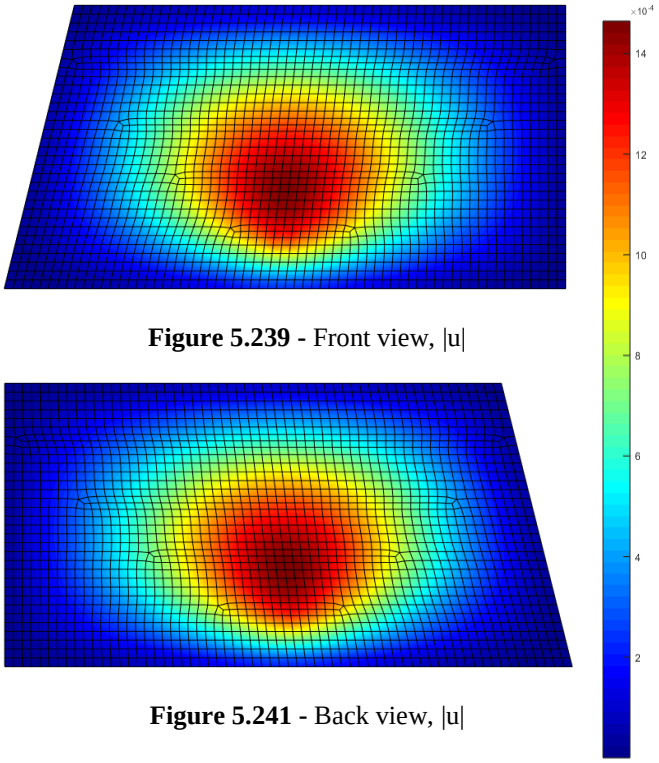

Figure 5.239 - Front view, |u|

Figure 5.241 - Back view, |u|

RPIM

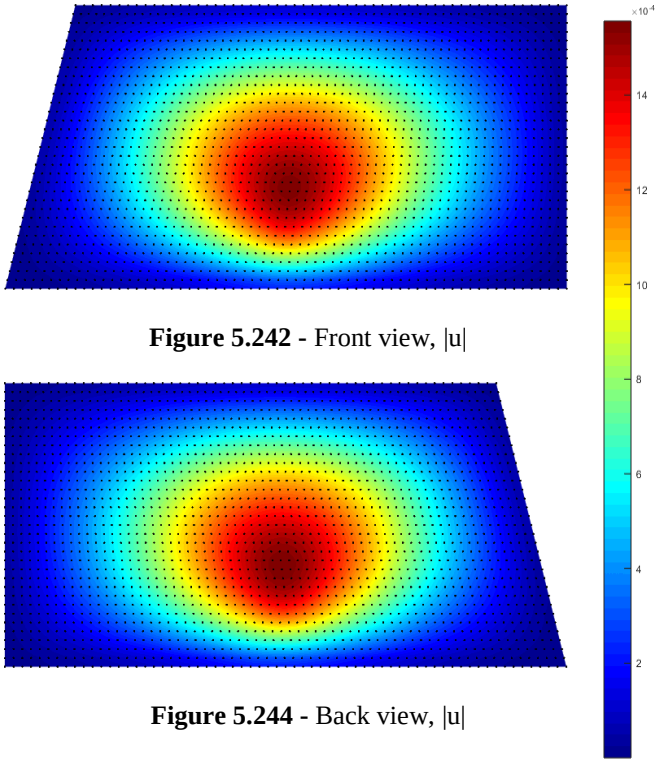

Figure 5.242 - Front view, |u|

Figure 5.244 - Back view, |u|

NNRPIM

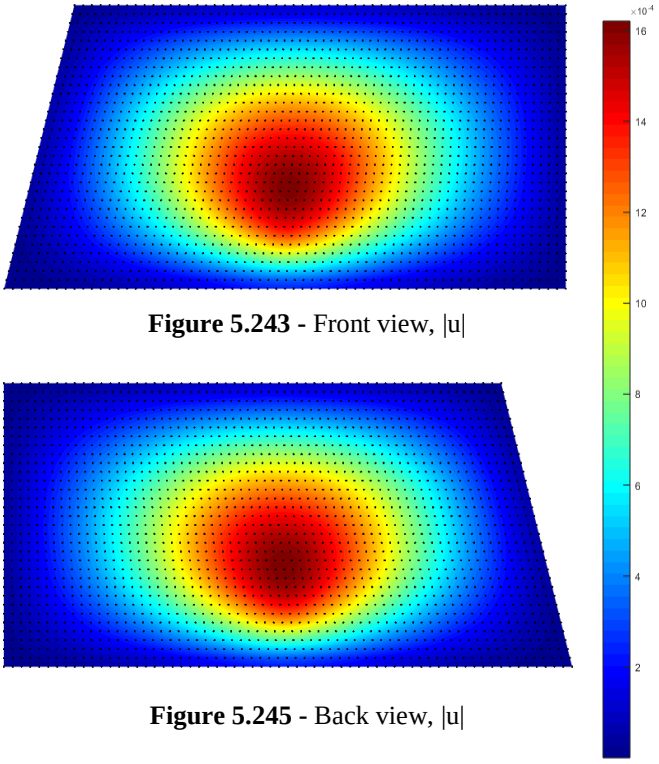

Figure 5.243 - Front view, |u|

Figure 5.245 - Back view, |u|

The following stress field was obtained,

FEM, 4n

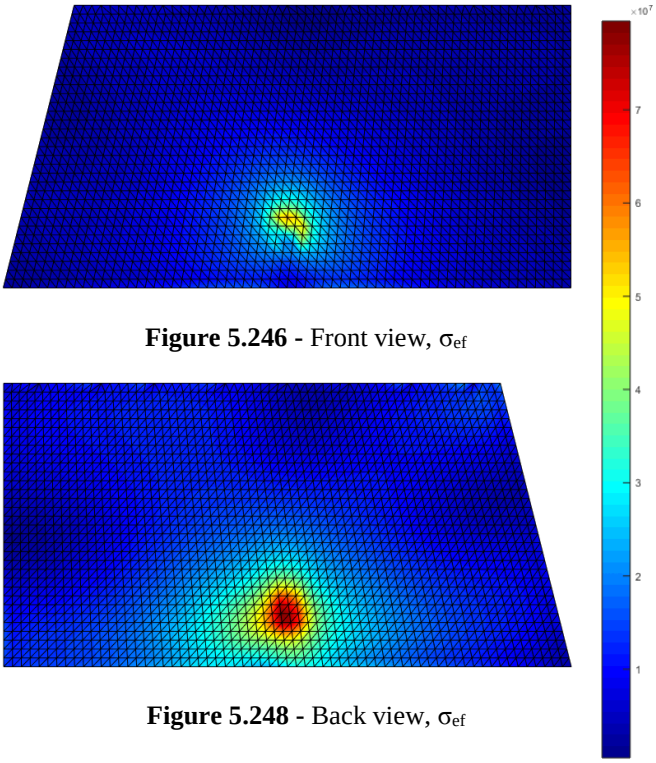

Figure 5.246 - Front view, σ_{ef}

Figure 5.248 - Back view, σ_{ef}

FEM, 8n

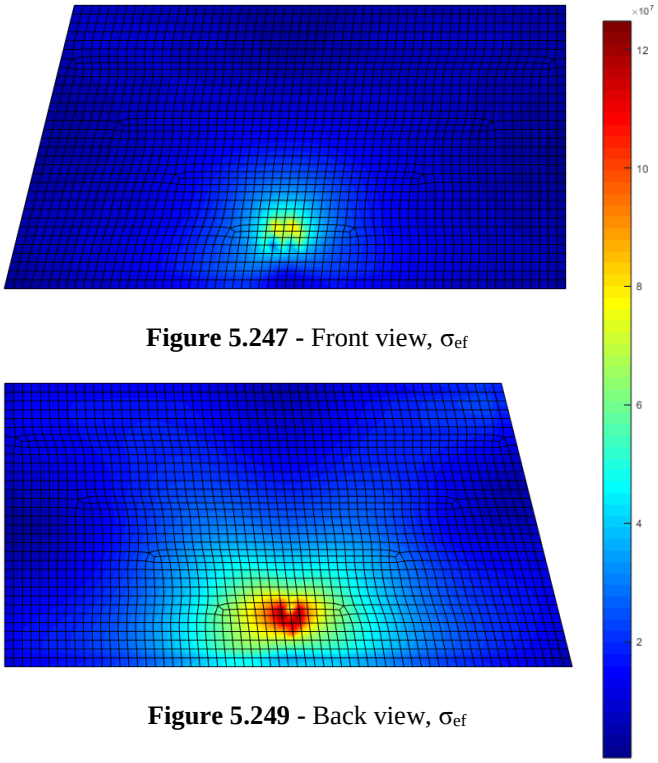

Figure 5.247 - Front view, σ_{ef}

Figure 5.249 - Back view, σ_{ef}

RPIM

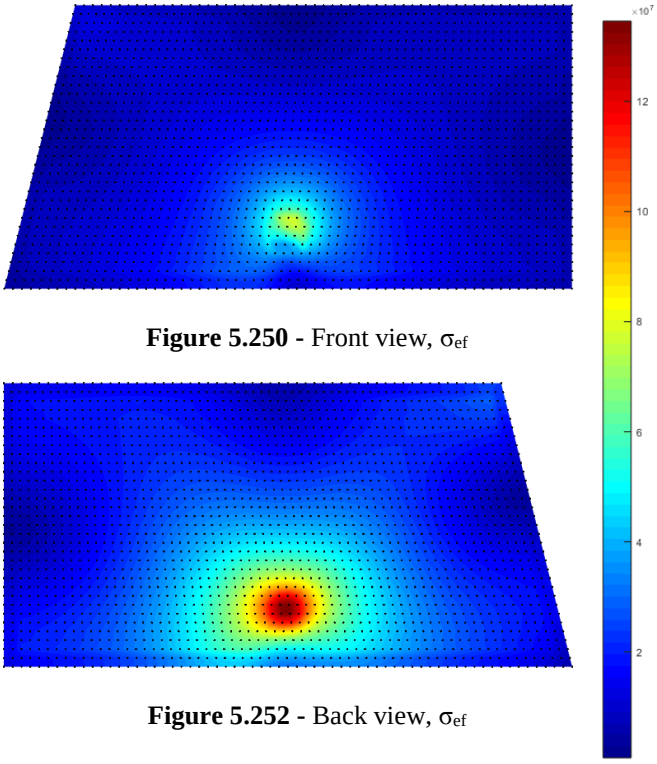

Figure 5.250 - Front view, σ_{ef}

Figure 5.252 - Back view, σ_{ef}

NNRPIM

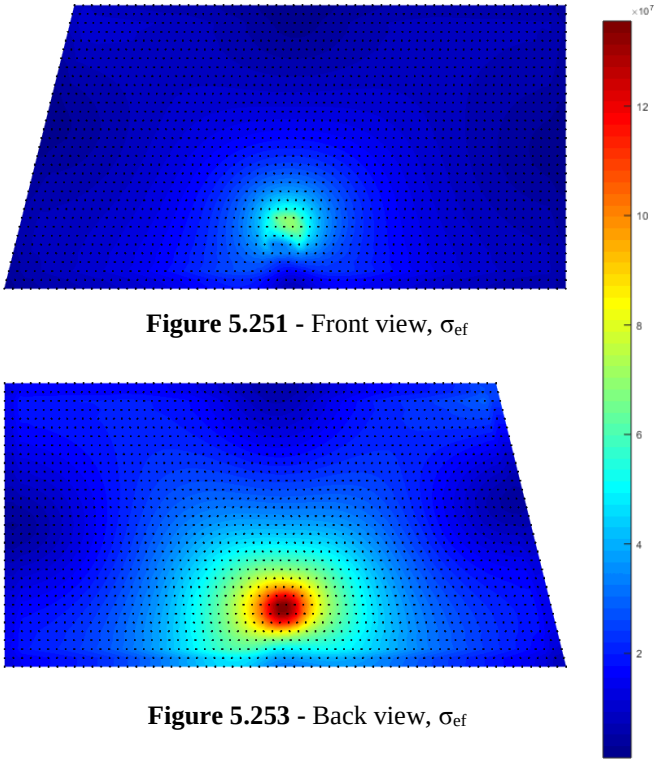

Figure 5.251 - Front view, σ_{ef}

Figure 5.253 - Back view, σ_{ef}

Impact location # 4

The displacement for each impact point was calculated across the thickness and following this, the average of the three nodal displacements discretizing the thickness comes,

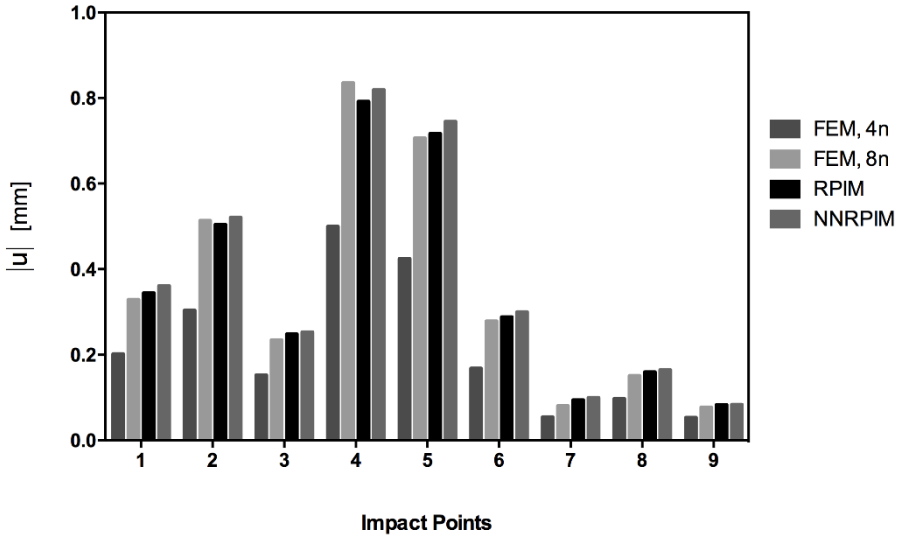

Figure 5.254 - Average nodal displacement along the thickness of each impact location caused by the impact to location 4.

The von Mises stress for each impact point was calculated across the thickness and following this, the average of the three nodal von Mises stresses discretizing the thickness comes,

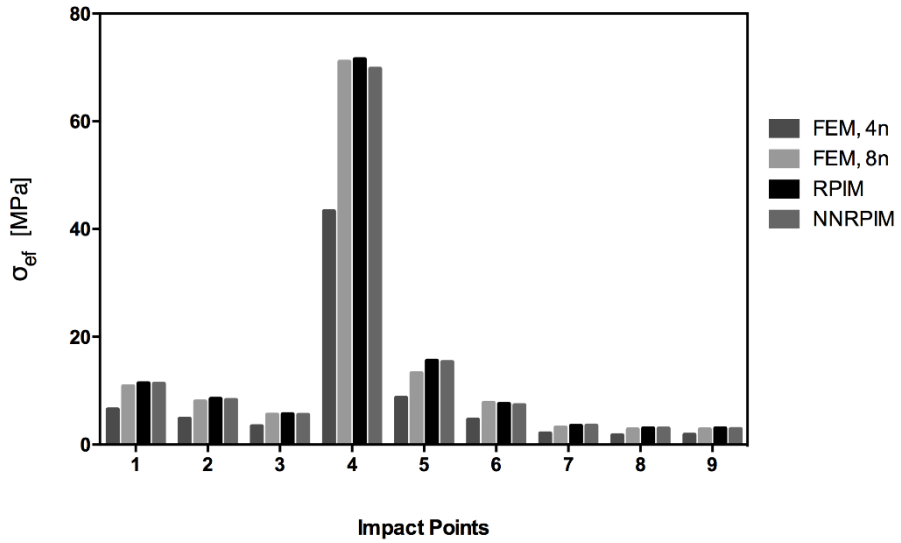

Figure 5.255 - Average nodal stress along the thickness of each impact location caused by the impact to location 4.

The von Mises stress for each node of the ABCD border of the windshield, shown in Figure 5.8, was calculated across the thickness and following this, the average of the three nodal von Mises stresses discretizing the ABCD border thickness comes,

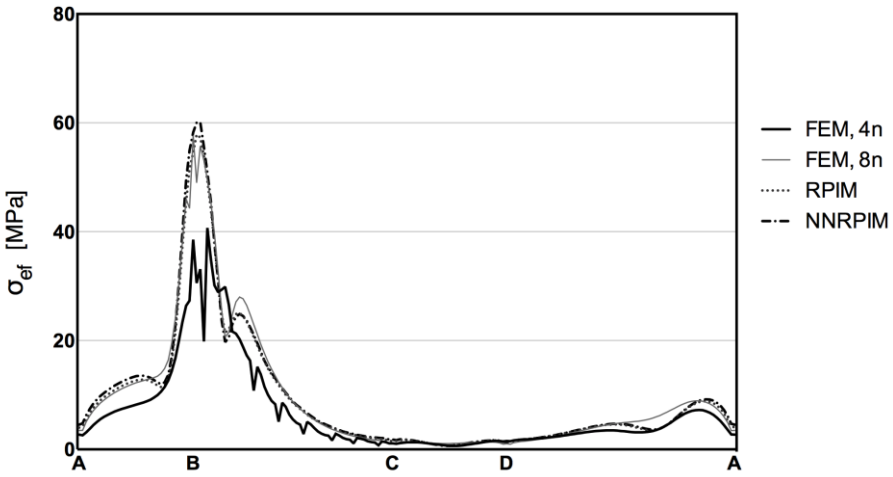

Figure 5.256 - Average nodal stress along the thickness of the clamped section of the windshield caused by the impact to location 4.

The following displacement field was obtained,

FEM, 4n

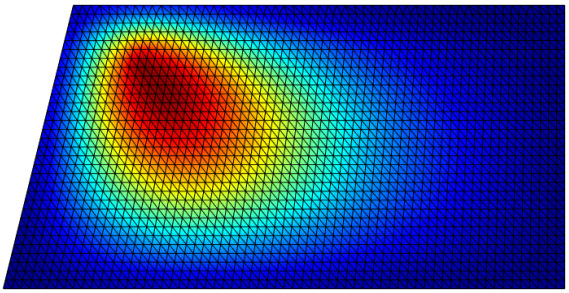

Figure 5.257 - Front view, |u|

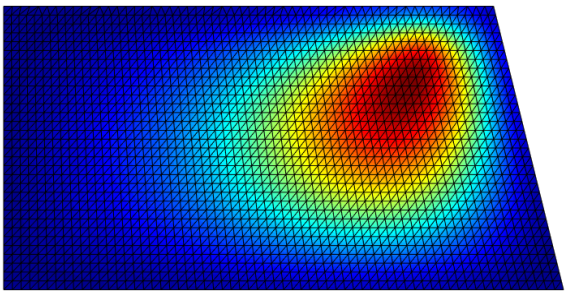

Figure 5.259 - Back view, |u|

FEM, 8n

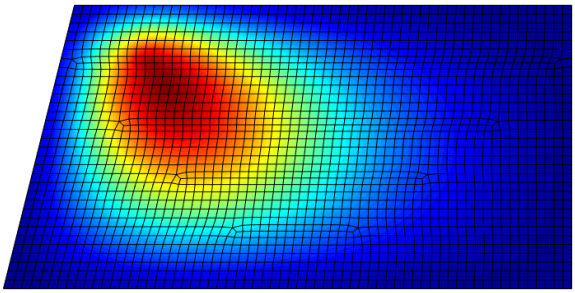

Figure 5.258 - Front view, |u|

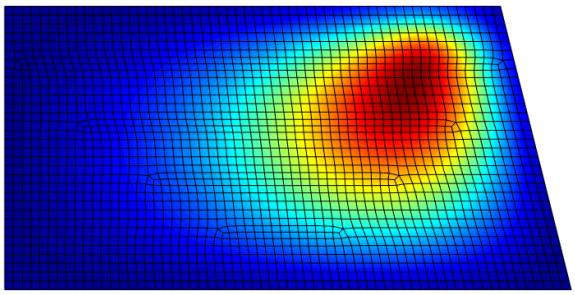

Figure 5.260 - Back view, |u|

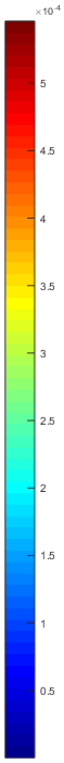

RPIM

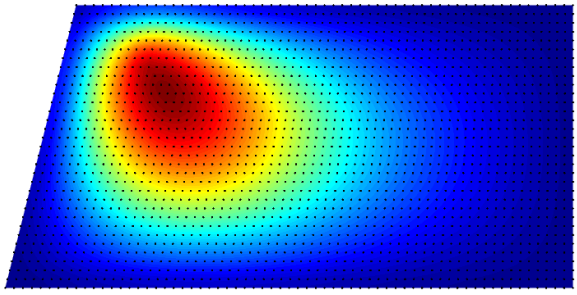

Figure 5.261 - Front view, |u|

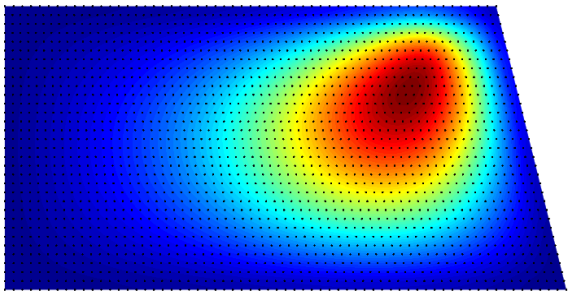

Figure 5.263 - Back view, |u|

NNRPIM

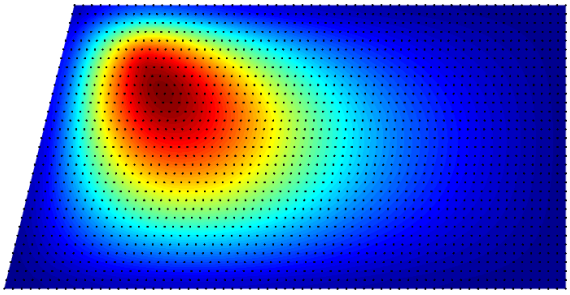

Figure 5.262 - Front view, |u|

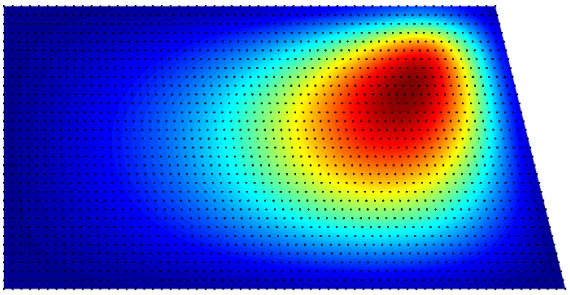

Figure 5.264 - Back view, |u|

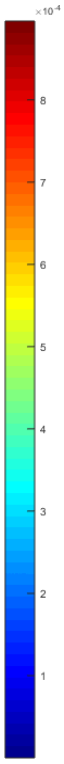

The following stress field was obtained,

FEM, 4n

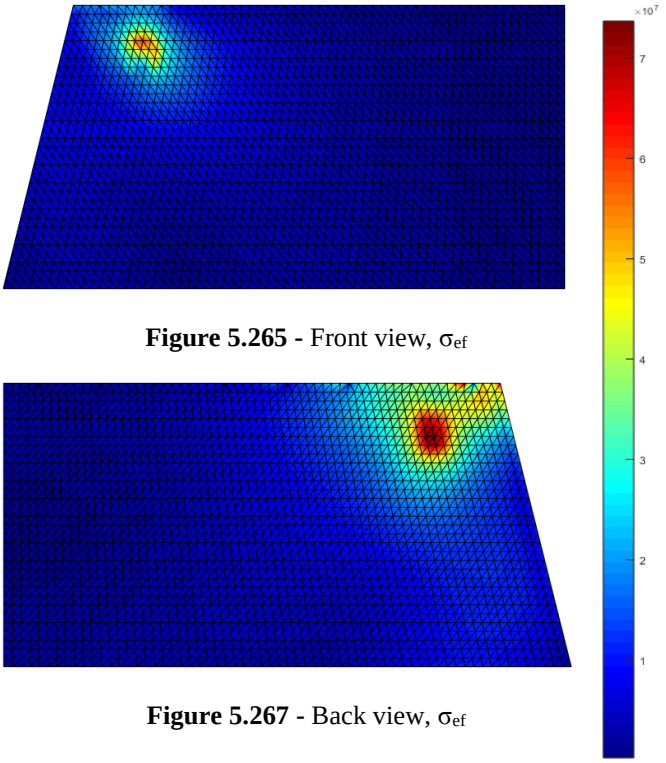

Figure 5.265 - Front view, σ_{ef}

Figure 5.267 - Back view, σ_{ef}

FEM, 8n

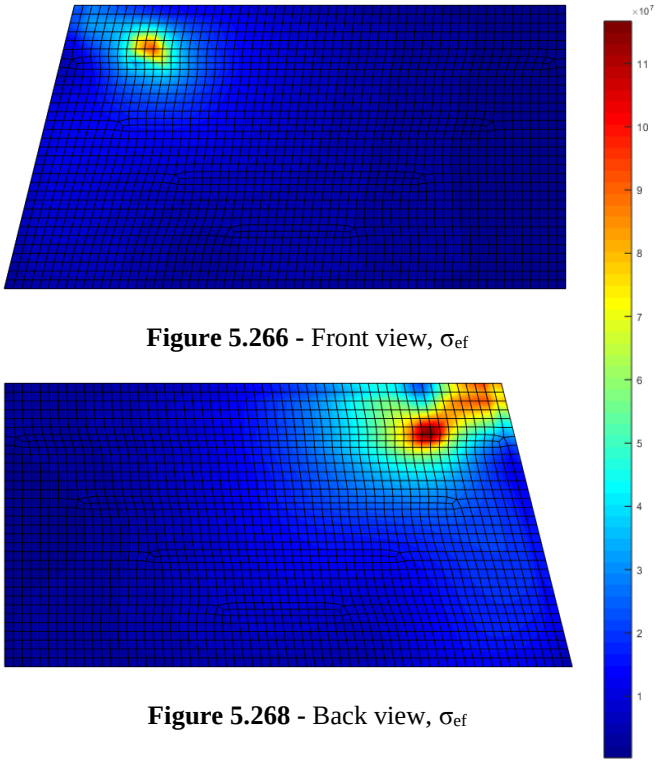

Figure 5.266 - Front view, σ_{ef}

Figure 5.268 - Back view, σ_{ef}

RPIM

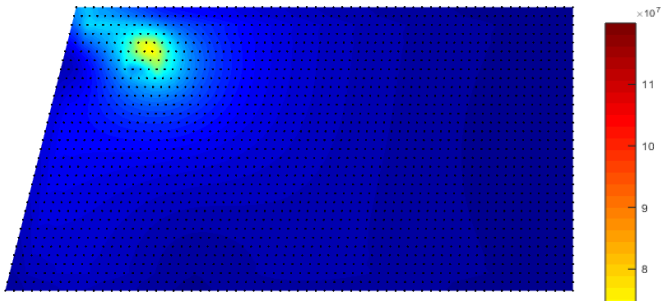

Figure 5.269 - Front view, σ_{ef}

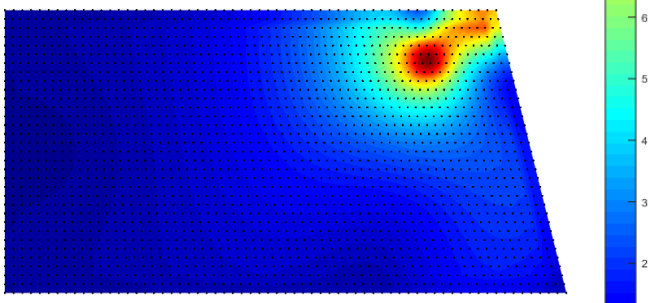

Figure 5.271 - Back view, σ_{ef}

NNRPIM

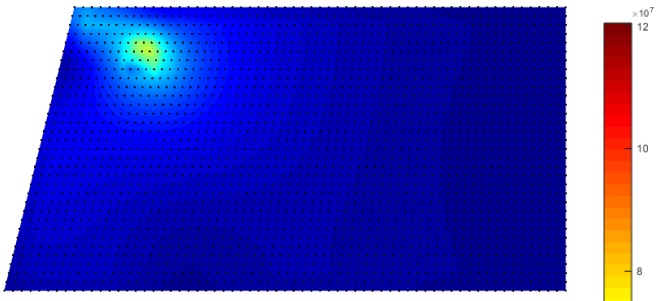

Figure 5.270 - Front view, σ_{ef}

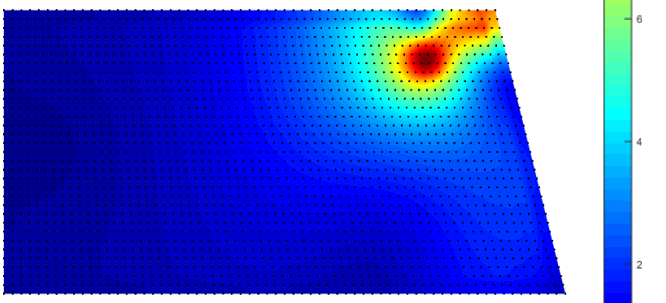

Figure 5.272 - Back view, σ_{ef}

Impact location # 5

The displacement for each impact point was calculated across the thickness and following this, the average of the three nodal displacements discretizing the thickness comes,

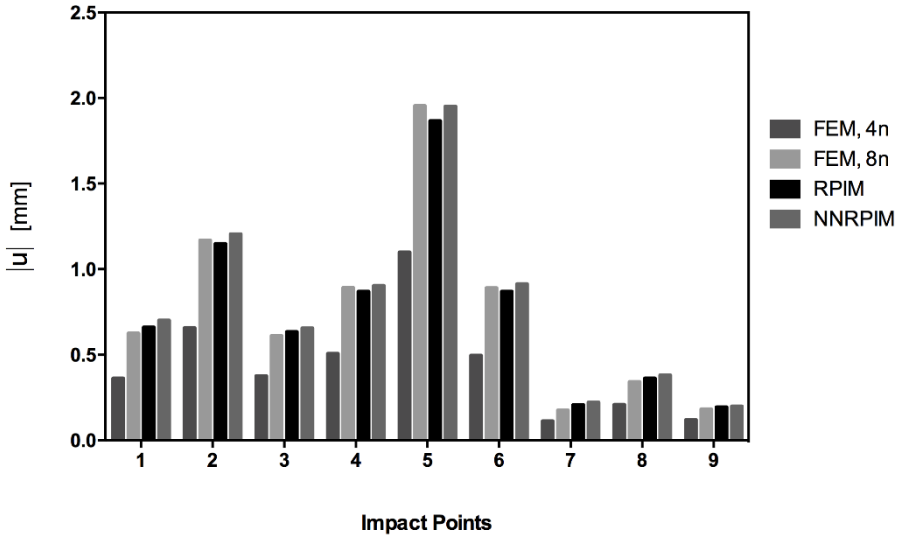

Figure 5.273 - Average nodal displacement along the thickness of each impact location caused by the impact to location 5.

The von Mises stress for each impact point was calculated across the thickness and following this, the average of the three nodal von Mises stresses discretizing the thickness comes,

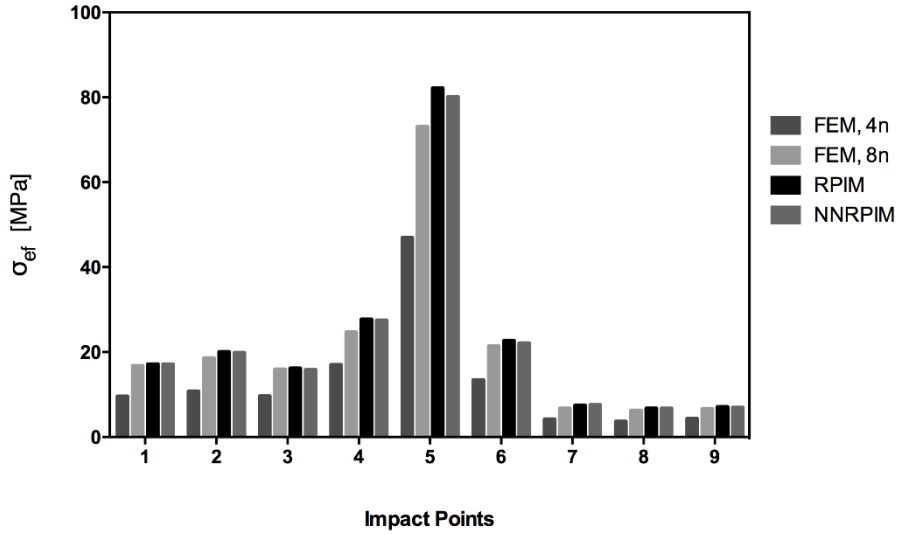

Figure 5.274 - Average nodal stress along the thickness of each impact location caused by the impact to location 5.

The von Mises stress for each node of the ABCD border of the windshield, shown in Figure 5.8, was calculated across the thickness and following this, the average of the three nodal von Mises stresses discretizing the ABCD border thickness comes,

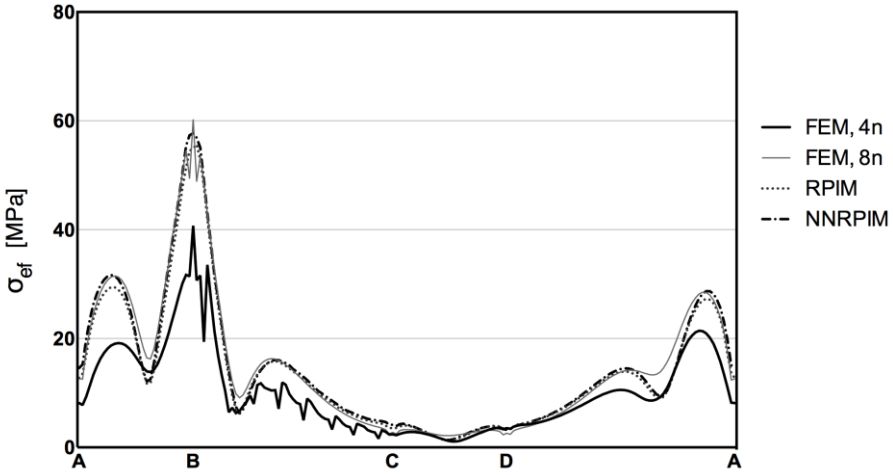

Figure 5.275 - Average nodal stress along the thickness of the clamped section of the windshield caused by the impact to location 5.

The following displacement field was obtained,

FEM, 4n

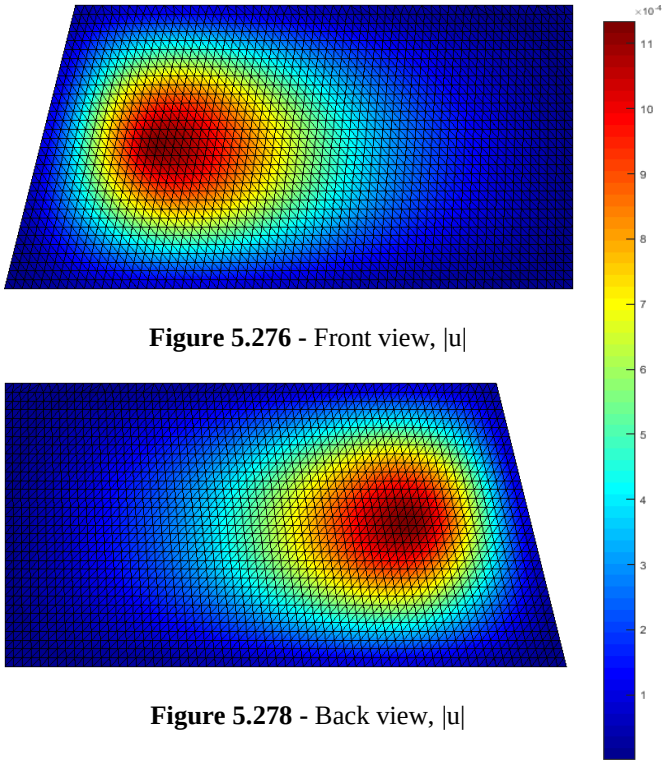

Figure 5.276 - Front view, |u|

Figure 5.278 - Back view, |u|

FEM, 8n

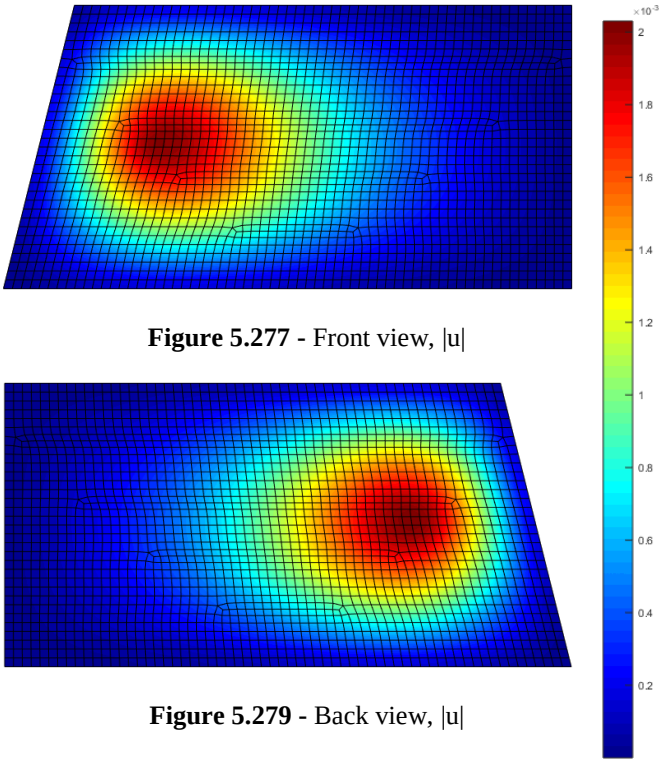

Figure 5.277 - Front view, |u|

Figure 5.279 - Back view, |u|

RPIM

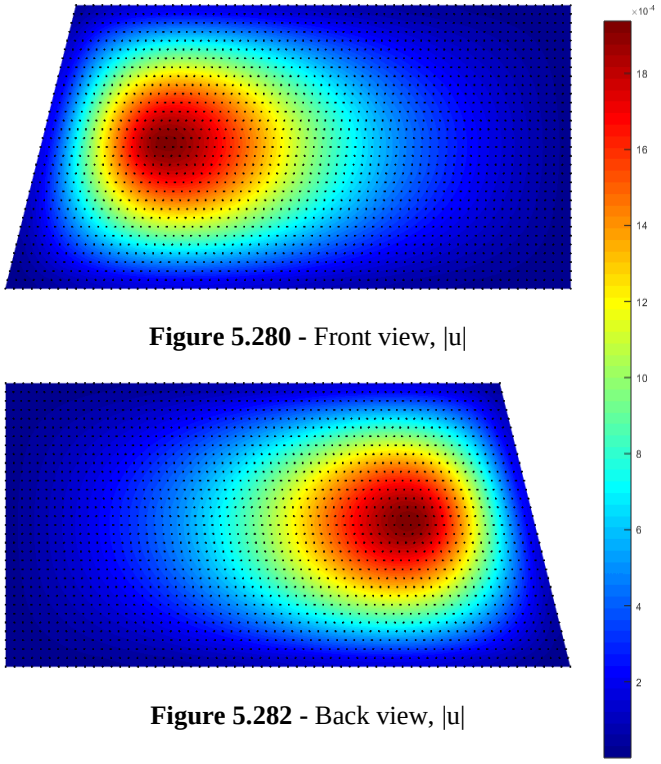

Figure 5.280 - Front view, |u|

Figure 5.282 - Back view, |u|

NNRPIM

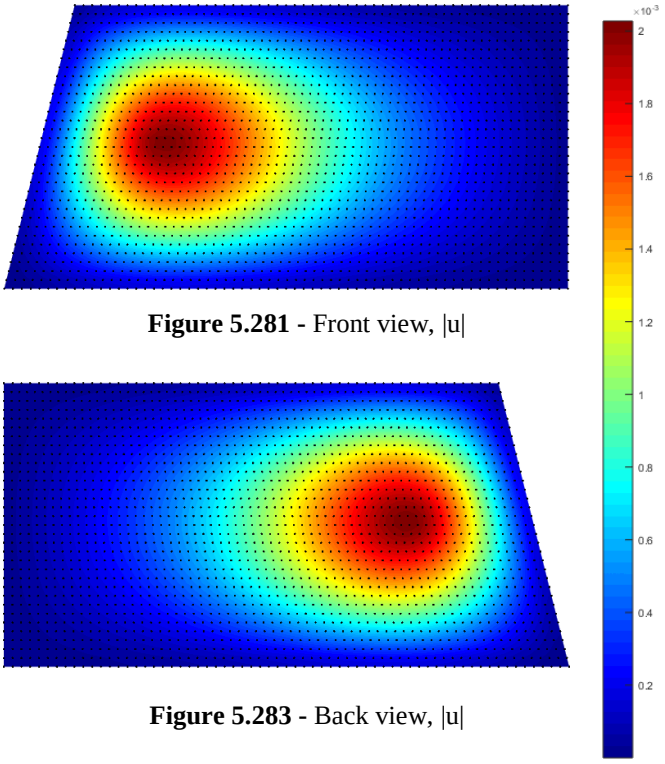

Figure 5.281 - Front view, |u|

Figure 5.283 - Back view, |u|

The following stress field was obtained,

FEM, 4n

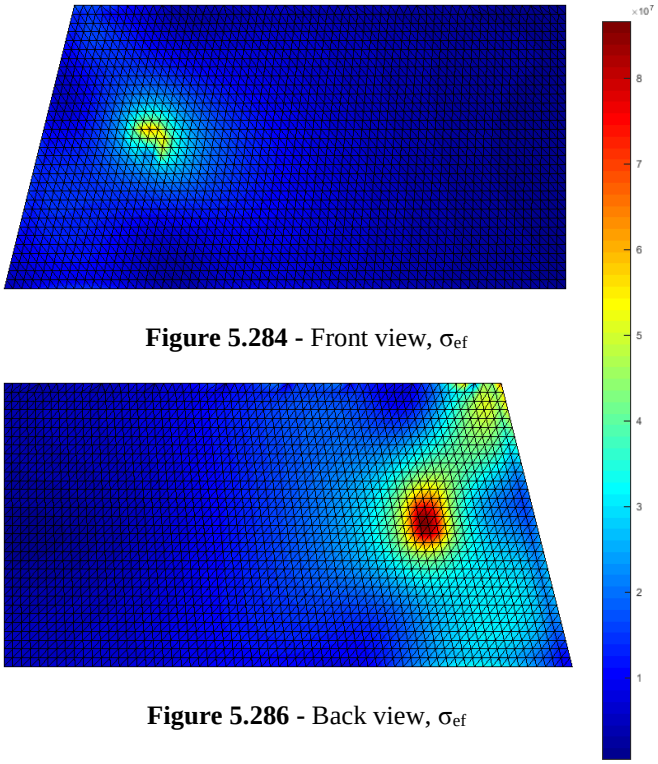

Figure 5.284 - Front view, σ_{ef}

Figure 5.286 - Back view, σ_{ef}

FEM, 8n

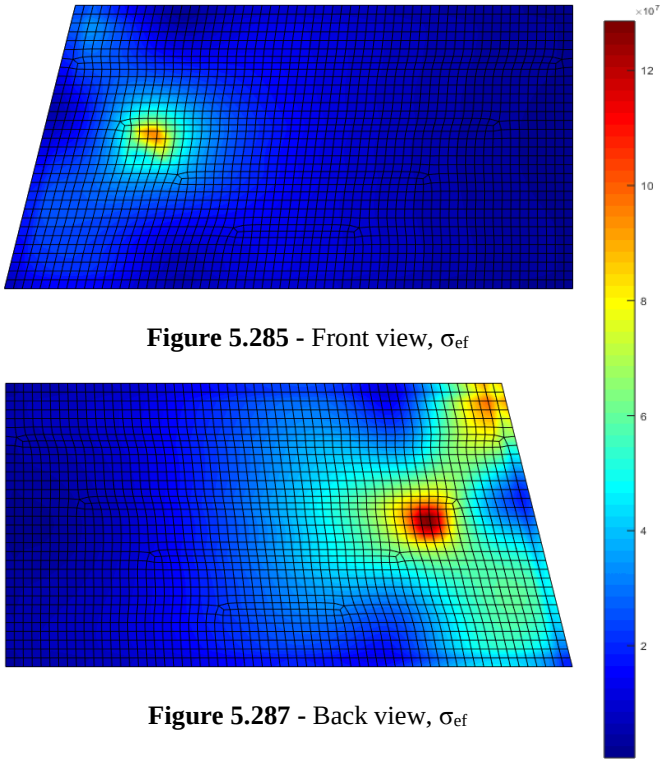

Figure 5.285 - Front view, σ_{ef}

Figure 5.287 - Back view, σ_{ef}

RPIM

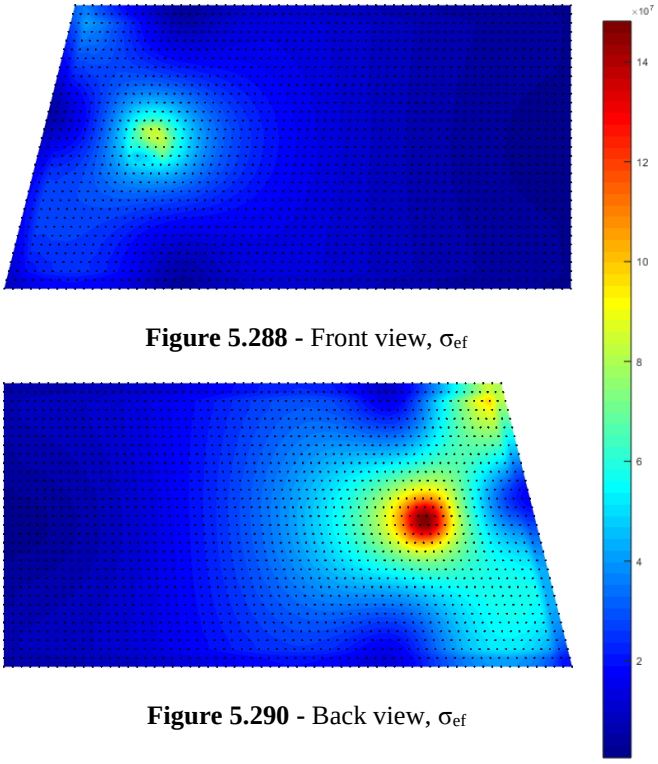

Figure 5.288 - Front view, σ_{ef}

Figure 5.290 - Back view, σ_{ef}

NNRPIM

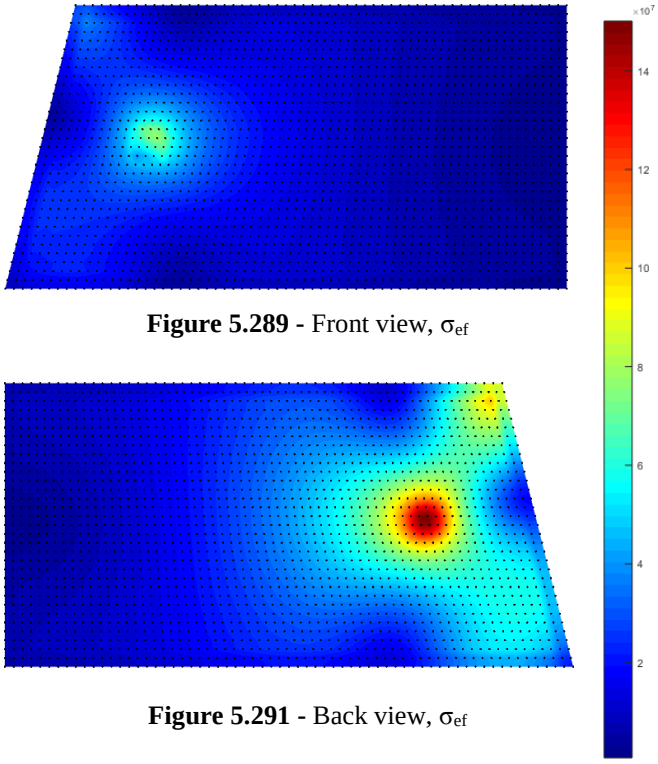

Figure 5.289 - Front view, σ_{ef}

Figure 5.291 - Back view, σ_{ef}

Impact location # 6

The displacement for each impact point was calculated across the thickness and following this, the average of the three nodal displacements discretizing the thickness comes,

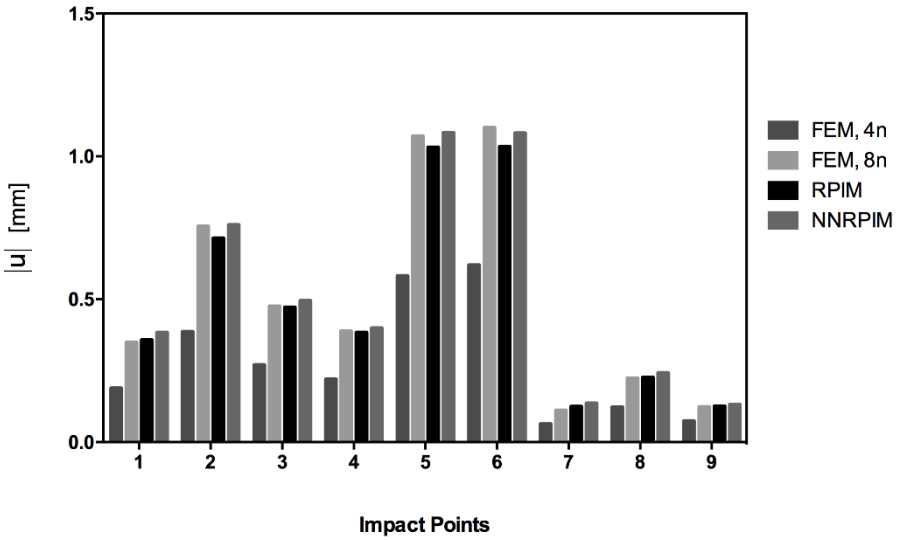

Figure 5.292 - Average nodal displacement along the thickness of each impact location caused by the impact to location 6.

The von Mises stress for each impact point was calculated across the thickness and following this, the average of the three nodal von Mises stresses discretizing the thickness comes,

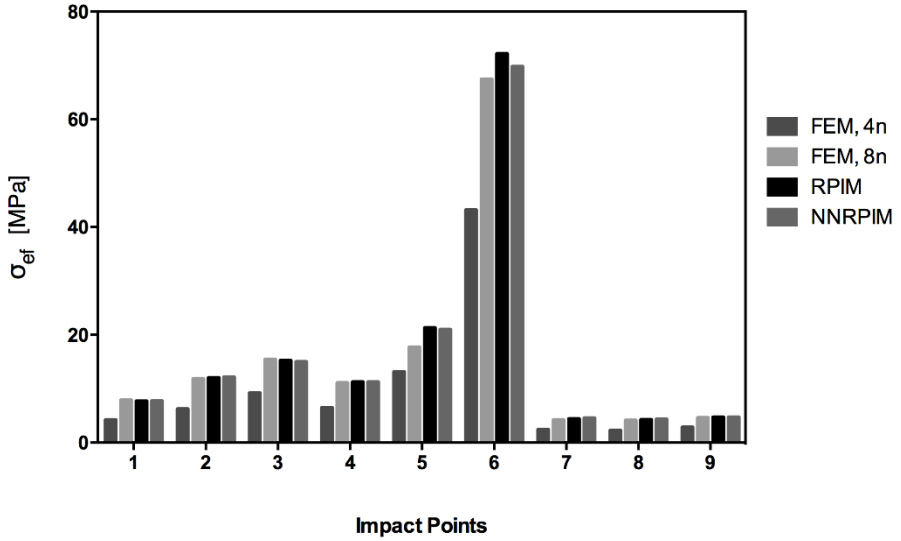

Figure 5.293 - Average nodal stress along the thickness of each impact location caused by the impact to location 6.

The von Mises stress for each node of the ABCD border of the windshield, shown in Figure 5.8, was calculated across the thickness and following this, the average of the three nodal von Mises stresses discretizing the ABCD border thickness comes,

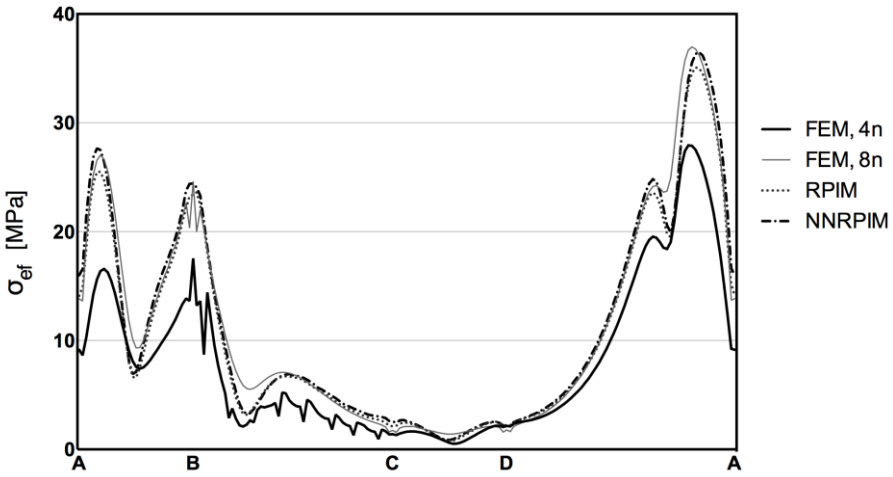

Figure 5.294 - Average nodal stress along the thickness of the clamped section of the windshield caused by the impact to location 6.

The following displacement field was obtained,

FEM, 4n

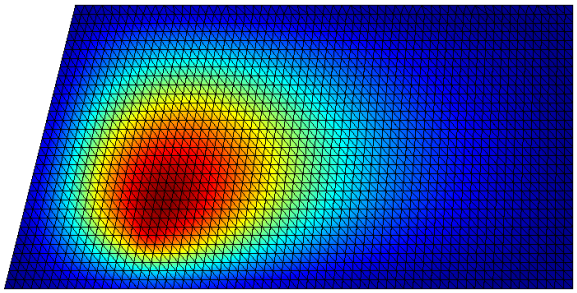

Figure 5.295 - Front view, |u|

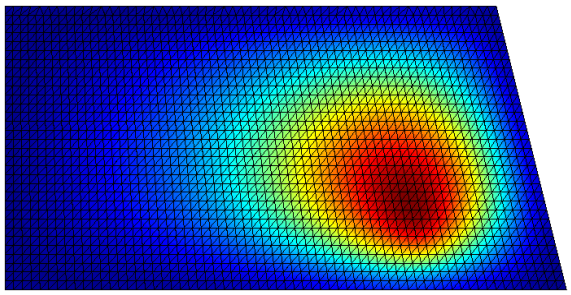

Figure 5.297 - Back view, |u|

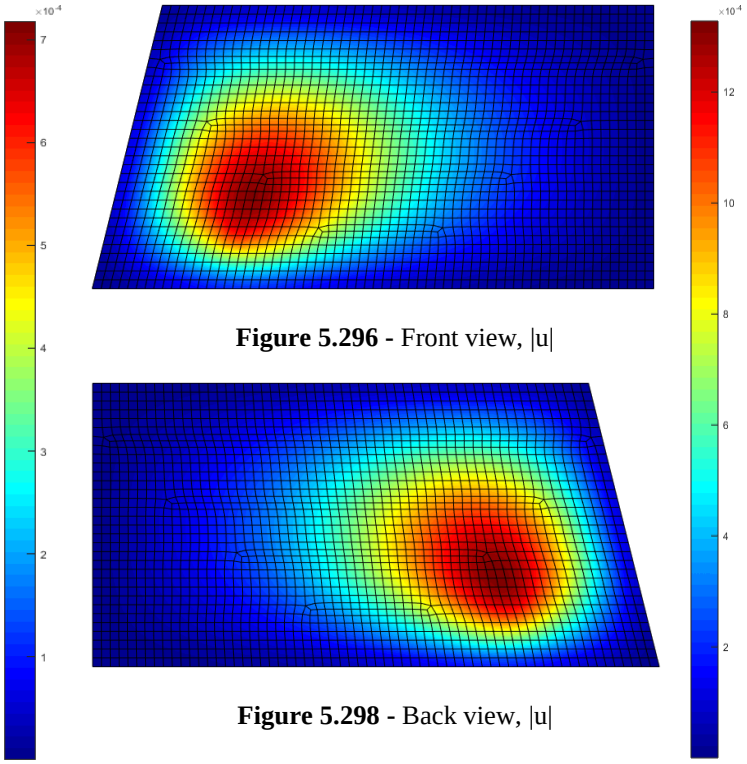

FEM, 8n

Figure 5.296 - Front view, |u|

Figure 5.298 - Back view, |u|

RPIM

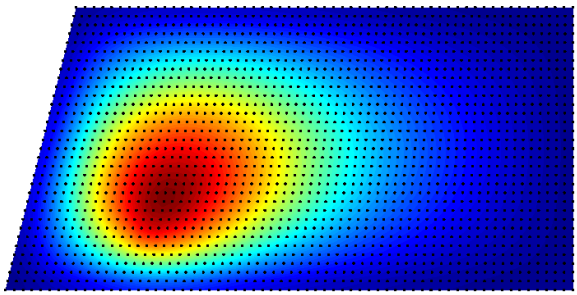

Figure 5.299 - Front view, |u|

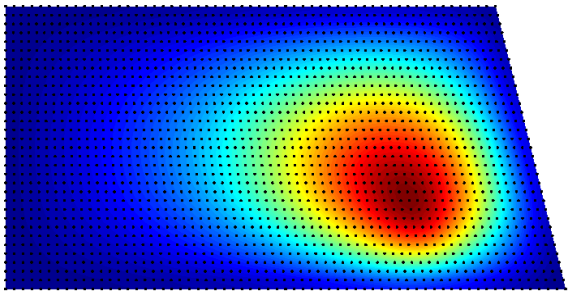

Figure 5.301 - Back view, |u|

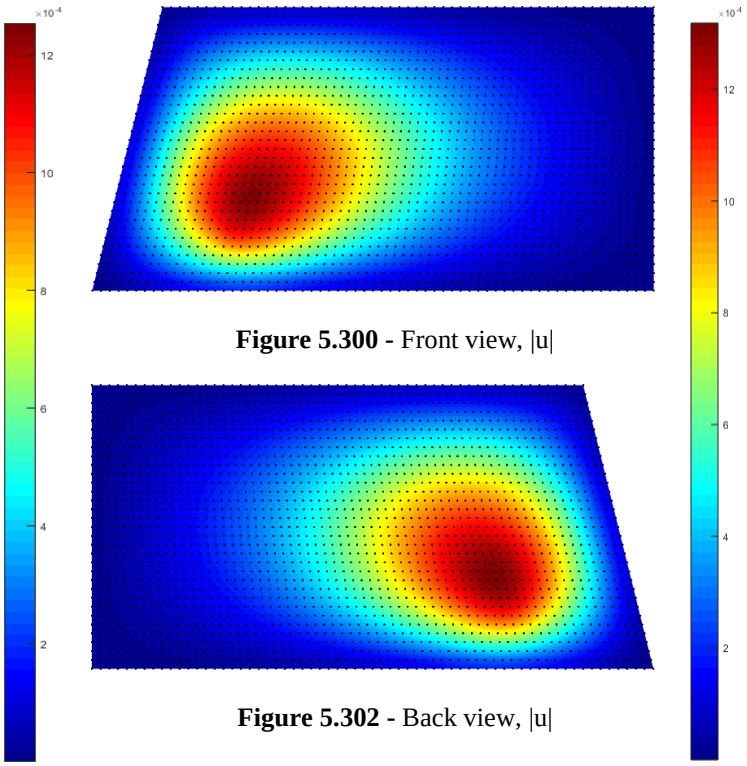

NNRPIM

Figure 5.300 - Front view, |u|

Figure 5.302 - Back view, |u|

The following stress field was obtained,

FEM, 4n

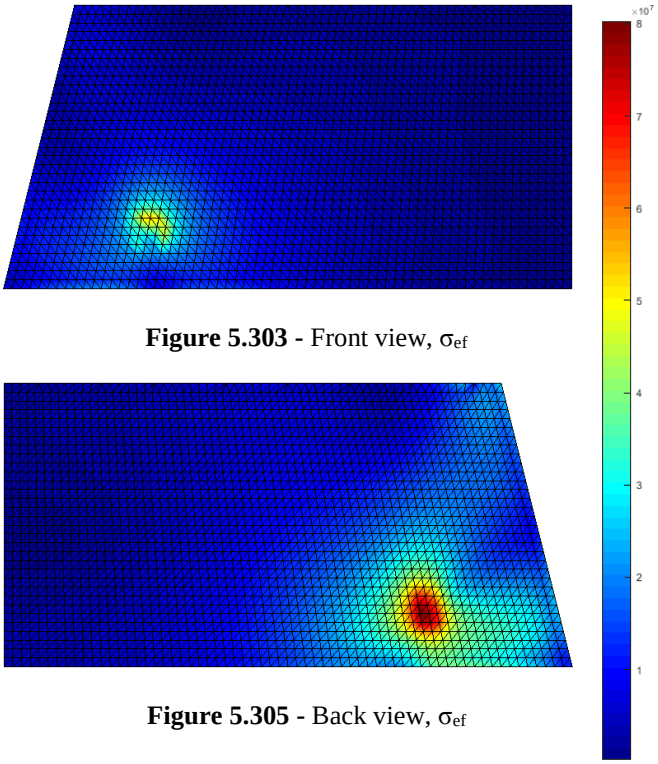

Figure 5.303 - Front view, σ_{ef}

Figure 5.305 - Back view, σ_{ef}

FEM, 8n

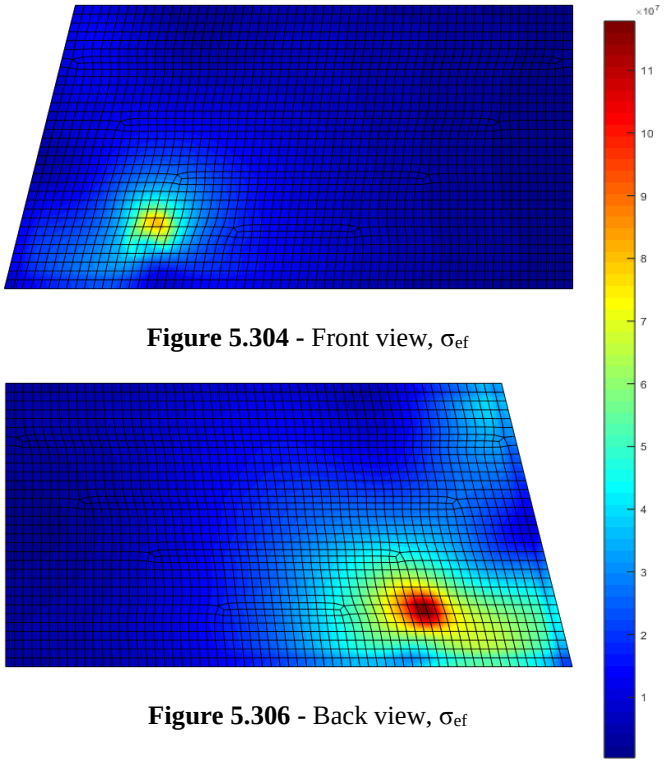

Figure 5.304 - Front view, σ_{ef}

Figure 5.306 - Back view, σ_{ef}

RPIM

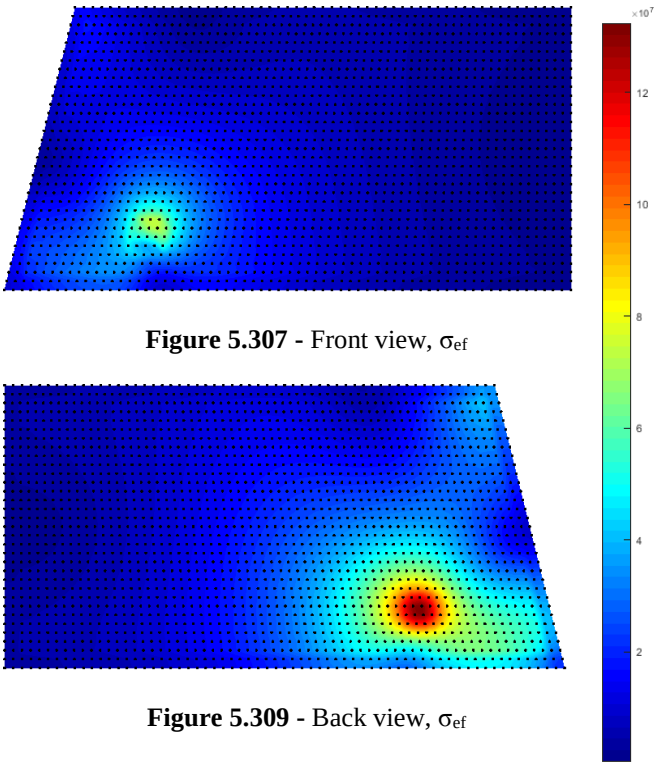

Figure 5.307 - Front view, σ_{ef}

Figure 5.309 - Back view, σ_{ef}

NNRPIM

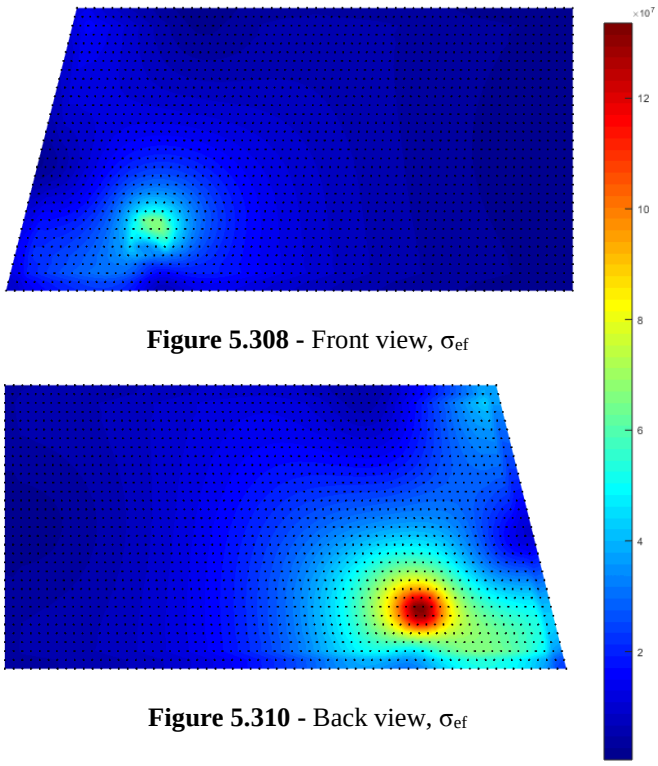

Figure 5.308 - Front view, σ_{ef}

Figure 5.310 - Back view, σ_{ef}

Impact location # 7

The displacement for each impact point was calculated across the thickness and following this, the average of the three nodal displacements discretizing the thickness comes,

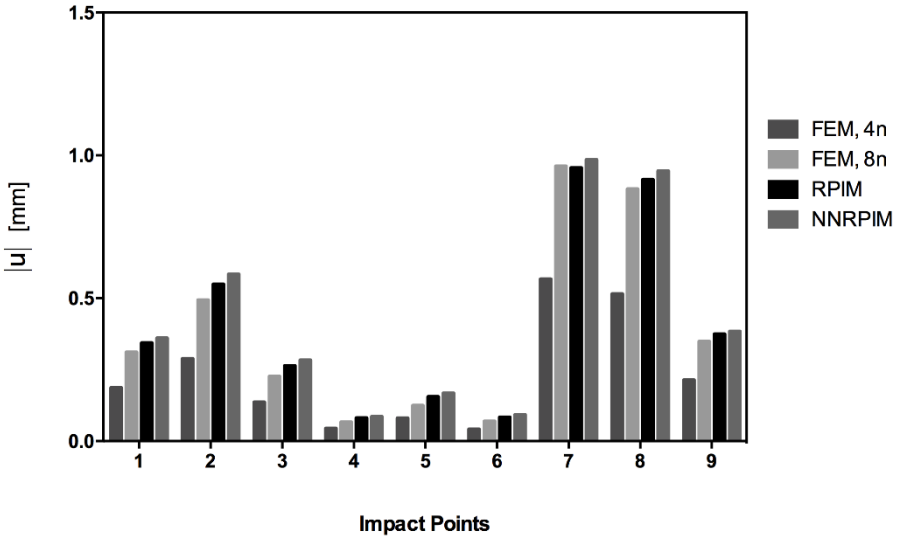

Figure 5.311 - Average nodal displacement along the thickness of each impact location caused by the impact to location 7.

The von Mises stress for each impact point was calculated across the thickness and following this, the average of the three nodal von Mises stresses discretizing the thickness comes,

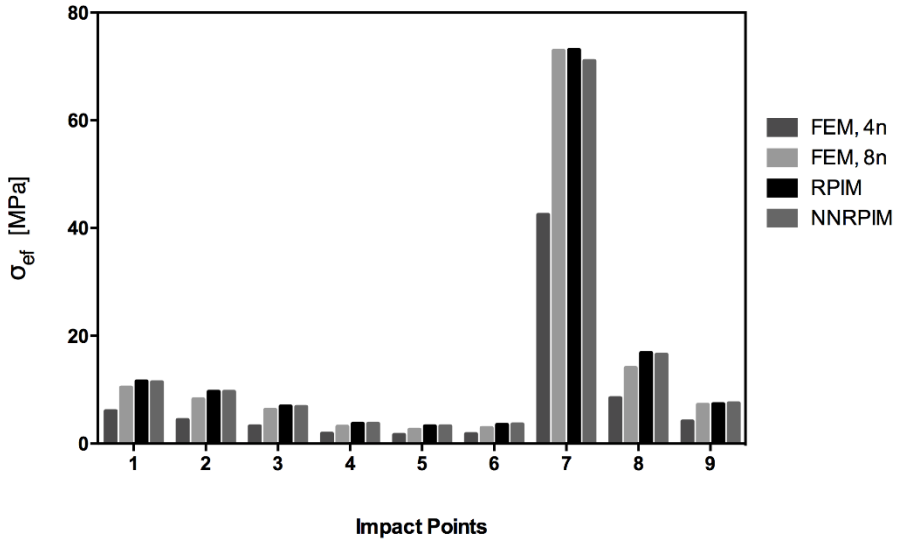

Figure 5.312 - Average nodal stress along the thickness of each impact location caused by the impact to location 7.

The von Mises stress for each node of the ABCD border of the windshield, shown in Figure 5.8, was calculated across the thickness and following this, the average of the three nodal von Mises stresses discretizing the ABCD border thickness comes,

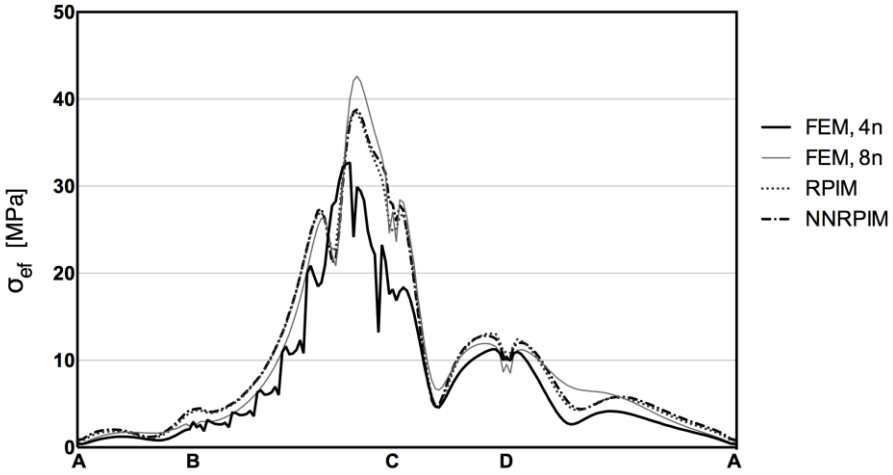

Figure 5.313 - Average nodal stress along the thickness of the clamped section of the windshield caused by the impact to location 7.

The following displacement field was obtained,

FEM, 4n

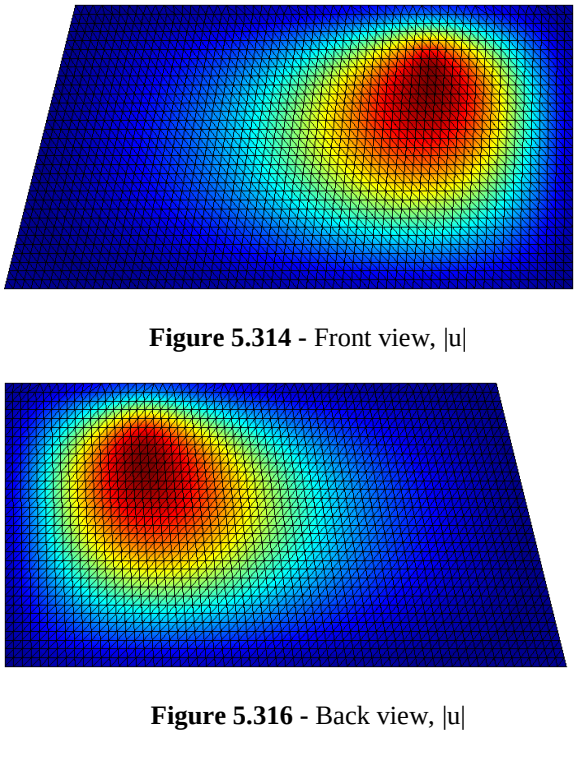

Figure 5.314 - Front view, |u|

Figure 5.316 - Back view, |u|

FEM, 8n

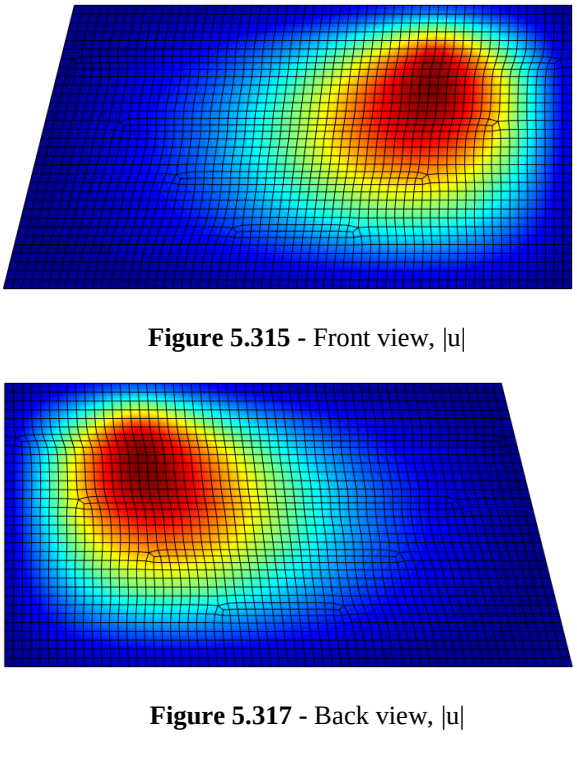

Figure 5.315 - Front view, |u|

Figure 5.317 - Back view, |u|

RPIM

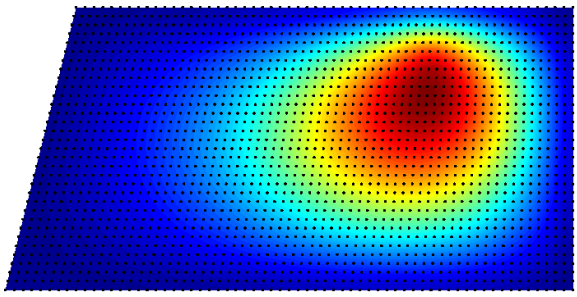

Figure 5.318 - Front view, |u|

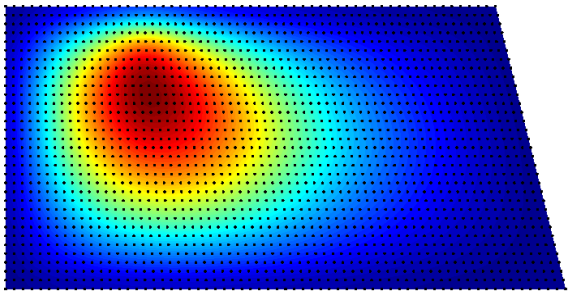

Figure 5.320 - Back view, |u|

NNRPIM

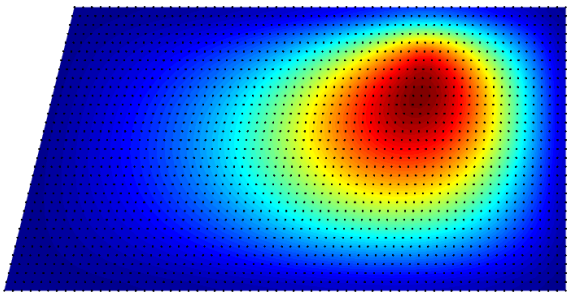

Figure 5.319 - Front view, |u|

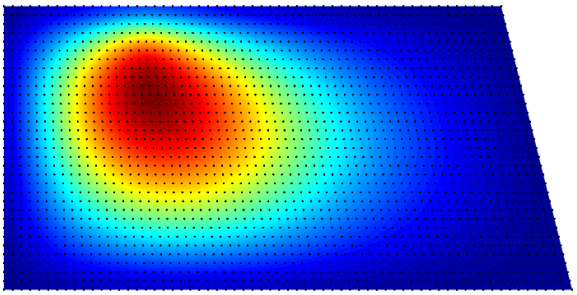

Figure 5.321 - Back view, |u|

The following stress field was obtained,

FEM, 4n

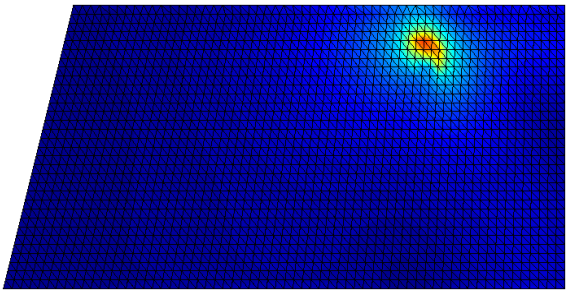

Figure 5.322 - Front view, σ_{ef}

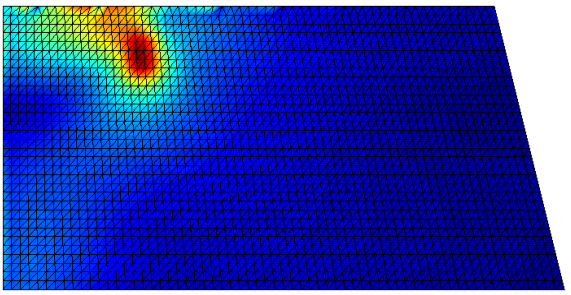

Figure 5.324 - Back view, σ_{ef}

FEM, 8n

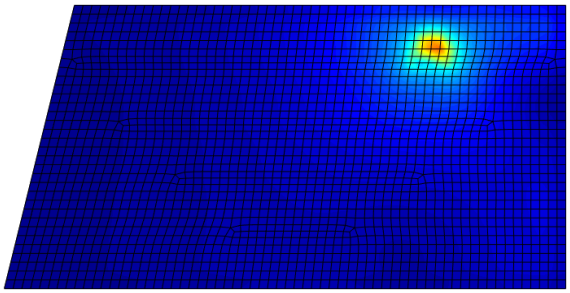

Figure 5.323 - Front view, σ_{ef}

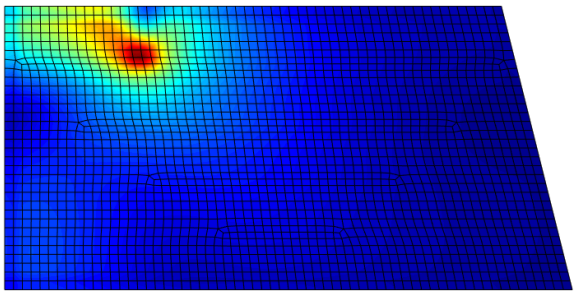

Figure 5.325 - Back view, σ_{ef}

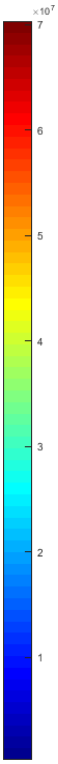

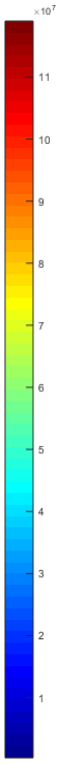

RPIM

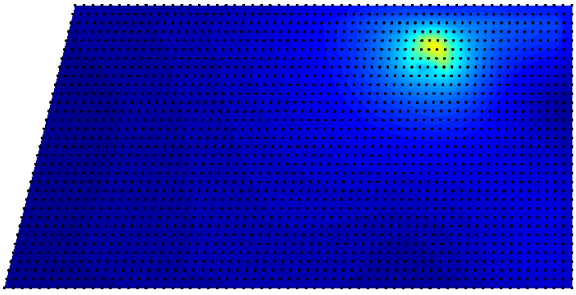

Figure 5.326 - Front view, σ_{ef}

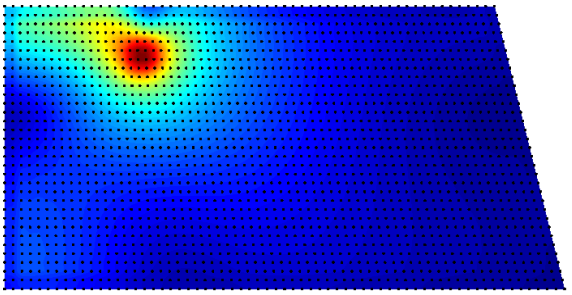

Figure 5.328 - Back view, σ_{ef}

NNRPIM

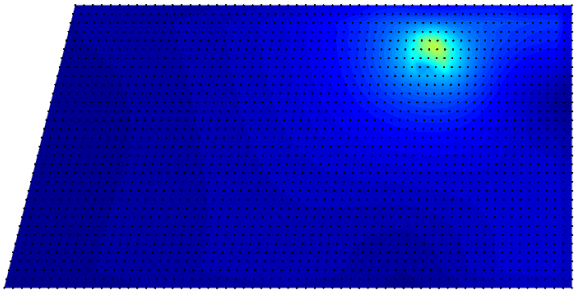

Figure 5.327 - Front view, σ_{ef}

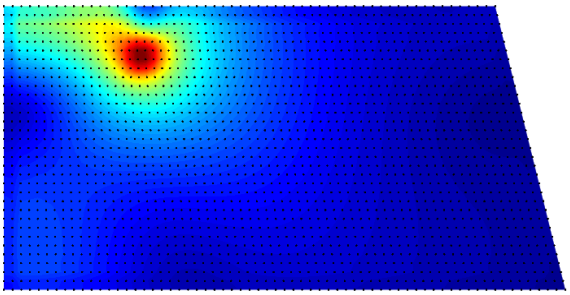

Figure 5.329 - Back view, σ_{ef}

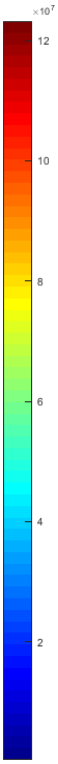

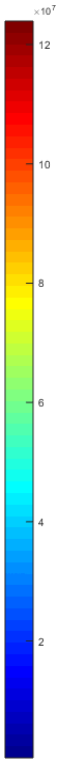

Impact location # 8

The displacement for each impact point was calculated across the thickness and following this, the average of the three nodal displacements discretizing the thickness comes,

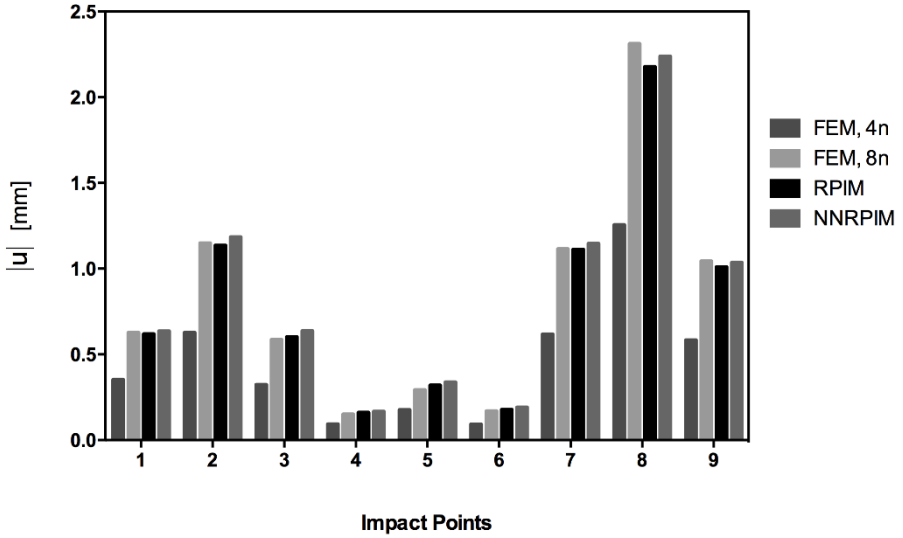

Figure 5.330 - Average nodal displacement along the thickness of each impact location caused by the impact to location 8.

The von Mises stress for each impact point was calculated across the thickness and following this, the average of the three nodal von Mises stresses discretizing the thickness comes,

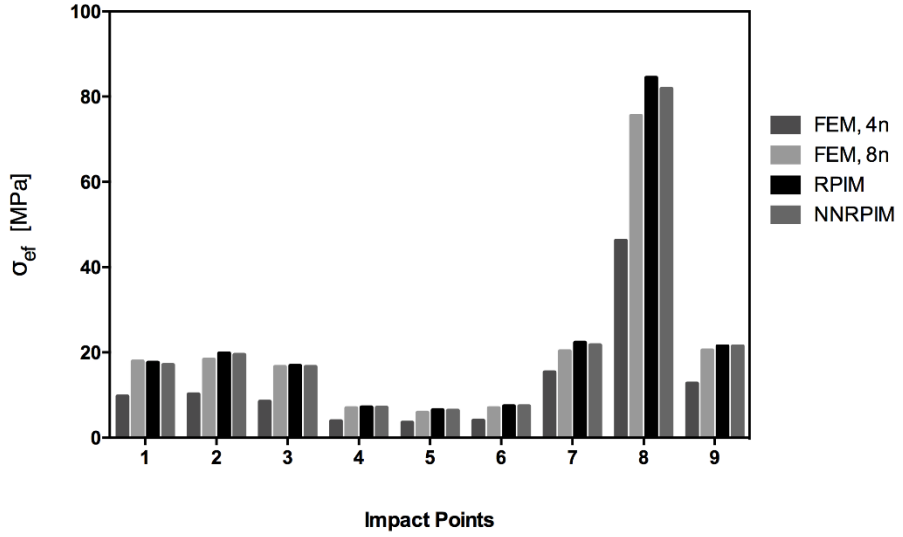

Figure 5.331 - Average nodal stress along the thickness of each impact location caused by the impact to location 8.

The von Mises stress for each node of the ABCD border of the windshield, shown in Figure 5.8, was calculated across the thickness and following this, the average of the three nodal von Mises stresses discretizing the ABCD border thickness comes,

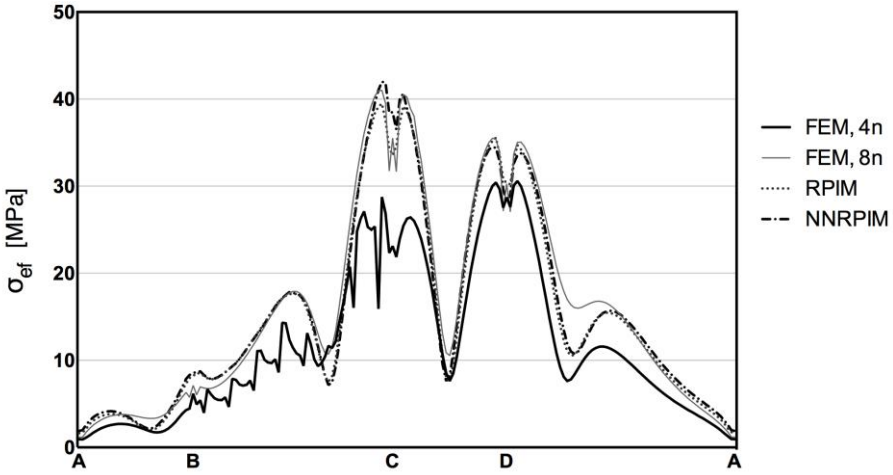

Figure 5.332 - Average nodal stress along the thickness of the clamped section of the windshield caused by the impact to location 8.

The following displacement field was obtained,

FEM, 4n

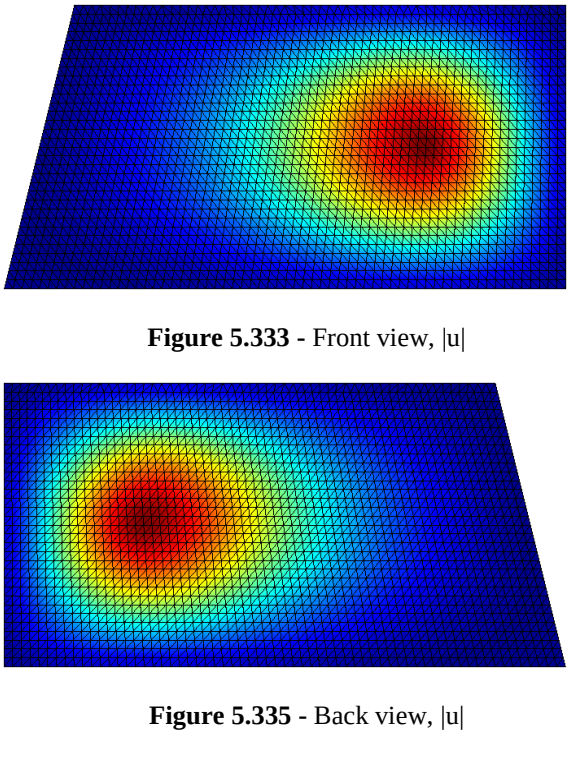

Figure 5.333 - Front view, |u|

Figure 5.335 - Back view, |u|

FEM, 8n

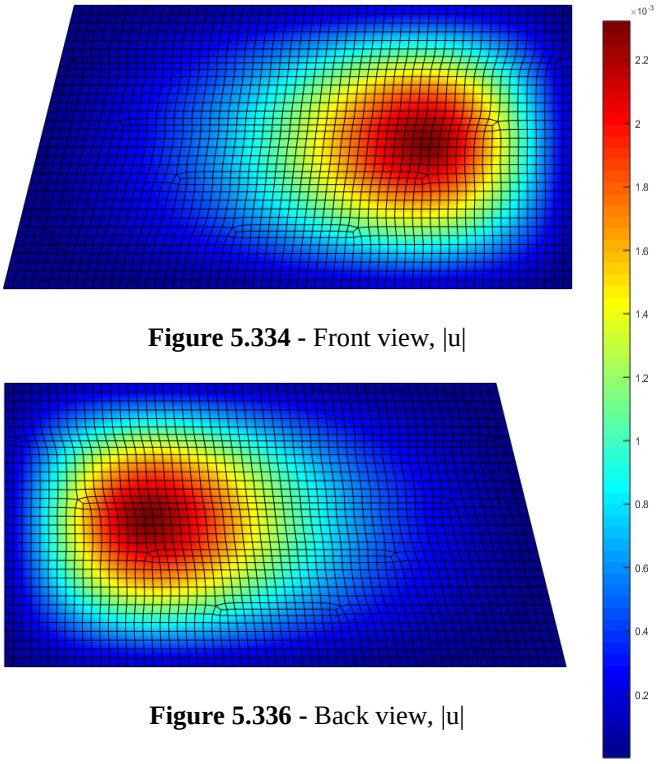

Figure 5.334 - Front view, |u|

Figure 5.336 - Back view, |u|

RPIM

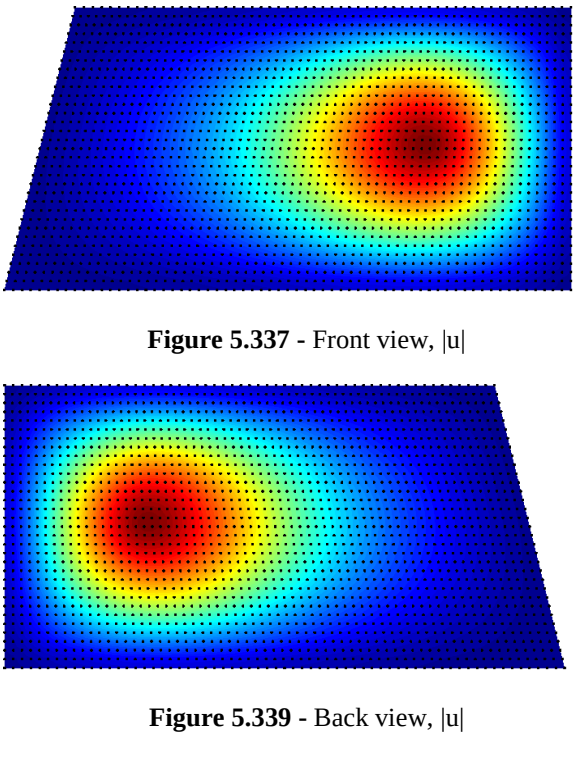

Figure 5.337 - Front view, |u|

Figure 5.339 - Back view, |u|

NNRPIM

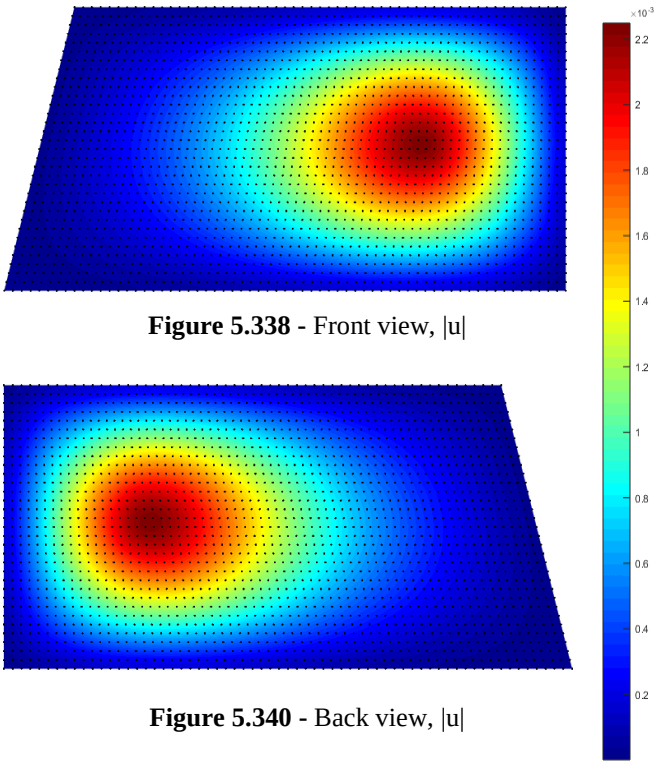

Figure 5.338 - Front view, |u|

Figure 5.340 - Back view, |u|

The following stress field was obtained,

FEM, 4n

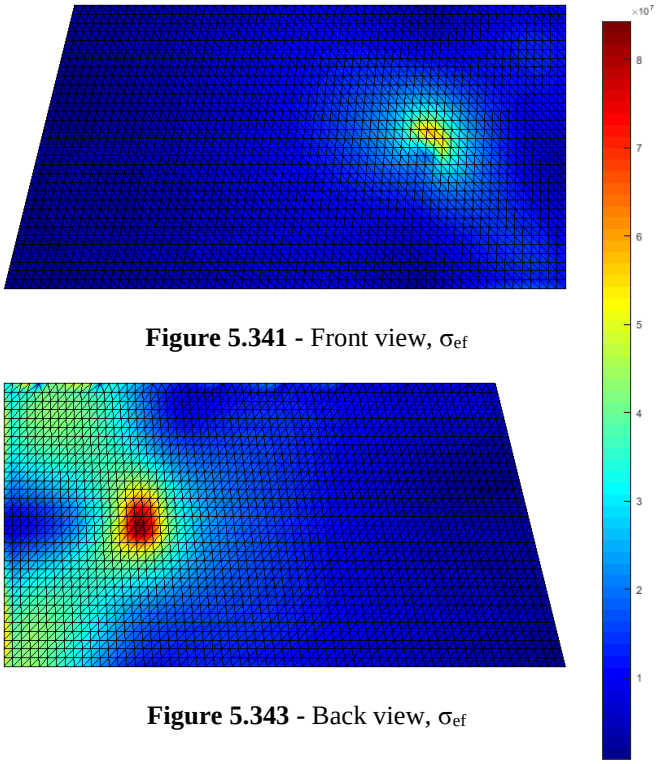

Figure 5.341 - Front view, σ_{ef}

Figure 5.343 - Back view, σ_{ef}

FEM, 8n

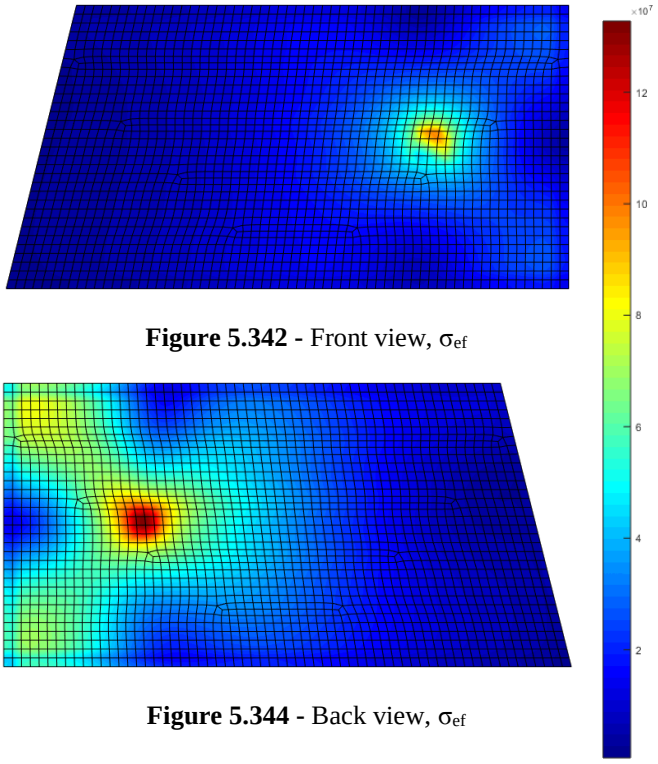

Figure 5.342 - Front view, σ_{ef}

Figure 5.344 - Back view, σ_{ef}

RPIM

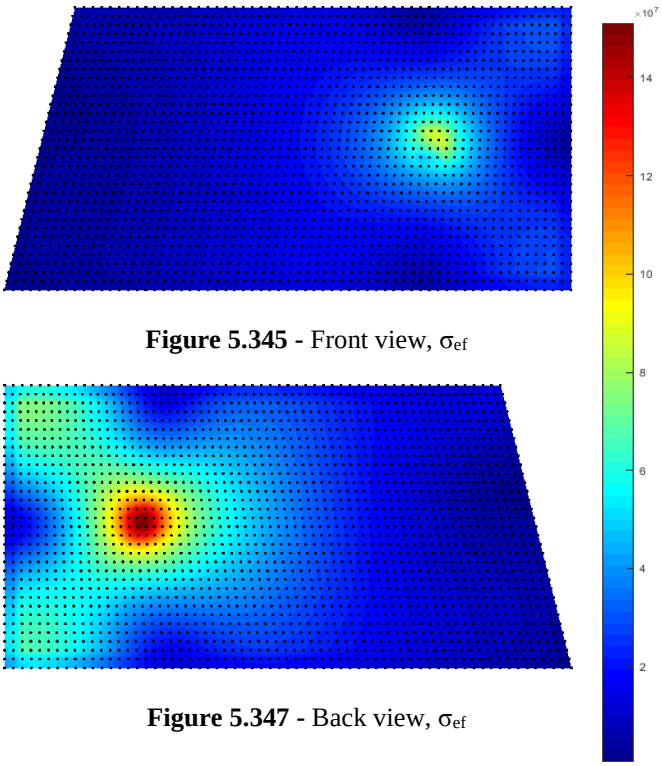

Figure 5.345 - Front view, σ_{ef}

Figure 5.347 - Back view, σ_{ef}

NNRPIM

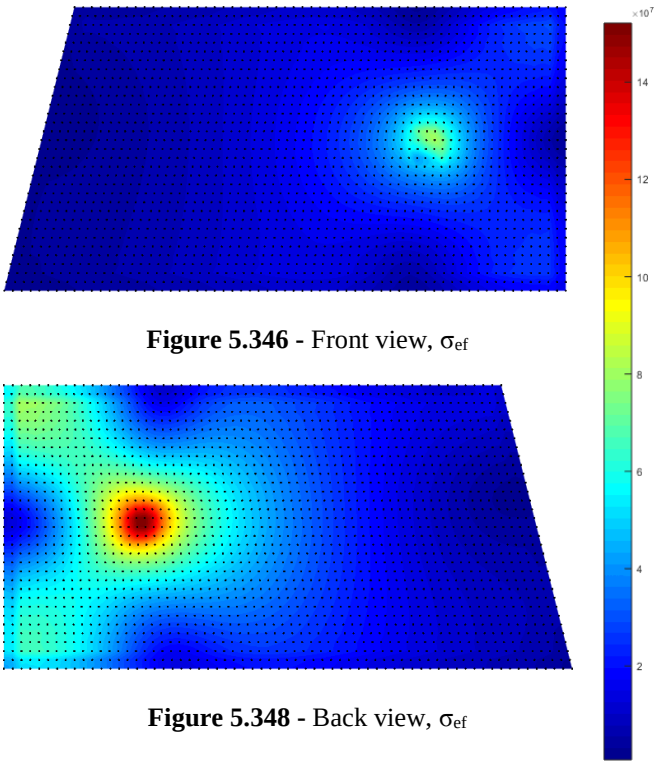

Figure 5.346 - Front view, σ_{ef}

Figure 5.348 - Back view, σ_{ef}

Impact location # 9

The displacement for each impact point was calculated across the thickness and following this, the average of the three nodal displacements discretizing the thickness comes,

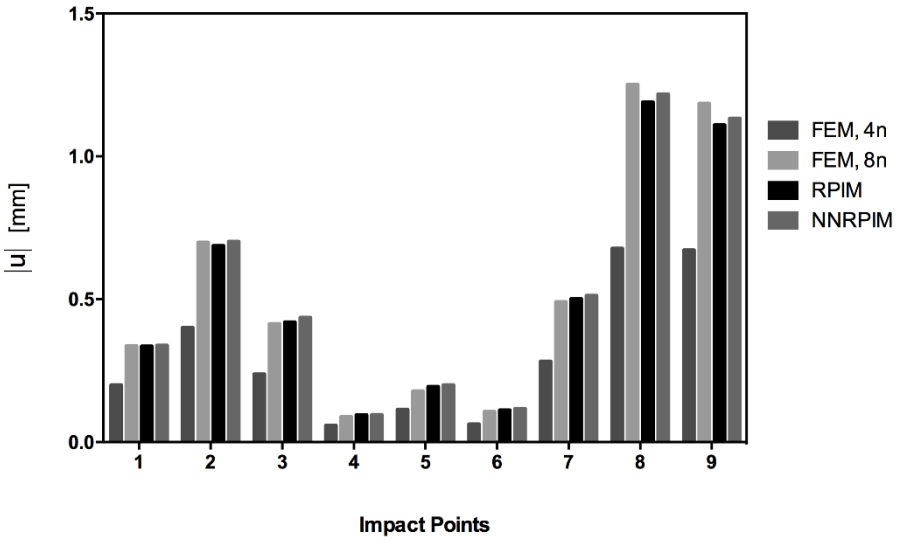

Figure 5.349 - Average nodal displacement along the thickness of each impact location caused by the impact to location 9.

The von Mises stress for each impact point was calculated across the thickness and following this, the average of the three nodal von Mises stresses discretizing the thickness comes,

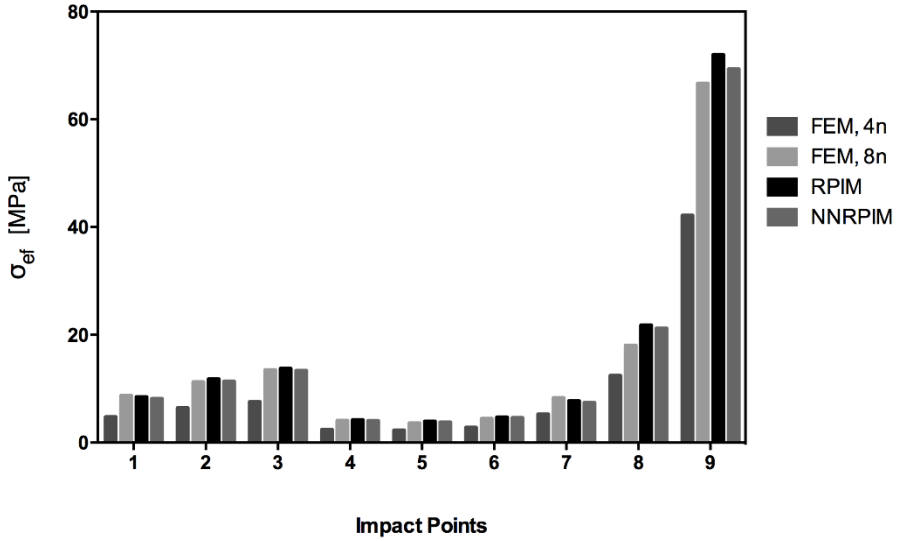

Figure 5.350 - Average nodal stress along the thickness of each impact location caused by the impact to location 9.

The von Mises stress for each node of the ABCD border of the windshield, shown in Figure 5.8, was calculated across the thickness and following this, the average of the three nodal von Mises stresses discretizing the ABCD border thickness comes,

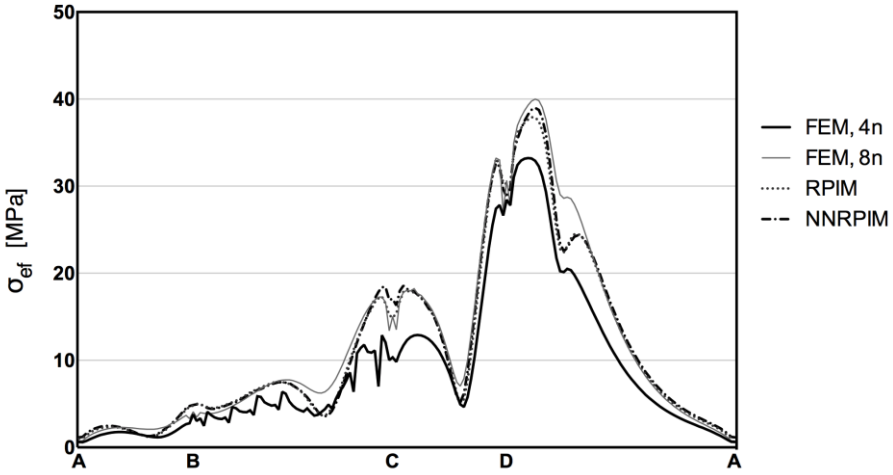

Figure 5.351 - Average nodal stress along the thickness of the clamped section of the windshield caused by the impact to location 9.

The following displacement field was obtained,

FEM, 4n

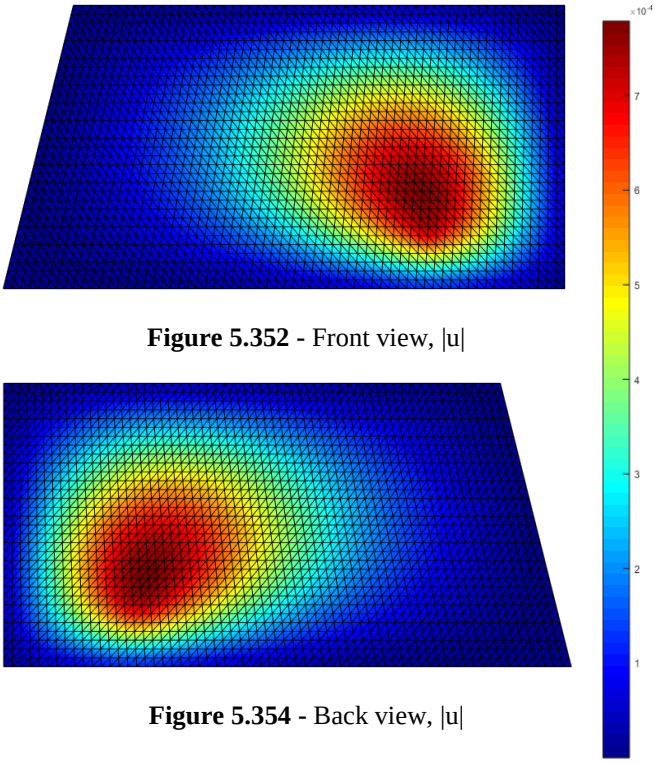

Figure 5.352 - Front view, |u|

Figure 5.354 - Back view, |u|

FEM, 8n

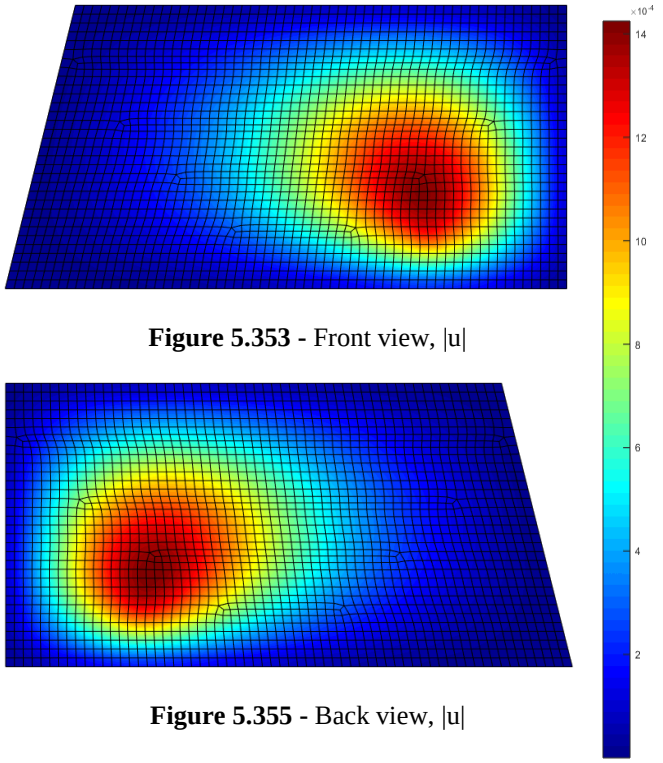

Figure 5.353 - Front view, |u|

Figure 5.355 - Back view, |u|

RPIM

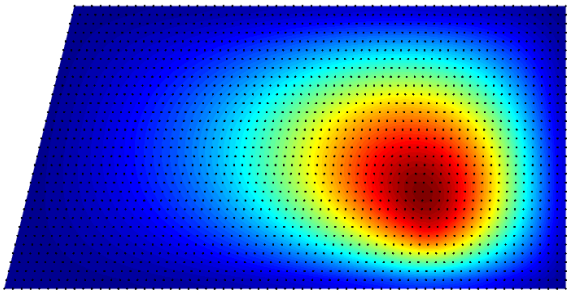

Figure 5.356 - Front view, |u|

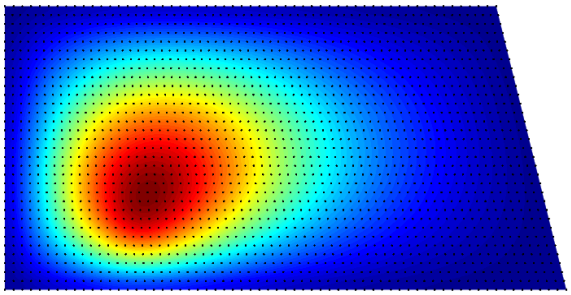

Figure 5.358 - Back view, |u|

NNRPIM

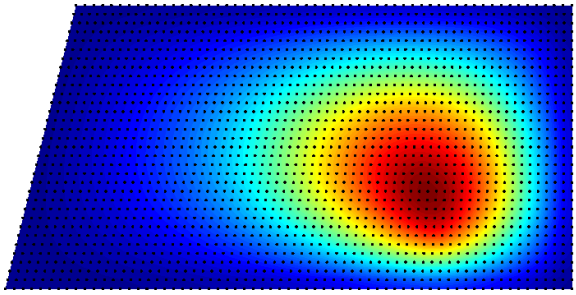

Figure 5.357 - Front view, |u|

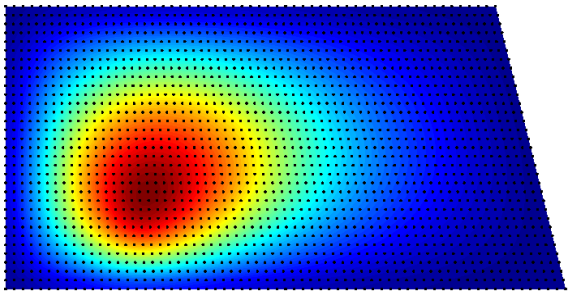

Figure 5.359 - Back view, |u|

The following stress field was obtained,

FEM, 4n

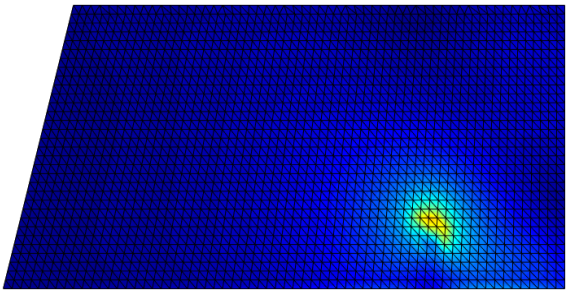

Figure 5.360 - Front view, σ_{ef}

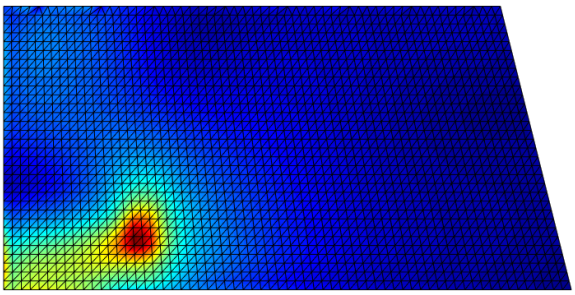

Figure 5.362 - Back view, σ_{ef}

FEM, 8n

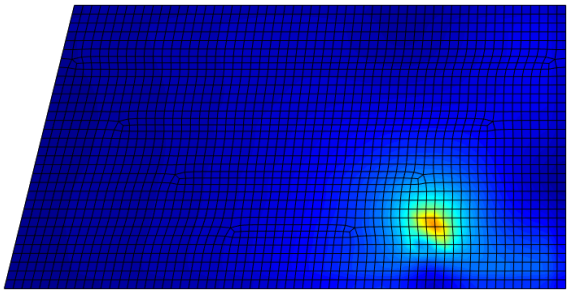

Figure 5.361 - Front view, σ_{ef}

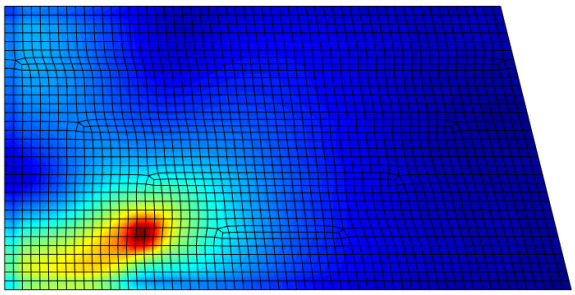

Figure 5.363 - Back view, σ_{ef}

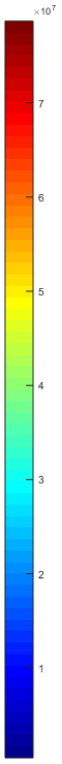

RPIM

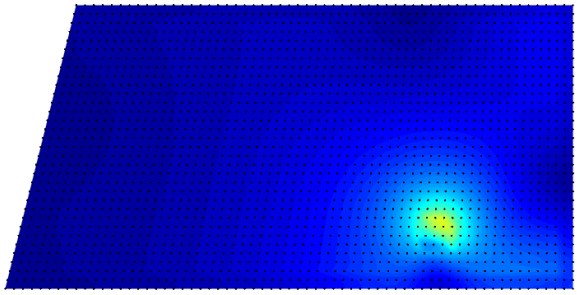

Figure 5.364 - Front view, σ_{ef}

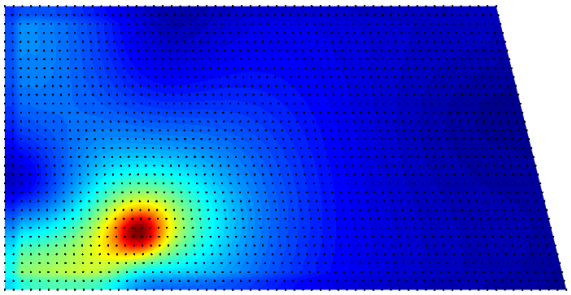

Figure 5.366 - Back view, σ_{ef}

NNRPIM

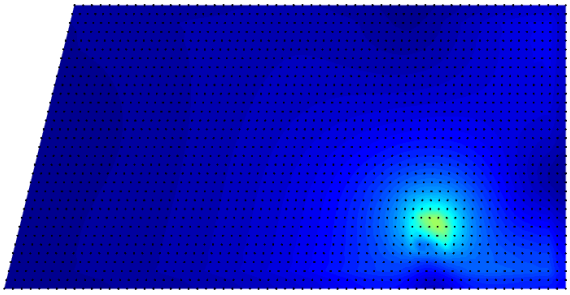

Figure 5.365 - Front view, σ_{ef}

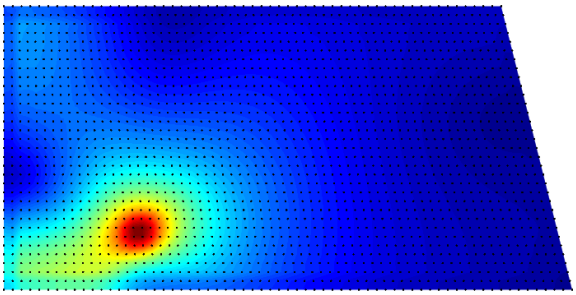

Figure 5.367 - Back view, σ_{ef}

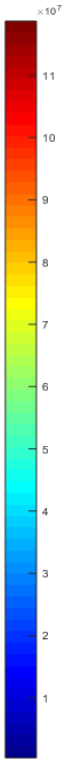

When considering a simply supported approach instead of a clamped approach, there are some expected differences. First, since we're relaxing the boundary conditions, the displacement values verified over the windshield geometry must be higher than the clamped approach. In the clamped approach, the displacement field values become gradually lower, the further it gets from the impact location and closer to the clamped section, in which the displacement is zero. In the simply supported approach, this is also expected but, the distance it takes for the displacement to become close to zero is meant to be larger than the clamped approach. This was verified for every impact location.

Once again, the FEM, 4n displacement and stress values are lower than the ones obtained with the meshless methods. This happens because of the same reasons mentioned for the previously considered clamped approach.

Even though the same occurs in every impact location, it is more prominent when looking at the stress field obtained for impact location #8. By comparing Figure 5.341 to Figures 5.345 and 5.346 as well as Figure 5.343 to Figures 5.347 and 5.348 it is possible to observe several differences between the FEM, 4n and the meshless methods stress field distribution. When looking at the average nodal stress along the thickness of the windshield, it is possible to see that it is often irregular, much more than when compared to the clamped approach.

This happens because of the smoothing of the results, inherent to FEMAS. As explained in Chapter 4, initially the stresses are obtained for the integration points, and then an average is calculated, between all the surrounding integration points. Nodes closer to the boundaries (like the graphs shown) demonstrate more this effect. Since this is a simply supported approach, this effect is exacerbated.

The hexaedral elements mesh once again shows similar results to the ones obtained with the meshless methods in both displacement and stress magnitudes and displacement and stress field distribution.

5.4.2 2D Surrounding structure analysis

The same 2D section used in the previous 2D study was considered and the study was repeated.

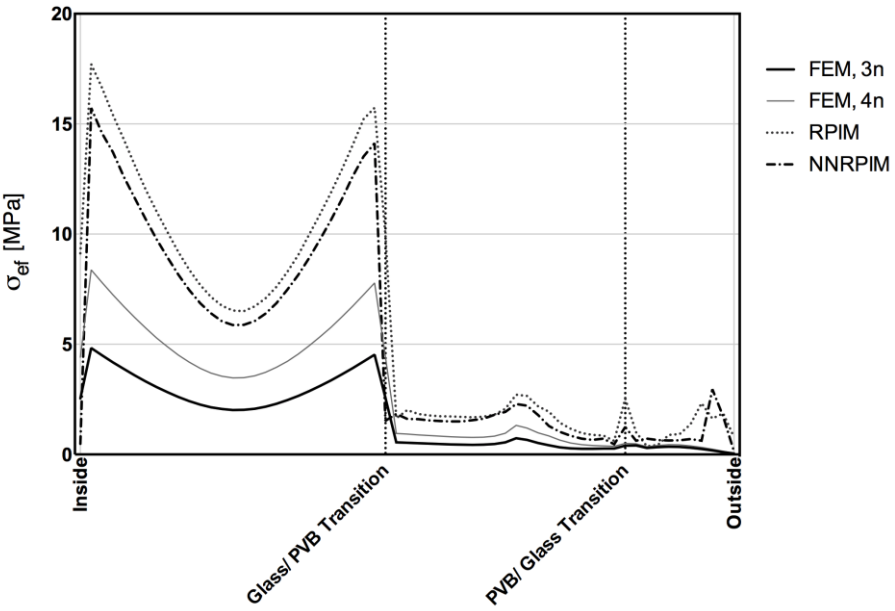

Figure 5.368 - Von Mises stress along the thickness of the clamped section of the windshield.

As expected, with a simple support approach, the stress values along the thickness of the windshield are higher.

They were then compared to the results obtained with the 3D analysis,

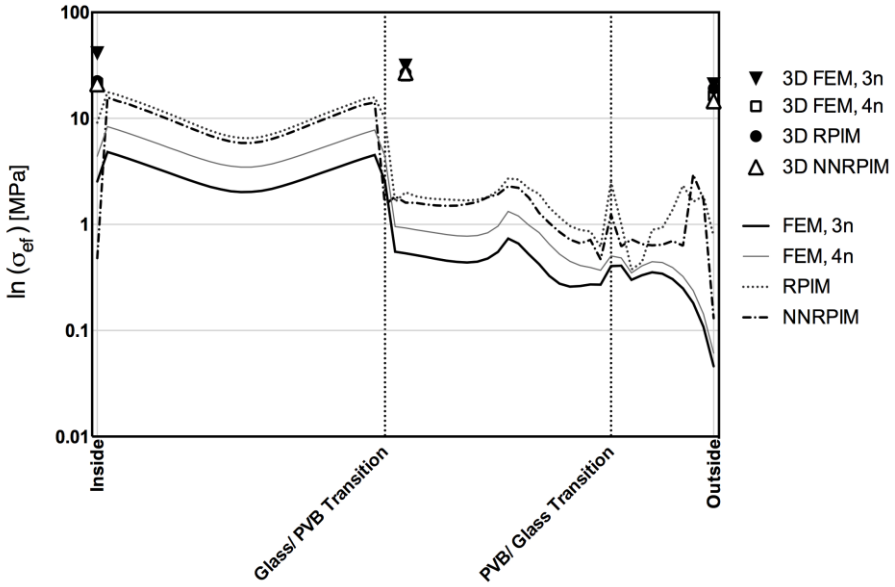

Figure 5.369 – Von Mises stress along stress along the thickness of the clamped section of the windshield with the values obtained in the 3D study for the 3 nodes discretizing the thickness

The results from comparing the 2D with the 3D analysis are much closer when considering the simple support approach. Therefore, it is possible to establish a correlation between the results obtained through the 3D and the 2D studies. The differences observed occur because of the simplifications made in the 2D study.

Chapter 6

Conclusions and Future Works

This work extended for the first time the Radial Point Interpolation Method (RPIM) and the Natural Neighbour Radial Point Interpolation Method (NNRPIM) in the analysis of airplane windshields.

The main conclusions drawn from this work were:

- Meshless methods are a robust and accurate numerical discretization tool which present a linear asymptotic convergence as shown in Chapter 4. Not only are the displacement and stress fields obtained smooth and accurate when compared with the analytical fields but the converged solution is also extremely close to the exact analytical solution as seen in Chapter 4.
- When compared to low order finite element meshes, such as linear triangles and linear quadrilaterals, in 2D analysis and linear tetrahedral and linear hexahedral meshes, in 3D analysis, the meshless methods yield more accurate results, and smoother stress fields.
- The meshless methods converge much faster than the FEM using triangular and tetrahedral element meshes. When compared with the FEM using quadrilateral and hexahedral element meshes the convergence rate is similar.
- Even though, for the same number of nodes, meshless methods require a higher computational time, the same solution can be achieved using fewer nodes than the FEM, using either triangular/ tetrahedral or quadrilateral/ hexahedral element meshes, which means the same accuracy in results can be obtained through a smaller mesh.
- This work shows that meshless methods are an alternative numerical tool to analyse plate sandwich structures using 3D formulations.

In the future, it would be interesting to continue this work, only this time using a different approach, which is possible because of the recent developments to FEMAS:

- Consider the different materials constituting both the windshield and its surrounding structure as visco-elastic.
- Perform a free vibration analysis.
- Perform a transient dynamic analysis including explicitly the bird impact.
- Compare the results obtained numerically with the ones obtained from experimental testing.

References

1. Hedayati R, Sadighi M. Bird Strike: An Experimental, Theoretical and Numerical Investigation: Elsevier Science; 2015.
2. Organization ICA. ICAO Safety Report. Montreal, Canada: 2015.
3. Agency EAS. Bird Strike Damage & Windshield Bird Strike. 2009.
4. MacKinnon B. Sharing the Skies: an aviation industry guide to the management of wildlife hazards: Transport Canada. Civil Aviation.; 2004. 366 p.
5. Huebner KH. The Finite Element Method for Engineers: Wiley; 2001.
6. Turner MJ. Stiffness and Deflection Analysis of Complex Structures. Journal of the Aeronautical Sciences. 1956 1956/09/01;23(9):805-23.
7. Reddy J. An Introduction to the Finite Element Method: McGraw-Hill Education; 2005.
8. Belytschko T, Krongauz Y, Organ D, Fleming M, Krysl P. Meshless methods: An overview and recent developments. Computer Methods in Applied Mechanics and Engineering. 1996 12/15/;139(1–4):3-47.
9. Nguyen VP, Rabczuk T, Bordas S, Duflot M. Meshless methods: A review and computer implementation aspects. Mathematics and Computers in Simulation. 2008 12/1/;79(3):763-813.
10. Gingold RA, Monaghan JJ. Smoothed particle hydrodynamics-theory and application to non-spherical stars. Monthly Notices of the Royal Astronomical Society. 1977 //;181:375-89.
11. Libersky LD, Petschek AG. Smooth particle hydrodynamics with strength of materials. In: Trease H, Fritts M, Crowley WP, editors. Advances in the Free-Lagrange Method Including Contributions on Adaptive Gridding and the Smooth Particle Hydrodynamics Method. Lecture Notes in Physics. 395: Springer Berlin Heidelberg; 1991. p. 248-57.
12. Belytschko T, Lu YY, Gu L. Element-free Galerkin methods. Int J Numer Meth Engng. 1994 01/30/;37(2):229-56.
13. Lancaster P, Salkauskas K. Surfaces Generated by Moving Least Squares Methods. Mathematics of Computation. 1981 //;37(155):141-58.
14. Nayroles B, Touzot G, Villon P. {Generalizing the finite element method: diffuse approximation and diffuse elements}. Computational mechanics. 1992 //;10(5):307-18.
15. Liu WK, Jun S, Li S, Adee J, Belytschko T. Reproducing Kernel Particle Methods for Structural Dynamics. International Journal for Numerical Methods in Engineering. 1995 //;38:1655-79.
16. Atluri SN, Zhu T. A new Meshless Local Petrov-Galerkin (MLPG) approach in computational mechanics. Computational Mechanics. 1998 08/04/;22(2):117-27.
17. Liu G-R, Gu Y. A point interpolation method for two-dimensional solids. International Journal for Numerical Methods in Engineering. 2001;50(4):937-51.
18. Wang JG, Liu GR, Wu YG. A point interpolation method for simulating dissipation process of consolidation. Computer Methods in Applied Mechanics and Engineering. 2001 8/31/;190(45):5907-22.
19. Wang JG, Liu GR. A point interpolation meshless method based on radial basis functions. International Journal for Numerical Methods in Engineering. 2002;54(11):1623-48.

20. Wang JG, Liu GR. On the optimal shape parameters of radial basis functions used for 2-D meshless methods. Computer Methods in Applied Mechanics and Engineering. 2002 3/29/;191(23–24):2611-30.
21. Belinha J. The natural neighbour radial point interpolation method : solid mechanics and mechanobiology applications. Porto: FEUP; 2010.
22. Dinis LMJS, Jorge RMN, Belinha J. Analysis of 3D solids using the natural neighbour radial point interpolation method. Computer Methods in Applied Mechanics and Engineering. 2007 3/1/;196(13–16):2009-28.
23. Dinis LMJS, Jorge RMN, Belinha J. Analysis of plates and laminates using the natural neighbour radial point interpolation method. Engineering Analysis with Boundary Elements. 2008 3//;32(3):267-79.
24. Dinis LMJS, Jorge RMN, Belinha J. An Unconstrained Third-Order Plate Theory Applied to Functionally Graded Plates Using a Meshless Method. Mechanics of Advanced Materials and Structures. 2010 2010/01/29;17(2):108-33.
25. Dinis LMJS, Jorge RMN, Belinha J. A 3D shell-like approach using a natural neighbour meshless method: Isotropic and orthotropic thin structures. Composite Structures. 2010 4//;92(5):1132-42.
26. Dinis L, Jorge R, Belinha J. Composite Laminated Plates: A 3D Natural Neighbor Radial Point Interpolation Method Approach%J Journal Of Sandwich Structures & Materials. 8th International Conference on Sandwich Structures (ICSS-08). 2010;12(2):119-38 (20) 20.
27. Dinis LMJS, Jorge RMN, Belinha J. The natural neighbour radial point interpolation method: dynamic applicationsnull. Engineering Computations. 2009 2009/11/13;26(8):911-49.
28. Dinis LMJS, Jorge RMN, Belinha J. Static and dynamic analysis of laminated plates based on an unconstrained third order theory and using a radial point interpolator meshless method. Computers & Structures. 2011 10//;89(19–20):1771-84.
29. Dinis LMJS, Jorge RMN, Belinha J. A natural neighbour meshless method with a 3D shell-like approach in the dynamic analysis of thin 3D structures. Thin-Walled Structures. 2011 1//;49(1):185-96.
30. Dinis LMJS, Jorge RMN, Belinha J. The Dynamic Analysis of Thin Structures Using a Radial Interpolator Meshless Method. In: Vasques CMA, Dias Rodrigues J, editors. Vibration and Structural Acoustics Analysis: Current Research and Related Technologies. Dordrecht: Springer Netherlands; 2011. p. 1-20.
31. Dinis LMJS, Jorge RMN, Belinha J. The Radial Natural Neighbours Interpolators Extended to ElastoplastiCity. In: Ferreira AJM, Kansa EJ, Fasshauer GE, Leitão VMA, editors. Progress on Meshless Methods. Dordrecht: Springer Netherlands; 2009. p. 175-98.
32. Belinha J, Dinis LMJS, Jorge RMN. Analysis of thick plates by the natural radial element method. International Journal of Mechanical Sciences. 2013 11//;76:33-48.
33. Moreira S, Belinha J, Dinis L, Natal Jorge R. Analysis of Laminated Beams Using the Natural Neighbour Radial Point Interpolation Method%J Revista Internacional de Metodos Numericos Para Calculo Y Diseno En Ingenieria. 2014;30(2):108-20 (13) 13.
34. Dinis L, Jorge R, Belinha J. Large deformation applications with the radial natural neighbours interpolators. Computer Modeling in Engineering and Sciences (CMES). 2009;44(1):1.
35. Belinha J. Meshless Methods in Biomechanics: Bone Tissue Remodelling Analysis: Springer International Publishing; 2014.

36. Belinha J, Jorge RMN, Dinis LMJS. Bone tissue remodelling analysis considering a radial point interpolator meshless method. Engineering Analysis with Boundary Elements. 2012 11//;36(11):1660-70.
37. Belinha J, Jorge RMN, Dinis LMJS. A meshless microscale bone tissue trabecular remodelling analysis considering a new anisotropic bone tissue material law. Computer Methods in Biomechanics and Biomedical Engineering. 2013 2013/11/01;16(11):1170-84.
38. Moreira S, Belinha J, Dinis L, Natal Jorge R. A Global Numerical Analysis of the "central Incisor / Local Maxillary Bone" System Using a Mesh Less Method%J Molecular & Cellular Biomechanics. 2014;11(3):151-84 (34) 34.
39. Belinha J, Dinis LMJS, Jorge RMN. The Mandible Remodelling Induced by Dental Implants: A Meshless Approach. Journal of Mechanics in Medicine and Biology. 2015 2015/08/01;15(04):1550059.
40. Belinha J, Dinis LMJS, Jorge RMN. The Meshless Methods in the Bone Tissue Remodelling Analysis. Procedia Engineering. 2015 //;110:51-8.
41. Tavares CSS, Belinha J, Dinis LMJS, Jorge RMN. The Elasto-plastic Response of the Bone Tissue Due to the Insertion of Dental Implants. Procedia Engineering. 2015 //;110:37-44.
42. Belinha J, Dinis LMJS, Jorge RMN. The analysis of the bone remodelling around femoral stems: A meshless approach. Mathematics and Computers in Simulation. 2016 3//;121:64-94.
43. Duarte HMS, Andrade JR, Dinis LMJS, Jorge RMN, Belinha J. Numerical analysis of dental implants using a new advanced discretization technique. Mechanics of Advanced Materials and Structures. 2016 2016/04/02;23(4):467-79.
44. Farahani BV, Berardo JM, Drgas R, César de Sá JMA, Ferreira AJM, Belinha J. The Axisymmetric Analysis of Circular Plates Using the Radial Point Interpolation Method. International Journal for Computational Methods in Engineering Science and Mechanics. 2015 2015/11/02;16(6):336-53.
45. Azevedo JMC, Belinha J, Dinis LMJS, Jorge RMN. Crack path prediction using the natural neighbour radial point interpolation method. Engineering Analysis with Boundary Elements. 2015 10//;59:144-58.
46. Chen J-S, Wu C-T, Yoon S, You Y. A stabilized conforming nodal integration for Galerkin mesh-free methods. International Journal for Numerical Methods in Engineering. 2001;50(2):435-66.
47. Elmer W, Chen JS, Puso M, Taciroglu E. A stable, meshfree, nodal integration method for nearly incompressible solids. Finite Elements in Analysis and Design. 2012 4//;51:81-5.
48. Sze KY, Chen JS, Sheng N, Liu XH. Stabilized conforming nodal integration: exactness and variational justification. Finite Elements in Analysis and Design. 2004 11//;41(2):147-71.
49. Wriggers P. Computational Contact Mechanics: Springer Berlin Heidelberg; 2006.
50. Sibson R. A vector identity for the Dirichlet tessellation. Mathematical Proceedings of The Cambridge Philosophical Society. 1980;87(01).
51. Moreira SF. Elastoplastic analysis using the Natural Neighbour Radial Point Interpolation Method. Porto: FEUP; 2013.
52. Timoshenko S, Goodier JN. Theory of elasticity: McGraw-Hill; 1969.
53. Quek SS, Liu GR. Finite Element Method: A Practical Course: Elsevier Science; 2003.
54. Compliance with CS-25 Bird Strike Requirements, (2011).

55. Brady C. The Boeing 737 Technical Guide: Tech Pilot Services, Limited; 2008.
56. Wurm J. Glass Structures: Design and Construction of Self-supporting Skins: Boston; 2007.
57. Xu J, Li Y, Ge D, Liu B, Zhu M. Experimental investigation on constitutive behavior of PVB under impact loading. International Journal of Impact Engineering. 2011 2//;38(2–3):106-14.
58. Wei J, Dharani LR. Fracture mechanics of laminated glass subjected to blast loading. Theoretical and Applied Fracture Mechanics. 2005 11//;44(2):157-67.
59. Dazet F, Chaumel P, Cavailles G, Beucher JC. Aircraft windshield attachment device. Google Patents; 2003.
60. Esmaeili F, Chakherlou TN, Zehsaz M. Prediction of fatigue life in aircraft double lap bolted joints using several multiaxial fatigue criteria. Materials & Design. 2014 7//;59:430-8.
61. ASM Aerospace Specification Metals I. Aluminum 2024-T4; 2024-T351 2016. Available from: http://asm.matweb.com/search/SpecificMaterial.asp?bassnum=MA2024T4.
62. Mittal KL, Pizzi A. Handbook of sealant technology: CRC Press; 2009.
63. Bondi S, McClelland N. Capturing structural silicone non-linear behaviour via the finite element method. Glass Processing Days 2009. 2009:183-5.
64. ASM Aerospace Specification Metals I. Aluminum 7075-T73; 7075-T735x 2016. Available from: http://asm.matweb.com/search/SpecificMaterial.asp?bassnum=MA7075T73.
65. Wang FS, Yue ZF. Numerical simulation of damage and failure in aircraft windshield structure against bird strike. Materials & Design. 2010 2//;31(2):687-95.
66. Benzley SE, Perry E, Merkley K, Clark B, Sjaardama G, editors. A comparison of all hexagonal and all tetrahedral finite element meshes for elastic and elasto-plastic analysis.
67. Wang E, Nelson T, Rauch R, editors. Back to elements-tetrahedra vs. hexahedra.